diagram in Fig. 8 assumes that for correct $Q$ the output of the $Q$ model is $K$ times as large as its input so that for correct $Q$ the inputs of the comparator are equal. The DC error signal $V_Q$ resulting from the comparison is fed back to the $Q$ model circuit to adjust the bias voltages appropriately, as well as to the filter. In these two interacting control loops, the frequency loop will converge independently of the $Q$ control loop, but to converge on the correct value of $Q$, the frequency must be accurate. Hence, the two loops must operate together. The correct operation and convergence of the frequency and $Q$ control scheme in Fig. 8 has been verified by experiments (see Schaumann et al. [3], Chapter 7, pp. 410–486) but because of the increased noise, power consumption, and chip area needed for the control circuitry, the method has not found its way into commercial applications.

## BIBLIOGRAPHY


1. G. Moschytz, *Linear Integrated Networks: Design*, Van Nostrand-Reinhold, New York, 1975.
2. P. Bowron and F. W. Stevenson, *Active Filters for Communications and Instrumentation*, McGraw-Hill, Maidenhead, UK, 1979.
3. R. Schaumann, M.S. Ghausi, and K.R. Laker, *Design of Analog Filters: Passive, Active RC and Switched Capacitor*, Prentice-Hall, Englewood Cliffs, NJ, 1990.
4. W. E. Heinlein and W. H. Holmes, *Active Filters for Integrated Circuits*, R. Oldenburg, Munich, 1974.
5. E. Christian, *LC Filters: Design, Testing and Manufacturing*, Wiley, New York, 1983.
6. D. A. Johns and K. Martin, *Analog Integrated Circuit Design*, Wiley, New York, 1997.
7. Y. Tsividis and J. A. Voorman, eds., *Integrated Continuous-Time Filters: Principles, Design and Implementations*, IEEE Press, Piscataway, NJ, 1993.
8. J. F. Parker and K. W. Current, A CMOS continuous-time bandpass filter with peak-detection-based automatic tuning, *Int. J. Electron.* **1996**(5):551–564 (1996).


# CIRCULAR WAVEGUIDES[1]


CONSTANTINE A. BALANIS
Arizona State University
Tempe, Arizona
(edited by Eric Holzman
Northrop Grumman Electronic
Systems, Baltimore, Maryland)


## 1. INTRODUCTION

The circular waveguide is occasionally used as an alternative to the rectangular waveguide. Like other waveguides constructed from a single, enclosed conductor, the circular waveguide supports transverse electric (TE) and transverse magnetic (TM) modes. These modes have a cutoff frequency, below which electromagnetic energy is severely attenuated. Circular waveguide's round cross section makes it easy to machine, and it is often used to feed conical horns. Further, the $TE_{0n}$ modes of circular waveguide have very low attenuation. A disadvantage of circular waveguide is its limited dominant mode bandwidth, which, compared to rectangular waveguide's maximum bandwidth of 2–1, is only 1.3. In addition, the polarization of the dominant mode is arbitrary, so that discontinuities can easily excite unwanted cross-polarized components.

In this article, the electromagnetic features of the circular waveguide are summarized, including the transverse and longitudinal fields, the cutoff frequencies, the propagation and attenuation constants, and the wave impedances of all transverse electric and transverse magnetic modes.

## 2. TRANSVERSE ELECTRIC ($TE^z$) MODES

The transverse electric to $z$ ($TE^z$) modes can be derived by letting the vector potential $\mathbf{A}$ and $\mathbf{F}$ be equal to

$$\mathbf{A} = 0 \tag{1a}$$

$$\mathbf{F} = \hat{a}_z F_z(\rho, \phi, z) \tag{1b}$$

The vector potential $\mathbf{F}$ must satisfy the vector wave equation, which reduces the $\mathbf{F}$ of (1b) to

$$\nabla^2 F_z(\rho, \phi, z) + \beta^2 F_z(\rho, \phi, z) = 0 \tag{2}$$

When expanded in cylindrical coordinates, (2) reduces to

$$\frac{\partial^2 F_z}{\partial \rho^2} + \frac{1}{\rho}\frac{\partial F_z}{\partial \rho} + \frac{1}{\rho^2}\frac{\partial^2 F_z}{\partial \phi^2} + \frac{\partial^2 F_z}{\partial z^2} + \beta^2 F_z = 0 \tag{3}$$

whose solution for the geometry of Fig. 1 is of the form

$$\begin{aligned} F_z(\rho, \phi, z) = {} & [A_1 J_m(\beta_\rho \rho) + B_1 Y_m(\beta_\rho \rho)] \\ & \times [C_2 \cos(m\phi) + D_2 \sin(m\phi)] \\ & \times [A_3 e^{-j\beta_z z} + B_3 e^{+j\beta_z z}] \end{aligned} \tag{4a}$$

where

$$\beta_\rho^2 + \beta_z^2 = \beta^2 \tag{4b}$$

The constants $A_1$, $B_1$, $C_2$, $D_2$, $A_3$, $B_3$, $m$, $\beta_\rho$, and $\beta_z$ can be found using the boundary conditions of

$$E_\phi(\rho = a, \phi, z) = 0 \tag{5a}$$

The fields must be finite everywhere (5b)

The fields must repeat every $2\pi$ radians in $\phi$ (5c)

[1]This article is derived from material in *Advanced Engineering Electromagnetics*, by Constantine Balanis, Wiley, New York, 1989, Sect. 9.2.

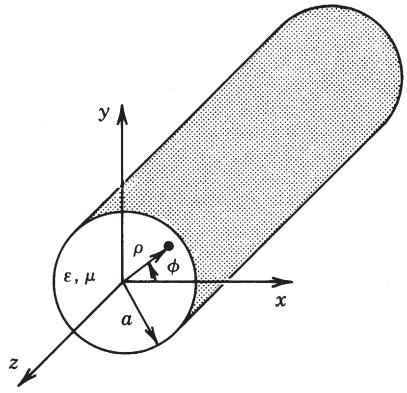


**Figure 1.** Cylindrical waveguide of circular cross section.

According to (5b), $B_1 = 0$ since $Y_m(\rho = 0) = \infty$. In addition, according to (5c)

$$m = 0, 1, 2, 3, \ldots \tag{6}$$

Consider waves that propagate only in the $+z$ direction. Then (4) reduces to

$$F_z^+(\rho, \phi, z) = A_{mn} J_m(\beta_\rho \rho)[C_2 \cos(m\phi) + D_2 \sin(m\phi)]e^{-j\beta_z z} \tag{7}$$

From Eq. (7), the electric field component of $E_\phi^+$ can be written as

$$E_\phi^+ = \frac{1}{\varepsilon}\frac{\partial F_z^+}{\partial \rho} = \beta_\rho \frac{A_{mn}}{\varepsilon} J_m'(\beta_\rho \rho)[C_2 \cos(m\phi) + D_2 \sin(m\phi)]e^{-j\beta_z z} \tag{8a}$$

where

$$' = \frac{\partial}{\partial(\beta_\rho \rho)} \tag{8b}$$

Applying the boundary condition of (5a) in (8a), we then have that

$$E_\phi^+(\rho = a, \phi, z) = \beta_\rho \frac{A_{mn}}{\varepsilon} J_m'(\beta_\rho a)[C_2 \cos(m\phi) + D_2 \sin(m\phi)]e^{-j\beta_z z} = 0 \tag{9}$$

which is satisfied only provided that

$$J_m'(\beta_\rho a) = 0 \Rightarrow \beta_\rho a = \chi_{mn}' \Rightarrow \beta_\rho = \frac{\chi_{mn}'}{a} \tag{10}$$

In (10) $\chi_{mn}'$ represents the $n$th zero ($n = 1, 2, 3, \ldots$) of the derivative of the Bessel function $J_m$ of the first kind of order $m (m = 0, 1, 2, 3, \ldots)$. An abbreviated list of the zeros $\chi_{mn}'$ of the derivative $J_m'$ of the Bessel function $J_m$ is found in Table 1. The smallest value of $\chi_{mn}'$ is 1.8412 ($m = 1$, $n = 1$).

Using (4b) and (10), $\beta_z$ of the $mn$ mode can be written as

$$(\beta_z)_{mn} = \begin{cases} \sqrt{\beta^2 - \beta_\rho^2} = \sqrt{\beta^2 - \left(\frac{\chi_{mn}'}{a}\right)^2} \\ \text{when } \beta > \beta_\rho = \dfrac{\chi_{mn}'}{a} \end{cases} \tag{11a}$$

$$(\beta_z)_{mn} = \begin{cases} 0 \quad \text{when } \beta = \beta_c = \beta_\rho = \dfrac{\chi_{mn}'}{a} \end{cases} \tag{11b}$$

$$(\beta_z)_{mn} = \begin{cases} -j\sqrt{\beta_\rho^2 - \beta^2} = -j\sqrt{\left(\frac{\chi_{mn}'}{a}\right)^2 - \beta^2} \\ \text{when } \beta < \beta_\rho = \dfrac{\chi_{mn}'}{a} \end{cases} \tag{11c}$$

Cutoff is defined when $(\beta_z)_{mn} = 0$. Thus, according to (11b)

$$\beta_c = \omega_c \sqrt{\mu\varepsilon} = 2\pi f_c \sqrt{\mu\varepsilon} = \beta_\rho = \frac{\chi_{mn}'}{a} \tag{12a}$$

$$(f_c)_{mn} = \frac{\chi_{mn}'}{2\pi a \sqrt{\mu\varepsilon}} \tag{12b}$$

By using (12a) and (12b), we can write (11a)–(11c) as

$$(\beta_z)_{mn} = \begin{cases} \sqrt{\beta^2 - \beta_\rho^2} = \beta\sqrt{1 - \left(\frac{\beta_\rho}{\beta}\right)^2} = \beta\sqrt{1 - \left(\frac{\beta_c}{\beta}\right)^2} \\ = \beta\sqrt{1 - \left(\frac{\chi_{mn}'}{\beta a}\right)^2} = \beta\sqrt{1 - \left(\frac{f_c}{f}\right)^2} \\ \text{when } f > f_c = (f_c)_{mn} \end{cases} \tag{13a}$$

$$(\beta_z)_{mn} = \{ 0 \quad \text{when } f = f_c = (f_c)_{mn} \tag{13b}$$

**Table 1. Zeros $\chi'_{mn}$ of Derivative $J'_m(\chi'_{mn}) = 0$ ($n = 1,2,3,\ldots$) of Bessel Function $J_m(x)$**

| | $m=0$ | $m=1$ | $m=2$ | $M=3$ | $m=4$ | $m=5$ | $m=6$ | $m=7$ | $m=8$ | $m=9$ | $m=10$ | $m=11$ |
|---|---|---|---|---|---|---|---|---|---|---|---|---|
| $n=1$ | 3.8318 | 1.8412 | 3.0542 | 4.2012 | 5.3175 | 6.4155 | 7.5013 | 8.5777 | 9.6474 | 10.7114 | 11.7708 | 12.8264 |
| $n=2$ | 7.0156 | 5.3315 | 6.7062 | 8.0153 | 9.2824 | 10.5199 | 11.7349 | 12.9324 | 14.1155 | 15.2867 | 16.4479 | 17.6003 |
| $n=3$ | 10.1735 | 8.5363 | 9.9695 | 11.3459 | 12.6819 | 13.9872 | 15.2682 | 16.5294 | 17.7740 | 19.0046 | 20.2230 | 21.4309 |
| $n=4$ | 13.3237 | 11.7060 | 13.1704 | 14.5859 | 15.9641 | 17.3129 | 18.6375 | 19.9419 | 21.2291 | 22.5014 | 23.7607 | 25.0085 |
| $n=5$ | 16.4706 | 14.8636 | 16.3475 | 17.7888 | 19.1960 | 20.5755 | 21.9317 | 23.2681 | 24.5872 | 25.8913 | 27.1820 | 28.4609 |

$$(\beta_z)_{mn}=\begin{cases}-j\sqrt{\beta_\rho^2-\beta^2}=-j\beta\sqrt{\left(\dfrac{\beta_\rho}{\beta}\right)^2-1}=-j\beta\sqrt{\left(\dfrac{\beta_c}{\beta}\right)^2-1}\\ =-j\beta\sqrt{\left(\dfrac{\chi'_{mn}}{\beta a}\right)^2-1}=-j\beta\sqrt{\left(\dfrac{f_c}{f}\right)^2-1}\\ \text{when } f<f_c=(f_c)_{mn}\end{cases}\tag{13c}$$

The guide wavelength $\lambda_g$ is defined as

$$(\lambda_g)_{mn}=\frac{2\pi}{(\beta_z)_{mn}}\tag{14a}$$

which, according to (13a) and (13b), can be written as

$$(\lambda_g)_{mn}=\begin{cases}\dfrac{2\pi}{\beta\sqrt{1-\left(\dfrac{f_c}{f}\right)^2}}=\dfrac{\lambda}{\sqrt{1-\left(\dfrac{f_c}{f}\right)^2}} & \text{when } f>f_c=(f_c)_{mn}\end{cases}\tag{14b}$$

$$(\lambda_g)_{mn}=\{\infty \text{ when } f=(f_c)_{mn}\tag{14c}$$

In (14b) $\lambda$ is the wavelength of the wave in an infinite medium of the kind that exists inside the waveguide. There is no definition of the wavelength below cutoff since the wave is exponentially decaying and there is no repetition of its waveform.

According to (12b) and the values of $\chi'_{mn}$ in Table 1, the order (lower to higher cutoff frequencies) in which the $TE^z_{mn}$ modes occur is $TE^z_{11}$, $TE^z_{21}$, $TE^z_{01}$, and so on. It should be noted that for a circular waveguide, the order in which the $TE^z_{mn}$ modes occur does not change, and the bandwidth between modes is also fixed. For example, the bandwidth of the first single-mode $TE^z_{11}$ operation is $3.042/1.8412=1.6588:1$, which is less than $2:1$. This bandwidth is fixed and cannot be varied. A change in the radius only varies, by the same amount, the absolute values of the cutoff frequencies of all the modes but does not alter their order or relative bandwidth.

The electric and magnetic field components can be written from Eq. (7) as

$$\begin{aligned}E_\rho^+&=-\frac{1}{\varepsilon\rho}\frac{\partial F_z^+}{\partial\phi}\\&=-A_{mn}\frac{m}{\varepsilon\rho}J_m(\beta_\rho\rho)[-C_2\sin(m\phi)\\&\quad+D_2\cos(m\phi)]e^{-j\beta_z z}\end{aligned}\tag{15a}$$

$$\begin{aligned}E_\phi^+&=\frac{1}{\varepsilon}\frac{\partial F_z^+}{\partial\rho}\\&=A_{mn}\frac{\beta_\rho}{\varepsilon}J'_m(\beta_\rho\rho)[C_2\cos(m\phi)\\&\quad+D_2\sin(m\phi)]e^{-j\beta_z z}\end{aligned}\tag{15b}$$

$$E_z^+=0\tag{15c}$$

$$\begin{aligned}H_\rho^+&=-j\frac{1}{\omega\mu\varepsilon}\frac{\partial^2F_z^+}{\partial\rho\partial z}\\&=-A_{mn}\frac{\beta_\rho\beta_z}{\omega\mu\varepsilon}J'_m(\beta_\rho\rho)[C_2\cos(m\phi)\\&\quad+D_2\sin(m\phi)]e^{-j\beta_z z}\end{aligned}\tag{15d}$$

$$\begin{aligned}H_\phi^+&=-j\frac{1}{\omega\mu\varepsilon}\frac{1}{\rho}\frac{\partial^2F_z^+}{\partial\phi\partial z}=-A_{mn}\frac{m\beta_z}{\omega\mu\varepsilon}\frac{1}{\rho}J_m(\beta_\rho\rho)\\&\quad\times[-C_2\sin(m\phi)+D_2\cos(m\phi)]e^{-j\beta_z z}\end{aligned}\tag{15e}$$

$$\begin{aligned}H_z^+&=-j\frac{1}{\omega\mu\varepsilon}\left(\frac{\partial^2}{\partial z^2}+\beta^2\right)F_z^+=-jA_{mn}\frac{\beta_\rho^2}{\omega\mu\varepsilon}J_m(\beta_\rho\rho)\\&\quad\times[C_2\cos(m\phi)+D_2\sin(m\phi)]e^{-j\beta_z z}\end{aligned}\tag{15f}$$

where

$$'=\frac{\partial}{\partial(\beta_\rho\rho)}\tag{15g}$$

By using (15a)–(15f), the wave impedance $(Z_w^{+z})^{TE}_{mn}$ of the $TE^z_{mn}$ $(H^z_{mn})$ modes in the $+z$ direction can be written as

$$Z^h_{mn}=(Z_w^{+z})^{TE}_{mn}=\frac{E_\rho^+}{H_\phi^+}=-\frac{E_\phi^+}{H_\rho^+}=\frac{\omega\mu}{(\beta_z)_{mn}}\tag{16a}$$

With the aid of (13a)–(13c) the wave impedance of (16a) reduces to

$$Z^h_{mn}=(Z_w^{+z})^{TE}_{mn}=\begin{cases}\dfrac{\omega\mu}{\beta\sqrt{1-\left(\dfrac{f_c}{f}\right)^2}}=\dfrac{\sqrt{\dfrac{\mu}{\varepsilon}}}{\sqrt{1-\left(\dfrac{f_c}{f}\right)^2}}=\dfrac{\eta}{\sqrt{1-\left(\dfrac{f_c}{f}\right)^2}}\\ \text{when } f>f_c=(f_c)_{mn}\end{cases}\tag{16b}$$

$$Z^h_{mn}=(Z_w^{+z})^{TE}_{mn}=\left\{\frac{\omega\mu}{0}=\infty\quad\text{when } f=f_c=(f_c)_{mn}\right.\tag{16c}$$

$$Z^h_{mn}=(Z_w^{+z})^{TE}_{mn}=\begin{cases}\dfrac{\omega\mu}{-j\beta\sqrt{\left(\dfrac{f_c}{f}\right)^2-1}}=+j\dfrac{\sqrt{\dfrac{\mu}{\varepsilon}}}{\sqrt{\left(\dfrac{f_c}{f}\right)^2-1}}=+j\dfrac{\eta}{\sqrt{\left(\dfrac{f_c}{f}\right)^2-1}}\\ \text{when } f<f_c=(f_c)_{mn}\end{cases}\tag{16d}$$

By examining through (16b)–(16d), we can make the following statements about the impedance.

1. Above cutoff it is real and greater than the intrinsic impedance of the medium inside the waveguide.
2. At cutoff it is infinity.

3. Below cutoff it is imaginary and inductive. This indicates that the waveguide below cutoff behaves as an inductor that is an energy storage element.

## 3. TRANSVERSE MAGNETIC ($TM^Z$) MODES

The transverse magnetic to $z$ ($TM^z$) modes can be derived in a similar manner as the $TE^z$ modes of Section 2 by letting

$$\mathbf{A} = \hat{a}_z A_z(\rho, \phi, z) \tag{17a}$$

$$\mathbf{F} = 0 \tag{17b}$$

The vector potential $\mathbf{A}$ must satisfy the vector wave equation, which reduces for the $\mathbf{A}$ of (17a) to

$$\nabla^2 A_z(\rho, \phi, z) + \beta^2 A_z(\rho, \phi, z) = 0 \tag{18}$$

The solution of (18) is obtained in a manner similar to that of (2), as given by (4), and it can be written as

$$\begin{aligned} A_z(\rho, \phi, z) = {} & [A_1 J_m(\beta_\rho \rho) + B_1 Y_m(\beta_\rho \rho)] \\ & \times [C_2 \cos(m\phi) + D_2 \sin(m\phi)] \\ & \times [A_3 e^{-j\beta_z z} + B_3 e^{+j\beta_z z}] \end{aligned} \tag{19a}$$

with

$$\beta_\rho^2 + \beta_z^2 = \beta^2 \tag{19b}$$

The constants $A_1$, $B_1$, $C_2$, $D_2$, $A_3$, $B_3$, $m$, $\beta_\rho$, and $\beta_z$ can be found using the boundary conditions of

$$E_\phi(\rho = a, \phi, z) = 0 \tag{20a}$$

or

$$E_z = (\rho = a, \phi, z) = 0 \tag{20b}$$

The fields must be finite everywhere (20c)

The fields must repeat every $2\pi$ radians in $\phi$ (20d)

According to (20c), $B_1 = 0$ since $Y_m(\rho = 0) = \infty$. In addition, according to (20d),

$$m = 0, 1, 2, 3, \ldots \tag{21}$$

Considering waves that propagate only in the $+z$ direction, (19a) then reduces to

$$\begin{aligned} A_z^+(\rho, \phi, z) = {} & B_{mn} J_m(\beta_\rho \rho)[C_2 \cos(m\phi) \\ & + D_2 \sin(m\phi)] e^{-j\beta_z z} \end{aligned} \tag{22}$$

The eigenvalues of $\beta_\rho$ can be obtained by applying either (20a) or (20b).

From Eq. (22), we can write the electric field component $E_z^+$ as

$$\begin{aligned} E_z^+ &= -j \frac{1}{\omega\mu\varepsilon} \left( \frac{\partial^2}{\partial z^2} + \beta^2 \right) A_z^+ \\ &= -jB_{mn} \frac{\beta_\rho^2}{\omega\mu\varepsilon} J_m(\beta_\rho \rho)[C_2 \cos(m\phi) \\ &\quad + D_2 \sin(m\phi)] e^{-j\beta_z z} \end{aligned} \tag{23}$$

Application of the boundary condition of (20b) using (23) gives

$$\begin{aligned} E_z^+(\rho = a, \phi, z) = {} & -jB_{mn} \frac{\beta_\rho^2}{\omega\mu\varepsilon} J_m(\beta_\rho a) \\ & \times [C_2 \cos(m\phi) + D_2 \sin(m\phi)] e^{-j\beta_z z} = 0 \end{aligned} \tag{24}$$

which is satisfied only provided that

$$J_m(\beta_\rho a) = 0 \Rightarrow \beta_\rho a = \chi_{mn} \Rightarrow \beta_\rho = \frac{\chi_{mn}}{a} \tag{25}$$

In (25) $\chi_{mn}$ represents the $n$th zero ($n = 1, 2, 3, \ldots$) of the Bessel function $J_m$ of the first kind of order $m$ ($m = 0, 1, 2, 3, \ldots$). An abbreviated list of the zeros $\chi_{mn}$ of the Bessel function $J_m$ is found in Table 2. The smallest value of $\chi_{mn}$ is 2.4049 ($m = 0$, $n = 1$).

By using (19b) and (25), $\beta_z$ can be written as

$$(\beta_z)_{mn} = \begin{cases} \sqrt{\beta^2 - \beta_\rho^2} = \sqrt{\beta^2 - \left(\frac{\chi_{mn}}{a}\right)^2} \\ \text{when } \beta > \beta_\rho = \dfrac{\chi_{mn}}{a} \end{cases} \tag{26a}$$

**Table 2. Zeros $\chi_{mn}$ of $J_m(\chi_{mn}) = 0$ ($n = 1, 2, 3, \ldots$) of Bessel function $J_m(x)$**

| | $m=0$ | $m=1$ | $m=2$ | $M=3$ | $m=4$ | $m=5$ | $m=6$ | $m=7$ | $m=8$ | $m=9$ | $m=10$ | $m=11$ |
|---|---|---|---|---|---|---|---|---|---|---|---|---|
| $n=1$ | 2.4049 | 3.8318 | 5.1357 | 6.3802 | 7.5884 | 8.7715 | 9.9361 | 11.0864 | 12.2251 | 13.3543 | 14.4755 | 12.8264 |
| $n=2$ | 5.5201 | 7.1056 | 8.4173 | 9.7610 | 11.0647 | 12.3386 | 13.5893 | 14.8213 | 16.0378 | 17.2412 | 18.4335 | 19.6160 |
| $n=3$ | 8.6537 | 10.1735 | 11.6199 | 13.0152 | 14.3726 | 15.7002 | 17.0038 | 18.2876 | 19.5545 | 20.8071 | 22.0470 | 23.2759 |
| $n=4$ | 11.7915 | 13.3237 | 14.7960 | 16.2235 | 17.6160 | 18.9801 | 20.3208 | 21.6415 | 22.9452 | 24.2339 | 25.5095 | 26.7733 |
| $n=5$ | 14.9309 | 16.4706 | 17.9598 | 19.4094 | 20.8269 | 22.2178 | 23.5861 | 24.9349 | 26.2668 | 27.5838 | 28.8874 | 80.1791 |

$$(\beta_z)_{mn} = \begin{cases} 0 & \text{when } \beta = \beta_c = \beta_\rho = \dfrac{\chi_{mn}}{a} \end{cases} \tag{26b}$$

$$(\beta_z)_{mn} = \begin{cases} -j\sqrt{\beta_\rho^2 - \beta^2} = -j\sqrt{\left(\dfrac{\chi_{mn}}{a}\right)^2 - \beta^2} \\ \text{when } \beta < \beta_\rho = \dfrac{\chi_{mn}}{a} \end{cases} \tag{26c}$$

By following the same procedure as for the $TE^z$ modes, we can write the expressions for the cutoff frequencies $(f_c)_{mn}$, propagation constant $(\beta_z)_{mn}$, and guide wavelength $(\lambda_g)_{mn}$ as

$$(f_c)_{mn} = \frac{\chi_{mn}}{2\pi a\sqrt{\mu\varepsilon}} \tag{27}$$

$$(\beta_z)_{mn} = \begin{cases} \sqrt{\beta^2 - \beta_\rho^2} = \beta\sqrt{1 - \left(\dfrac{\beta_\rho}{\beta}\right)^2} = \beta\sqrt{1 - \left(\dfrac{\beta_c}{\beta}\right)^2} \\ = \beta\sqrt{1 - \left(\dfrac{\chi_{mn}}{\beta a}\right)^2} = \beta\sqrt{1 - \left(\dfrac{f_c}{f}\right)^2} \\ \text{when } f > f_c = (f_c)_{mn} \end{cases} \tag{28a}$$

$$(\beta_z)_{mn} = \{ 0 \quad \text{when } f = f_c = (f_c)_{mn} \tag{28b}$$

$$(\beta_z)_{mn} = \begin{cases} -j\sqrt{\beta_\rho^2 - \beta^2} = -j\beta\sqrt{\left(\dfrac{\beta_\rho}{\beta}\right)^2 - 1} = -j\beta\sqrt{\left(\dfrac{\beta_c}{\beta}\right)^2 - 1} \\ = -j\beta\sqrt{\left(\dfrac{\chi_{mn}}{\beta a}\right)^2 - 1} = -j\beta\sqrt{\left(\dfrac{f_c}{f}\right)^2 - 1} \\ \text{when } f < f_c = (f_c)_{mn} \end{cases} \tag{28c}$$

$$(\lambda_g)_{mn} = \begin{cases} \dfrac{2\pi}{\beta\sqrt{1 - \left(\dfrac{f_c}{f}\right)^2}} = \dfrac{\lambda}{\sqrt{1 - \left(\dfrac{f_c}{f}\right)^2}} & \text{when } f > f_c = (f_c)_{mn} \end{cases} \tag{29a}$$

$$(\lambda_g)_{mn} = \{\infty \quad \text{when } f = f_c = (f_c)_{mn} \tag{29b}$$

According to (27) and the values of $\chi_{mn}$ of Table 2, the order (lower to higher cutoff frequencies) in which the $TM^z$ modes occur is $TM_{01}$, $TM_{11}$, $TM_{21}$, and so forth. The bandwidth of the first single-mode $TM_{01}^z$ operation is 3.8318/2.4059 = 1.5927:1. Comparing the cutoff frequencies of the $TE^z$ and $TM^z$ modes, as given by (12b) and (27) along with the data of Tables 1 and 2, the order of the $TE_{mn}^z$ and $TM_{mn}^z$ modes is that of $TE_{11}$ ($\chi'_{11} = 1.8412$), $TM_{01}$, ($\chi_{01} = 2.4049$), $TE_{21}$ ($\chi'_{21} = 3.0542$), $TE_{01}$ ($\chi'_{01} = 3.8318$) = $TM_{11}$ ($\chi'_{11} = 3.8318$), $TE_{31}$ ($\chi'_{31} = 4.2012$), and so forth. The dominant mode is $TE_{11}$ and its bandwidth of single-mode operation is 2.4049/1.8412 = 1.3062:1. Plots of the field configurations over a cross section of the waveguide, both $E$ and $H$, for the first 30 $TE_{mn}^z$ and/or $TM_{mn}^z$ modes are shown in Fig. 2 [1].

It is apparent that the cutoff frequencies of the $TE_{0n}$ and $TM_{1n}$ modes are identical; therefore they are referred to here also as *degenerate modes*.

The electric and magnetic field components can be written using (22) as

$$\begin{aligned} E_\rho^+ &= -j\frac{1}{\omega\mu\varepsilon}\frac{\partial^2 A_z^+}{\partial\rho\partial z} \\ &= -B_{mn}\frac{\beta_\rho\beta_z}{\omega\mu\varepsilon}J'_m(\beta_\rho\rho) \\ &\quad \times [C_2\cos(m\phi) + D_2\sin(m\phi)]e^{-j\beta_z z} \end{aligned} \tag{30a}$$

$$\begin{aligned} E_\phi^+ &= -j\frac{1}{\omega\mu\varepsilon}\frac{1}{\rho}\frac{\partial^2 A_z^+}{\partial\phi\partial z} \\ &= -B_{mn}\frac{m\beta_z}{\omega\mu\varepsilon\rho}J_m(\beta_\rho\rho) \\ &\quad \times [-C_2\sin(m\phi) + D_2\cos(m\phi)]e^{-j\beta_z z} \end{aligned} \tag{30b}$$

$$\begin{aligned} E_z^+ &= -j\frac{1}{\omega\mu\varepsilon}\left(\frac{\partial^2}{\partial z^2} + \beta^2\right)A_z^+ \\ &= -jB_{mn}\frac{\beta_\rho^2}{\omega\mu\varepsilon}J_m(\beta_\rho\rho) \\ &\quad \times [C_2\cos(m\phi) + D_2\sin(m\phi)]e^{-j\beta_z z} \end{aligned} \tag{30c}$$

$$H_\rho^+ = \frac{1}{\mu}\frac{1}{\rho}\frac{\partial A_z^+}{\partial\phi} = B_{mn}\frac{m}{\mu}\frac{1}{\rho}J_m(\beta_\rho\rho) \times [-C_2\sin(m\phi) + D_2\cos(m\phi)]e^{-j\beta_z z} \tag{30d}$$

$$H_\phi^+ = -\frac{1}{\mu}\frac{\partial A_z^+}{\partial\rho} = -B_{mn}\frac{\beta_\rho}{\mu}J'_m(\beta_\rho\rho) \times [C_2\cos(m\phi) + D_2\sin(m\phi)]e^{-j\beta_z z} \tag{30e}$$

$$H_z^+ = 0 \tag{30f}$$

where

$$' = \frac{\partial}{\partial(\beta_\rho\rho)} \tag{30g}$$

By using (30a)–(30f), the wave impedance in the $+z$ direction can be written as

$$(Z_w^{+z})_{mn}^{TM} = \frac{E_\rho^+}{H_\phi^+} = -\frac{E_\phi^+}{H_\rho^+} = \frac{(\beta_z)_{mn}}{\omega\varepsilon} \tag{31}$$

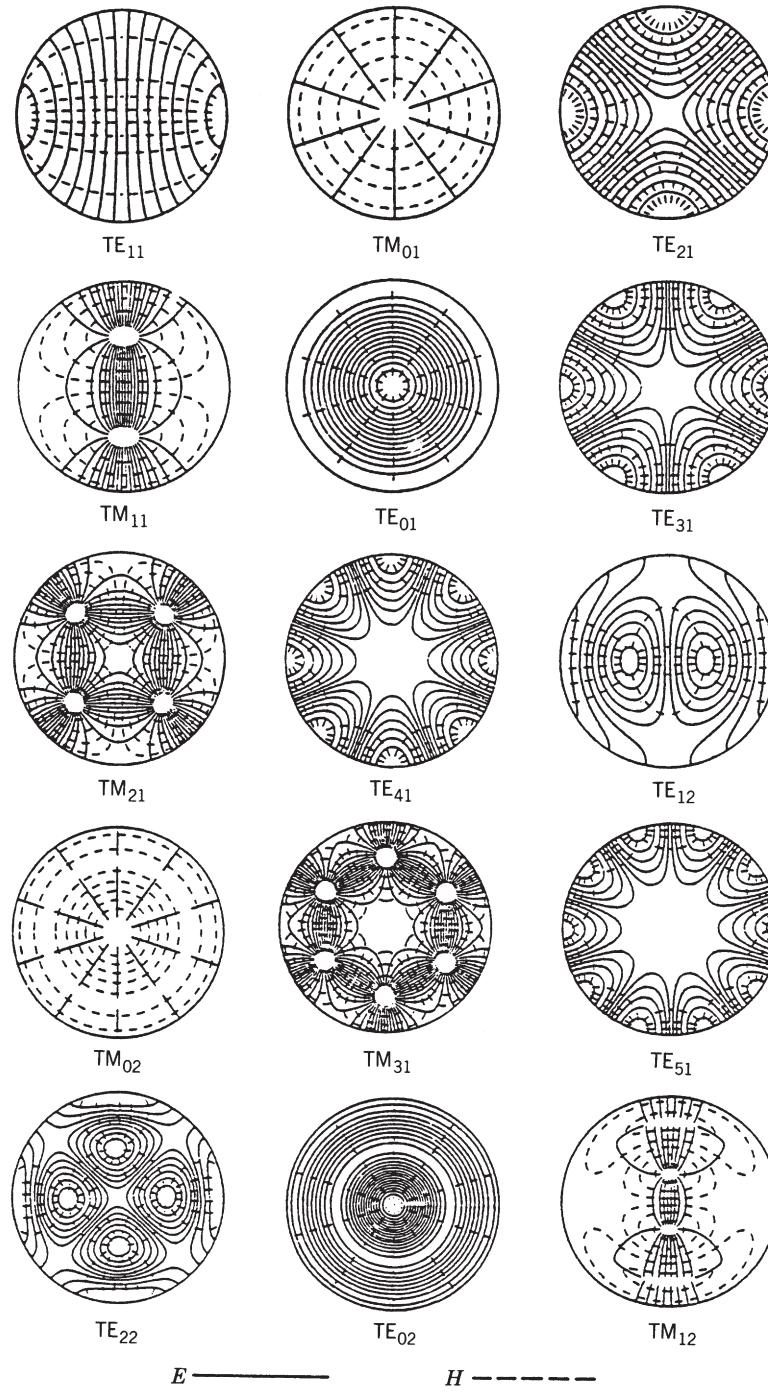


**Figure 2.** Field configurations of first 30 $TE^z$ and/or $TM^z$ modes in a circular waveguide. (*Source*: C. S. Lee, S. W. Lee, and S. L. Chuang, Plot of modal field distribution in rectangular and circular waveguides, *IEEE Trans. Microwave Theory Tech.*, © 1985, IEEE.)

With the aid of (28a)–(28c) the wave impedance of (31) reduces to

$$(Z_{\mathrm{w}}^{+z})_{mn}^{\mathrm{TM}} = \begin{cases} \dfrac{\beta\sqrt{1-\left(\dfrac{f_{\mathrm{c}}}{f}\right)^2}}{\omega\varepsilon} = \sqrt{\dfrac{\mu}{\varepsilon}}\sqrt{1-\left(\dfrac{f_{\mathrm{c}}}{f}\right)^2} = \eta\sqrt{1-\left(\dfrac{f_{\mathrm{c}}}{f}\right)^2} \\ \text{when } f > f_{\mathrm{c}} = (f_{\mathrm{c}})_{mn} \end{cases} \tag{32a}$$

$$(Z_{\mathrm{w}}^{+z})_{mn}^{\mathrm{TM}} = \left\{ \frac{0}{\omega\varepsilon} = 0 \quad \text{when } f = f_{\mathrm{c}} = (f_{\mathrm{c}})_{mn} \right. \tag{32b}$$

$$(Z_{\mathrm{w}}^{+z})_{mn}^{\mathrm{TM}} \begin{cases} \dfrac{-j\beta\sqrt{\left(\dfrac{f_{\mathrm{c}}}{f}\right)^2-1}}{\omega\varepsilon} = -j\sqrt{\dfrac{\mu}{\varepsilon}}\sqrt{\left(\dfrac{f_{\mathrm{c}}}{f}\right)^2-1} \\ \qquad = -j\eta\sqrt{\left(\dfrac{f_{\mathrm{c}}}{f}\right)^2-1} \\ \text{when } f < f_{\mathrm{c}} = (f_{\mathrm{c}})_{mn} \end{cases} \tag{32c}$$

Examining (32a)–(32c) we can make the following statements about the wave impedance for the $TM^z$ modes.

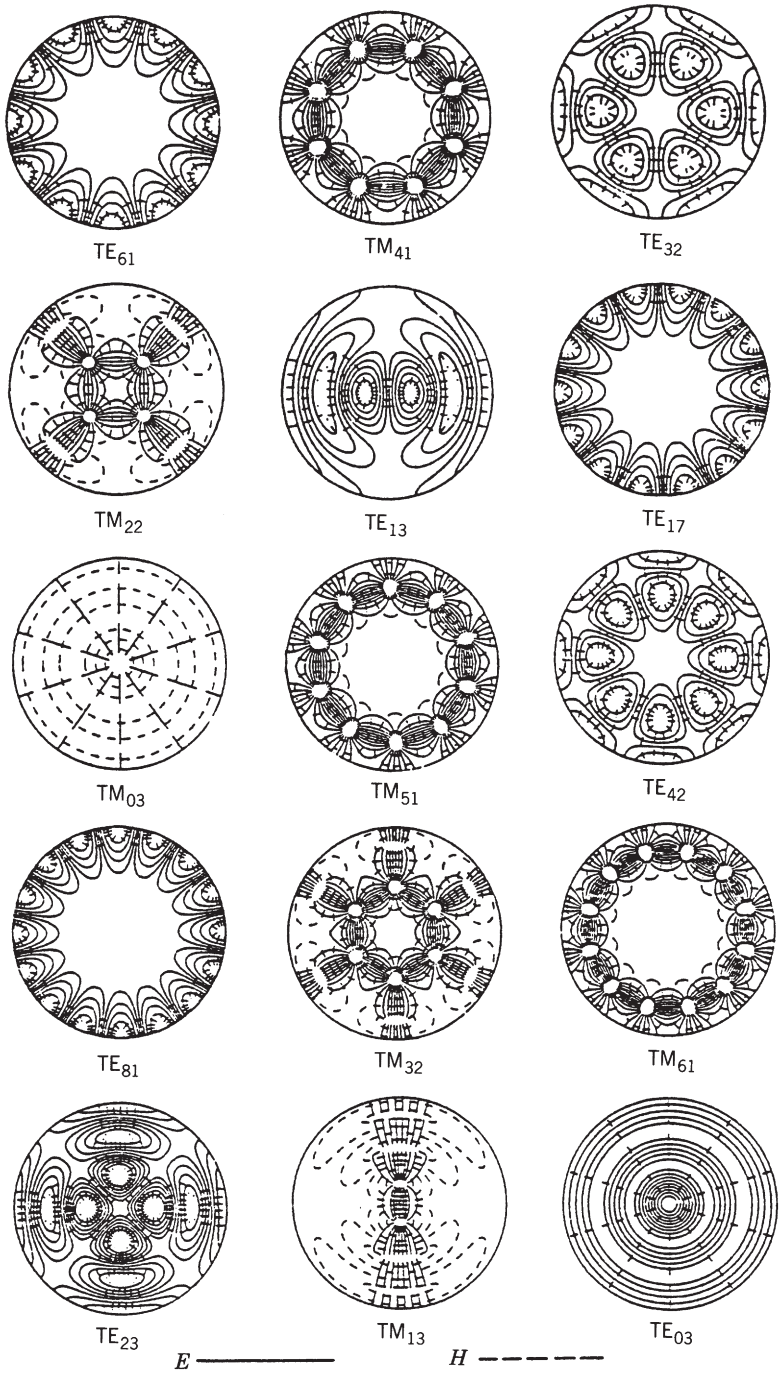


**Figure 2.** (Continued).

1. Above cutoff it is real and smaller than the intrinsic impedance of the medium inside the waveguide.
2. At cutoff it is zero.
3. Below cutoff it is imaginary and capacitive. This indicates that the waveguide below cutoff behaves as a capacitor that is an energy storage element.

Whenever a given mode is desired, it is necessary to design the proper feed to excite the fields within the waveguide and detect the energy associated with such modes. To maximize the energy exchange or transfer, this is accomplished by designing the feed, which is usually a probe or antenna, so that its field pattern matches that of the field configuration of the desired mode. Usually the probe is placed near the maximum of the field pattern of the desired mode; however, that position may be varied somewhat in order to achieve some desired matching in the excitation and detection systems. Shown in Fig. 3 are suggested designs to excite and/or detect the $TE_{11}$ and $TM_{01}$ modes in a circular waveguide, to transition between the $TE_{10}$ of a rectangular waveguide and the $TE_{11}$ mode of a circular waveguide, and to couple between the $TE_{10}$ of a rectangular waveguide and $TM_{01}$ mode of a circular waveguide.

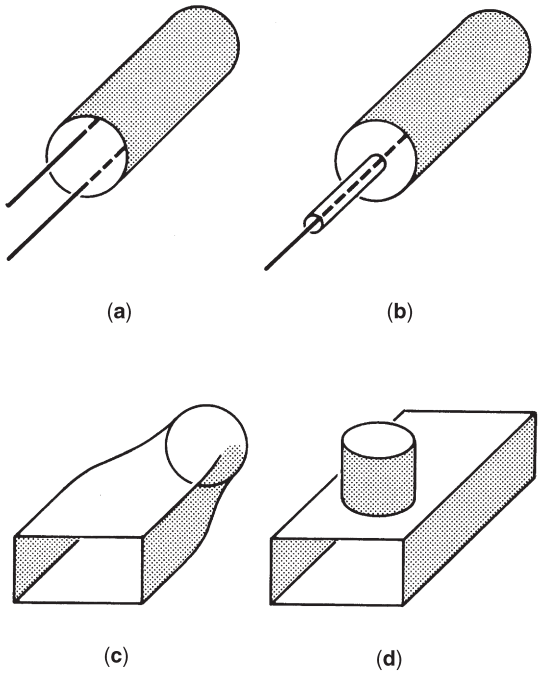


**Figure 3.** Excitation of $TE_{mn}$ and $TM_{mn}$ modes in a circular waveguide: (a) $TE_{11}$ mode; (b) $TM_{01}$ mode; (c) $TE_{10}$ (rectangular)–$TE_{11}$ (circular); (d) $TE_{10}$ (rectangular)–$TM_{01}$ (circular).

## 4. ATTENUATION FROM OHMIC LOSSES

It has been shown that the attenuation coefficients of the $TE_{0n}$ ($n = 1,2,\ldots$) modes in a circular waveguide monotonically decrease as a function of frequency [2,3]. This is a very desirable characteristic, and because of this the excitation, propagation, and detection of $TE_{0n}$ modes in a circular waveguide have received considerable attention. The attenuation coefficient for the $TE^z_{mn}$ and $TM^z_{mn}$ modes inside a circular waveguide are given, respectively, by

$$TE^z_{mn}$$

$$(\alpha_c)^{TE^z}_{mn} = \frac{R_s}{a\eta\sqrt{1-\left(\frac{f_c}{f}\right)^2}} \times \left[\left(\frac{f_c}{f}\right)^2 + \frac{m^2}{(\chi'_{mn})^2 - m^2}\right] \text{Np/m} \tag{33a}$$

$$TM^z_{mn}$$

$$(\alpha_c)^{TM^z}_{mn} = \frac{R_s}{a\eta}\frac{1}{\sqrt{1-\left(\frac{f_c}{f}\right)^2}} \text{Np/m} \tag{33b}$$

where

$$R_s = \sqrt{\frac{\omega\mu}{2\sigma}} \tag{34}$$

Plots of the attenuation coeficient versus the normalized frequency $f/f_c$, where $f_c$ is the cutoff frequency of the dominant $TE_{11}$ mode, are shown for six modes in Fig. 4a and b for waveguide radii of 1.5 and 3 cm, respectively. Within the waveguide is free space and its walls are made of copper ($\sigma = 5.7 \times 10^7$ S/m).

It is evident from the results of the preceding example that as $f_c/f$ becomes smaller the attenuation coefficient decreases monotonically (as shown in Fig. 4), which is a desirable characteristic. It should be noted that similar monotonically decreasing variations in the attenuation coefficient are evident in all $TE_{0n}$ modes ($n = 1,2,3,\ldots$). According to (15a)–(15f), the only tangential magnetic field component to the conducting surface of the waveguide for all these $TE_{0n}$ ($m = 0$) modes is the $H_z$ component, while the electric field lines are circular. Therefore these modes are usually referred to as circular electric modes. For a constant power in the wave, the $H_z$ component decreases as the frequency increases and approaches zero at infinite frequency. Simultaneously the current density and conductor losses on the waveguide walls also decrease and approach zero. Because of this attractive feature, these modes have received considerable attention for long-distance propagation of energy, especially at millimeter-wave frequencies. Typically attenuations as low as 1.25 dB/km (2 dB/mi) have been attained [2]. This is to be compared with attenuations of 120 dB/km for WR-90 copper rectangular waveguides, and 3 dB/km at 0.85 μm, and less than 0.5 dB/km at 1.3 μm for fiberoptic cables.

Although the $TE_{0n}$ modes are very attractive from the attenuation point of view, there are a number of problems associated with their excitation and retention. One of the problems is that the $TE_{01}$ mode, which is the first of the $TE_{0n}$ modes, is not the dominant mode. Therefore in order for this mode to be above its cutoff frequency and propagate in the waveguide, a number of other modes (such as the $TE_{11}$, $TM_{01}$, $TE_{21}$, and $TM_{11}$) with lower cutoff frequencies can also exist. Additional modes can also be present if the operating frequency is chosen well above the cutoff frequency of the $TE_{01}$ mode in order to provide a margin of safety from being too close to its cutoff frequency.

To support the $TE_{01}$ mode, the waveguide must be oversized and it can support a number of other modes. One of the problems faced with such a guide is how to excite the desired $TE_{01}$ mode with sufficient purity and suppress the others. Another problem is how to prevent coupling between the $TE_{01}$ mode and undesired modes. The presence of the undesired modes causes not only higher losses but also dispersion and attenuation distortion to the signal since each exhibits different phase velocities and attenuation. Irregularities in the inner geometry, surface, and direction (bends, nonuniform cross sections, etc.) of the waveguide are the main contributors to the coupling to the undesired modes. However, for the guide to be of any practical use, it must be able to sustain and propagate the desired $TE_{01}$ and other $TE_{0n}$ modes efficiently over bends of reasonable curvature. One technique that has been implemented to achieve this is to use mode conversion before entering the corner and another conversion when exiting to convert back to the desired $TE_{0n}$ mode(s).

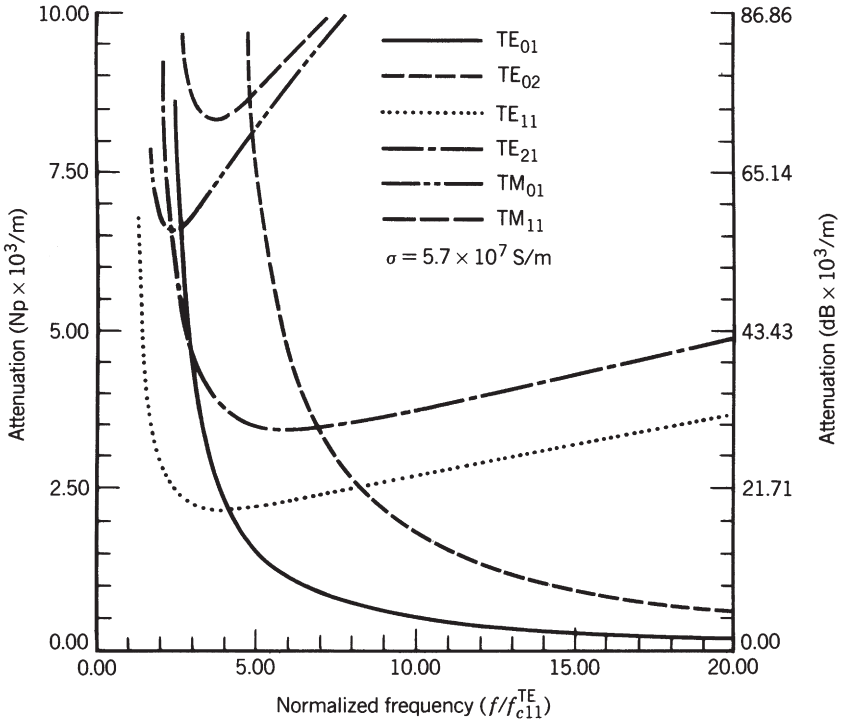


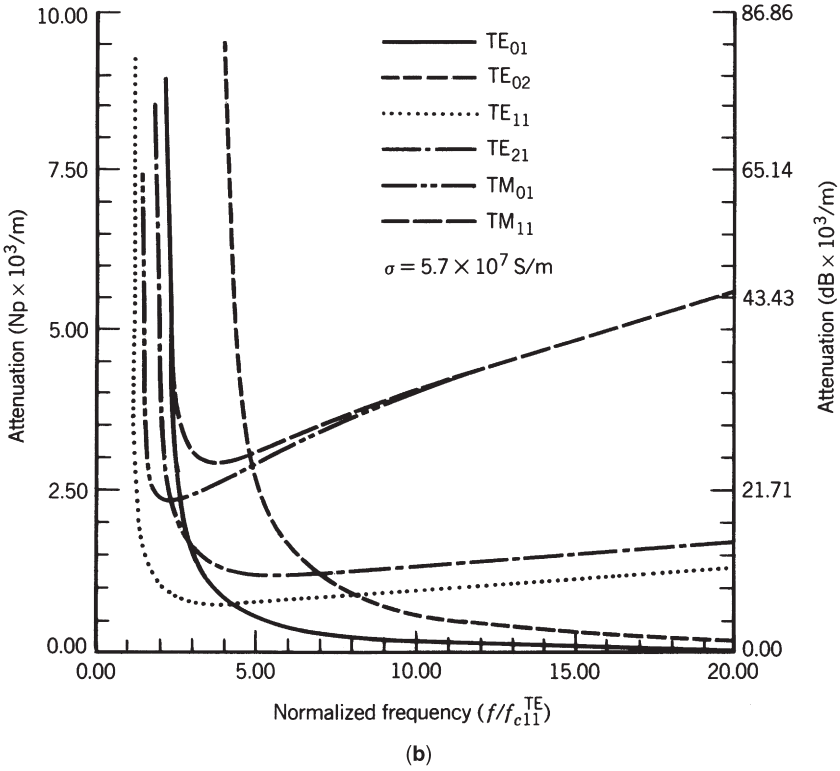


**Figure 4.** Attenuation for $TE_{mn}^{z}$ and $TM_{mn}^{z}$ modes in a circular waveguide: (a) $a = 1.5$ cm; (b) $a = 3$ cm.

Another method that has been used to discriminate against undesired modes and avoid coupling to them is to introduce filters inside the guide that cause negligible attenuation to the desired $TE_{0n}$ mode(s). These filters introduce cuts that are perpendicular to the current paths of the undesired modes and parallel to the current direction of the desired mode(s). Since the current path of the undesired modes is along the axis ($z$ direction) of the guide and the path of the desired $TE_{0n}$ modes is along the circumference ($\phi$ direction), a helical wound wire placed on the inside surface of the guide can serve as a filter that discourages any mode that requires an axial

**Table 3. Summary of $TE^z_{mn}$ and $TM^z_{mn}$ Mode Characteristics of Circular Waveguide**

| | $TE^z_{mn}\begin{pmatrix} m=0,1,2,\ldots, \\ n=1,2,3,\ldots \end{pmatrix}$ | $TM^z_{mn}\begin{pmatrix} m=0,1,2,3,\ldots, \\ n=1,2,3,4,\ldots \end{pmatrix}$ |
|---|---|---|
| $E_\rho^+$ | $-A_{mn}\frac{m}{\varepsilon\rho}J_m(\beta_\rho\rho)[-C_2\sin(m\phi)+D_2\cos(m\phi)]e^{-j\beta_z z}$ | $-B_{mn}\frac{\beta_\rho\beta_z}{\omega\mu\varepsilon}J'_m(\beta_\rho\rho)[C_2\cos(m\phi)+D_2\sin(m\phi)]e^{-j\beta_z z}$ |
| $E_\phi^+$ | $A_{mn}\frac{\beta_\rho}{\varepsilon}J'_m(\beta_\rho\rho)[C_2\cos(m\phi)+D_2\sin(m\phi)]e^{-j\beta_z z}$ | $-B_{mn}\frac{m\beta_z}{\omega\mu\varepsilon}\frac{1}{\rho}J_m(\beta_\rho\rho)[-C_2\sin(m\phi)+D_2\cos(m\phi)]e^{-j\beta_z z}$ |
| $E_z^+$ | 0 | $-jB_{mn}\frac{\beta_\rho^2}{\omega\mu\varepsilon}J_m(\beta_\rho\rho)[C_2\cos(m\phi)+D_2\sin(m\phi)]e^{-j\beta_z z}$ |
| $H_\rho^+$ | $-A_{mn}\frac{\beta_\rho\beta_z}{\omega\mu\varepsilon}J'_m(\beta_\rho\rho)[C_2\cos(m\phi)+D_2\sin(m\phi)]e^{-j\beta_z z}$ | $B_{mn}\frac{m}{\mu}\frac{1}{\rho}J_m(\beta_\rho\rho)[-C_2\cos(m\phi)+D_2\sin(m\phi)]e^{-j\beta_z z}$ |
| $H_\phi^+$ | $-A_{mn}\frac{m\beta_z}{\omega\mu\varepsilon}\frac{1}{\rho}J_m(\beta_\rho\rho)[-C_2\sin(m\phi)+D_2\cos(m\phi)]e^{-j\beta_z z}$ | $-B_{mn}\frac{\beta_\rho}{\mu}J'_m(\beta_\rho\rho)[-C_2\cos(m\phi)+D_2\sin(m\phi)]e^{-j\beta_z z}$ |
| $H_z^+$ | $-jA_{mn}\frac{\beta_\rho^2}{\omega\mu\varepsilon}J_m(\beta_\rho\rho)[C_2\cos(m\phi)+D_2\sin(m\phi)]e^{-j\beta_z z}$ | 0 |
| $\beta_c=\beta_\rho$ | $\frac{\chi'_{mn}}{a}$ | $\frac{\chi_{mn}}{a}$ |
| $f_c$ | $\frac{\chi'_{mn}}{2\pi a\sqrt{\mu\varepsilon}}$ | $\frac{\chi_{mn}}{2\pi a\sqrt{\mu\varepsilon}}$ |
| $\lambda_c$ | $\frac{2\pi a}{\chi'_{mn}}$ | $\frac{2\pi a}{\chi_{mn}}$ |
| $\beta_z(f\geq f_c)$ | $\beta\sqrt{1-\left(\frac{f_c}{f}\right)^2}=\beta\sqrt{1-\left(\frac{\lambda}{\lambda_c}\right)^2}$ | |
| $\lambda_g(f\geq f_c)$ | $\frac{\lambda}{\sqrt{1-\left(\frac{f_c}{f}\right)^2}}=\frac{\lambda}{\sqrt{1-\left(\frac{\lambda}{\lambda_c}\right)^2}}$ | |
| $v_p(f\geq f_c)$ | $\frac{v}{\sqrt{1-\left(\frac{f_c}{f}\right)^2}}=\frac{v}{\sqrt{1-\left(\frac{\lambda}{\lambda_c}\right)^2}}$ | |
| $Z_w(f\geq f_c)$ | $\frac{\eta}{\sqrt{1-\left(\frac{f_c}{f}\right)^2}}=\frac{\eta}{\sqrt{1-\left(\frac{\lambda}{\lambda_c}\right)^2}}$ | $\eta\sqrt{1-\left(\frac{f_c}{f}\right)^2}=\eta\sqrt{1-\left(\frac{\lambda}{\lambda_c}\right)^2}$ |
| $Z_w(f\leq f_c)$ | $j\frac{\eta}{\sqrt{\left(\frac{f_c}{f}\right)^2-1}}=j\frac{\eta}{\sqrt{\left(\frac{\lambda}{\lambda_c}\right)^2-1}}$ | $-j\eta\sqrt{\left(\frac{f_c}{f}\right)^2-1}=-j\eta\sqrt{\left(\frac{\lambda}{\lambda_c}\right)^2-1}$ |
| $\alpha_c$ | $\frac{R_s}{a\eta\sqrt{1-\left(\frac{f_c}{f}\right)^2}}\left[\left(\frac{f_c}{f}\right)^2+\frac{m^2}{(\chi'_{mn})^2-m^2}\right]$ | $\frac{R_s}{a\eta}\frac{1}{\sqrt{1-\left(\frac{f_c}{f}\right)^2}}$ |

component of current flow but propagates the desired $TE_{0n}$ modes [3,4].

Another means to suppress undesired modes is to introduce within the guide very thin baffles of lossy material that will act as attenuating sheets. The surfaces of the baffles are placed in the radial direction of the guide so that they are parallel to the $E_\rho$ and $E_z$ components of the undesired modes (which will be damped) and normal to the $E_\phi$ component of the $TE_{0n}$ modes that will remain unaffected. Typically two baffles are placed in a crossed pattern over the cross section of the guide.

A summary of the pertinent characteristics of the $TE^z_{mn}$ and $TM^z_{mn}$ modes of a circular waveguide are found listed in Table 3.

## BIBLIOGRAPHY

1. C. S. Lee, S. W. Lee, and S. L. Chuang, Plot of modal field distribution in rectangular and circular waveguides, *IEEE Trans. Microwave Theory* Tech. **MTT-33**(3):271–274 (March 1985).
2. S. E. Miller, Waveguide as a communication medium, *Bell Syst. Tech. J.* **33**:1209–1265 (Nov. 1954).

3. S. P. Morgan and J. A. Young, Helix waveguide, *Bell Syst. Tech. J.* **35**:1347–1384 (Nov. 1956).
4. S. Ramo, J. R. Whinnery, and T. Van Duzer, *Fields and Waves in Communication Electronics*, Wiley, New York, 1965, pp. 429–439.

## COAXIAL LINE DISCONTINUITIES

R. GARG
Indian Institute of Technology
Kharagpur
Kharagpur, India

Various types of coaxial-line discontinuities have been discussed in the literature [1–4], including: capacitive gaps, open-ended configuration, impedance steps, capacitive windows, T junctions, small elliptical and circular apertures, aperture coupling between two coaxial lines, and bifurcation of a coaxial line. The configurations and the equivalent circuits for some of the discontinuities are shown in Fig. 1. The mode-matching technique with variational formulation is the commonly used approach to arrive at the equivalent-circuit parameters of discontinuities. The available results for some of these discontinuities are summarized in the following sections.

### 1. CAPACITIVE GAPS IN COAXIAL LINES

A gap in the center conductor of a coaxial line, as shown in Fig. 1a, introduces mainly a series capacitance in the line. This type of discontinuity finds common use in microwave filters, DC blocks, and coaxial-line reentrant cavity.

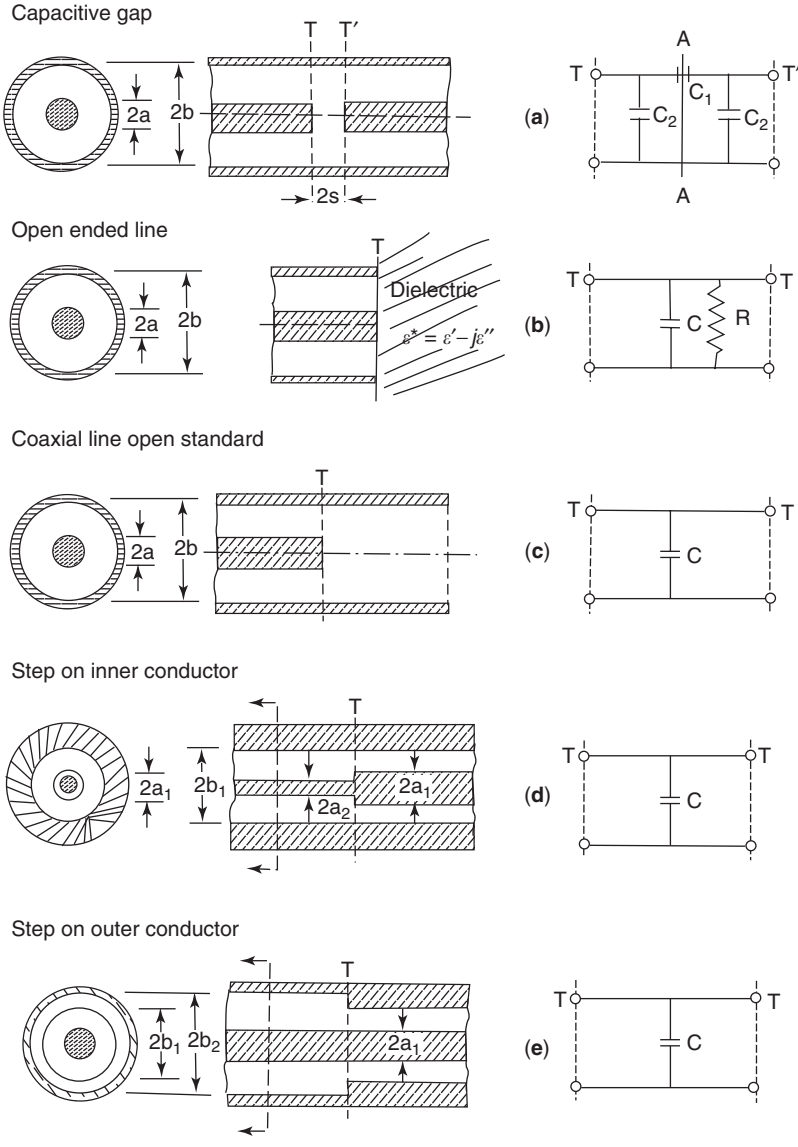


**Figure 1.** Discontinuities in coaxial lines and their equivalent circuits.

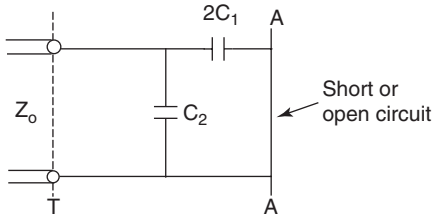


**Figure 2.** Equivalent circuit for the evaluation of capacitive gap discontinuities.

If the gap width is small compared to the wavelength, the problem can be treated electrostatically and the equivalent circuit of the gap discontinuity may be formulated as shown in Fig. 1a. For the purpose of analysis, the equivalent circuit may be written as shown in Fig. 2. The series and shunt capacitances are determined by computing three capacitances: total capacitances of a length of line (1) with a short circuit at plane *AA*, (2) with an open circuit at the plane *AA*, and (3) with no discontinuity. The section of line must be sufficiently long to ensure that an undisturbed field distribution is obtained at the end located away from the discontinuity. This condition is fulfilled if the linelength is equal to or greater than the diameter of the outer conductor. Numerical results for various gap widths and diameter ratios are given in Table 1 [3].

Gap capacitances for diameter ratios 5–1 and 7–1 are also given in Refs. 3 and 4. The values of capacitances $C_1$ and $C_2$ of Table 1 can also be utilized to determine capacitances for the open-end configuration and for the configuration shown in Fig. 3. The open-end capacitance is given by $C_2$ when $s \to \infty$. The capacitance with the short-circuiting plane at a distance $s$ from the inner conductor is $C$, and is given by $(2C_1 + C_2)$. A closed-form expression for the capacitance $C$ is written as follows [3,4]:

$$C = \frac{\pi a^2 \varepsilon_0 \varepsilon_r}{s} + 4a\varepsilon_0\varepsilon_r \ln\left(\frac{b-a}{s}\right) \qquad (1)$$

This equation is valid under the condition $\lambda_0 \gg (b-a) \gg s$. The first term in (1) is the parallel-plate capacitance between the face of the inner conductor and the short-circuiting plane. The second term is the fringing capacitance.

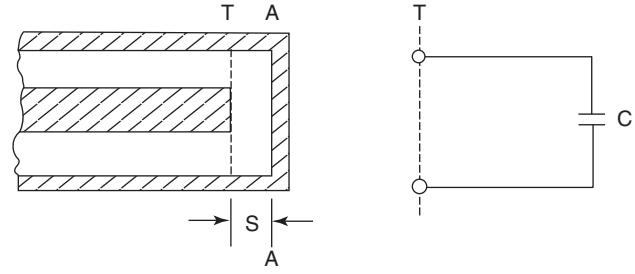


**Figure 3.** Coaxial line with short circuit (coaxial-line reentrant cavity) and its equivalent circuit.

It may be observed from Table 1 that $C_2$ approaches zero for vanishingly small gap width and therefore, the series capacitance $C_1$ is dominant in (1). As gap width increases, $C_2$ increases linearly but the decrease in $C_1$ is faster. Expression (1) is accurate to within 5% for small gaps ($s/a < 0.1$) For a 50-Ω line the error is less than 1.5%.

Variational analysis of the geometry of Fig. 2 shows that the capacitances $C_1$ and $C_2$ increase with frequency [5]. Variation of these capacitances with normalized frequency $k_0 b$ is shown in Fig. 4 for $s/a = 0.25$ and 0.025 in a 50-Ω line [5]. It is seen that while the shunt capacitance $C_2$ increases very slowly (almost negligibly) with frequency, the series capacitance $C_1$ increases much more rapidly and shows a sharp increase near the cutoff frequency of cylindrical waveguide $TM_{01}$ mode. Variational analysis of a gap in the central conductor of a rectangular coaxial line has been reported [6]. The behavior of gap capacitances with gap width and frequency is similar to that in a cylindrical coaxial line. The gap capacitance in the coaxial line can also be described in terms of the associated reflection coefficient Γ. Eom et al. have used the mode-matching method to determine Γ for a coaxial line terminated in a gap [7]. A rapidly converging series for Γ has been obtained. The effect of dielectric inhomogeneity in the gap has been included.

## 2. OPEN-ENDED COAXIAL LINE

The schematic of an open-ended coaxial line with an infinite flange and its equivalent circuit are shown in Fig. 1b. The equivalent circuit consists of a parallel combination

**Table 1. Capacitances $C_1$ and $C_2$ of Equivalent Circuit of Fig. 1a for Gaps in Coaxial Lines (pF/2π$b$, $b$ in cm)**

| | Diameter Ratio ($b:a$) | | | | | | | | | | | |
|---|---|---|---|---|---|---|---|---|---|---|---|---|
| | 10:9 | | 4:3 | | 5:3 | | 2:1 | | 2.3:1 | | 3:1 | |
| Gap Ratio ($s/b$) | $C_1$ | $C_2$ | $C_1$ | $C_2$ | $C_1$ | $C_2$ | $C_1$ | $C_2$ | $C_1$ | $C_2$ | $C_1$ | $C_2$ |
| 0.05 | 0.367 | 0.0354 | 0.275 | 0.0143 | 0.188 | 0.0082 | 0.138 | 0.0061 | 0.109 | 0.00509 | 0.0702 | 0.0039 |
| 0.075 | 0.238 | 0.0486 | 0.183 | 0.0206 | 0.127 | 0.0120 | 0.0946 | 0.0089 | 0.0757 | 0.00746 | 0.0498 | 0.0057 |
| 0.100 | 0.173 | 0.0598 | 0.136 | 0.0265 | 0.0960 | 0.0156 | 0.0719 | 0.0116 | 0.0578 | 0.00972 | 0.0384 | 0.0074 |
| 0.150 | 0.106 | 0.0767 | 0.0858 | 0.0366 | 0.0623 | 0.0221 | 0.0474 | 0.0166 | 0.0384 | 0.0139 | 0.0259 | 0.0105 |
| 0.200 | 0.0718 | 0.0890 | 0.0598 | 0.0450 | 0.0443 | 0.0277 | 0.0340 | 0.0210 | 0.0277 | 0.0176 | 0.0188 | 0.0133 |
| 0.250 | 0.0516 | 0.0985 | 0.0436 | 0.0520 | 0.0328 | 0.0327 | 0.0254 | 0.0248 | 0.0217 | 0.0208 | 0.0143 | 0.0157 |
| 0.300 | 0.0383 | 0.1060 | 0.0328 | 0.0579 | 0.0249 | 0.0369 | 0.0194 | 0.0281 | 0.0161 | 0.0235 | 0.0109 | 0.0178 |

*Source*: Table 6 of H. E. Green, The numerical solution of some important transmission line problems, *IEEE Trans. Microwave Theory Tech.* **MTT-13**:676–692 (Sept. 1965) (© 1965 IEEE).

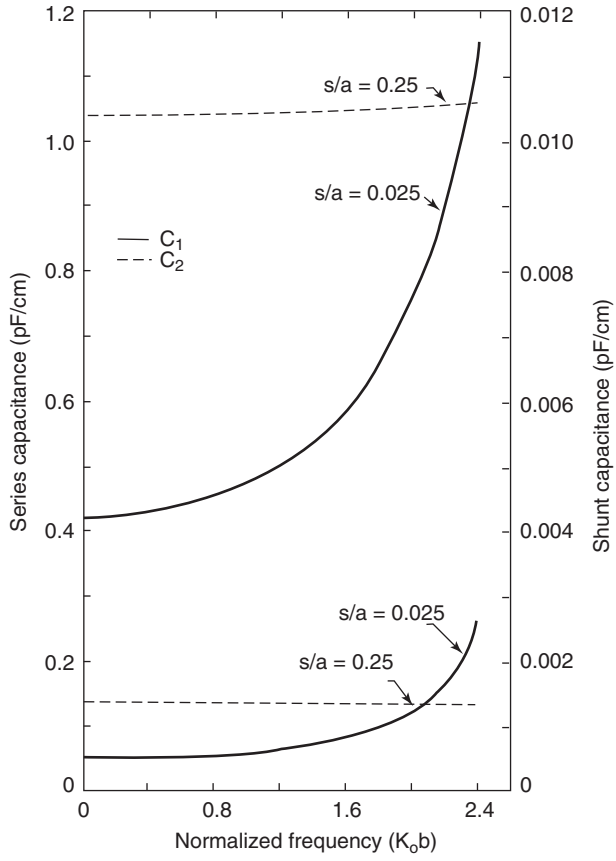


**Figure 4.** Frequency dependence of gap discontinuities of Fig. 2. [From Figure 3 of S. Sen and P. K. Saha, Equivalent circuit of a gap in the central conductor of a coaxial line, *IEEE Trans. Microwave Theory Tech*. **MTT-30**:2026–2029 (Nov. 1982) (© 1982 IEEE).]

of a capacitor $C$ and a resistor $R$ at the flange. The capacitance $C$ arises from the fringing electric field between the center conductor and outer conductor of the coaxial line. The shunt resistance $R$ represents the power loss due to radiation from the open end. Quasistatic analysis of the open-ended coaxial line has been described [8]. The aperture admittance at the flange may be written as [8]

$$Y_L = G_r + jB \tag{2}$$

where $G_r = 1/R$ and $B = \omega C$ and

$$B = \frac{2\omega\varepsilon^*}{[\ln(b/a)]^2}\left[I_1 - \frac{k^2 I_2}{2}\right] \tag{3}$$

$$G_r = \frac{k^3\pi\omega\varepsilon^*}{12}\left[\frac{b^2 - a^2}{\ln(b/a)}\right]^2 \tag{4}$$

$$k^2 = \omega^2\mu_0\varepsilon^*$$

where $\varepsilon^* = \varepsilon' - j\varepsilon''$ represents the terminating medium at the flange. The coefficients $I_1$ and $I_2$ are defined as

**Table 2. Value of Integrals $I_1$ and $I_2$ for a Few Coaxial Lines**

| Line (mm) | $b$ (cm) | $a$ (cm) | $I_1$ ($\times 10^{-3}$) | $I_2$ ($\times 10^{-9}$) |
|---|---|---|---|---|
| 14 (air) | 0.7145 | 0.3102 | 5.88293048 | − 103.784060 |
| 7 (air) | 0.35 | 0.1520 | 2.88055348 | − 12.194870 |
| 8.3 (Teflon) | 0.362 | 0.1124 | 4.21373732 | − 17.5606001 |
| 6.4 (Teflon) | 0.2655 | 0.0824 | 3.09155881 | − 6.92967372 |
| 3.6 (Teflon) | 0.1499 | 0.0455 | 1.77531131 | − 1.2618826 |
| 2.2 (Teflon) | 0.0838 | 0.0255 | 0.99058927 | − 0.22018405 |

*Source*: Table 1 of D. K. Misra, A quasi-static analysis of open-ended coaxial lines, *IEEE Trans. Microwave Theory Tech*. **MTT-35**:925–928 (Oct. 1987) (© 1987 IEEE).

follows:

$$I_1 = \int_a^b \int_a^b \int_0^\pi \frac{\cos\phi'}{(\rho^2 + \rho'^2 - 2\rho\rho'\cos\phi')^{1/2}} \times d\phi' d\rho' d\rho \tag{5a}$$

$$I_2 = \int_a^b \int_a^b \int_0^\pi \cos\phi'(\rho^2 + \rho'^2 - 2\rho\rho'\cos\phi')^{1/2} \times d\phi' d\rho' d\rho \tag{5b}$$

Computed values of integrals $I_1$ and $I_2$ for a few commercially available coaxial lines are given in Table 2 [8].

It may be pointed out that the first term in (3) describes the upper bound for the static capacitance of the opening, while the second term gives the frequency-dependent part of the capacitance. Comparison with the data based on finite-element method (FEM) or method-of-moment (MoM) analysis shows good agreement [8].

Using the values of $I_1$ and $I_2$ from Table 2, the following expressions for the capacitance $C$ may be derived from (3):

For a 3.6-mm Teflon-filled coaxial line in free space ($f$ in MHz):

$$C\,(\text{pF}) = 0.0221 + 0.3453 \times 10^{-11} f^2 \tag{6a}$$

For a 6.4-mm Teflon-filled coaxial line in free space ($f$ in MHz):

$$C(\text{pF}) = 0.03999 + 1.9687 \times 10^{-11} f^2 \tag{6b}$$

An open-ended coaxial line exciting a monopole probe (Fig. 5) has been used for permittivity measurements of biological materials. The biological tissues consist essentially of water; free ions such as $Na^+$, $K^+$, $Ca^{2+}$, $Cl^-$; and a number of proteins. This composition makes the dielectric properties of the tissues similar to those of saline solutions, which are characterized by a high loss factor at microwave frequencies. The probe is used as a sensor for permittivity measurements. The sensor is placed in

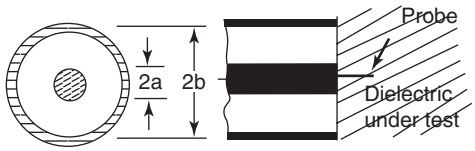


**Figure 5.** Coaxial-line-excited monopole probe for permittivity measurement.

contact with the material under test, and the reflection coefficient $\Gamma$ is measured. Knowledge of the relationship between the measured $\Gamma$ and the permittivity $\varepsilon$ then allows one to determine the latter. A number of models have been developed to determine $\varepsilon$, including the capacitive model, the antenna model, the equivalent transmission-line model, and the rational function model. A comparative study of these models for a lossy material is available in Ref. 9, where it is concluded that the equivalent transmission-line model for biological tissue characterization is adequate.

## 3. REFLECTION STANDARD FOR COAXIAL LINES

A short-circuited coaxial line can be used as a reflection standard only at one frequency for which it is a quarter-wave long. However, an open-circuited coaxial line with extended outer conductor as shown in Fig. 1c, can be used as a broadband reflection standard with minimal losses. Also, this reflection standard can be fabricated easily using commercially available components. Variational analysis of this device has been reported elsewhere in the literature [2,10–12]. If the coaxial line/circular waveguide combination is operated below the cutoff frequency of the dominant mode in circular waveguide, the signal will get attenuated in the waveguide. In addition, if the waveguide is sufficiently long to attenuate the signal by $\sim 50$ dB, the radiation from the waveguide will be negligible. Therefore, the coaxial line/waveguide junction will be capacitive in nature. Bianco et al. [12] have computed the junction capacitance. The variation of junction capacitance with frequency for a 50-Ω 7-mm airline ($2b = 7$ mm, $\varepsilon_r = 1.000640$) is given by the following expression [12]

$$C = \frac{C(0)}{(1 - (f_{\mathrm{MHz}}/34450)^2)^{1/2}} \tag{7}$$

where $C(0)$ is the static capacitance and is 79.70 fF for the 7-mm line.

## 4. STEPS IN COAXIAL LINES

The step in a coaxial line can be due to (1) an abrupt change in the diameter of either the inner conductor (Fig. 1d) or the outer conductor (Fig. 1e) or (2) a simultaneous change in diameters of both the conductors. In other words, the step discontinuity may arise when two coaxial lines with different characteristic impedances are connected in cascade. Here, $a_1$ and $b_1$ are the radii of the inner and outer conductors of one coaxial line and $a_2$ and $b_2$ represent the same for the other coaxial line. The step discontinuity may also result when a coaxial line is butt-terminated in a connector with the same impedance. The equivalent circuit of a step can be described by a shunt capacitance at the plane of the step as shown in Figs. 1d and 1e. The capacitance does not vary appreciably with frequency if the cross-sectional dimensions of the line at the plane of discontinuity are small fractions of the wavelength.

Discontinuity capacitance can be computed using the mode-matching technique for determining the difference in capacitances between that of the structure with the discontinuity, and that computed by adding the contributions of two single unperturbed lines with cross-sectional dimensions and lengths equal to the actual lines on each side of the step. The lines may be terminated by magnetic walls after a distance equal to one diameter on each side of the step. This technique has been used in Refs. 1 and 13. Gogioso et al. [14] have used the variational method to calculate the discontinuity capacitance. FEM has been used in Ref. 15 to analyze the double-step discontinuity; computed results for a butt transition between a coaxial line and a 7-mm precision connector are presented there.

Somlo [13] has obtained closed-form expressions for the discontinuity capacitance:

Step on the inner conductor (i.e., $b_1 = b_2 = b$; Fig. 1d):

$$\frac{C}{2\pi b}(\mathrm{F/m}) = \frac{\varepsilon}{\pi}\left[\frac{\alpha^2+1}{\alpha}\ln\frac{1+\alpha}{1-\alpha} - 2\ln\frac{4\alpha}{1-\alpha^2}\right] + 1.11\times 10^{-15}(1-\alpha)(\tau-1) \tag{8}$$

where $\alpha = (b-a_2)/(b-a_1)$ and $\tau = (b/a_1)$. The maximum error in (8) is $\pm 30$ fF/m for $0.01 \le \alpha \le 1.0$ and $1.0 < \tau \le 6.0$. In the limiting case when $a_1 \to 0$, $\tau \to \infty$, an expression for the step discontinuity obtained from Fig. 1 of Ref. 13 is given as follows:

$$\frac{C}{2\pi b}(\mathrm{F/m}) = \frac{2\varepsilon}{\pi}(1.477 - \ln 4\alpha) \tag{9}$$

where $\alpha = (b-a)/b$. Equation (9) may be used to determine $C(0)$ for (7) [e.g., one obtains $C(0) = 80.7$ fF for 50-Ω 7-mm airline; this compares favorably with the computed value of 79.7 fF].

Step on the outer conductor (i.e., $a_1 = a_2 = a$; Fig. 1e):

$$\frac{C}{2\pi a}(\mathrm{F/m}) = \frac{\varepsilon}{\pi}\left[\frac{\alpha^2+1}{\alpha}\ln\frac{1+\alpha}{1-\alpha} - 2\ln\frac{4\alpha}{1-\alpha^2}\right] + 4.12\times 10^{-15}(0.8-\alpha)(\tau-1.4) \tag{10}$$

where $\alpha = (b_1 - a)/(b_2 - a)$ and $\tau = (b_2/a)$. The maximum error in (10) is $\pm 60$ fF/m for $0.01 \leq \alpha \leq 0.7$ and $1.5 \leq \tau \leq 6.0$. The stepsize decreases as $\alpha$ increases from 0 to 1. For simultaneous steps in both the conductors, the discontinuity capacitance can be determined approximately from the discontinuity capacitances associated with step in either (inner or outer) conductor [3,4].

The frequency dependence of step capacitance has been included in Ref. 13 through a multiplier factor $K$ that has been plotted for five different combinations of $\alpha$ and $\tau$. This plot is included here as Fig. 6. The $S$ matrix for a step discontinuity in the inner conductor of rectangular coaxial lines has been described by Xu et al. [16]. The mode-matching method in conjunction with FEM has been employed to improve accuracy and efficiency.

## 5. T JUNCTION OR STUB IN COAXIAL LINES

The configuration of a T junction and its equivalent circuit are shown in Fig. 7. The branchline can be viewed as a shunt circuit in parallel with the mainline. Experimental results for a specific set of parameters are available for $\lambda_0 = 10$ cm [17]. The T junction finds application in branchline couplers, filters, and other components and has been analyzed in a rectangular coaxial line [16] using mode matching, and FEM techniques. The analysis has been extended to a branchline directional coupler.

Other types of discontinuity in coaxial lines that occur less frequently, such as capacitive windows in a coaxial line, aperture coupling between two coaxial lines, bifurcation of a coaxial line, small elliptical and circular apertures in the outer conductor, and a coaxial line with infinite central conductor, are discussed in Ref. 1.

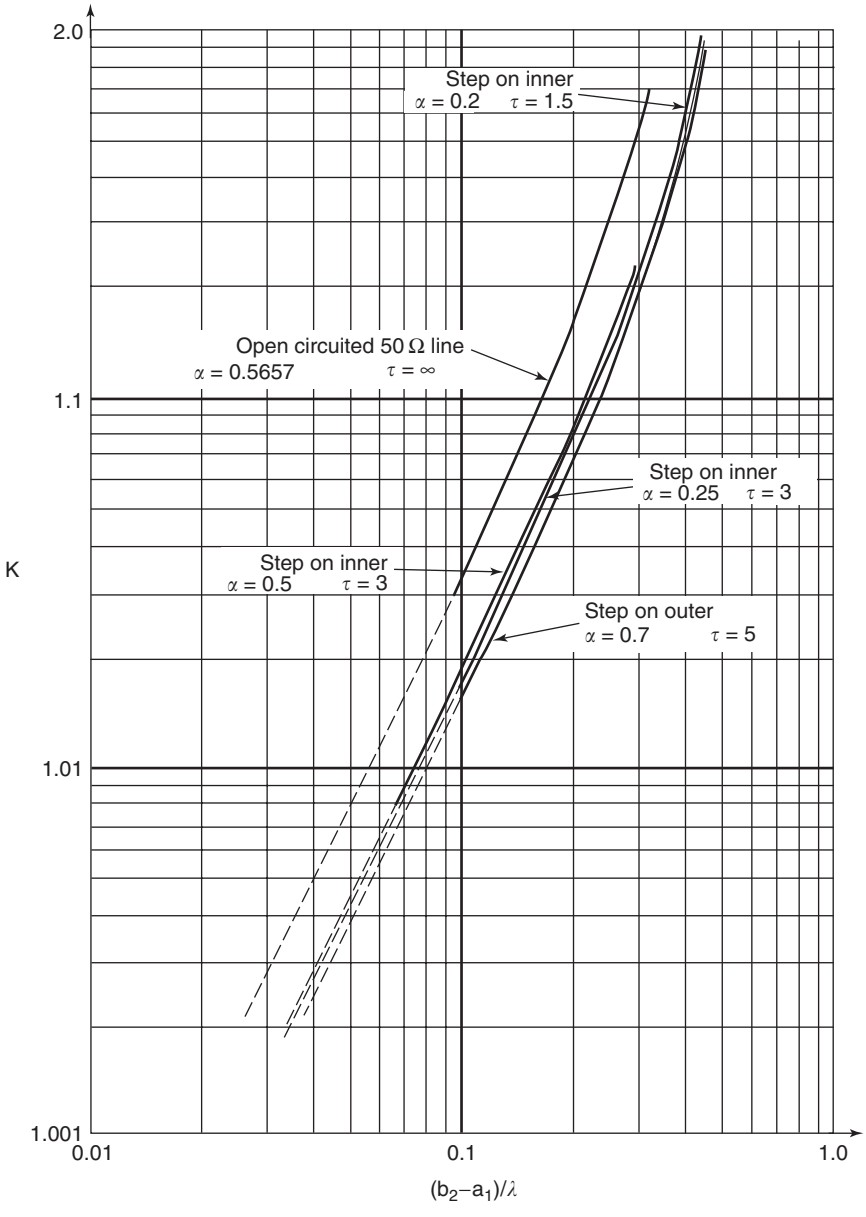


**Figure 6.** Frequency correction factor $K$ for step capacitance versus $(b_2 - a_1)/\lambda$. [From Figure 3 of P. I. Somlo, Computation of coaxial-line step capacitance, *IEEE Trans. Microwave Theory Tech.* **MTT-15**:48–53 (Jan. 1967) (© 1982 IEEE).]

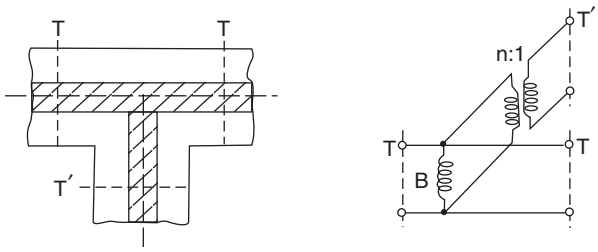


**Figure 7.** T junction and its equivalent circuit.

## BIBLIOGRAPHY


1. N. Marcuvitz, ed., *Waveguide Handbook*, Peter Peregrinus, London, 1986.
2. J. R. Whinnery, H. W. Jamieson, and T. E. Robbins, Coaxial line discontinuities, *Proc. IRE* **32**:695–709 (Nov. 1944).
3. H. E. Green, The numerical solution of some important transmission line problems, *IEEE Trans. Microwave Theory Tech*. **MTT-13**:676–692 (Sept. 1965).
4. H. E. Green, The numerical solution of transmission line problems, in L. Young, ed., *Advances in Microwaves*, Vol. 2, Academic Press, New York, 1967, pp. 327–393.
5. S. Sen and P. K. Saha, Equivalent circuit of a gap in the central conductor of a coaxial line, *IEEE Trans. Microwave Theory Tech*. **MTT-30**:2026–2029 (Nov. 1982).
6. S. Chattopadhyay and P. K. Saha, Variational analysis of a gap in the central conductor of a rectangular coaxial line, *IEEE Trans. Microwave Theory Tech*. **47**:246–249 (Feb. 1999).
7. H. J. Eom, Y. C. Noh, and J. K. Park, Scattering analysis of a coaxial line terminated by a gap, *IEEE Microwave Guided Wave Lett*. **8**:218–219 (June 1998).
8. D. K. Misra, A quasi-static analysis of open-ended coaxial lines, *IEEE Trans. Microwave Theory Tech*. **MTT-35**:925–928 (Oct.1987).
9. D. Berube, F. M. Ghannouchi, and P. Savard, A comparative study of four open-ended coaxial probe models for permittivity measurements of lossy dielectric/biological materials at microwave frequencies, *IEEE Trans. Microwave Theory Tech*. **44**:1928–1934 (Dec. 1996).
10. E. W. Risley, Jr., Discontinuity capacitance of a coaxial line terminated in a circular waveguide, *IEEE Trans. Microwave Theory Tech*. **MTT-17**:86–92 (Feb. 1969).
11. E. W. Risley, Jr., Discontinuity capacitance of a coaxial line terminated in a circular waveguide: Part II—Lower bound solution, *IEEE Trans. Microwave Theory Tech*. **MTT-21**:564–566 (Aug. 1973).
12. B. Bianco, A. Cosana, L. Gogioso, S. Ridella, and M. Parodi, Open-circuited coaxial lines as standards for microwave measurements, *Electron. Lett*. **16**:373–374 (May 8, 1980).
13. P. I. Somlo, Computation of coaxial-line step capacitance, *IEEE Trans. Microwave Theory Tech*. **MTT-15**:48–53 (Jan. 1967).
14. L. Gogioso, M. Marchesi, and M. Parodi, A variational approach to compute the equivalent capacitance of coaxial line discontinuities, *Proc. Int. Microwave Symp*. 1979, pp. 580–583.
15. E. Marouby, M. Aubourg, and P. Guillon, Application of the finite element method to the design of transitions between coaxial lines, *IEE Proc. H* **137**:219–225 (Aug. 1990).
16. S. Xu, X. Wu, W. Guo, and Z. Li, Scattering characteristics of rectangular coaxial line discontinuities, *IEE Proc. Microwave Anten. Propag*. **142**:257–264 (June 1995).
17. C. G. Montgomery, R. H. Dicke, and E. M. Purcell, eds., *Principles of Microwave Circuits*, Peter Peregrinus, London, 1987, Sect. 9.6, p. 295.


# COAXIAL LINES AND WAVEGUIDES

NEMAI CHANDRA KARMAKAR
Monash University
Clayton, Victoria, Australia
SHANTANU KUMAR PADHI
University of Queensland
St. Lucia, Queensland, Australia

## 1. INTRODUCTION

Starting with Maxwell's theoretical concept of wave propagation in the 1870s, followed by Heinrich Hertz' experimental proof of the transmission of electromagnetic wave energy in the 1890s, RF–microwave technologies saw extraordinary advances during the nineteenth and twentieth centuries. Progress in this field, particularly its application in high-frequency wired and wireless communications technology, has hinged most critically on the efficient transmission and reception of electromagnetic energy through various media. Without carefully designed transmission lines, RF and microwave technologies could not have undergone further development and modern civilization could certainly not have reached the present "information age." In everything from a handheld GPS receiver to a jumbo jet, transmission-line design is of crucial importance to proper operation. The sheer diversity of RF–microwave devices available today means that RF–microwave designers must spend most of their time tuning transmission lines, matching various sections, and designing controlled attenuation to other parts of the system. For example, while a mobile phone consists of high-frequency microstrip transmission lines in planar multilayered circuits, a jumbo jet has 275 km of cables of various forms, including low-frequency lighting, high-frequency navigation tools, and wireless terrestrial and satellite navigation and communication equipment. Just as High-frequency devices and gadgets such as radios, television sets, satellite ground stations, and satellite payloads are useless without efficient transmission lines, adapters, and assemblies in the same way that the main engine block in an automobile is useless without conduits, nuts, and bolts. Transmission lines are guiding structures that convey high-frequency electromagnetic energy from one block to another. Their careful design for amplitude and phase matching is therefore extremely important.

The high-frequency transmission line industry is a huge enterprise. According to *http://www.globalspec.com*, 186 coaxial cable manufacturing companies and 60 waveguide manufacturing companies operate in the United States alone. Moreover, 585 companies

manufacture cable assemblies, including connectors, adapters, and attenuators. In the year 2000, the market volume increased by about 25%. This is due to rapid growth of wireless mobile communications and other sectors. With the emergence of new innovative technologies in the twenty-first century, such growth is expected to continue at a still higher rate.

High-frequency cables, waveguides, and accessories are usually very expensive items because they require manufacturing to high standards and tolerances. The most common forms of such transmission lines are coaxial cables and waveguides. For RF–microwave frequencies, which span anything from a few MHz to 30 GHz, the coaxial line is the oldest and most widely used devices for transferring RF energy from one point to another. Heinrich Hertz used coaxial cables in his experiments to prove Maxwell's theory of electromagnetic wave propagation. Hertz used coaxial lines to generate the standing waves. In the 1930s when radios became very popular, coaxial transmission lines were used exclusively at low frequencies such as VHF and UHF applications. The shielding properties of coaxial lines minimize the static interference of charge leakage at low frequencies. For higher-frequency applications such as 1 GHz and above, waveguide structures are generally used. The waveguide is preferred because of its low transmission losses and high power-handling capabilities. In 1897, Lord Rayleigh mathematically proved the concept of wave propagation through single-conductor rectangular and circular waveguides. He also proved the existence of a cutoff frequency below which no wave can propagate through the waveguide. Following the example of Lord Rayleigh, Sir Jagadish Chandra Bose invented waveguides and used these waveguides in his wireless experiments in 1894. He also invented waveguide horn antennas for millimeter-wave transmission and reception. Sir Jagadish Bose extensively used scientific demonstrations of EM wave propagations and detections in his teaching classes in the Presidency College of Kolkata, India. Also in 1894, Sir Oliver Lodge observed directional radiation when he surrounded a spark oscillator with a metal tube. Because high-frequency sources were not widely available, not much work was conducted on waveguides until about 1930. After this time, scientists from AT&T and MIT radiation laboratory rediscovered the waveguide and developed a theoretical framework to explain the cutoff frequencies and propagation modes. During and after World War II, the design and use of various coaxial cables and waveguides advanced with new thrusts for emerging applications in radars and wireless communications.

In this article we first describe the classical theory in which transmission lines are assumed to be a distributed section of series resistance and inductance, as well as shunt capacitance and conductance. This model is then evolved into the "telegrapher equation," which explains the wave nature of electromagnetic energy guided by a two-conductor transmission line. Basic characteristic parameters such as the propagation constant, phase velocity, and characteristic impedance are derived. This generalized transmission line theory can be applied to any transmission-line type. Finally, the field theory of transmission lines is used to derive coaxial transmission-line theory. Practical examples of various coaxial cables and cable assemblies available on the market are also presented. Different waveguide configurations such as parallel-plate, rectangular, circular, and elliptical waveguides are discussed and propagation modes in the waveguide are defined. Planar waveguides such as microstrip lines, slotlines, and coplanar waveguides are also presented.

## 2. CLASSIFICATION OF TRANSMISSION LINES

Most practical waveguide structures rely on single-mode propagation in a particular direction. They can consequently be conveniently classified according to the polarization properties of the electromagnetic waves they carry: transverse electromagnetic (TEM), transverse electric (TE), or transverse magnetic (TM) modes. TEM modes have both electric and magnetic fields transverse to the direction of propagation. In TM mode, the magnetic field is transverse to the direction of propagation and in TE mode, the electric field is transverse to the direction of propagation. Mathematically, these modes for a wave propagating in the $z$ direction can be represented as follows:

1. TEM waves: $E_z = 0, H_z = 0$
2. TM waves: $E_z \neq 0, H_z = 0$
3. TE waves: $E_z = 0, H_z \neq 0$
4. Hybrid waves: $E_z \neq 0, H_z \neq 0$

Transmission lines can be classified with respect to polarization, as shown in the tree diagram in Fig. 1. TEM is the dominant mode of propagation in coaxial lines and parallel-plate transmission lines where two conductors are involved. TE and TM propagation modes are typically found in single-conductor waveguides, which have rectangular, circular, elliptical or ridge-type cross sections. Other than TEM, TE, or TM modes, hybrid modes are also known that contain all six components ($E_x, E_y, E_z, H_x, H_y, H_z$) of electric and magnetic fields. Examples of transmission lines that support hybrid modes of propagation include microstrip (MS) transmission line, slotline (SL), and coplanar waveguide (CPW) structure.

The various forms of transmission lines are shown in Fig. 2. Figure 2a illustrates the most typical such lines: a parallel, two-conductor transmission line in which the conductors are uniformly separated by an air dielectric. The evolution of waveguides away from the two-conductor transmission line can perhaps be best understood in terms of the theory of quarter-wave transformers. A quarter-wave section of a short-circuited transmission line is transformed by an operating frequency into an open circuit at the input end of the line. The waveguide is then considered to be two short-circuited, quarter-wave sections along the two-wire transmission line. The cutoff in the waveguide's frequency dependence can be understood in terms of the behavior of the quarter-wave section of the line.

Figure 2b depicts a coaxial cable where the center conductor is concentric with the outer cylindrical conductor,

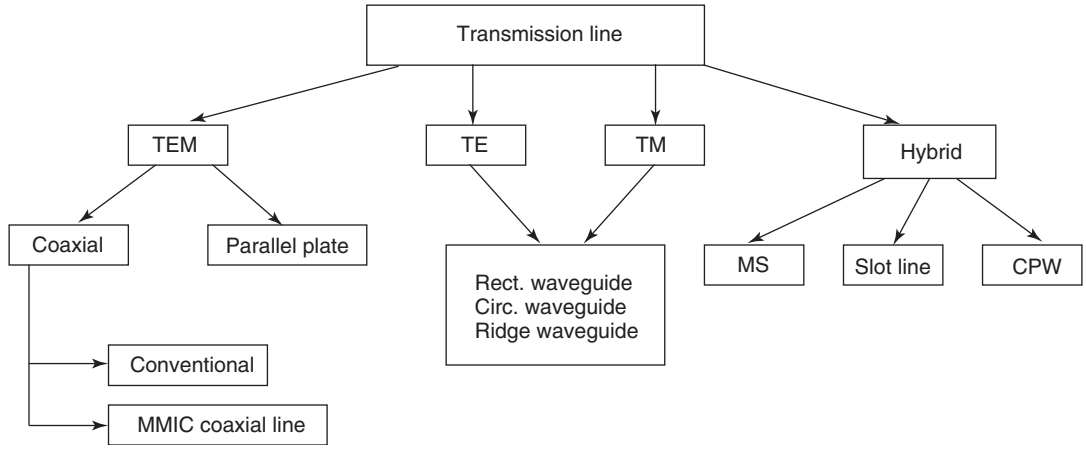


**Figure 1.** Classification of transmission lines based on a single mode of wave propagation.

which is usually the ground for the transmission line. As such, it acts as the shield for outside interference. The uniform gap between the two conductors is filled with a dielectric material. The advantage of the coaxial cable is its high immunity to interfering signals due to the shielding provided by the outer conductor of the information-carrying signal.

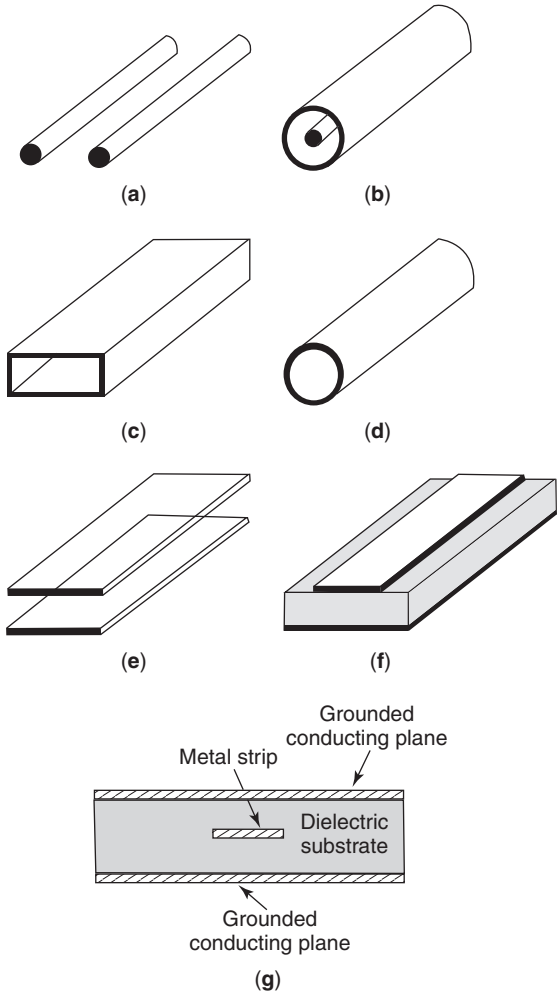


**Figure 2.** Commonly used waveguide structures: (a) open two-wire line; (b) coaxial line; (c) rectangular waveguide; (d) circular waveguide; (e) parallel-plate waveguide; (f) microstrip line; (g) stripline.

Other forms of high-frequency transmission lines are dielectric waveguides (not shown here), parallel-plate waveguides (Fig. 2e), and planar transmission lines such as microstrip lines (Fig. 2f) and striplines (Fig. 2g).

Table 1 compares the three most popular transmission lines used in modern microwave circuits and systems: coaxial cables, waveguides, and microstrip lines. As can be seen, each line has its own advantages and disadvantages. While coaxial cables are popular in network-related, low- and medium-frequency operation, waveguides are preferred in high-frequency and high-power applications. At high frequencies, both coaxial cables and microstrip lines exhibit high power losses and signal distortions. Because of their better power-handling capability, waveguides are popular for radars and similar high-power, high-frequency applications in which their physical bulk is not a hindrance. For compact and portable, lightweight gadgets such as mobile phones, handheld GPS receivers, and some solid-state, high-power amplifier modules, microstrip lines are preferred. To compensate for the losses they suffer as a result of high attenuation, amplifiers are typically used. Transmission lines and circuit formats are therefore selected according to their specification requirements and applications.

## 3. TRANSMISSION LINE THEORY: LUMPED-ELEMENT CIRCUIT MODEL

A transmission line is often schematically represented by a two-wire line, because transmission lines for TEM wave propagation always have at least two conductors. Figure 3 illustrates a differential length ($\Delta z$) of a two-conductor transmission line represented by a distributed parameter network. The voltages and currents vary in magnitude and phase over its length. The distributive parameters are

$R =$ resistance per unit length
$L =$ inductance per unit length

**Table 1. Comparison of Common Transmission Lines and Waveguides**

| Characteristic | Coaxial line | Rectangular Waveguide | Microstrip line |
|---|---|---|---|
| Preferred mode | TEM | $TE_{10}$ | Quasi-TEM |
| Dispersion | None | Medium | Low |
| Bandwidth | High | Low | High |
| Power-handling capacity | Medium | High | Low |
| Loss/attenuation | Medium | Low | High |
| Physical size | Large | Large | Small |
| Ease of fabrication | Medium | Medium | Easy |
| Integration with other components | Hard | Hard | Easy |

$G =$ conductance per unit length
$C =$ capacitance per unit length
$\Delta z =$ incremental length

One can determine the current and voltage relations for the short length of line $\Delta z$. Kirchhoff's voltage and current laws are applied along the transmission line shown in Fig. 3. In the derivation, the line length of $\Delta z \to 0$ is assumed. Equations for the instantaneous voltages and currents and for time-harmonic equivalents are as follows:

Instantaneous equations

$$-\frac{\partial v}{\partial z} = Ri + L\frac{\partial i}{\partial t} \tag{1}$$

$$-\frac{\partial i}{\partial z} = Gv + C\frac{\partial v}{\partial t} \tag{2}$$

Time-harmonic equations where $e^{j\omega t}$ is assumed

$$-\frac{dV}{dz} = RI + j\omega LI \tag{3}$$

$$-\frac{dI}{dz} = GV + j\omega CV \tag{4}$$

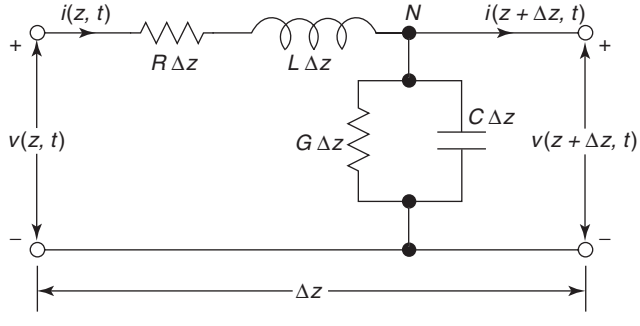


**Figure 3.** Lumped-element equivalent-circuit model of the differential length of a transmission line.

The solution for instantaneous voltages and currents is

$$v(z,t) = \mathrm{Re}[V(z)e^{j\omega t}]; \quad i(z,t) = \mathrm{Re}[I(z)e^{j\omega t}] \tag{5}$$

Wave equations for time-harmonic voltages and currents are rewritten as

$$\begin{aligned} -\frac{dV}{dz} &= (R + j\omega L)I \\ -\frac{dI}{dz} &= (G + j\omega C)V \\ \Rightarrow &\begin{cases} -\dfrac{d}{dz}\left(\dfrac{dV}{dz}\right) = (R + j\omega L)\dfrac{dI}{dz} \\ \dfrac{d^2V}{dz^2} = (R + j\omega L)(G + j\omega C)V \end{cases} \end{aligned} \tag{6}$$

The final expressions for time-harmonic voltage and current wave equations along the line are

$$\frac{d^2V}{dz^2} = \gamma^2 V \tag{7}$$

$$\frac{d^2I}{dz^2} = \gamma^2 I \tag{8}$$

The propagation constant $\gamma$ for the line is defined as

$$\gamma = \sqrt{(R + j\omega L)(G + j\omega C)} = \alpha + j\beta \tag{9}$$

where $\alpha$ is the attenuation constant (Np/m) and $\beta$ is the propagation constant (rad/m).

The traveling-wave solutions are

$$V(z) = V^+(z) + V^-(z) = V_0^+ e^{-\gamma z} + V_0^- e^{+\gamma z} \tag{10}$$

$$I(z) = I^+(z) + I^-(z) = I_0^+ e^{-\gamma z} + I_0^- e^{+\gamma z} \tag{11}$$

The plus sign indicates the forward-traveling wave, and the minus sign indicates the backward-traveling wave. Applying (11) to the voltage of (3) gives the current on the line:

$$I(z) = \frac{-1}{R + j\omega L}\frac{dV(z)}{dz} = \frac{\gamma}{R + j\omega L}[V_0^+ e^{-\gamma z} - V_0^- e^{+\gamma z}] \tag{12}$$

The characteristic impedance of the line is

$$Z_0 = \frac{V_0^+}{I_0^+} = \frac{R + j\omega L}{\gamma} = \sqrt{\frac{R + j\omega L}{G + j\omega C}} \tag{13}$$

To relate the voltage and current on the line; $Z_0 = (V_0^+/I_0^+) = -(V_0^-/I_0^-)$. The wavelength of the wave along the line is

$$\lambda_g = \frac{2\pi}{\beta} \tag{14}$$

and the phase velocity of the wave along the transmission line is

$$v_p = \frac{\omega}{\beta} = \lambda f \tag{15}$$

For lossless transmission lines, $R = G = 0$; the propagation constant is $\gamma = j\omega\sqrt{LC} = \alpha + j\beta$. Therefore, the attenuation constant $\alpha = 0$ and $\beta = \omega\sqrt{LC}$. The characteristic impedance is

$$Z_0 = \sqrt{\frac{L}{C}} \tag{16}$$

The general solution of a lossless transmission line is

$$V(z) = V^+(z) + V^-(z) = V_0^+ e^{-j\beta z} + V_0^- e^{j\beta z} \tag{17}$$

$$I(z) = I^+(z) + I^-(z) = (V_0^+/Z_0)e^{-j\beta z} - (V_0^-/Z_0)e^{j\beta z} \tag{18}$$

The wavelength of the wave along the line $\lambda_g = (2\pi/\beta) = (2\pi/\omega\sqrt{LC})$ and the phase velocity of the wave along the transmission line is $v_p = (\omega/\beta) = \lambda f$.

### 3.1. Coaxial Lines

The key feature of coaxial lines is that their characteristic impedance is very broadband. The fundamental mode of operation is TEM, where the electric and magnetic fields are transverse in the direction of propagation. A typical coaxial cable, shown in Fig. 4, consists of two concentric conductors of inner and outer radii $a$ and $b$, respectively, with the space between them filled with a dielectric ($\varepsilon_r$) such as Teflon or polyethylene. In this section we perform a field analysis on a coaxial cable to calculate the equivalent circuit parameters such as $R$, $G$, $L$, and $C$ as defined earlier in the telegrapher equation.

Let the voltage between the conductors be $V_0\, e^{\pm j\beta z}$ and the current $I_0\, e^{\pm j\beta z}$. The fields of a traveling TEM wave inside the coaxial line along the $+z$ direction are then given as follows:

$$\mathbf{E} = \frac{V_0\hat{\rho}}{\rho \ln(b/a)} e^{-\gamma z} \quad \text{(V/m)} \tag{19}$$

$$\mathbf{H} = \frac{I_0\hat{\phi}}{2\pi\rho} e^{-\gamma z} \quad \text{(A/m)} \tag{20}$$

The conductors are assumed to have a surface resistivity $R_s$. The material filling the space between the conductors is assumed to have a complex permittivity $\varepsilon = \varepsilon' - j\varepsilon''$, and the permeability is $\mu = \mu_0\mu_r$. We now determine the transmission line parameters $R$, $G$, $L$, and $C$.

The time-average magnetic energy store is defined as

$$W_m = \frac{\mu}{4}\int_S HH^* ds = L|I_0|^2/4 \tag{21}$$

The self-inductance per unit length is

$$\begin{aligned} L &= \frac{\mu}{|I_0|^2}\int_S HH^* ds \quad \text{(H/m)} \\ &= \frac{\mu}{2\pi}\ln(b/a) \ \text{(H/m)} \end{aligned} \tag{22}$$

The time-average electric energy stores is defined as

$$W_e = \frac{\varepsilon}{4}\int_S EE^* ds = C|V_0|^2/4 \tag{23}$$

The self-capacitance per unit length is

$$C = \frac{\varepsilon}{|V_0|^2}\int_S EE^* ds \quad \text{(F/m)} = \frac{2\pi\varepsilon'}{\ln(b/a)} \quad \text{(F/m)} \tag{24}$$

The power loss per unit length due to the finite conductivity $\sigma$ of the metallic conductor is

$$P_c = \frac{R_S}{2}\int_{C_1+C_2} HH^* dl = R|I_0|^2/2$$

where the surface resistivity is defined as $R_S = 1/\sigma\delta_S$, where $\delta_S$ is the skin depth of the conductor. The series resistance $R$ per unit length of the line is

$$\begin{aligned} R &= \frac{R_S}{|I_0|^2}\int_{C_1+C_2} HH^* dl \ (\Omega/\text{m}) \\ &= \frac{R_S}{2\pi}\left(\frac{1}{a} + \frac{1}{b}\right) \ (\Omega/m) \end{aligned} \tag{25}$$

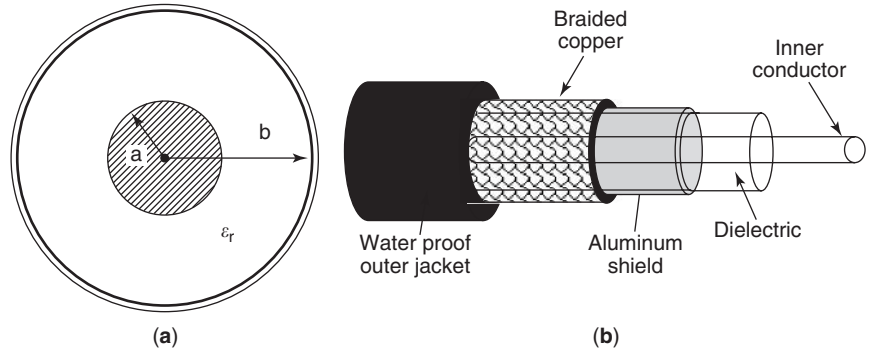


**Figure 4.** Coaxial cable: (a) cross-sectional view; (b) isometric view.

Due to the "lossy" dielectric, the time-average power dissipated per unit length is

$$P_d = \frac{\omega\varepsilon''}{2}\int_S EE^* ds = G|V_0|^2/2 \tag{26}$$

The conductance per unit length is

$$G = \frac{\omega\varepsilon''}{|V_0|^2}\int_S EE^* ds \quad (\text{S/m}) = \frac{2\pi\omega\varepsilon''}{\ln(b/a)} \quad (\text{S/m}) \tag{27}$$

So far we have calculated the equivalent-circuit model parameters of a coaxial cable with the radii of the outer and inner conductors of $b$ and $a$, respectively. Now we opt to calculate the characteristic impedance of the coaxial line $Z_0$, which is frequency-independent and can be calculated as

$$Z_0 = \frac{V_0}{I_0} = \sqrt{\frac{\mu}{\varepsilon}}\ln\left(\frac{b}{a}\right) = \frac{60}{\sqrt{\varepsilon_r}}\ln\left(\frac{b}{a}\right) \quad (\Omega) \tag{28}$$

The approximate cutoff frequency of the cable can be calculated from (29), at which point the first non-TEM mode of propagation begins. At a frequency above $f_{\text{cutoff}}$ [5], other propagation modes dominate and the characteristic impedance becomes frequency-dependent:

$$F_{\text{cutoff}}(\text{GHz}) = \frac{7.51}{\sqrt{\varepsilon_r}}\left(\frac{1}{a+b}\right) \tag{29}$$

The line parameters $L$, $R$, $C$, and $G$ of coaxial lines can be calculated from

$$C = \frac{55.63\varepsilon_r}{\ln\left(\frac{b}{a}\right)} \quad (\text{pF/m}) \tag{30}$$

$$L = 200\ln\left(\frac{b}{a}\right) \quad (\text{nH/m}) \tag{31}$$

$$R = 10\left[\frac{1}{a} + \frac{1}{b}\right]\sqrt{\frac{f_{\text{GHz}}}{\sigma}} \quad (\Omega/\text{m}) \tag{32}$$

$$G = \frac{0.3495\varepsilon_r f_{\text{GHz}}\tan(\delta)}{\ln\left(\frac{a}{b}\right)} \quad (\text{S/m}) \tag{33}$$

where $\tan\delta$ is the loss tangent of the dielectric material, $\sigma$ is the conductivity of the conductor in S/m, and $f_{\text{GHz}}$ is the signal frequency in GHz.

**3.1.1. Cable Losses.** The losses in a coaxial cable arise from two sources: resistance of the conductors and the dielectric losses between the two conductors. The conductor losses are ohmic and increase with the square root of the frequency due to the skin effect. The dielectric loss is due to the finite conductivity of the dielectric material and increases linearly with the frequency. Figure 5a shows the attenuation per foot and power-handling capability of a MegaPhase TM Series test cable. As can be seen in Fig. 5a, the per unit length attenuation increases with frequency. In Fig. 5b the power-handling capacity of the cable reduces with frequency. The frequency dependence of the attenuation and the power-handling capability is explained in the following section.

The transmitted power can be expressed in terms of the voltage or maximum value of the electric field inside the line:

$$P_T = \frac{1}{2Z_0}|V|^2 = \frac{1}{\eta}|E_a|^2(\pi a^2)\ln\left(\frac{b}{a}\right) \tag{34}$$

The attenuation coefficients due to conductor and dielectric losses are

$$\begin{aligned} P'_{\text{loss}} &= \frac{1}{2}R_s[(2\pi a)|H_a|^2 + (2\pi a)|H_b|^2] \\ &= \frac{R_s|I^2|}{4\pi}\left(\frac{1}{a} + \frac{1}{b}\right) \end{aligned} \tag{35}$$

$$\alpha_c = \frac{P'_{\text{loss}}}{2P_T} = \frac{R_s}{2\eta}\frac{\left(\frac{1}{a}+\frac{1}{b}\right)}{\ln\left(\frac{b}{a}\right)} \tag{36}$$

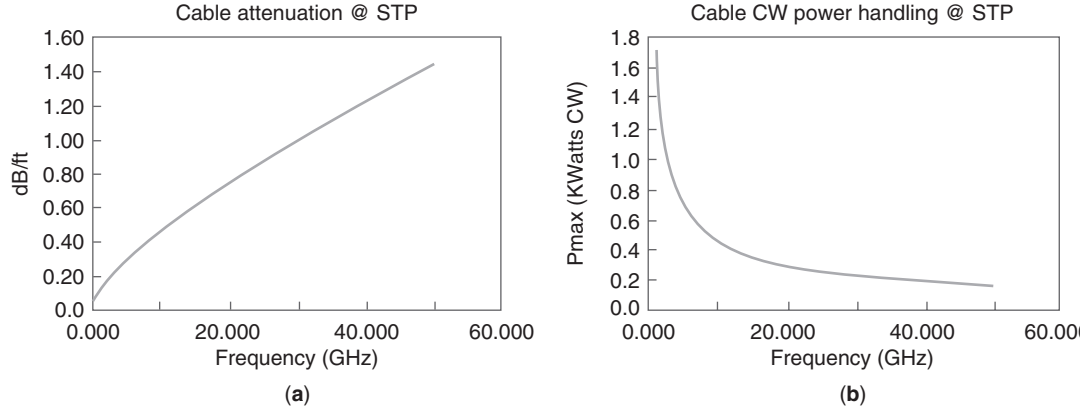


**Figure 5.** Attenuation per foot and power-handling capability of a coaxial cable as a function of frequency. (*Source*: *http://www.megaphase.com/html/test02.html*.)

$$\alpha_d = \frac{w}{2c}\tan(\delta) \tag{37}$$

Total losses will be

$$\alpha = \alpha_c + \alpha_d = \frac{R_s}{2\eta}\frac{\left(\frac{1}{a}+\frac{1}{b}\right)}{\ln\left(\frac{b}{a}\right)} + \frac{\omega}{2c}\tan(\delta) \tag{38}$$

where the surface resistivity is

$$R_s = \sqrt{\frac{\omega\mu_0}{2\sigma}} \tag{39}$$

**3.1.2. Types of Coaxial Cable.** There are various types of coaxial cables available in the commercial market. They are broadly categorized as flexible cables and semirigid cables. Flexible cables are most widely used as measurement tools for test and characterization. There are two varieties of flexible cable available. The overall cable diameters vary from $<0.25$ in. to $>1$ in. depending on the power-handling capability of the wire. Some cables use a stranded inner conductor, while others employ solid wire with single braid or double-braided outer conductor. The outer jacket plays no part in the electrical performance of the cable—it simply holds everything together and supplies a waterproof covering. Selection of cable types depends primarily on the characteristic impedance of the cable, capacitance per unit length, power-handling capability, outer diameter, and attenuation per unit length at the specific frequency. Preference is also given to double-shielded/braided cable over the corresponding single-shielded cable due to the resilience against interference and physical ruggedness. Figure 6b shows an air-filled coaxial cable with spiral dielectric fin support. This cable displays low loss due to the air dielectric; the phase velocity is very close to that of the free space.

**3.1.3. Semirigid Cables.** Another popular transmission line is semirigid cable. Both inner and outer conductors are solid, and the two conductors are uniformly separated with dielectric material. Semirigid cables can be bent to moderate angles but, once bent, cannot be brought back to their original shape. Cables of this type are neither rigid nor flexible; hence their name. Semirigid cables have better shielding capabilities and are more immune to outside interference than are flexible cables. Semirigid cables also have reduced attenuation and enhanced power-handling capabilities. Figure 7 shows various forms of semirigid cables soldered with SMA connectors at both ends. The inner conductors are made from various materials such as silver-coated copper, silver-plated copper-clad steel, and silver-plated aluminum. The dielectric filling is typically polyethylene, polytetrafluoroethylene (TFE Teflon), polytetrafluoroethylene–hexafluoropropylene (FEP Teflon), or kapton. The outer conductor is made of copper, aluminum, stainless steel, and special copper alloys. Selection of a particular type of semirigid cable involves consideration of factors such as power-handling capability, attenuation per unit length, size, higher-mode cutoff frequency, dielectric strength, and breakdown voltages (corona discharge voltage).

**3.1.4. Coaxial Connectors.** Coaxial cable is no use if interfacing with various components in a system is made. Various types of coaxial connectors and cable assemblies are used. Each type of connector can be attached to a cable in several waves: direct solder, crimpon, and screwon. Figure 7 shows various bent coaxial cable assemblies.

Interfacing cables with connectors and adapters need special care. Bending also requires special jigs to ensure minimum distortion of its regular shape. The cable must be cut to the exact length and then bent to the shape required. After shaping, the inner conductors are made in exact lengths such that they can be inserted into the inner conductor of a connector. Then solder is applied to the outer jacket to electrically connect the adapter and the cable. Adapter assemblies of this type are shown in Fig. 8.

**3.1.5. More Recent Developments of Coaxial Line.** Coaxial cables are nonplanar in nature, and compatibility with modern monolithic microwave integrated circuits (MMICs) and microelectromechanical structures (MEMS) is an issue. MMIC and MEMS support planar transmission lines such as microstrip lines, striplines, slotted lines, and coplanar waveguides (CPWs). More recently, with the advent of new processing techniques,

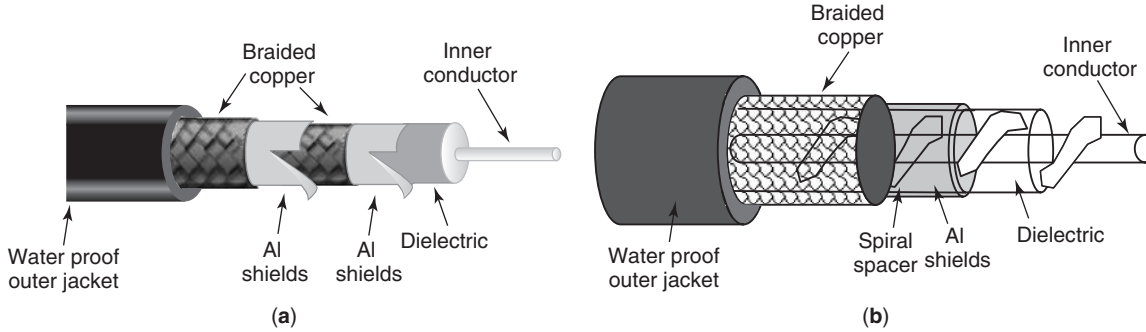


**Figure 6.** Flexible coaxial cable (coax) configurations: (a) double-braided solid-filled coax; (b) air-filled coax with spiral dielectric fin support.

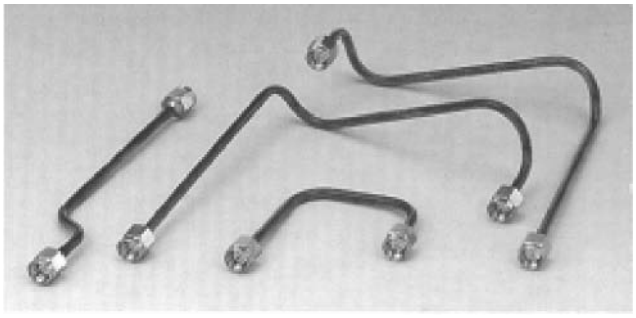

**Figure 7.** Various semirigid cable bends. (*Source*: *http://www.shibata.co.jp/etxt/3_g_g6.htm*.)


**Figure 8.** Various coaxial cable assemblies. (*Source: http://www.gordontech.com.au/*.)

MMIC and MEMS coaxial lines have been developed. These lines are designed for use in extremely wide frequency ranges from DC to THz. Monolithic implementation of coaxial lines in silicon and gallium arsenide (GaAs) substrate up to 40 GHz (c.f. Fig. 9a) has been reported [12]. The MMIC line is composed of a center conductor surrounded by a homogeneous dielectric (Polmide) covered entirely with a gold-plated ground plane. The pure TEM mode propagation of the proper mode is verified from the measurement. The authors also theoretically verify the losses up to 1000 GHz frequency band, and the transmission loss is about 15 dB/mm. The line has a measured maximum attenuation of 1.6 dB/mm at 40 GHz.

Developments in MEMS technology have made many breakthroughs in RF and microwave technologies. This state-of-the-art manufacturing technology supports IC batch processing on silicon wafers. A MEMS microcoaxial transmission line with inclined shields has been developed by the Korea Advanced Institute of Science and Technology [13]. With the removal of dielectric between the conductors, a very low attenuation of 0.03 dB/mm at 10 GHz has been obtained from the fabricated microcoaxial transmission line. Investigation reveals that the microcoaxial line fabricated on a glass line is less lossy than that fabricated on a silicon device. The MEMS microcoaxial line is shown in Fig. 9b.

Thus far, we have discussed the two main types of microwave transmission lines, namely, coaxial cables and waveguides, including their historical perspectives and more recent market statistics. The basic transmission-line theory of the telegrapher equation is presented. The theories of coaxial lines based on lumped elements as well as field theory have been presented. Two types of coaxial lines—flexible and semirigid cables—are discussed. Different connectors and adaptors of coaxial cables and cable assemblies are presented. Finally, the most recent development in MMIC and MEMS microcoaxial lines at higher frequencies are presented. In the following section, we will discuss waveguides.

### 3.2. Waveguide

In the preceding section, we discussed various types of coaxial transmission lines. In this section we shall discuss various nonplanar and planar waveguide structures and their modes of operations. Waveguides are extensively used to transfer electromagnetic energy efficiently from one point to another in a wide spectrum of frequency. Nonplanar waveguides are hollow tubes in which waves can propagate only at certain frequencies and cannot propagate below the cutoff frequencies. The cross section of the enclosed boundaries of the waveguide is transverse to the direction of propagation. Waveguides are used at microwave frequencies for two reasons: (1) they are often easier to fabricate than are coaxial lines and (2) they can be made to have less attenuation. Coaxial lines require the center conductor to be supported by the solid dielectric in the center of the outer cylindrical jacket. In contrast, a waveguide does not need any center conductor and its dielectric is air. Because of the high losses in a coaxial line over any distance ($>2$ ft), along with the cable leakage at

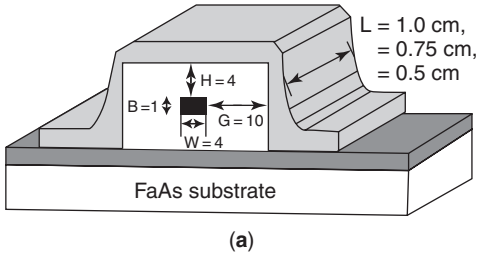


(a)

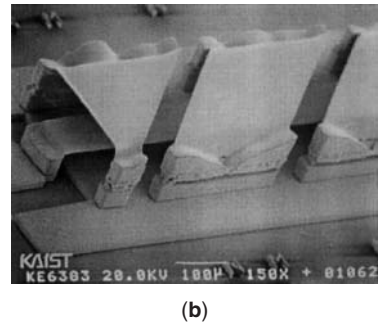


(b)

**Figure 9.** (a) MMIC rectangular coaxial line on GaAs [12]; (b) MEMS microcoaxial line [13].

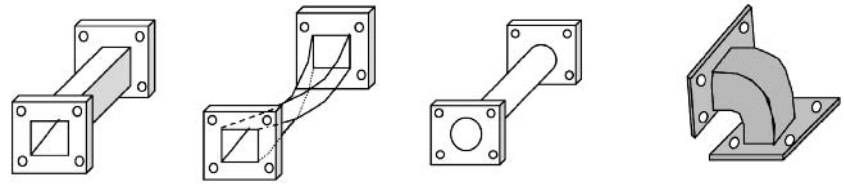

**Figure 10.** Different forms of waveguides: (a) rectangular waveguide; (b) twist polarizer; (c) circular waveguide; (d) rectangular waveguide bend.

higher frequencies, the waveguide structure is preferred at higher frequencies. If the waveguide boundaries change direction within reasonable limits, the wave is bound to follow the changing direction without much distortion and discontinuity. In practice, such bends and junctions are very common in high-power radar systems where waveguides carry high-power high-frequency EM energy from the transmitter to the antenna. In waveguides, the waves are guided according to the distributions of the EM fields in the waveguide and their dependence on currents and charges on the conducting boundaries and the reflections of the fields in the conducting boundaries.

The most common hollow waveguides have rectangular or circular cross sections; however, the rectangular waveguides are preferred over circular ones for many applications. Figure 10 illustrates various forms of rectangular waveguides. Very often rectangular waveguides are designed such that one side of the rectangular wall is twice the length of the other side. This cross-sectional dimension has the advantage of enabling the operator to control the polarization of the wave to be transmitted. The electrical fields remain parallel to the smaller dimension of the waveguide cross section. If the dimension is made much larger, the electric field does not remain parallel to the side any more. On the other hand, if the dimension is made much smaller, then there will be considerable attenuation. The dimensions of the waveguide are generally designed such that only the fundamental or dominant mode can propagate. All other higher-order modes attenuate quite rapidly. Furthermore the dimensions are to be chosen such that there is a significant difference between the cutoff frequencies of the successive modes. This is necessary to ensure that only one designed mode may propagate.

Another popular type is the circular waveguide. In contrast to the rectangular waveguide, a circular waveguide lacks the sense of polarization of the wave that is being transmitted through. This is because there is no preferred direction across the circular cross-sectional plane. Furthermore, the cutoff frequencies of different modes are very close. As a consequence, it is very hard to determine an operating frequency that will yield a low attenuation for the dominant mode and high attenuation for the other higher-order modes. The advantage of the circular waveguide is exploited from its circular symmetry. Rotary joints use circular symmetry. For rotating antenna feeds used in radars, rotary joints are employed. The quality ($Q$) factor of the circular waveguide cavity is higher than that of the rectangular waveguide. This inherent characteristic is exploited in frequency meters.

Before proceeding further with the discussion of the hollow metallic waveguides, we shall first examine whether any wave can propagate within the waveguide (i.e., in a guide whose conducting boundaries form a simple connected region) and, if so, how the propagation takes place. As mentioned earlier with respect to coaxial cables, a TEM wave can propagate through the two-conductor transmission line. In contrast, in the single-conductor hollow waveguide such a TEM wave cannot propagate. This can be proved by field theory and solving the Helmoltz wave equation. Another very simple and interesting concept has been developed [14]. The waveguide can be perceived by a two-conductor transmission line supported by two quarter-wavelength short-circuited sections as shown in Fig. 11. Since the short-circuited quarter-wavelength section transforms into an open circuit (with infinity impedance, which is electrically invisible) at its input, there is no effect on power transmission. In many sections of this type, a rectangular waveguide such as that shown in Fig. 11 is used. To preserve the transmission-line property of the waveguide, the dimension $d$ must not be less than one wavelength. Any frequency in the dimension $a$ less than a half-wavelength (i.e., $<0.5\lambda$) causes the circuit to become an inductive shunt ($j\omega L$), which prevents propagation. The frequency at which the $a$ dimension is a half-wavelength is called the *cutoff frequency.*

Complete solutions to field equations are known for a limited number of structures with a well-defined geometry that is compatible with the coordinate system. Each mode

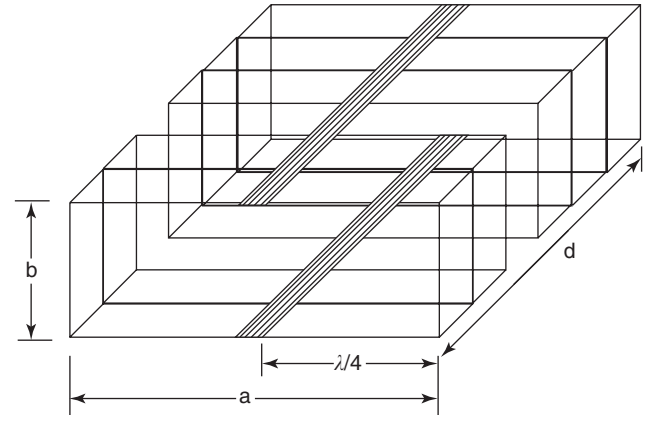


**Figure 11.** A rectangular waveguide derived from a two-wire transmission line supported by two quarter-wavelength short-circuited sections.

can be characterized by its electrical and magnetic components and can be visualized as field patterns by its electric and magnetic vectors.

In wave propagating structures, the transmission of microwave energy takes place in a region surrounded by boundaries, in most cases a metallic wall; and, for analytical purpose, these are assumed lossless. Other assumption is that, within the frequency of interest, a waveguide can support at least one propagating mode above its cutoff frequency, which is the function of waveguide geometry.

The time-harmonic electric and magnetic fields are assumed to have the following forms

$$E(x,y,z,t) = E(x,y)e^{jwt-j\beta z} \tag{40}$$

$$H(x,y,z,t) = H(x,y)e^{jwt-j\beta z} \tag{41}$$

where $\beta$ is the propagation constant along the guide direction. The corresponding wavelength is the guide wavelength ($\lambda_g = 2\pi/\beta$):

$$\lambda_g = \frac{\lambda_0}{\sqrt{1-\left(\frac{f_c}{f}\right)^2}} \tag{42}$$

where $\lambda_0$ is the wavelength of a plane wave propagating in an infinite medium. Two important features can be noted from this equation: (1) at higher operating frequency $\lambda = \lambda_0$ and (2) as $f$ approaches $f_c$, $\lambda_g$ becomes infinite and the corresponding mode does not propagate. Therefore, for a given mode of propagation, the operating frequency is always selected above the cutoff frequency.

**3.2.1. Parallel-Plate Waveguide.** The parallel-plate waveguide normally supports TM and TE modes. It can also support the TEM mode of propagation as it is formed with two flat plates or strips as shown in Fig. 2e. The stripwidth $W$ is assumed to be much greater than the separation distance $d$ so that the fringing field and any $x$ components of the field can be ignored. A material with relative permittivity $\varepsilon_r$ and permeability $\mu_0$ is assumed to fill the region between the plates.

***3.2.1.1. TEM Modes.*** The TEM mode solution can be obtained by solving Laplace's equation as in (43) for the electrostatic potential $\phi$ between the two plates:

$$\nabla_t^2 \phi(x,y) = 0 \quad \text{for } 0 \le x \le W \quad \text{and} \quad 0 \le y \le d \tag{43}$$

The initial boundary conditions for potentials are

$$\begin{aligned} \phi(x,0) &= 0 \\ \phi(x,d) &= V_0 \end{aligned} \tag{44}$$

Since there is no variation in the $x$ plane, the equation can be solved with given boundary conditions and the transverse electric field and magnetic field components can be calculated. Once the electric field is derived, the voltage and the current on the top plate can be calculated from the electric field component and the surface current density, respectively. The characteristic impedance of the parallel plate can be found as follows:

$$Z_0 = \frac{V}{I} = \frac{d\eta}{\omega} \tag{45}$$

The $Z_0$ depends only on geometry and the material parameter. The attenuation due to dielectric loss is given as follows:

$$\alpha_d = \frac{k\tan\delta}{2} \text{ (Np/m)} \tag{46}$$

The conductor attenuation for different mode of propagation can be calculated from the following equations:

$$\alpha_c = \frac{R_s}{\eta d} \text{ (Np/m) (for TEM mode)} \tag{47}$$

$$\alpha_c = \frac{2k_c^2 R_s}{k\beta\eta d} \text{ (Np/m) (for TE}_n \text{ mode)} \tag{48}$$

$$\alpha_c = \frac{2kR_s}{\beta\eta d} \text{ (Np/m) (for TM}_n \text{ modes)} \tag{49}$$

The cutoff frequency and propagation constant for TE$_n$ and TM$_n$ modes are

$$f_{c,TM} = \frac{\eta}{2d\sqrt{\mu\varepsilon}} \tag{50}$$

and the propagation constant is

$$\beta_{TE} = \sqrt{k^2 - \left(\frac{n\pi}{d}\right)^2} \tag{51}$$

The wave impedance of TE$_n$ and TM$_n$ modes are frequency-dependent and are given as

$$Z_{TM} = \frac{-E_y}{H_x} = \frac{\beta\eta}{k} \tag{52}$$

$$Z_{TE} = \frac{E_x}{H_y} = \frac{k\eta}{\beta} \tag{53}$$

The attenuation due to conductor loss for TM$_1$, TE$_1$, and TEM modes in a parallel-plate waveguide is shown in Fig. 12. At the cutoff frequency the attenuation reaches infinity, prohibiting the propagation of modes.

**3.2.2. Rectangular Waveguide.** The rectangular waveguide can propagate TM or TE modes, but not TEM modes. The uniform rectangular waveguide structure is shown in Fig. 13. The propagation is in the $z$ direction.

The cutoff frequency for TE$_{mn}$ modes can be calculated as follows:

$$f_{c,mn} = \frac{1}{2\pi\sqrt{\mu\varepsilon}}\sqrt{\left(\frac{m\pi}{a}\right)^2 + \left(\frac{n\pi}{b}\right)^2} \tag{54}$$

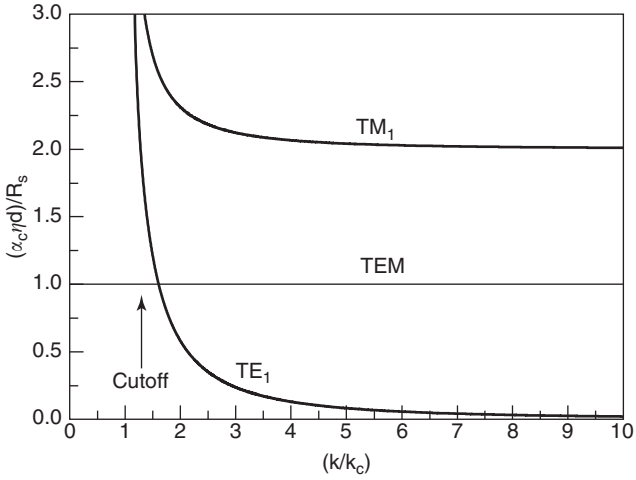


**Figure 12.** Attenuation due to conductor loss for TEM, $TM_1$, and $TE_1$ modes of a parallel-plate waveguide.

The mode with the lowest cutoff frequency is called the *dominant mode*. As we have assumed previously that $a > b$, the lowest $f_c$ occurs for the $TE_{10}$ mode (for $m = 1$ and $n = 0$):

$$f_{c,10} = \frac{1}{2a\sqrt{\mu\varepsilon}} \tag{55}$$

The propagation constant of TE mode is

$$\beta_{TE} = \sqrt{k^2 - k_c^2} = \sqrt{k^2 - \left(\frac{m\pi}{a}\right)^2 - \left(\frac{n\pi}{b}\right)^2} \tag{56}$$

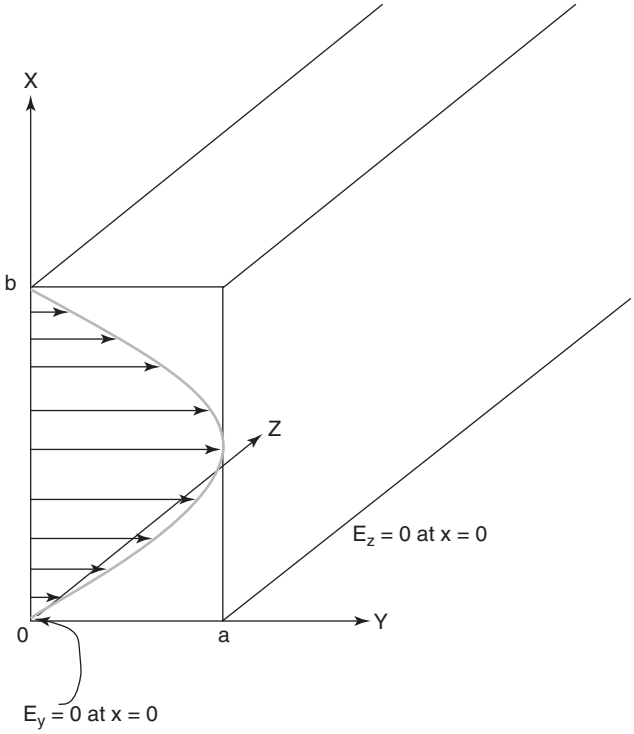


**Figure 13.** Coordinate system and electric field distribution in a rectangular waveguide.

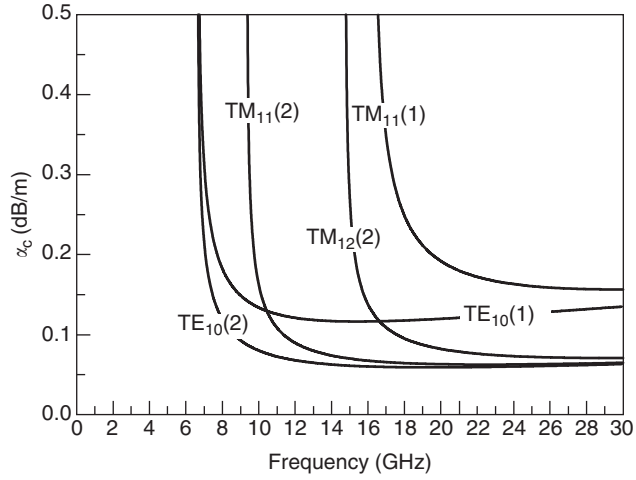


**Figure 14.** Attenuation of various modes of rectangular waveguide WR-90 with aluminum wall: (1) WR-90 waveguide; (2) WR-90 waveguide with $b = 2a$.

The wave impedance that relates the transverse electric and magnetic fields is

$$Z_{TE} = \frac{E_x}{H_y} = \frac{k\eta}{\beta} \tag{57}$$

where $\eta = \sqrt{\mu\varepsilon}$, the intrinsic impedance of the material filling the waveguide.

The attenuation due to dielectric loss is shown in Fig. 14 for various TE and TM modes of rectangular waveguide WR-90 with an aluminum wall.

**3.2.3. Circular Waveguide.** The cross sectional view of a circular waveguide is shown in Fig. 15. Circular waveguides support TE and TM modes of propagation. Circular waveguides also used in many applications as guiding structures in the propagation of microwave energy.

The field equations are solved in cylindrical coordinates for both $TE_{mn}$ and $TM_{mn}$ modes as

$$\frac{\left(\dfrac{\partial^2}{\partial\rho^2} + \dfrac{1}{\rho}\dfrac{\partial}{\partial\rho} + \dfrac{1}{\rho^2}\dfrac{\partial^2}{\partial\varphi^2} + k_c^2\right)h_z(\rho,\varphi)}{e_z(\rho,\varphi)} = 0 \tag{58}$$

where $h_z$ and $e_z$ respectively are electric and magnetic fields. The dominant mode in circular waveguide is $TE_{11}$ mode. The propagation constant and cutoff frequency for $TE_{mn}$ modes are expressed as follows:

$$\beta_{TE,nm} = \sqrt{k^2 - k_c^2} = \sqrt{k^2 - \left(\frac{\rho'_{nm}}{a}\right)^2} \tag{59}$$

$$f_{c,nm} = \frac{k_c}{2\pi\sqrt{\mu\varepsilon}} = \frac{\rho'_{nm}}{2a\pi\sqrt{\mu\varepsilon}} \tag{60}$$

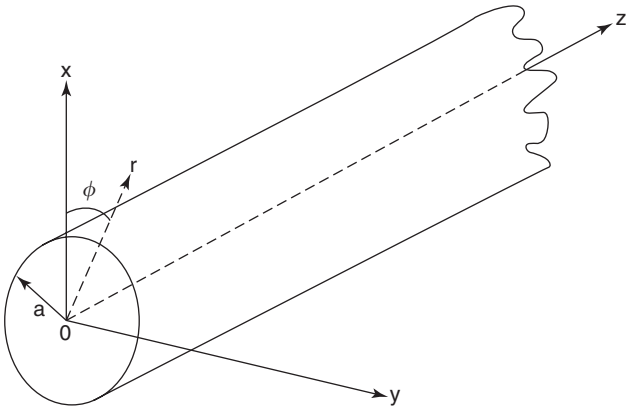


**Figure 15.** Cross sectional view of a circular waveguide.

For $TM_{mn}$ modes the propagation constant and cutoff frequency are expressed as

$$\beta_{TM,nm} = \sqrt{k^2 - k_c^2} = \sqrt{k^2 - \left(\frac{\rho_{nm}}{a}\right)^2} \tag{61}$$

$$f_{c,nm} = \frac{k_c}{2\pi\sqrt{\mu\varepsilon}} = \frac{\rho_{nm}}{2a\pi\sqrt{\mu\varepsilon}} \tag{62}$$

where $\rho$ and $\rho'$ are the $m$th roots of Bessel's functions $J_n(x)$ and its first derivatives $J_n'(x)$ with order $n$, respectively. The attenuation due to conductor loss in an aluminum circular guide with radius 2.45 cm for different modes is shown in Fig. 16. As can be seen, the attenuation decreases to a very small quantity at higher frequency of operation. The transverse field patterns and the cutoff frequencies of various modes are shown in Figs. 17a and 17b, respectively.

**3.2.4. Elliptic Waveguide.** The elliptic waveguide is a cylindrical waveguide where the transverse section is of elliptical form, as shown in Fig. 18.

The readers are referred to other sources [1–3] for quantitative information on elliptic waveguides. The dominant mode in elliptic waveguide is the $eH_{11}$ mode. One major application of elliptical waveguide is impedance matching. The transverse electric and magnetic field patterns of several lower order modes in an elliptical waveguide with eccentricity $e = 0.75$ are shown in Fig. 19 [2].

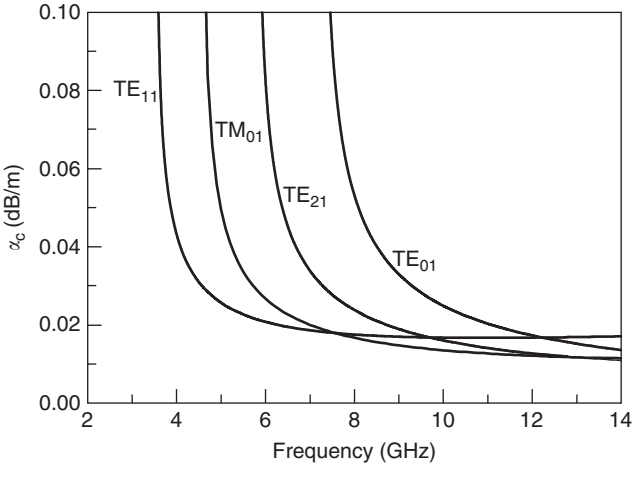


**Figure 16.** Attenuation due to metallic conductor of various modes of circular aluminum waveguide, with $a = 2.54$ cm.

**3.2.5. Microstrip Line.** The microstrip line is one of the most popular transmission lines [10] because it can be fabricated using the photolithography process and easily integrated with other active and passive microwave devices up to the millimeter-wave frequency band. The geometry of the microstrip transmission line is shown in Fig. 20.

The broad range of microwave components such as filters, resonators, diplexer, distribution networks, and matching circuits are made with microstrip lines. Although the microstrip structure is physically simple, the theoretical analysis is rather complex. A number of methods are employed to analyze the behavior of the microstrip line. However, there are closed-form analytical expressions for the characteristic impedance and propagation velocity [11]. The microstrip line supports quasi-TEM mode as the pure TEM mode is impossible because of the air–dielectric interface. Most of the power is confined to the region bounded by the width of the microstrip line,called the *fringing field*. Due to the presence of air in the fringing-field region, some of the power may radiate into free space. However, using a high-dielectric substrate and shielding the structure, the power loss due to radiation can be minimized. The microstrip medium is dispersive and supports higher-order modes. Nevertheless, its popularity is the result of the ease in integration with surface mountable chip components such as chip capacitors, chip resistors, and other lumped elements with good thermal dissipation properties of the medium without disturbing the RF propagation.

To design a basic microstrip line, it is important to know the characteristic impedance and effective permittivity, which is normally frequency-dependent. Many varieties of approximations have been reported in the literature [3]. However, the fairest and most accurate method in determining the characteristic impedance and effective permittivity [7] is outlined below:

$$Z_0 = \frac{\eta}{2\pi\sqrt{\varepsilon_{re}}} \ln\left(\frac{8d}{W} + 0.25\frac{W}{d}\right) \quad \text{for } \left(\frac{W}{d} \le 1\right)$$

$$Z_0 = \frac{\eta}{\sqrt{\varepsilon_{re}}} \left(\frac{W}{d} + 1.393 + 0.667 \ln\left(1.444 + \frac{W}{d}\right)\right)^{-1} \quad \text{for } \left(\frac{W}{d} \ge 1\right) \tag{63}$$

where $W$ is the width of the microstrip line, $h$ is the height, and $\varepsilon_{re}$ is the effective relative permittivity of the dielectric slab.

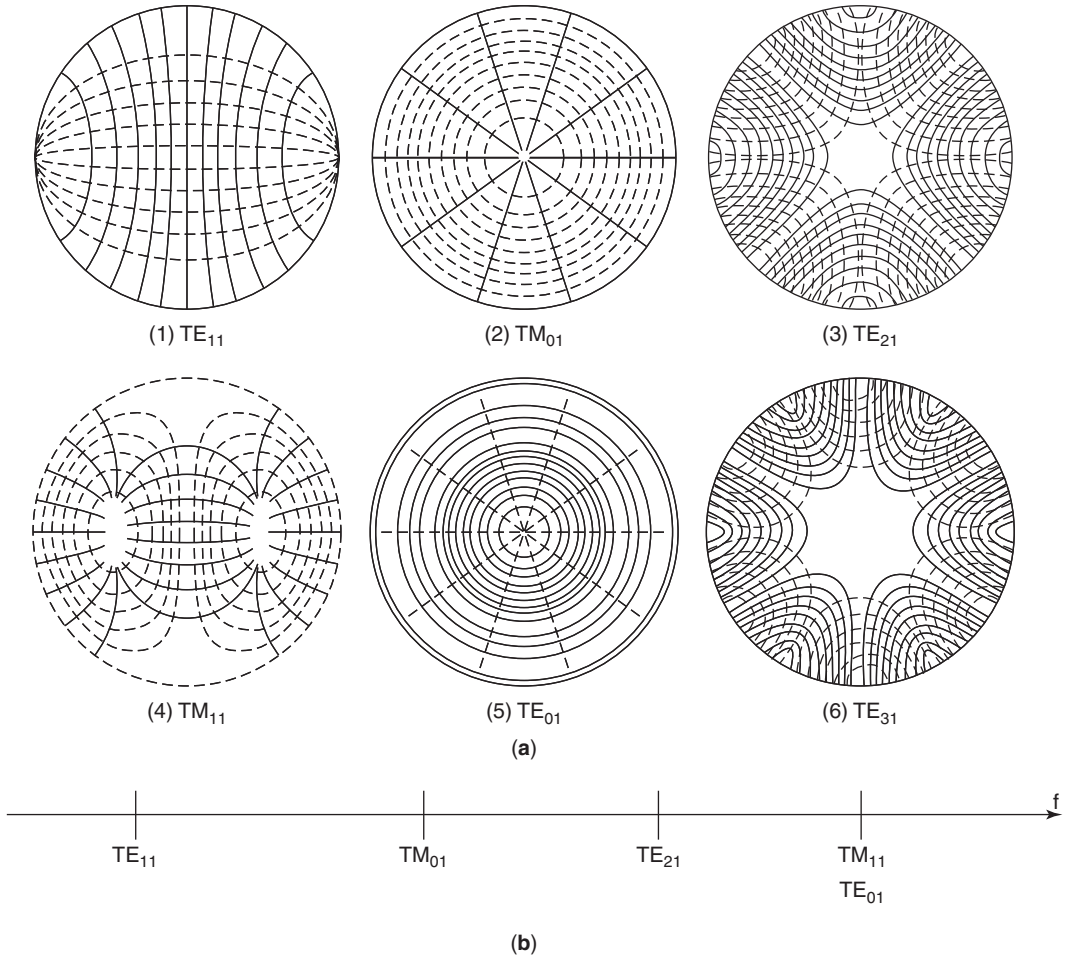


**Figure 17.** (a) Transverse field patterns of various modes in circular waveguide; (b) locations of cutoff frequencies of the first few TE and TM modes.

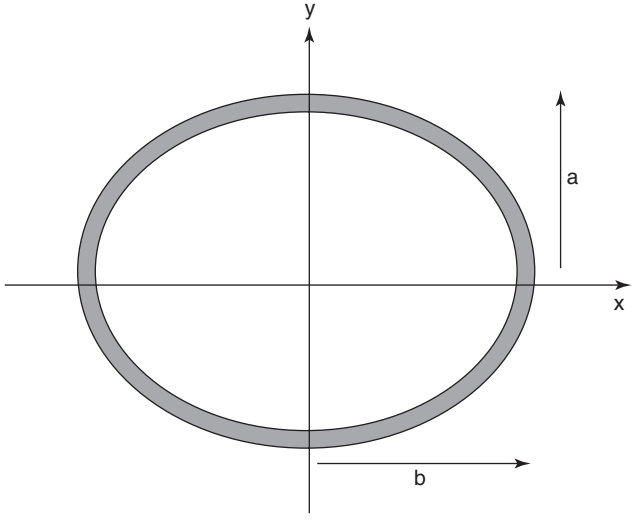


**Figure 18.** Geometry of the elliptical waveguide.

The effective permittivity can be expressed as

$$\varepsilon_{re} = \frac{\varepsilon_r + 1}{2} + \frac{\varepsilon_r - 1}{2} F\frac{W}{d} \tag{64}$$

$$F\frac{W}{d} = \left(1 + 12\frac{d}{W}\right)^{-0.5} + 0.04\left(1 - \frac{W}{d}\right)^2 \quad \text{for} \quad \left(\frac{W}{d} \geq 1\right)$$

$$F\frac{W}{d} = \left(1 + 12\frac{d}{W}\right)^{-0.5} \quad \text{for} \quad \left(\frac{W}{d} \leq 1\right) \tag{65}$$

With these equations, the characteristic impedance and effective dielectric constant of a microstrip line can be evaluated. All modern microwave computer-aided design tools are equipped with these calculations for the characteristic impedance, linewidth, and effective dielectric constant of microstrip lines. At higher-frequency operation other factors such as decreased $Q$ factors, radiation loss, surface-wave loss, and higher-order mode propagation are very critical in the design of microstrip lines. Figure 21 illustrates variation in the characteristic impedance and effective dielectric constants with respect to width for a microstrip line designed for two different substrates of

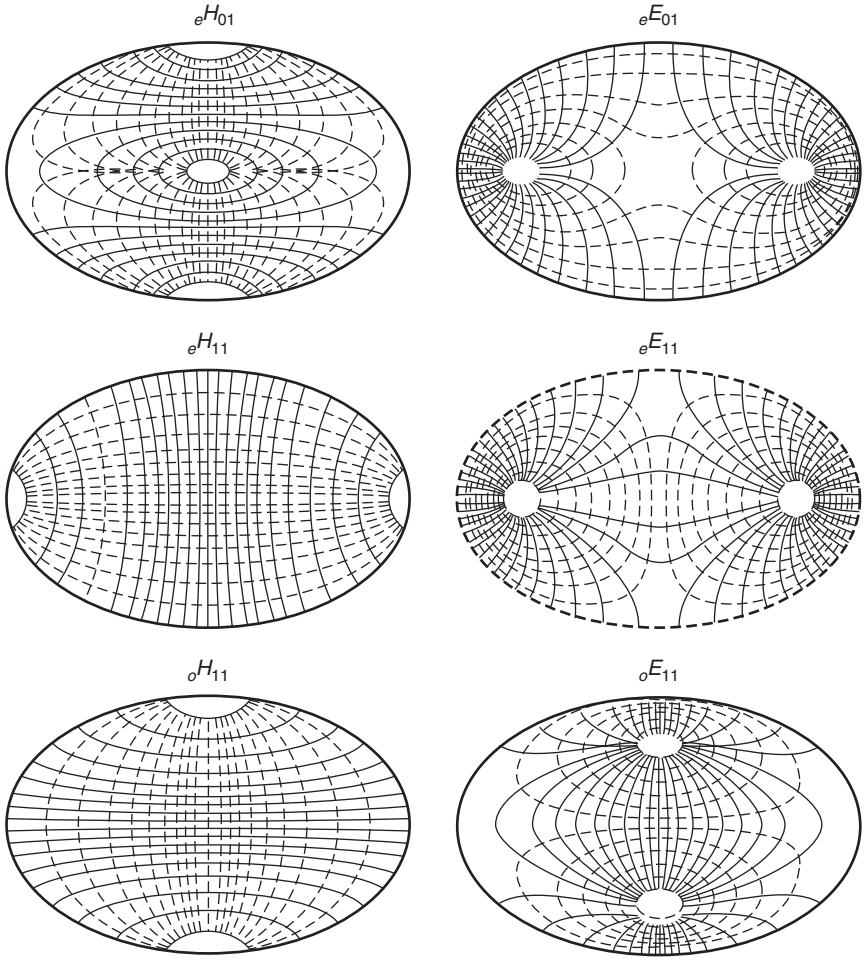


**Figure 19.** Field distribution of modes in elliptic waveguides [2].

dielectric constant of 2.0 and 10.5. As can be seen in Fig. 21a, the characteristic impedance decreases with the width–height ratio of the dielectric substrate. With higher dielectric constants the characteristic impedance is lower for the same dimension of line. As shown in Fig. 21b, the effective dielectric constant increases with the width–height ratio of microstrip lines. A microstrip realization of a quadrature direct conversion receiver [15] designed on RT Duroid substrate of dielectric constant of 10.5 and 0.635 mm thickness is presented in Fig. 22. As can be seen in the figure, all active and passive microwave devices such as quadrature hybrid coupler, asymmetric coupled-line bandpass filters, lowpass filters, Wilkinson power divider, and even harmonic mixer (EHMIX) are designed using photolithographic processes. The lumped components such as chip resistors, capacitors, and diode mixers are soldered on the microstrip lines. Thus microstrip lines have created a revolution in high-frequency and microwave circuits.

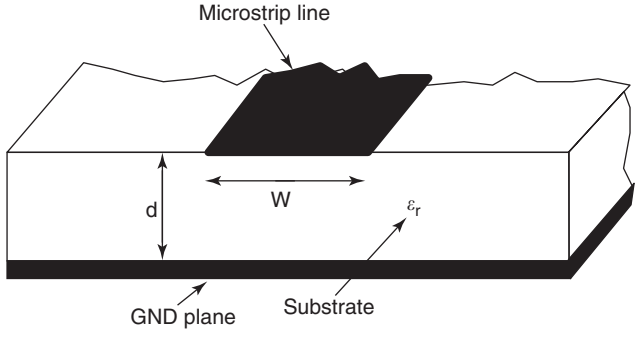


**Figure 20.** Structure of the microstrip line.

**3.2.6. Slotline.** Slotlines are planar transmission-line structures that are widely used in MMIC circuits. The basic slotline structure, shown in Fig. 23, consists of a dielectric slab with a narrow slot etched on the ground plane on only one side of the dielectric slab. This geometry is planar and well suited for MIC/MMIC designs. The wave propagates along the slot with the major electric field component oriented across the slot while the magnetic field is in the plane perpendicular to the slot. The mode of propagation in slotline is non-TEM in nature. Unlike the conventional waveguide, in the slotline there is no cutoff frequency and propagation occurs at all frequencies down to zero. Because of the slotline's non-TEM

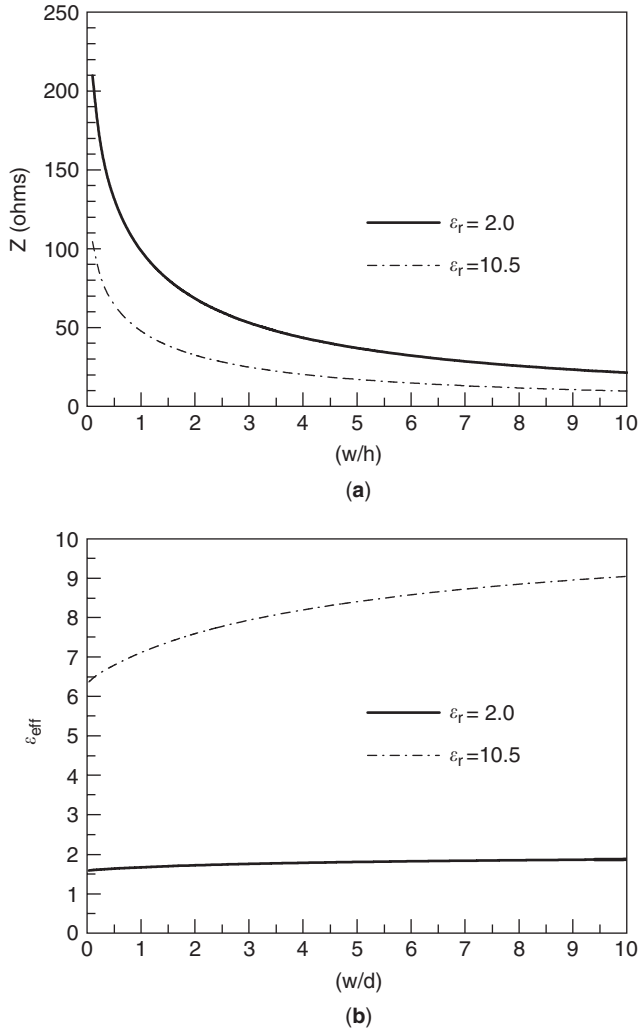


**Figure 21.** The characteristic of microstrip line. The variation of (a): characteristic impedance and (b): effective permittivity of the medium as a parameter of width.

nature, the characteristic impedance and phase velocity are not constant but vary with frequency at a slow rate. The characteristics of the slotline with regard to dielectric thickness are shown in Fig. 24 [6]. Readers are referred to

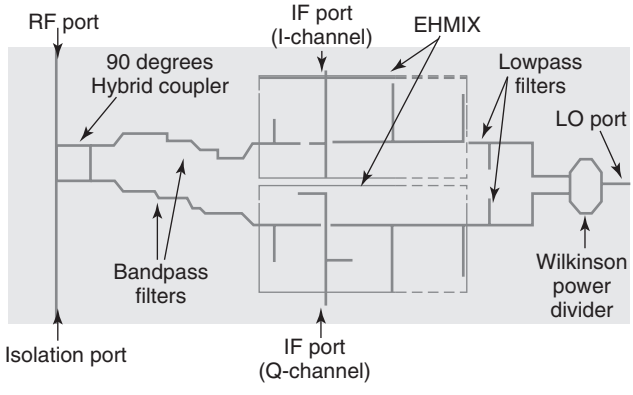


**Figure 22.** Microstrip realization of a mixer circuit.

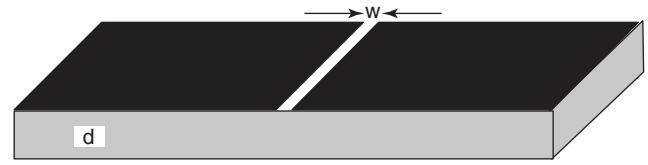


**Figure 23.** Slotline geometry.

the literature [3] for a detailed theoretical analysis of slotline structures.

**3.2.7. Coplanar Waveguide Transmission Line.** The geometry of coplanar waveguide (CPW), shown in Fig. 25, consists of two slots of width w etched on the ground plane of a dielectric substrate and separated by a spacing s. This structure is also referred to as a *uniplanar structure* as the signal-carrying line lies along with the ground plane in the same plane. This structure often demonstrates better dispersion behavior than does the microstrip line [4,5]. As a result of low parasitic effects, this structure is a good choice for higher-frequency operation. The characteristic impedance of the line depends primarily on the width of slots and their spacing for a given substrate.

The characteristic of a CPW line are shown in Fig. 26. The variation of effective dielectric constant and charac-

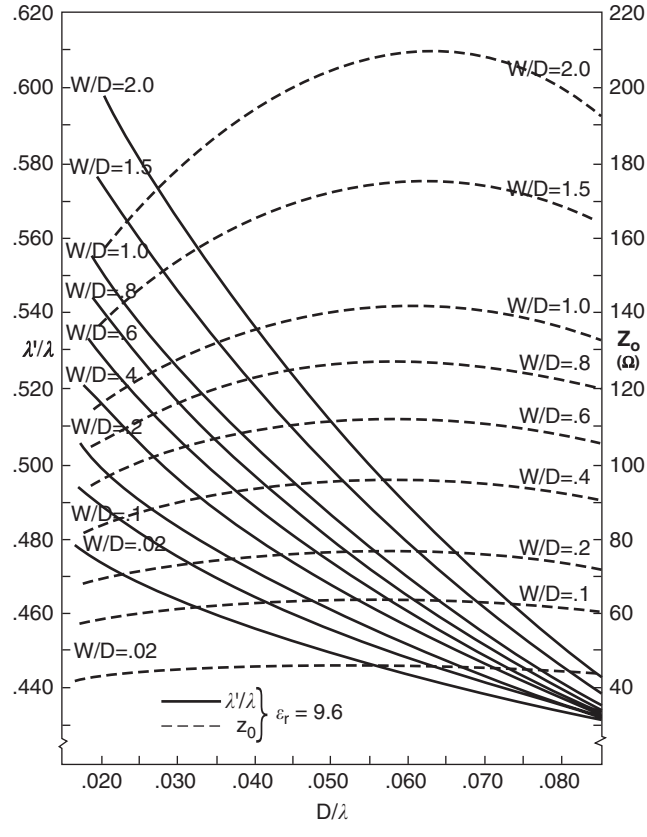


**Figure 24.** The dispersion characteristics of slotline from Ref. 6.

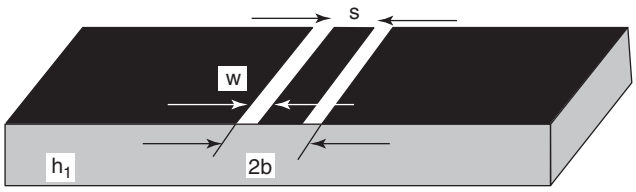


**Figure 25.** The geometry of a CPW line.

teristic impedance as line parameters can be a useful tool for the design of the CPW line and its associated components. A detailed analysis and closed-form expressions of CPWs are reported in Ref. 8.

Figure 27 is a photograph of various MMIC slot antennas on coplanar waveguides designed on GaAs substrate near 24 GHz. The slot dipole is fed through a CPW line, and the calculated and measured performances of the antenna is shown in Fig. 28. The details of antenna design are reported in Ref. 9.

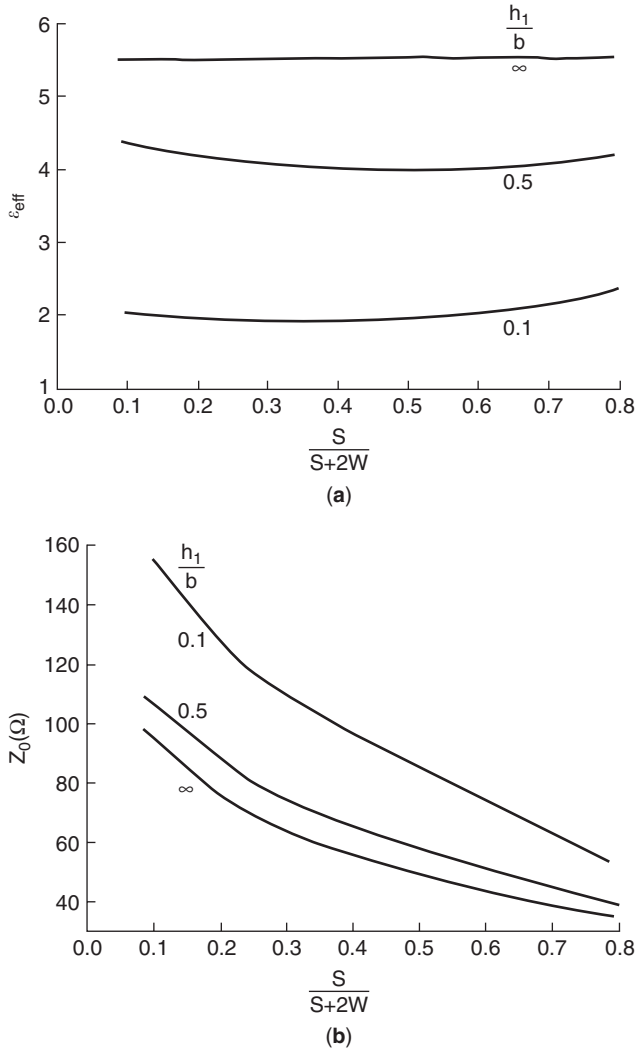


**Figure 26.** The characteristics of a CPW line: (a) variation of effective dielectric constant; (b) variation of characteristic impedance of $Z_0$ with CPW line parameters [8].

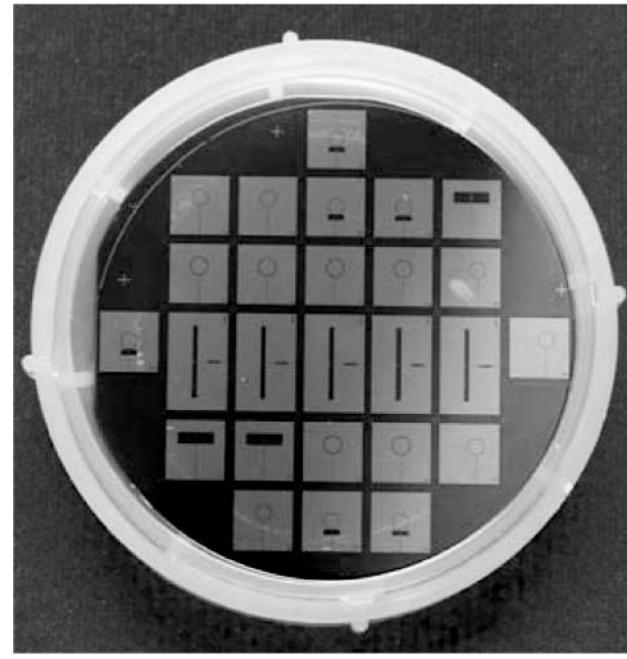

**Figure 27.** Photograph of a coplanar-waveguide-fed MMIC antenna on GaAs substrate near 24 GHz. (Courtesy PWTC, Nanyang Technological University, Singapore.)

## 4. CONCLUSION

This article has presented a historic perspective of coaxial cables and waveguides and has reviewed market potentials of coaxial cables, waveguides, and accessories. The classifications of various transmission lines according to the modes excited in the particular transmission lines have been shown. Two-wire transmission lines such as coaxial cables, parallel-plate waveguides, and microstrip lines support TEM mode fields. The single-conductor transmission lines support non-TEM mode fields such as TE and TM modes. Next, the classical transmission line theory has been derived in the "telegrapher" equation. Next, the coaxial cable has been discussed. The design parameters, higher-order mode cutoff frequency, and attenuation of coaxial cables were presented. The two main types of coaxial cable are flexible and semirigid coaxial cables. The most recent developments of extremely high-frequency coaxial cables exploiting MMIC and MEMS processing techniques were presented. It was shown that MEMS microcoaxial cable is low-loss even at very high frequencies such as in the millimeter-wave range.

Various waveguides in the form of parallel-plate waveguides and rectangular, circular, and elliptical waveguides were presented in terms of their cutoff frequencies and attenuation. Finally different planar waveguides such as microstrip lines, slotlines, and coplanar waveguides were presented. Their design formulas were also given for the benefit of designers.

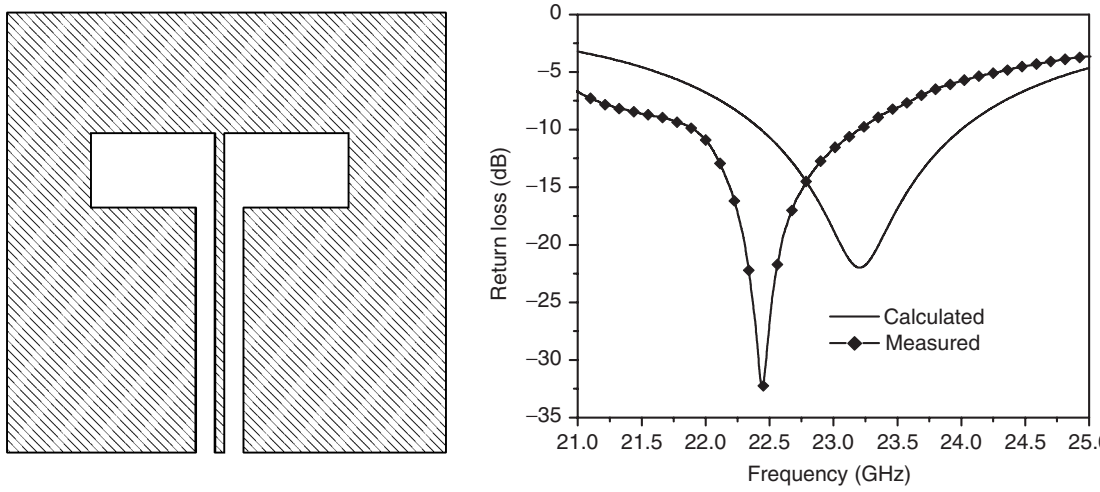


**Figure 28.** (a) CPW-fed slot dipole antenna at 24 GHz; (b) calculated and measured return loss of the antenna [9].

## BIBLIOGRAPHY


1. D. M. Pozar, *Microwave Engineering*, Wiley, New York, 1998.
2. K. S. Packard, The origin of waveguides: A case of multiple rediscovery, *IEEE Trans. Microwave Theory Tech*. **MTT-32**:961–969 (Sept. 1984).
3. N. Marcuvitz, *Waveguide Handbook*, Peter Peregrinus, IEE, London, 1986.
4. R. N. Simons, *Coplanar Waveguide Circuits, Components and Systems*, J Wiley, New York, 2001.
5. R. E. Collins, *Foundation of Microwave Engineering*, 2nd ed., McGraw-Hill, New York, 1992.
6. E. A. Mariani et al., Slotline characteristics, *IEEE Trans. Microwave Theory Tech*. **MTT-17**:1091–1096 (1969).
7. M. Kobayashi, A dispersion formula satisfying recent requirements in microstrip CAD, *IEEE Trans. Microwave Theory Tech*. **MTT-36**:1246–1250 (Aug. 1998).
8. K. C. Gupta, R. Garg, I. Bahl, and R. Bhatia, *Microstripline and Slotlines*, Artech House, Norwood MA, 1996.
9. S. K. Padhi and N. C. Karmakar, Computer aided design of an CPW-fed slot antenna for MM-wave applications, *Int. J. RF Microwave Comput. Aided Design Eng*. **14**(1):4–14 (Jan. 2004).
10. I. J. Bahl and T. D. K. Trivedi, A designer's guide to microstrip line, *Microwaves* 174–182 (May 1977).
11. R. F. Harrington, *Time Harmonic Electromagnetic Field*, McGraw-Hill, New York, 1961.
12. J. A. Bishop, M. M. Hashemi, K. Kiziloglu, L. Larson, N. Dagli, and U. Mishra, Monolithic coaxial transmission lines for mm-wave ICs, *Proc. IEEE/Cornell Conf. Advanced Concepts in High Speed Semiconductor Devices and Circuits*, Aug. 1991, 5–7.
13. J.-B. Yoon, B.-I. Kim, Y.-S. Choi, and E. Yoon, 3-D construction of monolithic passive components for RF and microwave ICs using thick-metal surface micromachining technology, *IEEE Trans. Microwave Theory Tech*. **MTT-51**(1):279–288 (2003).
14. W. S. Cheung and F. H. Levien, *Microwaves Made Simple: Principles and Applications*, Artech House, Norwood, MA, 1985.
15. N. C. Karmakar, QPSK direct conversion receiver for wireless communications, *Int. J. RF Microwave Comput. Aided Eng*. (Jan. 2005).


# COMBLINE FILTERS

CHI WANG
Orbital Sciences Corporation
Dulles, Virginia

## 1. INTRODUCTION

Combline filters are one of the most widely used types of bandpass filters in many communication systems and other microwave applications because of many of their unique merits. The first combline filter was introduced by Matthaei in 1963 [2]. The design equations and procedures of the rectangular bar combline filter with narrow to moderate bandwidth, using the coupled rectangular bar design data from Getsinger [3], were also given by Matthaei [1,2]. Cristal [4,5] later presented the data for coupled circular cylindrical rods between parallel ground planes; thus, more manufacturing-advantageous and cost-effective cylindrical rod combline filters can be designed with reasonable accuracy and excellent electrical performance. Although Matthaei's design equations were based on approximations, the results were shown to be reasonably good for narrow-to-octave bandwidth applications. Wenzel's exact analysis approach or full-wave electromagnetic simulations can be used for more accurate designs [9–11]. Combline filters with elliptic function frequency responses, first presented by Rhodes and Levy, give great flexibility in their configuration and responses [6].

With the rapid development of satellite communications since the 1970s and mobile communications since the 1980s, generalized filters with elliptic function responses having cross-couplings between nonadjacent resonators are widely used [6–8,13,22–27]. Combline filters are particularly suitable for achieving elliptic function response and for high-volume, low-cost production, because all the resonator rods can be mounted or built in on the common surface of the filter housing, while all the tuning

screws are mounted in a single cover. In addition, the resonator locations of the combline filter may be flexibly arranged according to the filter's coupling matrix and system mechanical requirement. The combination allows filters with large numbers of resonators and complicated cross-coupling configuration to be tuned nearly to theoretical performance without excessive cost.

In the physical realization of combline filters, the input and output couplings can be achieved by a short-circuited coupled line as part of an impedance transforming section, or an inductively coupled loop, a capacitive coupled probe, or by a direct, tapped-in line. The direct-tapped input/output configuration makes the combline filter more compact and easy to fabricate and therefore is more advantageous than other types of input/output structures [14–20]. This method was first described in the literature by Dishal [15] for small-percentage-bandwidth interdigital filters, and by Cohn [16] for combline filters. Cristal [17] gave exact general equivalent circuits for combline and interdigital arrays using graph transformations; thus the tapped line can be designed with high accuracy.

It is well known that the difference between the measured results and the design based on the conventional TEM combline theory can be as much as 30% depending on the filter's bandwidth [21]. Using full-wave electromagnetic computer-aided design (CAD) tools, combline filters can be designed in high accuracy with arbitrary resonator and coupling aperture dimensions [21,48]. The unloaded $Q$ and the spurious responses of the resonators can be computed accurately from the electromagnetic simulators. Furthermore, the temperature characteristic and power handling capability of combline filters can be accurately determined [50–52].

Ceramic combline filters were introduced in the 1980s to satisfy the needs for miniature filters for mobile communications taking advantage of the development of high-dielectric-constant, low-loss dielectric materials. They have been widely used in many communication systems [40–47]. Ceramic combline filters can be manufactured using single or multiple solid ceramic blocks with a metallized exterior. The resonator rods are realized by a series of metallized holes that are grounded at one end of the block, where the opposite ends of the blocks are kept open. Therefore, the resonator lines are around a quarter-wavelength long at resonance. Couplings between adjacent resonators can be achieved by either series capacitors or apertures [42,48]. These ceramic combline filters can be designed and manufactured with high accuracy, and are very suitable for low-cost mass production.

Combline filters are most suitable for applications requiring relatively low insertion loss in the frequency range between 500 MHz and 12 GHz, and they have following attractive features:

1. They are compact. The length of the resonator rods may be designed to be $\lambda_0/8$ or less at resonance. The unloaded $Q$ of the resonator cavity is a function of its cross section. Therefore the size of the combline filter can be varied depending on the applications.
2. Combline filters possess the ability to be tuned over a wide range of frequencies without suffering significant degradation in performance [2,12]. The tuning range is a function of the amount of capacitance adjustment provided by the tuning screw.
3. The combline resonator has very high unloaded $Q$: volume ratio compared with other types of resonators, such as empty waveguide cavity and dielectric loaded resonators, although the combline resonator doesn't give the highest unloaded $Q$ value.
4. They have strong stopbands, and the stopband above the primary passband can be made very broad. Combline filters may be designed to be spurious-free over 3–4 times the center frequency of the filter.
5. Adequate coupling can be maintained between resonator elements with sizable spacing between such resonator lines.
6. They are reliable, low in cost, and very suitable for manufacturing. All resonator rods can be mounted or built in to the filter housing, and all tuning screws can be directly attached to the housing or cover. In addition, all the materials are readily available and can be modified easily.

## 2. CONFIGURATIONS

A combline filter usually consists of a conductive enclosure and a number of parallel conductive rods serving as resonators, which are short-circuited at one end and open-circuited at the other end. The open ends of the resonator rods are usually close to one side of the enclosure in order to create sufficient capacitance between the rod and the ground. Coupling between resonators is achieved by way of the EM coupling between resonator lines. The input and output coupling may be achieved in several ways as stated in the introduction.

Figure 1 shows a combline bandpass filter in transmission-line form. The resonators of the filter consist of TEM-mode transmission-line elements that have a lumped capacitor $C_k^s$ between the open end of each resonator line element and ground. Lines 1 through $n$ and their associated capacitances $C_1^s$ to $C_n^s$ constitute resonators, while lines 0 and $n+1$ are not resonators but part of impedance transforming sections at both ends of the filter.

With the lumped capacitors present, the resonator lines will be less than a quarter-wavelength long at resonance, and the coupling between resonators will be predominantly magnetic in nature. It is usually desirable to make the capacitances of the combline filter sufficiently large so that the resonator lines will have a length of $\lambda_0/6$ or less at resonance.

The second passband of the combline filter occurs when the resonator line elements are somewhat over a half-wavelength long, so if the resonator lines are $\lambda_0/8$ long at the primary passband, the second passband will be centered at somewhat over 4 times the frequency of the first passband [2]. Therefore, the combline filters can have

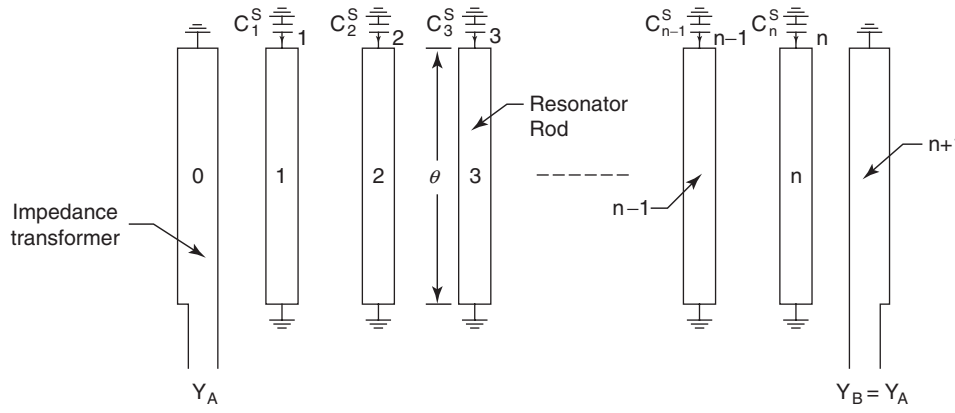


**Figure 1.** A combline filter with short-circuited input/output lines.

extremely broad spurious-free stopband compared with other types of filter.

Figure 2 shows the original four-pole combline filter having the configuration shown in Fig. 1 published by Matthaei in 1963 with its top cover removed. Figure 3 shows an alternate configuration of the combline filter that is currently widely used in the industry and is more favorable for manufacturing. The cross section of the resonator rods may be rectangular or circular; the circular configuration is more common because it is easier to manufacture. Each resonator rod has a counterbored hole at its open end. A tuning screw in the cover can be adjusted to penetrate in or out concentrically to the resonator rod to adjust the resonant frequency of the resonator to the desired value. The tuning screws between the resonator rods are used to adjust the coupling coefficient between the resonators.

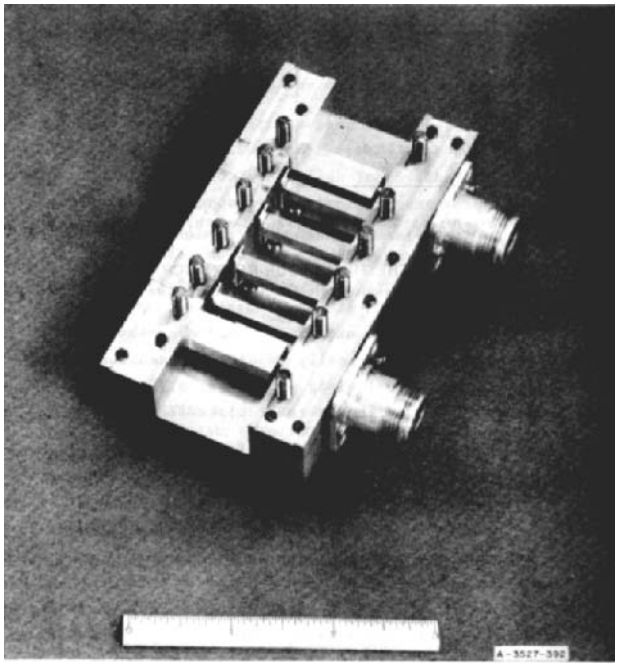

**Figure 2.** The original combline filter [1].

The input/output coupling can be achieved by short (or open)-circuited impedance transformer bars as shown in Matthaei's original configuration [2], or by direct tap as shown in Fig. 3. The input/output coupling can also be achieved by a coupling loop or probe. As the later input/output coupling methods do not need an extended transmission rod at each end of the combline filter, the filter is more compact.

The resonator rods can be separate parts mounted into the filter housing, using screws to achieve good contact, or can be built into the filter housing so that resonators and enclosure constitute a single piece, with only a top cover, tuning screws, and connectors needed to complete the filter. The couplings between resonators can be controlled by the spacing between them or by varying the aperture dimension on a conductive wall between two resonators. The resonators can be arranged in a row or in any desired layout depending on the coupling structure of the filter.

Significant progress in microwave filter technology has taken place since the 1970s, particularly the use of elliptic function responses using nonadjacent couplings between resonators together with compact filter configurations [6–8,13,22,23]. Transmission zeros can be achieved on the lower, higher side or both sides of the filter's passband depending on the attenuation requirements. The resultant filter may have sharper attenuation response; thus fewer resonators are required, which results in a more compact filter with lower insertion loss. Figure 4 shows an example of an elliptic function combline filter with built-in resonators and a very compact configuration [39].

There are several ways to design a combline filter, but the most popular method is to use a lowpass prototype filter. This is transformed into the desired bandpass filter, and then the physical dimensions are determined by either approximation or full-wave 3D electromagnetic simulations. Figure 5 shows the typical design procedure of a combline filter based on this approach. First, the specifications are used to determine the desired filter parameters, such as number of resonators, bandwidth, passband ripple, and the desired ideal frequency responses from the lowpass prototype filter. Then the filter topology and equivalent-circuit parameters, such as filter element values $g_k$, the admittance inverters $J_{k,k+1}$, impedance inverters $K_{k,k+1}$, or coupling matrix $M_{k,k+1}$, are

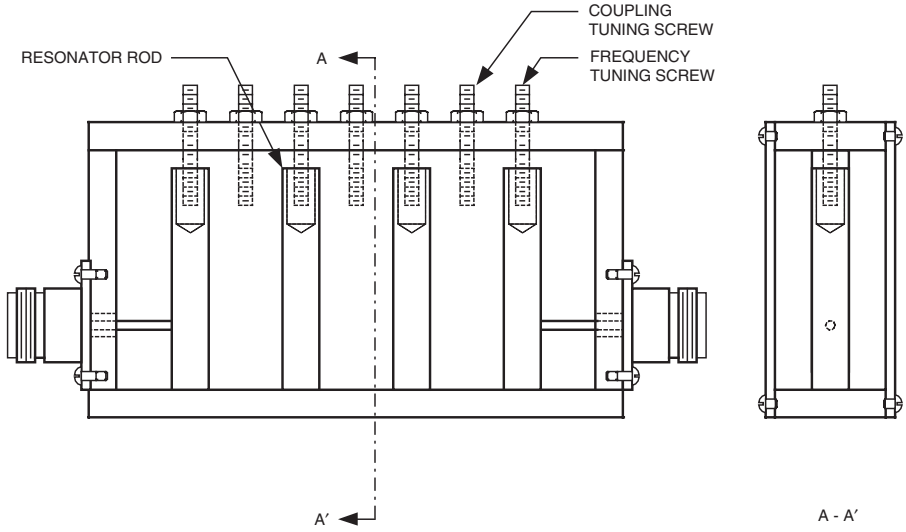


**Figure 3.** A combline filter with tapped-in input/output couplings.

determined. The required unloaded $Q$ of the resonators is determined, and the basic cavity and rod dimensions can then be decided. Finally the rod, spacing, or aperture dimensions can be obtained from Matthaei's approximate design equations using Getsinger's or Cristal's design charts. A prototype is mode to verify the correctness of the design and to perform some minor adjustments. Other practical issues such as temperature compensation and power handling capability should also be considered.

## 3. LOWPASS PROTOTYPE

Figure 6 shows a typical Chebyshev response of a lowpass prototype filter and that of the corresponding bandpass filter. The lowpass prototype filter is usually chosen to have unit bandwidth $\omega_1'$ for convenience, while the bandwidth of the bandpass filter can be arbitrarily specified.

The relationship between the lowpass prototype response and the corresponding bandpass filter is given as [1,2]

$$L_A(\omega) = L'_A(\omega') \tag{1}$$

where

$$\omega' = \frac{\omega'_1}{\overline{\omega}}\left(\frac{\omega}{\omega_0} - \frac{\omega_0}{\omega}\right) \tag{2}$$

$$\overline{\omega} = \frac{\omega_2 - \omega_1}{\omega_0}, \quad \omega_0 = \sqrt{\omega_2 \omega_1} \tag{3}$$

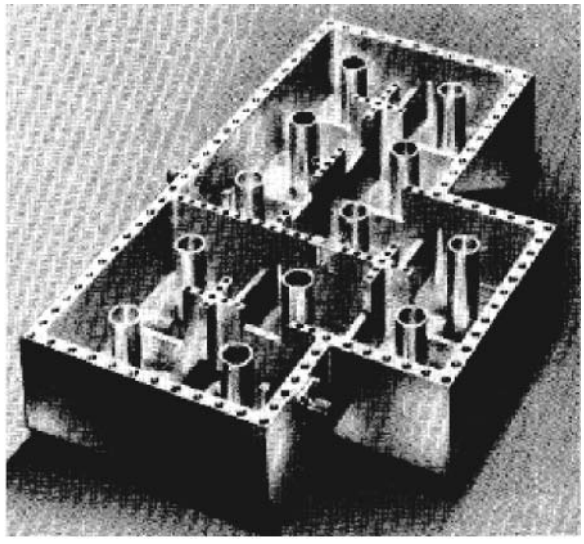

**Figure 4.** A 12-pole elliptic function combline filter [39].

The mapped lowpass prototype filter response has the same characteristics as that of the bandpass filter, or vice versa. Therefore, if the desired bandpass filter has $n$ return loss poles in passband and $m$ finite transmission zeros in stopband, the corresponding lowpass prototype filter will also have $n$ poles in passband from $-\omega_1'$ to $\omega_1'$ at location $a_i$ ($i = 1, 2, \ldots, n$) and $m$ zeros in stopband at location $b_i$ ($i = 1, 2, \ldots, m$). The insertion loss and return loss of the lowpass prototype filter versus frequency can be expressed in terms of the poles and zeros as

$$L_A = 10 \log\left(\frac{1}{1 + \varepsilon|\phi|^2}\right) \tag{4}$$

$$L_R = 10 \log\left(\frac{\varepsilon|\phi|^2}{1 + \varepsilon|\phi|^2}\right) \tag{5}$$

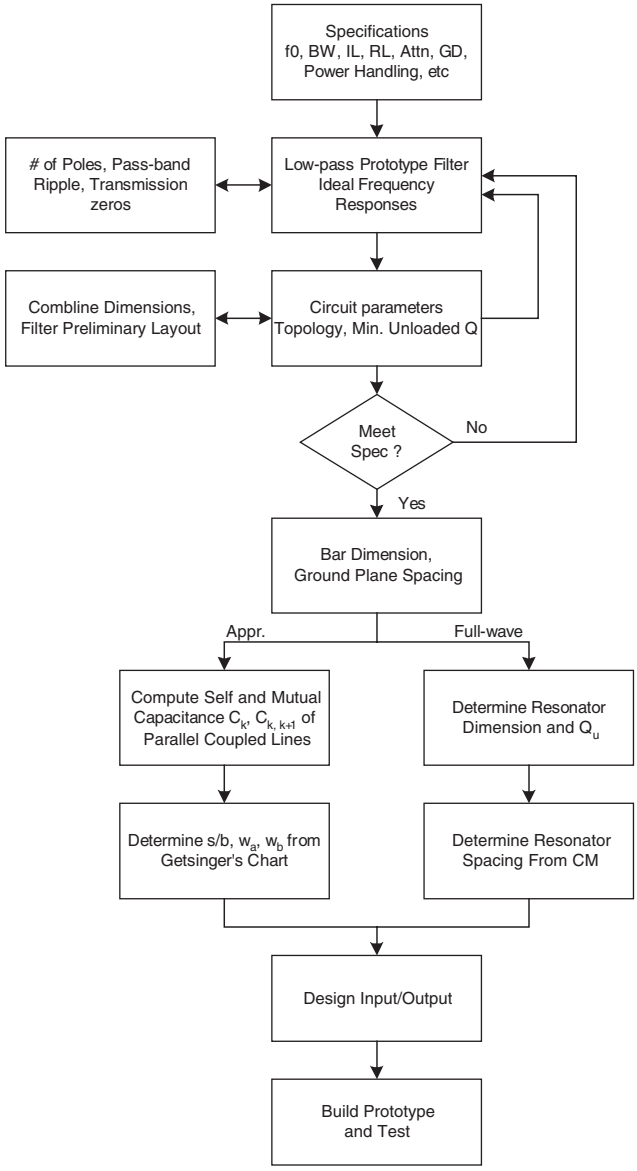


**Figure 5.** Typical combline filter design procedure.

where

$$\phi = \frac{P(\omega')}{Q(\omega')} = \frac{\prod_{i=1}^{n}(\omega' - a_i)}{\prod_{i=1}^{m}(\omega' - b_i)} \tag{6}$$

$$\varepsilon = 10^{L_{\mathrm{Ar}}/10} - 1 \tag{7}$$

The approximation problem is to find the locations of the poles with locations of the given zeros to determine the equal-ripple passband response. The pole and zero locations of the transfer function can be determined by optimizing the polynomial function $P(\omega')$ through iterations [7] or by the recursive technique shown by Cameron [26]. For a Chebyshev response, all the transmission zeros are at infinity, and a closed-form expression for the pole locations exists, as follows:

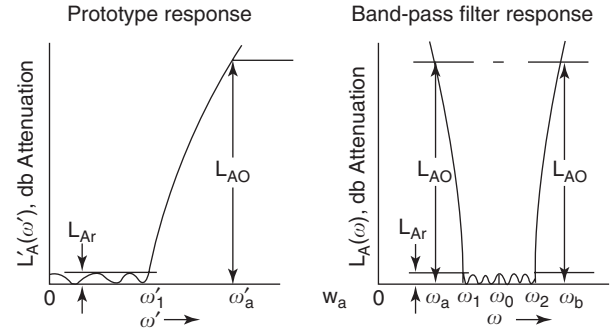


**Figure 6.** Lowpass prototype and corresponding bandpass filter responses.

$$a_i = \cos\left[\frac{(2i-1)\pi}{2n}\right], \quad i = 1, 2, \ldots, n \tag{8}$$

Figure 7 shows the attenuation characteristics for a 0.01-dB-ripple Chebyshev filter versus number of poles. The 0.01-dB passband ripple gives better than 25 dB return loss for the ideal case; therefore it is often used as the starting point for a practical filter design.

Given the transfer function and pole–zero locations of the lowpass prototype filter, the circuit element values of the lowpass and bandpass filters can be obtained by network synthesis. The commonly used forms for the prototype filter circuits are shown in Fig. 8 using $g_k$ ($k = 0, 1, \ldots, n, n+1$) *as* the element values. The prototype filters in Fig. 8a using the shunt capacitor as the first element and in Fig. 8b using the series inductor as the first element have identical responses and $g_k$ values; therefore, either form may be used depending on the applications. When converting a prototype filter to a bandpass filter, a lowpass prototype with $n$ reactive elements leads to a bandpass filter with $n$ resonators.

For Chebyshev filters having passband ripple $L_{\mathrm{Ar}}$ dB, $g_0 = 1$, and $\omega'_1 = 1$, the remaining $g$ values can be obtained analytically as follows:

$$g_1 = \frac{2a_1}{\sinh\left(\dfrac{\beta}{2n}\right)} \tag{9}$$

$$g_k = \frac{4a_{k-1}a_k}{b_{k-1}g_{k-1}} \tag{10}$$

$$g_{n+1} = \begin{cases} 1 & \text{for } n \text{ odd} \\ \coth^2\left(\dfrac{\beta}{4}\right) & \text{for } n \text{ even} \end{cases} \tag{11}$$

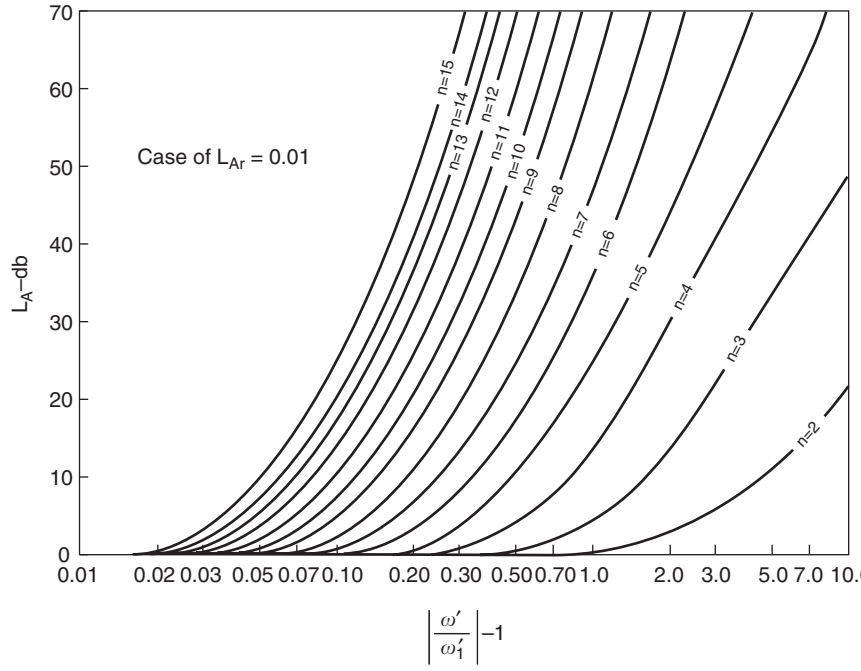


**Figure 7.** Attenuations of the 0.01-dB-ripple Chebyshev filters.

Here

$$\beta = \ln\left(\coth\frac{L_{Ar}}{17.37}\right) \tag{12}$$

$$a_k = \sin\left[\frac{(2k-1)\pi}{2n}\right] \tag{13}$$

$$b_k = \sinh^2\left(\frac{\beta}{2n}\right) + \sin^2\left(\frac{k\pi}{n}\right) \tag{14}$$

Table 1 presents the computed $g$ element values for Chebyshev filters for $n = 1$ through 10 with 0.01- and 0.1-dB passband ripple levels.

The $g$ values of the lowpass prototype filter given in Eqs. (9)–(11) are normalized to unit input impedance $g_0 = 1$ and unit bandwidth $\omega_1' = 1$. For filters having different input port impedance and bandwidth, the desired inductance or capacitance values can be easily scaled from the normalized $g$ values by the following equations

$$L = \frac{R_0}{\omega'} L' \tag{15}$$

$$C = \frac{C'}{R_0\omega'} \tag{16}$$

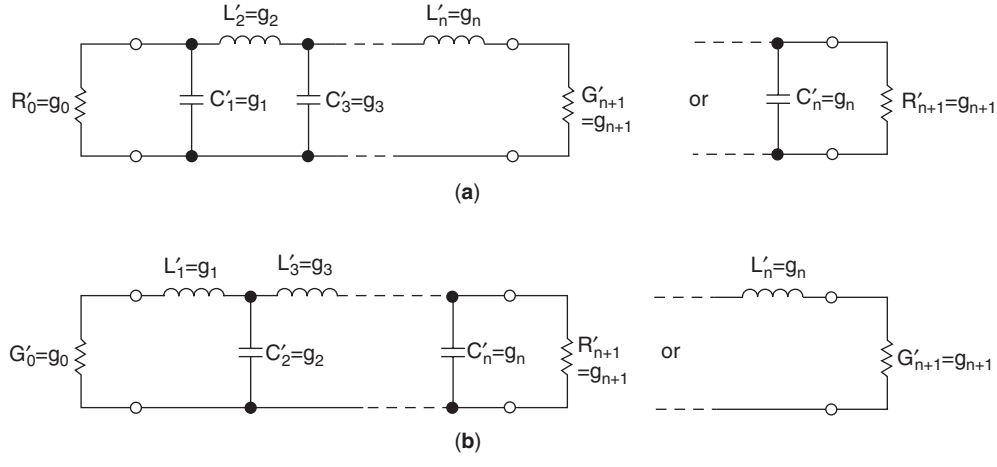


**Figure 8.** Lowpass filter circuit and parameters (a) a shunt capacitor as first element; (b) a series inductor as first element.

**Table 1. Element Values for Chebyshev Filters Having $g_0 = 1$, $\omega_0' = 1$ for 0.01- and 0.1-dB Ripples**

| Value of $n$ | $g_1$ | $g_2$ | $g_3$ | $g_4$ | $g_5$ | $g_6$ | $g_7$ | $g_8$ | $g_9$ | $g_{10}$ | $g_{11}$ |
|---|---|---|---|---|---|---|---|---|---|---|---|
| **0.01 dB ripple** | | | | | | | | | | | |
| 1 | 0.0960 | 1.0000 | | | | | | | | | |
| 2 | 0.4488 | 0.4077 | 1.1007 | | | | | | | | |
| 3 | 0.6291 | 0.9702 | 0.6291 | 1.0000 | | | | | | | |
| 4 | 0.7128 | 1.2003 | 1.3212 | 0.6476 | 1.1007 | | | | | | |
| 5 | 0.7563 | 1.3049 | 1.5773 | 1.3049 | 0.7563 | 1.0000 | | | | | |
| 6 | 0.7813 | 1.3600 | 1.6896 | 1.5350 | 1.4970 | 0.7098 | 1.1007 | | | | |
| 7 | 0.7969 | 1.3924 | 1.7481 | 1.6331 | 1.7481 | 1.3924 | 0.7969 | 1.0000 | | | |
| 8 | 0.8072 | 1.4130 | 1.7824 | 1.6833 | 1.8529 | 1.6193 | 1.5554 | 0.7333 | 1.1007 | | |
| 9 | 0.8144 | 1.4270 | 1.8043 | 1.7125 | 1.9057 | 1.7125 | 1.8043 | 1.4270 | 0.8144 | 1.0000 | |
| 10 | 0.8196 | 1.4369 | 1.8192 | 1.7311 | 1.9362 | 1.7590 | 1.9055 | 1.6527 | 1.5817 | 0.7446 | 1.1007 |
| **0.1 dB ripple** | | | | | | | | | | | |
| 1 | 0.3052 | 1.0000 | | | | | | | | | |
| 2 | 0.8430 | 0.6220 | 1.3554 | | | | | | | | |
| 3 | 1.0315 | 1.1474 | 1.0315 | 1.0000 | | | | | | | |
| 4 | 1.1088 | 1.3061 | 1.7703 | 0.8180 | 1.3554 | | | | | | |
| 5 | 1.1468 | 1.3712 | 1.9750 | 1.3712 | 1.1468 | 1.0000 | | | | | |
| 6 | 1.1681 | 1.4039 | 2.0562 | 1.5170 | 1.9029 | 0.8618 | 1.3554 | | | | |
| 7 | 1.1811 | 1.4228 | 2.0966 | 1.5733 | 2.0966 | 1.4228 | 1.1811 | 1.0000 | | | |
| 8 | 1.1897 | 1.4346 | 2.1199 | 1.6010 | 2.1699 | 1.5640 | 1.9444 | 0.8778 | 1.3554 | | |
| 9 | 1.1956 | 1.4425 | 2.1345 | 1.6167 | 2.2053 | 1.6167 | 2.1345 | 1.4425 | 1.1956 | 1.0000 | |
| 10 | 1.1999 | 1.4481 | 2.1444 | 1.6265 | 2.2253 | 1.6418 | 2.2046 | 1.5821 | 1.9628 | 0.8853 | 1.3554 |

where the values of the normalized inductor $L'$ and capacitor $C'$ are equal to the particular $g$ value of the prototype filter.

The lowpass prototype filter circuits in Fig. 8 consist of both inductors and capacitors. However, in bandpass and bandstop filter designs, it is desirable to use the same type of resonator having all inductors or all capacitors in the prototype filters.

This can be achieved by using the impedance inverter ($K$ inverter) or admittance inverter ($J$ inverter) as shown in Fig. 9. The inverters act like frequency-independent quarter-wavelength lines, so that only inductors exist in the $K$-inverter prototype, and only capacitors in the $J$-inverter prototype networks. Figure 9 also gives the equations for converting the $g$ value of the lowpass filter prototype to these forms. The components value such as $R$, $L$, $C$, or $G$ in the prototype circuit using $J$ or $K$ inverters can be chosen arbitrarily. The frequency responses of the inverter circuits in Fig. 9 are identical to those of the original prototype filters.

Another commonly used analysis method in the cavity-type bandpass filter design is to use the coupling matrix. Figure 10 presents the equivalent circuit of a generalized coupled bandpass prototype filter using the coupling matrix [7,26].

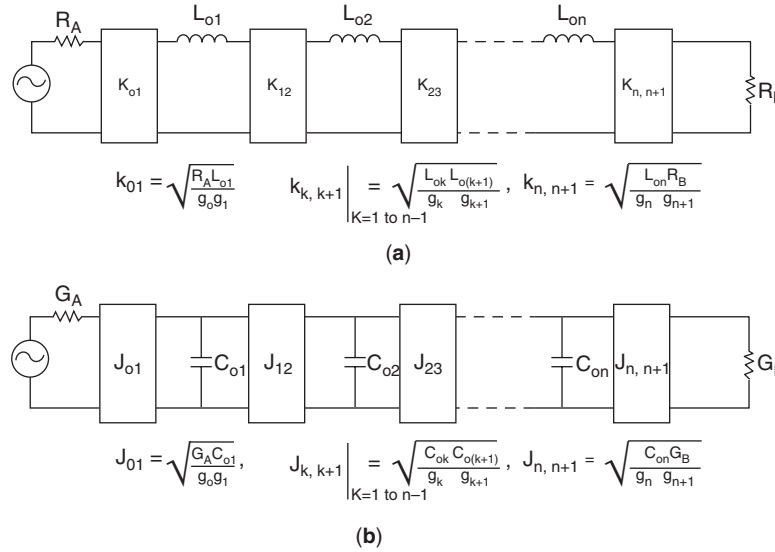


**Figure 9.** Modified prototype using impedance and admittance inverters.

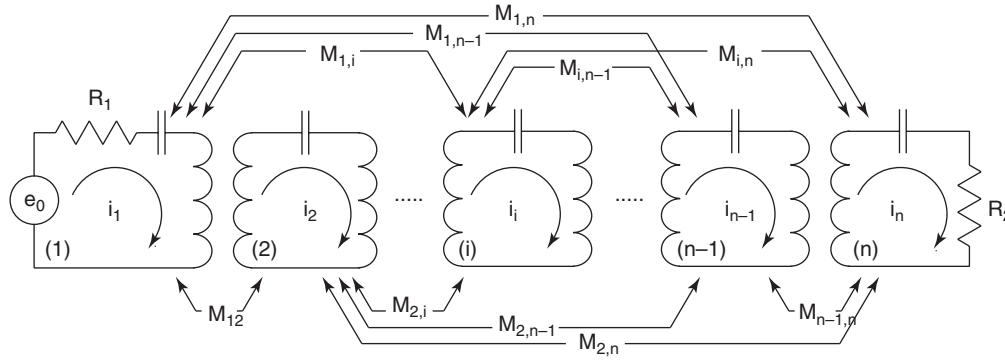


**Figure 10.** A bandpass filter equivalent circuit.

A general solution of the narrowband coupled cavity filter described above has been presented in a paper by Atia and Williams in the form of the loop equations as [7]

$$[Z]\cdot[I]=[V] \tag{17}$$

$$([R]+s[I]+j[M])\begin{bmatrix} i_1 \\ i_2 \\ \vdots \\ i_{n-1} \\ i_n \end{bmatrix}=\begin{bmatrix} e_1 \\ 0 \\ \vdots \\ 0 \\ 0 \end{bmatrix} \tag{18}$$

where

$$s=j\omega' \tag{19}$$

$$[M]=\begin{bmatrix} \lambda_{11} & M_{12} & M_{13} & \cdots & M_{1,n-1} & M_{1n} \\ M_{12} & \lambda_{22} & M_{23} & \cdots & M_{2,n-1} & M_{2n} \\ M_{13} & M_{23} & \lambda_{33} & \cdots & M_{3,n-1} & M_{3n} \\ \vdots & \vdots & \vdots & \ddots & \vdots & \vdots \\ M_{1,n-1} & M_{2,n-1} & M_{3,n-1} & \cdots & \lambda_{n-1,n-1} & M_{n-1,n} \\ M_{1n} & M_{2n} & M_{3n} & \cdots & M_{n-1,n} & \lambda_{nn} \end{bmatrix} \tag{20}$$

The matrix $R$ has all-zero entries except for the $(1,1)$ and $(n,n)$ elements, which are $R_1$ and $R_n$, respectively. $M$ is the so-called coupling matrix and has general entries of $M_{ij}$ for $i\neq j$, and $\lambda_{ii}$ for $i=j$. $\lambda_{ii}$ gives the resonant frequency of each resonator mapped to the lowpass prototype domain according to Eqs. (2) and (3).

The coupling matrix of the bandpass filter can be determined by the network synthesis method as described in Refs. 7 and 26 or by optimization from the pole and zero locations of the filter's transfer function [24]. For the case of direct network optimization, the coupling matrix elements are the optimization variables and the objective error function can be established by determining the difference between the transfer function frequency response of the prototype filter and the frequency response of the optimized filter. The Chebyshev coupling matrix of the same order can be used as the starting guess of the coupling matrix.

For filters with Chebyshev frequency responses, the coupling matrix of the filter can be obtained analytically from the $g$ values of the prototype filter as

$$R_1=\frac{1}{g_0g_1} \tag{21}$$

$$M_{i,i+1}=\frac{1}{\sqrt{g_ig_{i+1}}} \tag{22}$$

$$R_n=\frac{1}{g_{n-1}g_n} \tag{23}$$

where the remaining elements in the coupling matrix are zero.

As in the case of the lowpass prototype filter, the coupling matrix shown in Eq. (20) is normalized to the passband from –1 to +1 and zero center frequency. For a bandpass filter with center frequency $f_0$, and bandwidth BW, the required couplings of the filter are the normalized filter's coupling elements multiplied by the bandwidth with the unit same as that of the bandwidth.

## 4. DIRECT-COUPLED COMBLINE FILTER DESIGN

Matthaei gave the approximate design equations for the direct-coupled combline filter shown in Fig. 1 in terms of the resonator rod's self-capacitance to ground $C_j$ per unit length, and the mutual capacitance $C_{j,j+1}$ per unit length between neighboring resonator bars $j$ and $j+1$ [1,2]. The design equations use the lowpass prototype filter parameters $g_j$ $(i=0,1,\ldots,n,n+1)$ to achieve the desired frequency responses. The equations are sufficiently accurate for the applications of narrow bandpass filters with bandwidths up to octave.

By specifying the width of the filter enclosure and the resonator rod dimension, the admittance $Y_{aj}$ of the resonator lines can be computed. It is usually desirable

to choose the ratio of enclosure width to resonator linewidth in the range between 3 and 4 so that optimum unloaded $Q$ can be achieved. In addition, the electrical length $\theta_0$ of the resonator lines ranges between $\pi/4$ and $\pi/3$ at center frequency so that the filter will have both wide spurious-free stopband and less unloaded $Q$ degradation due to excessive end loading in case shunt resonators are used.

### 4.1. Design Equations

The normalized $J$-inverter parameters of the combline filter can then be computed as

$$G_{T1} = \frac{(\omega_2 - \omega_1)b_1}{g_0 g_1 \omega_0 \omega_1'} \tag{24}$$

$$J_{j,j+1} = \frac{(\omega_2 - \omega_1)}{\omega_0 \omega_1'} \sqrt{\frac{b_j b_{j+1}}{g_j g_{j+1}}} \tag{25}$$

$$G_{Tn} = \frac{(\omega_2 - \omega_1)b_n}{g_n g_{n+1} \omega_0 \omega_1'} \tag{26}$$

where

$$b_j = Y_{aj}\left(\frac{\cot\,\theta_0 + \theta_0 \csc^2\theta_0}{2}\right) \tag{27}$$

The normalized self-capacitances per unit length between each resonator rod and ground are

$$\frac{C_0}{\varepsilon} = \frac{Z_0 Y_A}{\sqrt{\varepsilon_r}}\left(1 - \frac{G_{T1}}{Y_A}\right) \tag{28}$$

$$\frac{C_1}{\varepsilon} = \frac{Z_0 Y_A}{\sqrt{\varepsilon_r}}\left(\frac{Y_{a1}}{Y_A} - 1 + \frac{G_{T1}}{Y_A} - \frac{J_{12}}{Y_A}\tan\,\theta_0\right) + \frac{C_0}{\varepsilon} \tag{29}$$

$$\frac{C_j}{\varepsilon} = \frac{Z_0 Y_A}{\sqrt{\varepsilon_r}}\left(\frac{Y_{aj}}{Y_A} - \frac{J_{j-1,j}}{Y_A}\tan\,\theta_0 + \frac{G_{Tn}}{Y_A} - \frac{J_{j,j+1}}{Y_A}\tan\,\theta_0\right), \quad j = 2 \text{ to } n-1 \tag{30}$$

$$\frac{C_n}{\varepsilon} = \frac{Z_0 Y_A}{\sqrt{\varepsilon_r}}\left(\frac{Y_{an}}{Y_A} - 1 + \frac{G_{Tn}}{Y_A} - \frac{J_{n-1,n}}{Y_A}\tan\,\theta_0\right) + \frac{C_{n+1}}{\varepsilon} \tag{31}$$

$$\frac{C_{n+1}}{\varepsilon} = \frac{Z_0 Y_A}{\sqrt{\varepsilon_r}}\left(1 - \frac{G_{Tn}}{Y_A}\right) \tag{32}$$

The normalized mutual capacitances per unit length between two adjacent resonator rods are

$$\frac{C_{01}}{\varepsilon} = \frac{Z_0 Y_A}{\sqrt{\varepsilon_r}} - \frac{C_0}{\varepsilon} \tag{33}$$

$$\frac{C_{j,j+1}}{\varepsilon} = \frac{Z_0 Y_A}{\sqrt{\varepsilon_r}}\left(\frac{J_{j,j+1}}{Y_A}\tan\,\theta_0\right), \quad j = 1 \text{ to } n-1 \tag{34}$$

$$\frac{C_{n,n+1}}{\varepsilon} = \frac{Z_0 Y_A}{\sqrt{\varepsilon_r}} - \frac{C_{n+1}}{\varepsilon} \tag{35}$$

The required lumped capacitances $C_j^s$ between the open end of the resonator rod and ground are

$$C_j^s = Y_{aj}\frac{\cot\,\theta_0}{\omega_0}, \quad j = 1 \text{ to } n \tag{36}$$

Knowing the desired self- and mutual capacitances of the combline filter resonator rods, we can determine the spacing between the adjacent resonators from the Getsinger or Cristal's design curves for the parallel-coupled rectangular or circular bars as described in the following section.

### 4.2. Parallel-Coupled Bars

The resonator bars of a combline filter can be considered as an array of the parallel lines. The cross section of the bar is usually rectangular or circular. The dimensions of the lines can be related to the various line capacitances per unit length. The self- and mutual capacitances obtained from Eqs. (28)–(36) can be used to determine the bar dimensions from Getsinger's parallel-coupled rectangular line curves for the rectangular cross section resonator rod combline filters, or from Cristal's parallel-coupled cylindrical rod design data for the circular cross section resonator rod combline filters.

**4.2.1. Coupled Rectangular Bars between Parallel Plates.** The cross section of a parallel-coupled rectangular bars under consideration and various line capacitances are shown in Fig. 11. There are two parallel ground planes spaced a distance $b$ apart, and a pair of rectangular bars located parallel to and midway between the ground planes. Assuming that $C_a$ is the self-capacitance per unit length between line $a$ and ground, $C_{ab}$ is the mutual capacitance per unit length between lines $a$ and $b$, and $C_b$ is the capacitance per unit length between line $b$ and ground, then, in terms of odd- and even-mode capacitances for lines $a$ and $b$, respectively, we have

$$C_{oo}^a = C_a + 2C_{ab}, \quad C_{oe}^a = C_a \tag{37}$$

$$C_{oo}^b = C_b + 2C_{ab}, \quad C_{oe}^b = C_b \tag{38}$$

In Fig. 11, the capacitance per unit length of each line has been separated into component parts by their contributions. $C_p$ is the parallel-plate capacitance per unit length from the top or bottom side of one bar to the adjacent ground plane, $C_{fe}'$ is the fringing capacitance per unit length to ground from the inner corner when the bars

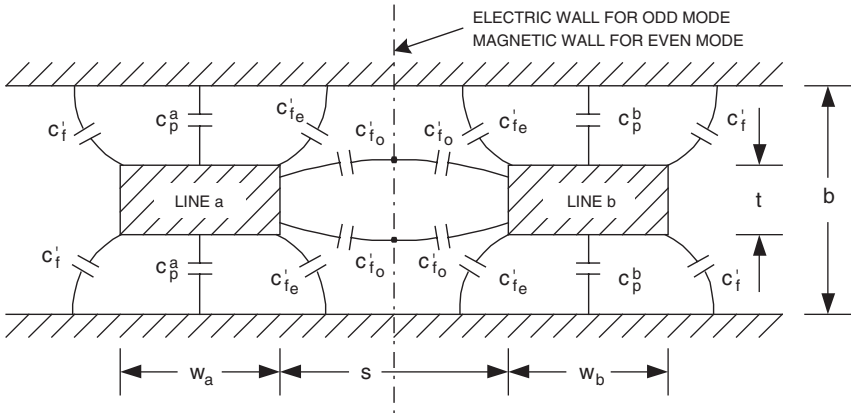


**Figure 11.** Cross section of parallel-coupled rectangular lines.

are excited in the even mode, and $C'_{fo}$ is the fringing capacitance per unit length to ground from the inner corner when the bars are excited in the odd mode. The capacitance $C'_f$ is the fringing capacitance per unit length for any of the outer corners of the rods. Assuming that all the coupled bars have the same height and thickness, so that the fringing capacitances are the same for both bars, the total self- and mutual capacitances of the coupled bars are

$$C_a = 2(C_p^a + C'_f + C'_{fe}) \tag{39}$$

$$C_{ab} = (C'_{fo} - C'_{fe}) \tag{40}$$

$$C_b = 2(C_p^b + C'_f + C'_{fe}) \tag{41}$$

Figures 12–14 give the normalized design charts by Getsinger [3], which relate $\Delta C/\varepsilon$, $C'_{fe}/\varepsilon$, $C'_{fo}/\varepsilon$, and $C'_f/\varepsilon$ to the rectangular bar dimensions, where

$$\Delta C = C_{ab} \tag{42}$$

To design a combline filter with rectangular cross section resonator bars, first compute the $C_j$ and $C_{j,\,j+1}$ values of the filter using Eqs. (28)–(36), and then select a convenient value for $t/b$, and use Fig. 12 of $\Delta C/\varepsilon$ and $C_{fe}'/\varepsilon$ versus $s/b$ to determine $s_{j,\,j+1}/b$ and also $C_{fe}'/\varepsilon$. Using $t/b$ and Fig. 14 of $C_f'/\varepsilon$ versus $t/b$, $C_f'/\varepsilon$ can be determined. As the parallel-plate capacitance $C_p/\varepsilon$ is given by

$$\frac{C_p}{\varepsilon} = 2\frac{w/b}{1 - t/b} \tag{43}$$

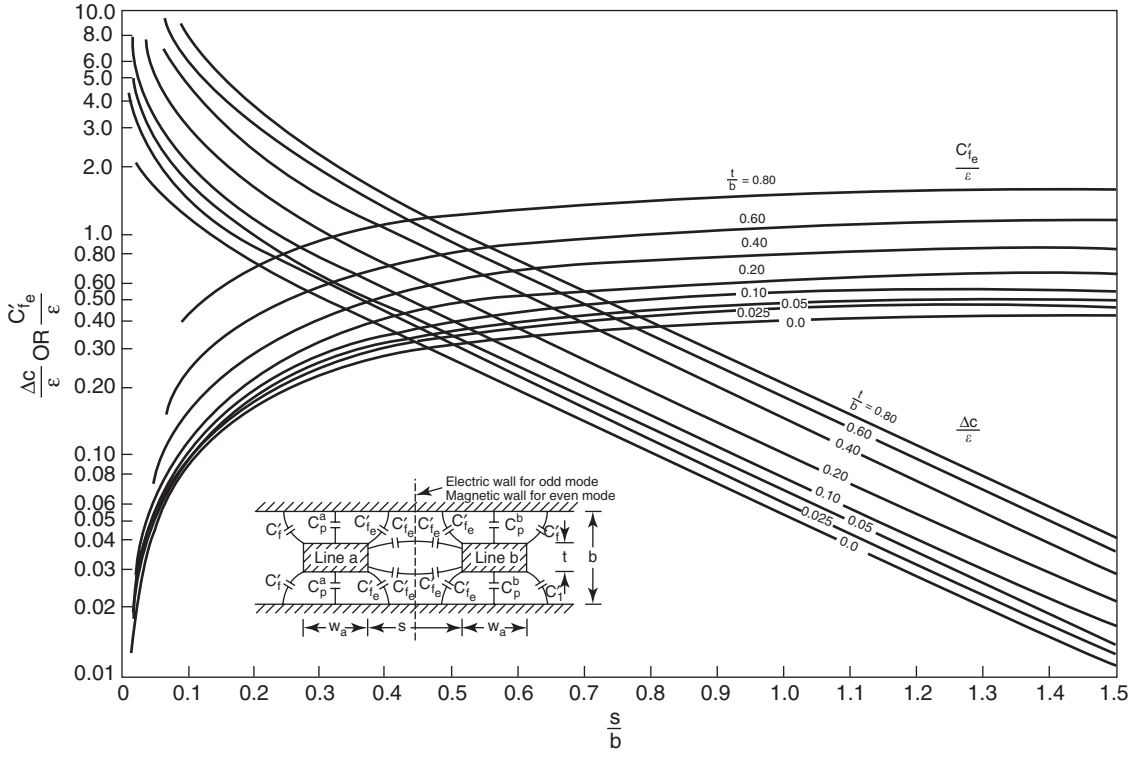


**Figure 12.** Fringing capacitances for coupled rectangular bars.

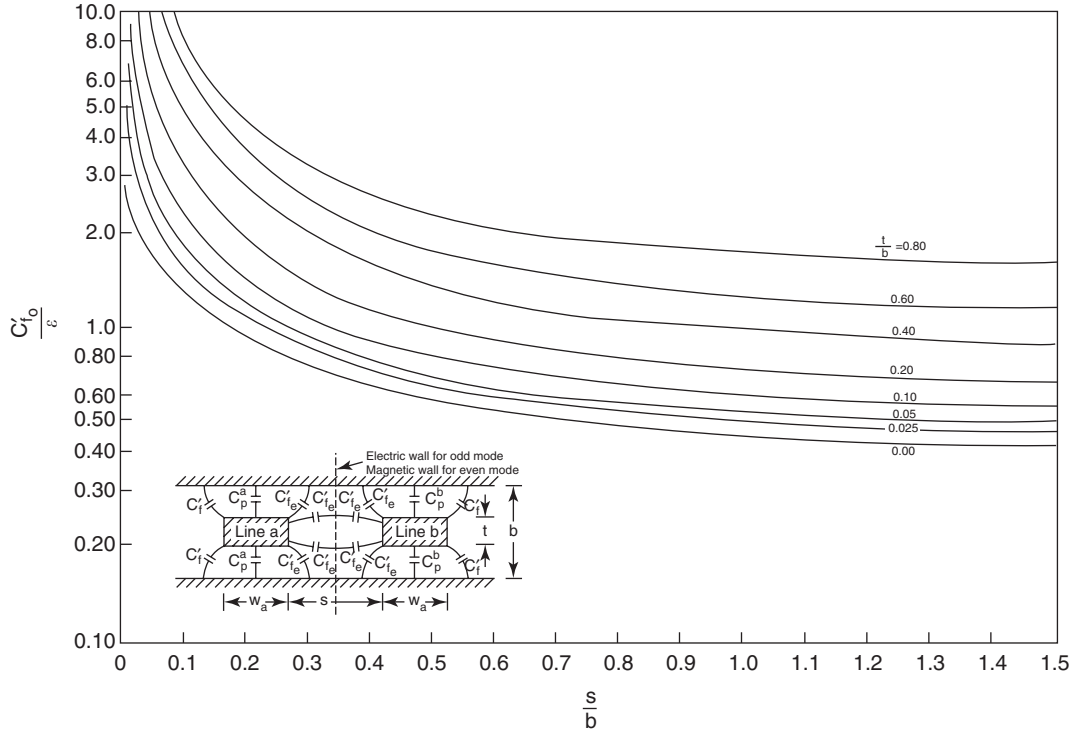


**Figure 13.** Odd-mode fringing capacitances for coupled rectangular bars.

when the ground-plane spacing $b$ is specified, the desired bar width $w_j$ can be determined as follows:

$$\frac{w_j}{b} = \frac{1}{2}\left(1 - \frac{t}{b}\right)\left[\frac{1}{2}\left(\frac{C_j}{\varepsilon}\right) - \frac{(C'_{\text{fe}})_{j-1,j}}{\varepsilon} - \frac{(C'_{\text{fe}})_{j,j+1}}{\varepsilon}\right] \tag{44}$$

$$\frac{w_j}{b} = \frac{1}{2}\left(1 - \frac{t}{b}\right)\left[\frac{1}{2}\left(\frac{C_j}{\varepsilon}\right) - \frac{C'_{\text{fe}}}{\varepsilon} - \frac{C'_{\text{f}}}{\varepsilon}\right] \tag{45}$$

**4.2.2. Coupled Circular Rods between Parallel Plates.** Combline filters made from circular cylindrical resonator rods can achieve the same excellent electrical performance and at the same time may offer manufacturing advantages. Cristal has given design data for coupled circular cylindrical rods between parallel ground planes [4] that can be used to accurately design a combline filter with circular resonator rods. Figure 15 shows the geometry of the periodic, circular cylindrical rods between parallel ground planes under consideration. The circular rods have diameter $d$ and are spaced periodically at a distance $c$. The ground planes are separated at distance $b$.

The spacing between adjacent rod surfaces is denoted by $s$ and is given by

$$s = c - d \tag{46}$$

The total static capacitances of the rods are related to the mutual capacitance between two adjacent rods $C_{\text{m}}$ and the self-capacitance $C_{\text{g}}$ of each rod. The total capacitance measured between one rod and ground when the rods are driven in the odd mode is

$$C_{\text{o}} = C_{\text{g}} + 4C_{\text{m}} \tag{47}$$

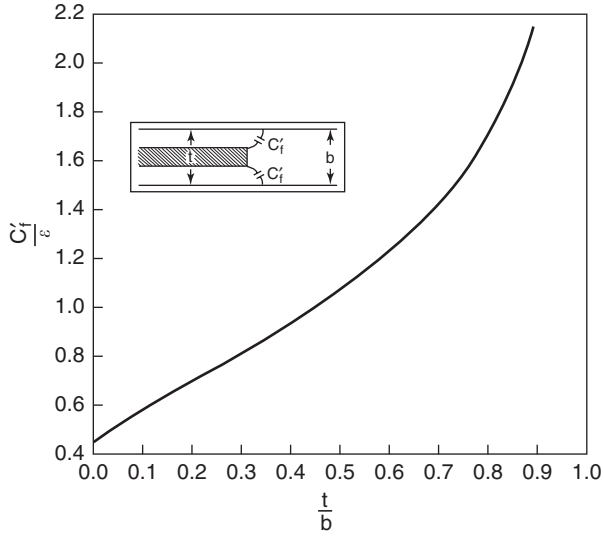


**Figure 14.** Fringing capacitance for an isolated rectangular bar.

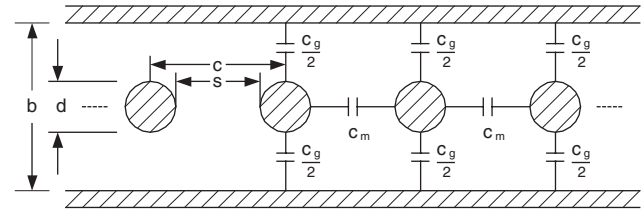


**Figure 15.** Cross section of parallel-coupled circular rods.

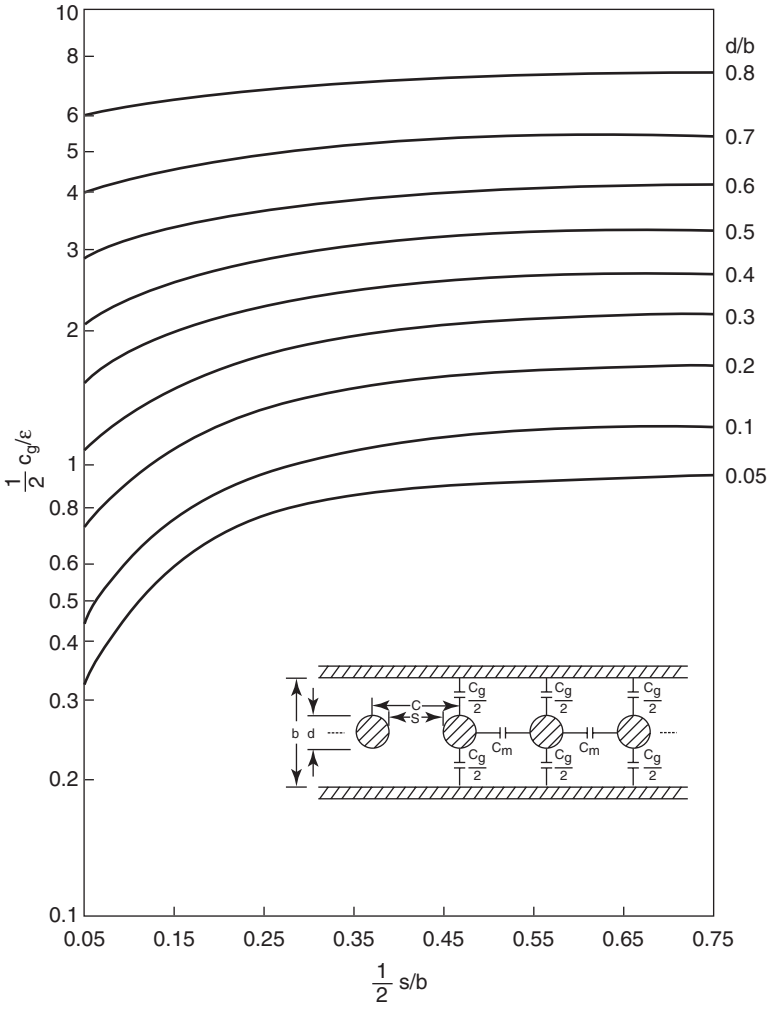


**Figure 16.** Graph of normalized mutual capacitance $C_m/\varepsilon$ versus $\frac{1}{2}(s/b)$.

assuming that both sides of the rod are having the same potential conditions. The total capacitance measured between one rod and ground when the rods are driven in the even mode is

$$C_e = C_g \tag{48}$$

From Eqs. (47) and (48) we can obtain

$$C_m = \tfrac{1}{4}(C_o - 4C_e) \tag{49}$$

Cristal's design graphs of the normalized capacitance $C/\varepsilon$ versus normalized spacing $s/b$ are given in Fig. 16 for $C_m/\varepsilon$ and in Fig. 17 for $\frac{1}{2}C_g/\varepsilon$.

As in the rectangular cross section resonator bar case, to design a combline filter with circular cylindrical resonator rod, one first needs to compute the $C_j$ and $C_{j,j+1}$ values of the filter using Eqs. (28)–(36), where

$$C_o = C_j \tag{50}$$

$$C_m = C_{j,j+1} \tag{51}$$

and then use Fig. 17 of $C_m/\varepsilon$ to determine the rod spacing $s_{j,j+1}/b$ and use Fig. 16 of $C_g/\varepsilon$ to determine the normalized rod diameter $d/b$.

### 4.3. Tapped-Line Input and Output

For a tap point located around the bottom 20% of a $\lambda/4$-long resonator rod, the relationship between the tap point and the resulting loaded $Q_e$ is given approximately by [15]

$$Q_e = \frac{\pi}{4}\left(\frac{R}{Z_0}\right)\left[\frac{1}{\sin^2[(\pi/2)(l/L)]}\right] \tag{52}$$

$$Q_e = \frac{f_0}{R_1 \mathrm{BW}} \tag{53}$$

where $l$ is the height of the tap point to the bottom of the resonator rod; $L$ is the equivalent height of the resonator rod, which is equal to $\lambda/4$; $R$ is the impedance of the input or output port; $R_1$ is the element of the filter's coupling matrix; and $Z_0$ is the impedance of the resonator rod. Figure 18 shows the graph of the equation for the loaded $Q$.

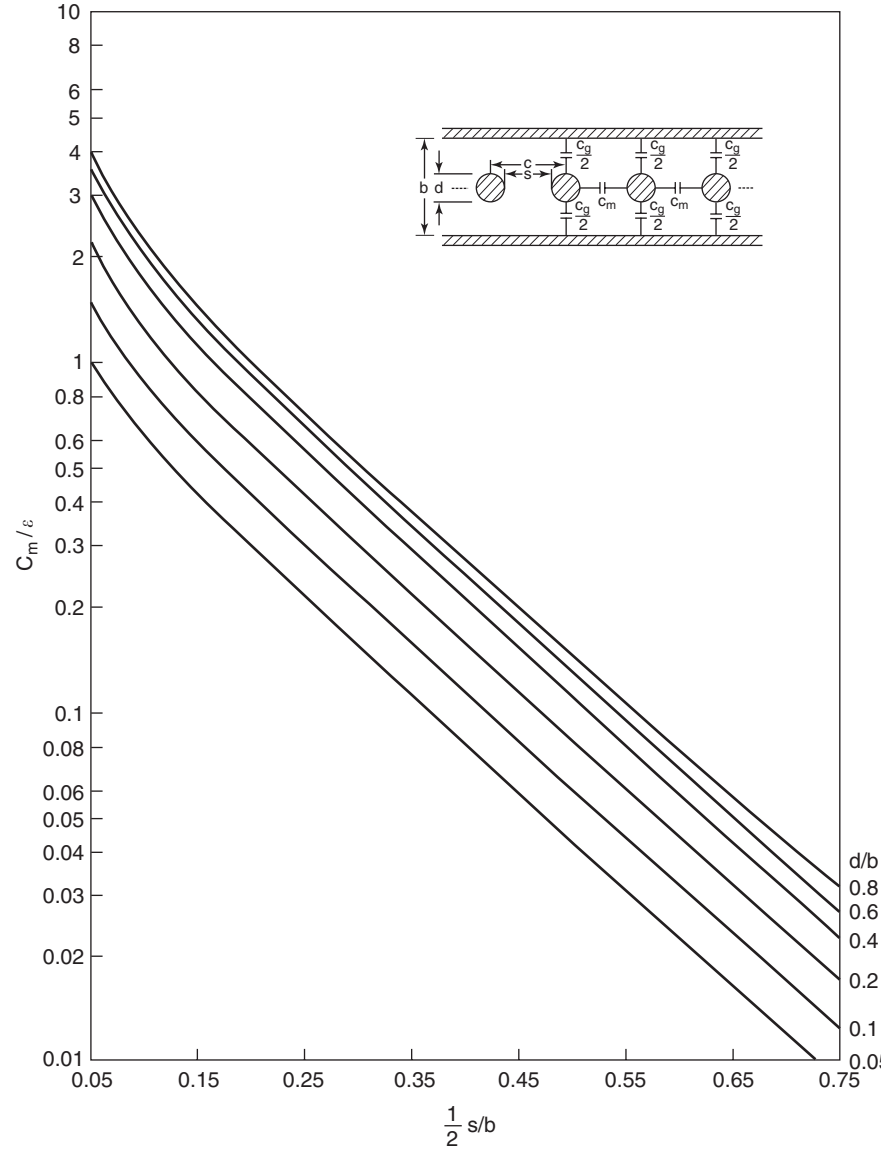


**Figure 17.** Graph of normalized half self-capacitance $\frac{1}{2} C_g/\varepsilon$ versus $\frac{1}{2}(s/b)$.

Cristal [17] later presented a general open-wire equivalent circuit considering the effects of the coupled resonators using a graph transformation process for combline and interdigital filter designs. In previous papers he assumed that the input or output port will be directly connected to the tapped-in point. However, for practical applications, the tapped line will have an impedance different from that of the input/output port and resonator rod with a given electrical length. The tapped-line length and impedance can have significant effect and therefore should be included in the analysis of the combline filter input/output couplings. Figure 19 shows an equivalent circuit of the tapped-line input/output coupling neglecting the effect of the rest of the resonators. In Cristal's approach, the graph transformation process or a circuit simulator can be used to solve the tapped-line coupling circuit.

## 5. FILTER TOPOLOGIES

The combline filter design equations presented in the previous sections are approximate and based on the direct-coupled filter type, typically exhibiting Chebyshev frequency responses. The stopband attenuation level is determined mainly by the number of stages of the filter. The use of nonadjacent or cross-couplings in the narrow-bandwidth bandpass filter with elliptic function response permits great flexibility in the choice of the frequency response. As a result, a smaller number of resonators are required to meet the attenuation specification.

Theoretically, cross-coupling can be applied between any two nonadjacent resonators of the filter, and also including the input and output ports. However, in practical applications the cross-couplings that can be applied are usually limited by the physical layout and complexity of

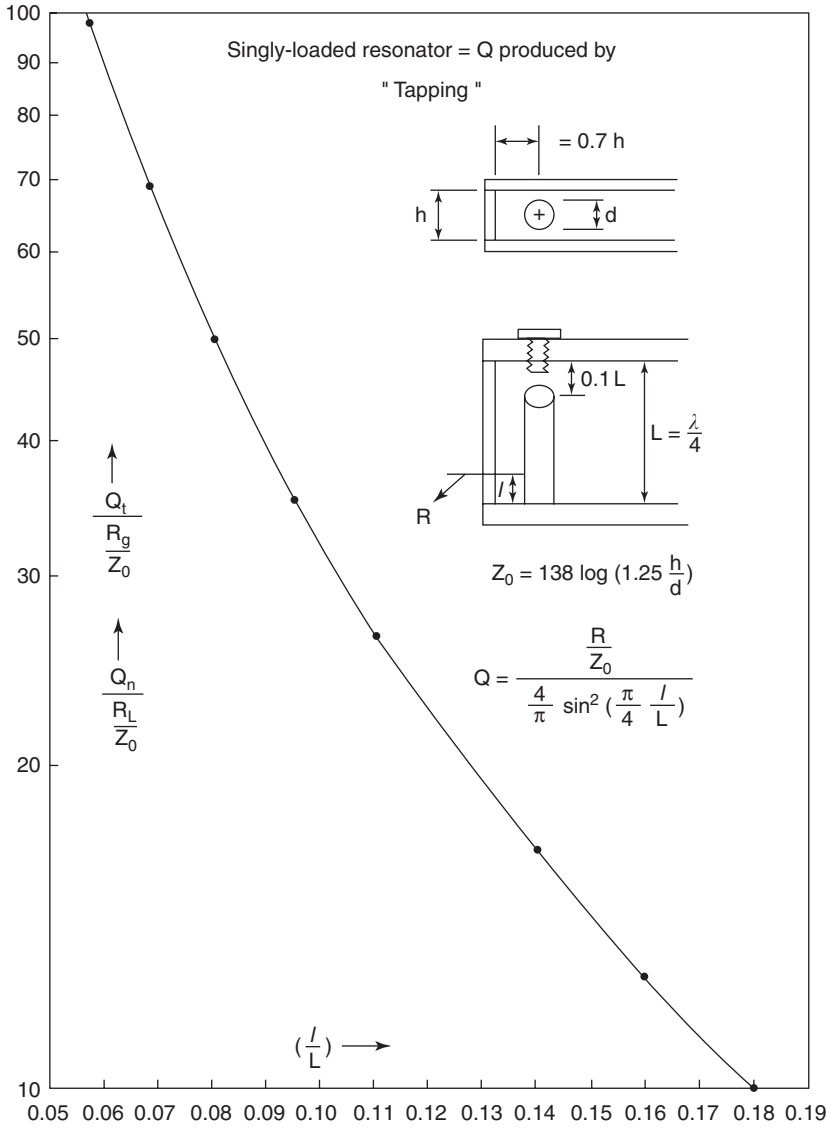


**Figure 18.** Loaded combline resonator $Q$ versus tapped-line position.

the filters. The advantage of the filter with an extra number of cross-couplings may be offset by the layout limitation, with much more development effort and the sensitivity of the filter network, leading to longer tuning time and poorer temperature stability.

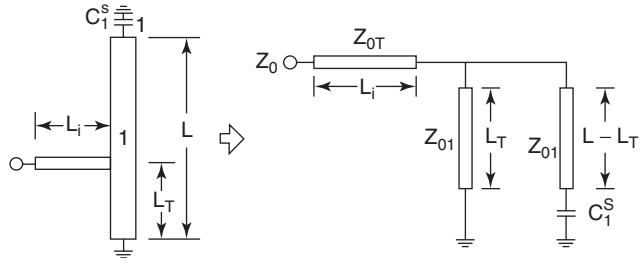


**Figure 19.** An equivalent circuit for the tapped-line input/output coupling geometry.

Combline filters with either asymmetric or symmetric frequency response may be realized to meet the desired attenuation characteristics by applying the proper cross-coupling topology and values. For each desired filter transfer function, the configuration or topology that can achieve the targeted frequency response is not unique. However, it is usually preferable to achieve the desired frequency response by using known simple topologies. Figure 20 shows typical canonical-form coupled resonator filters with cross-couplings that can achieve the asymmetric frequency response in part (a), and symmetric frequency response in part (b) [13]. Topologies for so-called CQ and CT filters are shown in Fig. 21.

Filters having complicated cross-coupling structures as shown in Fig. 20 can achieve more transmission zeros using a minimum number of cross-couplings. However, each cross-coupling may affect more than one transmission zero location, which usually makes them more difficult to tune. For commercial applications when cost is a main concern,

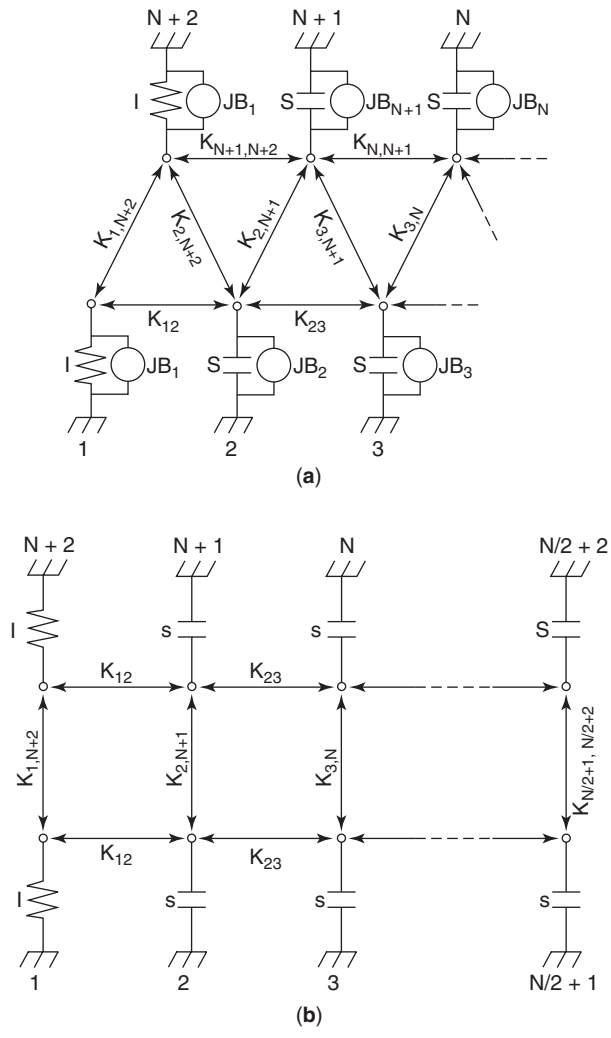


**Figure 20.** Canonical prototype networks having (a) asymmetric and (b) symmetric frequency responses.

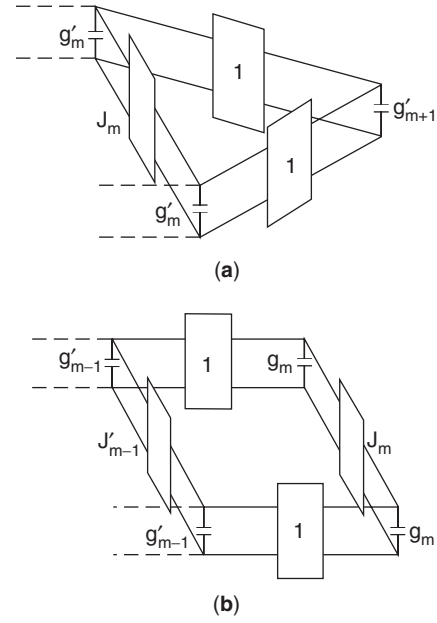


**Figure 21.** Typical filter building blocks: (a) cascaded triplet (CT) section; (b) cascaded quadruplet (CQ) section.

the filter topology that makes the filter easy to design and to tune will be very attractive to filter designers.

The cascaded triplet (CT) or cascaded quadruplet (CQ) sections are relatively simple to tune. Each section is typically responsible only for the transmission zeros that it generates and therefore can be used as a basic building block to create more complicated filter structures. Figure 22 presents the examples using two CT or CQ sections in the cascaded filters.

A CT filter consists of cascaded groups of three cavities or nodes, each with one cross-coupling between first and third resonators in the CT section. The cross section will introduce one transmission zero at either the lower or the higher side of the passband depending on the sign of the cross-coupling. A cross-coupling with negative sign or capacitive-type coupling will generate the transmission zero at the lower side, while the positive or inductive cross-coupling will generate the transmission zero at the higher side. An aperture between two combline resonators usually achieves positive coupling unless the aperture is at the top of the cavity and the electrical length of the combline rod is over 75° [48]. A coupling bar or probe between the top of the resonators can usually achieve the required capacitive coupling.

Similarly, a CQ filter consists of cascaded groups of four cavities or nodes, each with one cross-coupling between the first and fourth resonators in the CQ section. When the cross-coupling is capacitive, one symmetric pair of transmission zeros one at each side can be achieved. For inductive cross-coupling, a pair of zeros will be on the real axes, and as a result the group delay frequency response of the filter may be equalized.

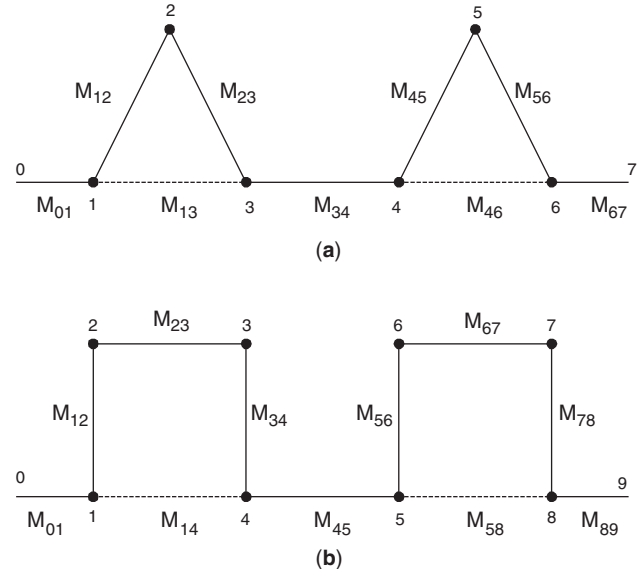


**Figure 22.** Cascaded coupling diagram: (a) a six-pole CT filter; (b) an eight-pole CQ filter.

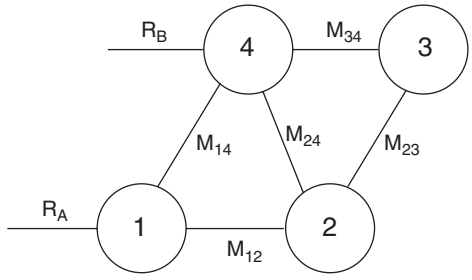


**Figure 23.** Generalized quadruplet section for two-transmission-zero implementation.

If the quadruplet section has two cross-couplings as shown in Fig. 23, two asymmetric transmission zeros may then be achieved. The locations of the zeros depend on the relative sign of the couplings. Assuming that all the adjacent couplings are inductive, Table 2 summarizes the locations of the zeros corresponding to the sign of the cross-couplings. Similarly, a general five-resonator section with three transmission zeros can be analyzed [25]. Figure 24 gives an example of an eight-pole combline filter having five transmission zeros using multiple cross-coupling four- and five-resonator sections. The three high-side zeros are realized by the 1–5 cross-coupled five-resonator section, while the two low-side zeros are realized by the 5–8 cross-coupled four-resonator section.

As a general rule, a simple Chebyshev response filter that meets the passband, but not the stopband, requirements would be used as the starting point of the design. By bringing transmission zeros from DC or infinity to finite frequencies, the desired stopband characteristics can be achieved. In most cases, the overall degree of the filter can be reduced compared with a Chebyshev design that meets the same requirements.

## 6. EM SIMULATIONS

To realize narrowband combline filters with relatively complex resonator topologies, all physical parameters such as cavity and aperture dimensions need to be determined from the given coupling matrix. Such filter designs are now increasingly dependent on accurate electromagnetic (EM) computer simulations, due to complexity of the filter structures. As a result, strong interaction between resonators cannot be neglected and should be considered in the design. These requirements usually can be satisfied only by EM simulation. As shown in Fig. 5, the approximate design equations from Eqs. (24)–(53) for space-coupled combline cases can be replaced completely by EM simulations.

**Table 2. Locations of Transmission Zeros for Generalized Quadruplet Section**

| Case | $M_{14}$ | $M_{24}$ | Number of Zeros ($<f_0, >f_0$) |
|---|---|---|---|
| 1 | $=0$ | $<0$ | $1(1,0)$ |
| 2 | $=0$ | $>0$ | $1(0,1)$ |
| 3 | $<0$ | $=0$ | $2(1,1)$ |
| 4 | $>0$ | $=0$ | $2(j,j)$ |
| 5 | $>0$ | $>0$ | $2(0,2)$ |
| 6 | $>0$ | $<0$ | $2(2,0)$ |
| 7 | $<0$ | $<0$ | $2(1,1)$ |
| 8 | $<0$ | $>0$ | $2(1,1)$ |

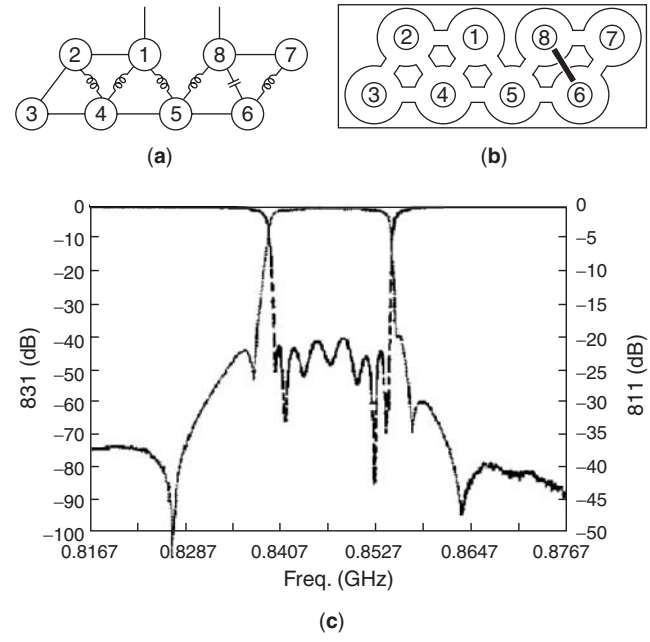


**Figure 24.** An eight-pole combline filter with five transmission zeros: (a) equivalent circuit; (b) layout; (c) measured frequency response.

### 6.1. EM Simulators and Methods

Three-dimensional (3D) EM simulation software is usually preferred for use in cavity-type combline filter design. The most commonly used numerical techniques for arbitrary structures are the finite-element method (FEM) and the finite-difference time-domain method (FDTD). These methods can analyze complex structures but usually require large amounts of memory and long computation time. Other computer software can solve some common structures very efficiently (using much less memory) by utilizing the properties of the structure, such as the mode-matching (MM) and transmission-line matrix (TLM) methods. For planar structure problems, the method of moment method (MoM) is usually used.

The commonly used commercial EM simulators are Ansoft or Agilent's HFSS using FEM, CST's Microwave Studio using the FDTD method for 3D arbitrary structures, Agilent's Momentum using FEM, Sonnet's Em, and Zeland's IE3D using MoM for 3D planar structures.

For narrow-bandwidth-coupled resonator filter design, it is usually convenient to divide the filter into individual pieces to determine the cavity and aperture dimension separately when using the EM simulation software to perform the design from the efficiency and memory usage point of view; otherwise too much simulation time will be

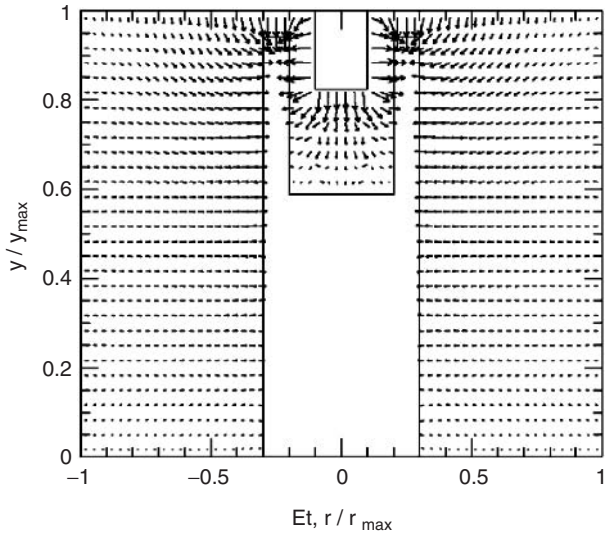


**Figure 25.** Typical electric field distributions of a combline cavity.

needed. Most of the parameters will be fine-tuned by tuning screws at the prototype stage and during production.

### 6.2. Resonant Frequency

An EM simulator can model the resonator and determine the resonant frequencies of both the fundamental and higher-order modes. In addition, the field distributions of the resonant cavity can be obtained, including the tuning screw as shown in Fig. 25. Figure 26 presents the typical higher-order mode chart of the combline resonators with the airgap between the rod and enclosure as a variable. It is shown that $TM_{02}$ and $HE_{11}$ are the first two higher-order modes of the typical combline resonator. For the small-gap case, a resonator with a shorter length has a larger mode separation. The resonant frequency of the first higher-order mode can be 3–5 times the dominant mode resonant frequency when the height of the cavity is 0.5–1.0 times the diameter of the cavity. The typical small-gap reentrant cavity bandpass filter can achieve a spurious-free range of more than twice the center frequency. This mode separation ratio decreases as the gap increases.

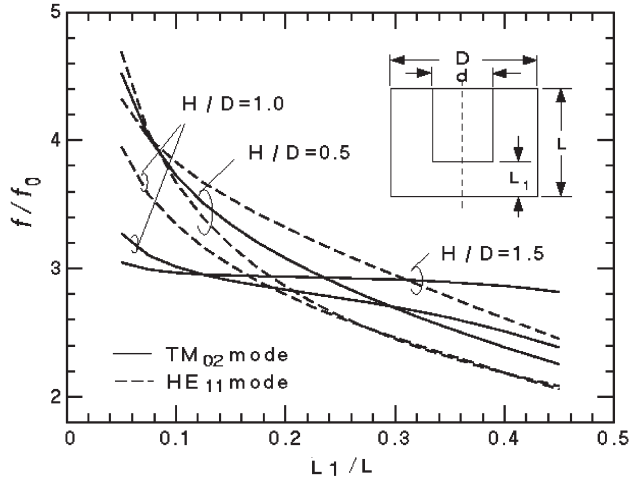


**Figure 26.** Typical mode chart of a combline resonator relative to dominant mode as a function of gap.

### 6.3. Unloaded *Q*

Accurate determination of the unloaded $Q$ factor of the resonator is very important for combline filter design, since it directly relates to loss, size, and cost of the filter. Empirically, the unloaded $Q$ of a combline resonator can be estimated from the measurements of many practical filters using the equation [21]

$$Q = Kb\sqrt{f_0} \tag{54}$$

where $b$ is the width of the cavity in inches, $f_0$ is the resonant frequency in gigahertz, and $K$ is a constant approximately equal to 1600 with $b$ less than $0.08\lambda$ for a practical silver-plated combline resonator. However, when $b$ is above $0.08\lambda$, $K$ increases, and can be as much as 2800 for $b = 0.18\lambda$. Figure 27 shows the measured unloaded $Q$ of the combline resonator expressed in $K$ values with $b/\lambda$ in terms of $K$ as a function of $b/\lambda$ in the range between 0.12 and 0.20. The practical $Q$ is dependent on factors such as surface roughness, plating quality, tuning screw penetration, and possible surface contact problems, which partially explains the spread in the $K$ values of various designs having the same $b/\lambda$.

EM simulation software can compute the unloaded $Q$ of a cavity accurately. Since a combline resonator has small

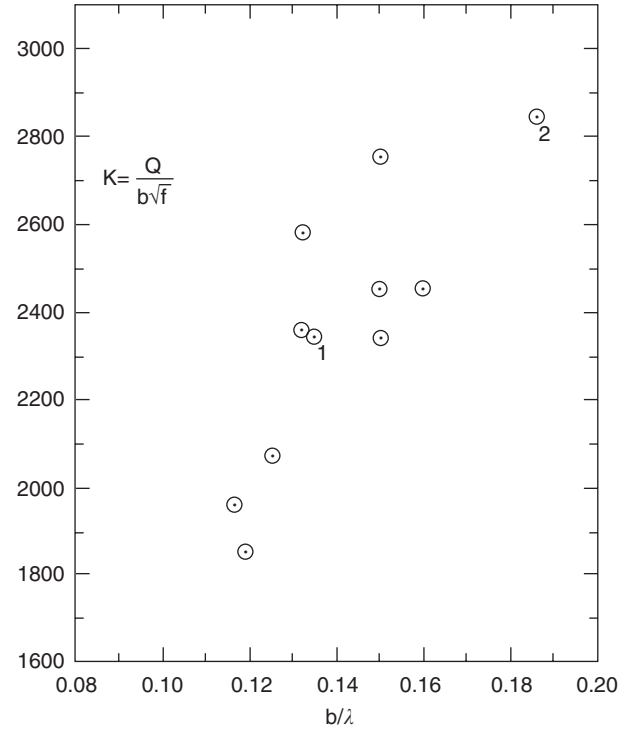


**Figure 27.** Measured normalized unloaded Q as a function of $b/\lambda$.

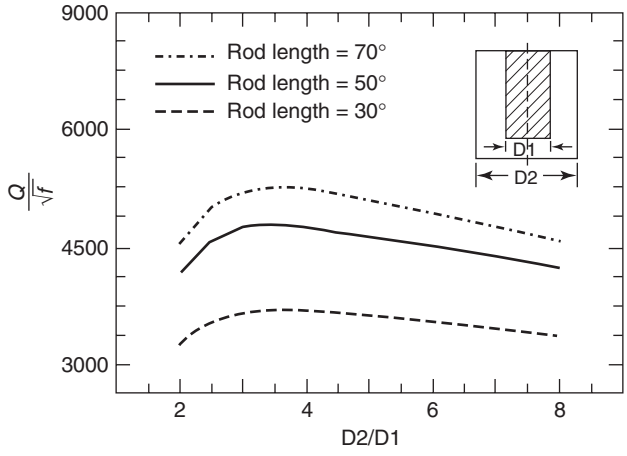


**Figure 28.** Computed unloaded $Q$ of a combline resonator versus $D_2/D_1$ Ratio.

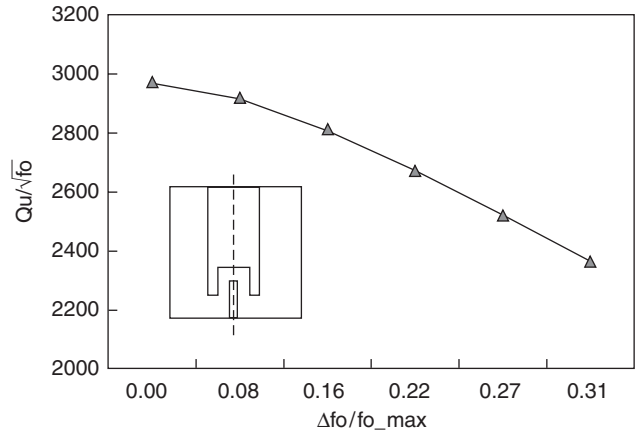


**Figure 29.** Unloaded $Q$ of a combline resonator versus resonant frequency as an effect of the tuning screw.

loss, a perturbation method is usually incorporated for this kind of computation. Figure 28 shows the computed unloaded $Q$ of the combline resonators versus the ratio of the outer/inner diameter ratio $D_2/D_1$ with different rod lengths. It is shown that maximum unloaded $Q$ of the resonators occurs when $D_2/D_1$ is approximately 3.6. Longer rod length yields higher unloaded $Q$ for the same $D_1$ and $D_2$.

Both the resonant frequency and unloaded $Q$ decrease when the tuning screw penetrates into the cavity. The tuning screw may have a strong effect on unloaded $Q$ of the combline resonator, which should be considered in the filter design. Figure 29 shows the computed unloaded $Q$ of a combline resonator versus resonant frequency change by the tuning screw.

## 7. TYPICAL APPLICATIONS

Combline filters have been widely used in many communication systems and microwave applications. They have become more and more important for low-loss microwave filters in the 0.5–12 GHz frequency band for both narrow- and wideband applications. Applications of combline filters also include diplexers (duplexers), multiplexers, and delay-line filters. When a combline cavity is filled with a high dielectric constant material, it results in a dielectric resonator having significantly reduced dimensions.

Another application for combline filters is to replace the lowpass filter to achieve a very wideband spurious-free response in the system [49]. For this type of application, the bandwidth of the filter is usually relatively large and

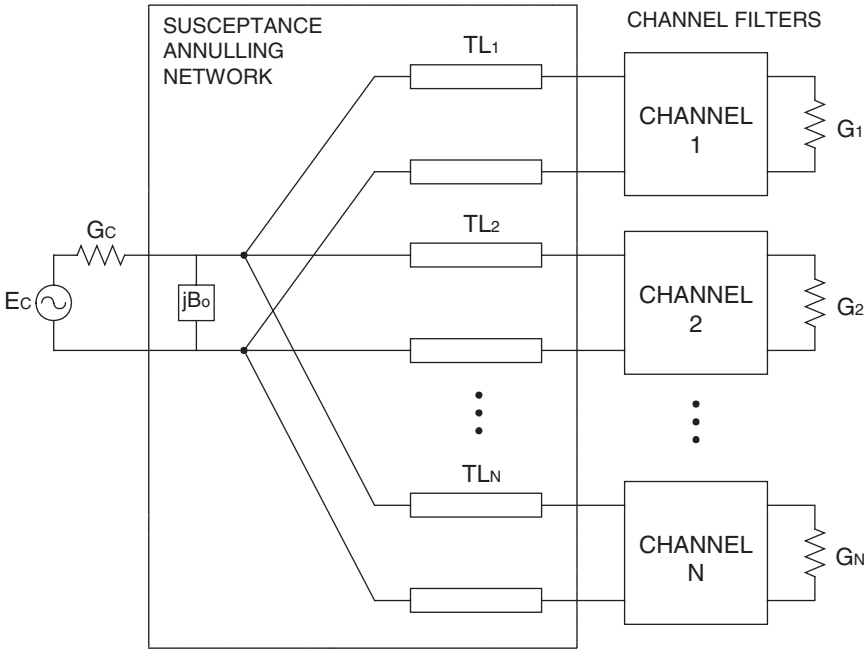


**Figure 30.** Schematic of a parallel-connected multiplexer.

**Figure 31.** A 1.8-GHz DCS duplexer.

therefore does not require very high unloaded $Q$; thus the filter can be very small in size. As the combline resonator can have superior stopband performance, wideband spurious-free performance with a sharp rolloff skirt can be achieved easily with combline resonator filters.

Multiplexers, particularly duplexers, are frequently required by communication systems for RF front ends to separate or combine both transmit and receive signals [28–37]. A schematic drawing of a commonly used parallel-connected multiplexer with $N$ channels is shown in Fig. 30. The multiplexer consists of channel filters and a susceptance annulling network, which in turn consists of transmission lines series-connected to each channel filter and a shunt susceptance element at a common input port to help provide a nearly constant total input admittance [33–38]. The susceptance annulling network is achieved by optimizing the length and characteristic impedance of the transmission lines and the shunt susceptance element value to minimize the interaction among the channels. For narrowband applications, the suceptance $jB_0$ of the annulling network can be maintained by offsetting the resonant frequency of the first cavities of the channel filters to cancel the susceptance of the channel filters. Figure 31 is a photograph of a DCS (digital communication system) duplexer consisting of two 6-pole combline filters. Each channel filter has two CT sections having two transmission zeros at one side. Figure 32 presents the measured frequency response of the duplexer.


### Acknowledgment

The author would like to thank reviewers for reviewing the article and many valuable suggestions.


## BIBLIOGRAPHY


1. G. L. Matthaei, L. Young, and E. M. T. Jones, *Design of Microwave Filters, Impedance-Matching Networks and Coupling Structures*, McGrawHill, New York, 1964.
2. G. L. Matthaei, Combline bandpass filters of narrow or moderate bandwidth, *Microwave J.* **6**: 82–91 (Aug. 1963).
3. W. J. Getsinger, Coupled rectangular bars between parallel plates, *IEEE Trans. Microwave Theory Tech.* **MTT-10**:65–72 (Jan. 1962).
4. E. G. Cristal, Coupled circular cylindrical rods between parallel ground planes, *IEEE Trans. Microwave Theory Tech.* **MTT-12**:428–439 (July 1964).


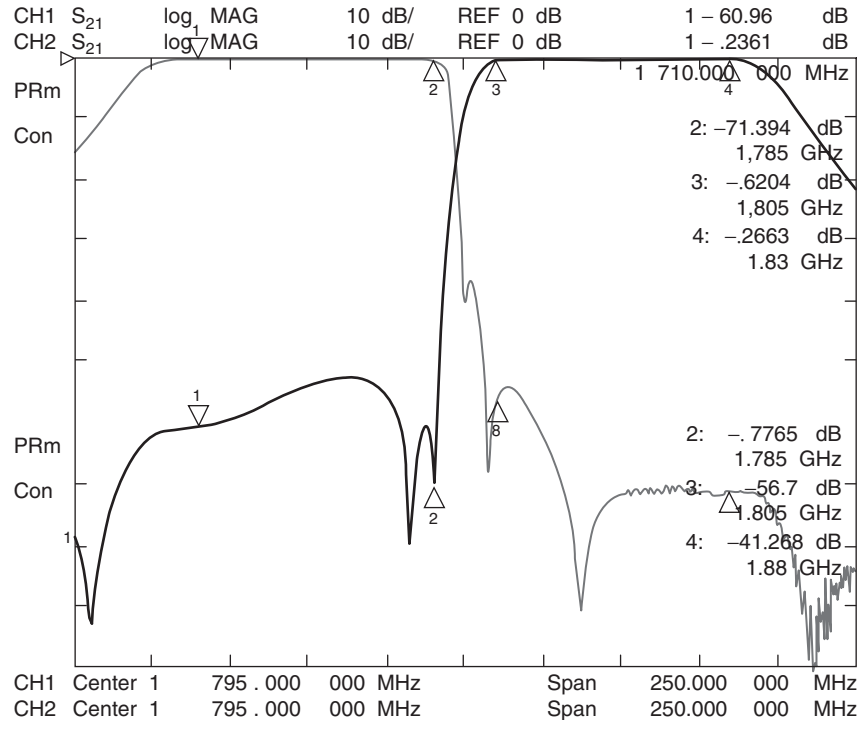


**Figure 32.** Measured frequency response of the duplexer.

5. E. G. Cristal, Data for partially decoupled round rods between parallel ground planes (corresp.), *IEEE Trans. Microwave Theory Tech*. **MTT-16**:311–314 (May 1968).
6. R. Levy and J. D. Rhodes, A combline elliptic filter, *IEEE Trans. Microwave Theory Tech*. **MTT-19**: 26–29 (Jan. 1971).
7. A. Atia, A. Williams, and R. Newcomb, Narrow-band multiple-coupled cavity synthesis, *IEEE Trans. Circ. Syst*. **MTT-21**: 649–655 (Sept. 1974).
8. R. Levy, Filters with single transmission zeros at real or imaginary frequencies, *IEEE Trans. Microwave Theory Tech*. **MTT-24**:172–181 (April 1976).
9. R. J. Wenzel, Synthesis of combline and capacitively loaded interdigital bandpass filters of arbitrary bandwidth, *IEEE Trans. Microwave Theory Tech*. **MTT-19**:678–686 (Aug. 1971).
10. R. J. Wenzel, Synthesis of combline and capacitively loaded interdigital bandpass filters of arbitrary bandwidth, *IEEE Trans. Microwave Theory Tech*. **MTT-19**:678–686 (Aug. 1971).
11. R. J. Wenzel, Exact design of wideband equal-ripple bandpass filters with non-adjacent resonator couplings, *IEEE MTT-S Int. Microwave Symp. Digest*, 1976, Vol. I, pp. 125–127.
12. G. D. O'Clock, Jr., Tunable frequency range and mismatch adjustment for combline bandpass filters, *IEEE Trans. Microwave Theory Tech*. **MTT-20**:238–239 (March 1972).
13. H. C. Bell, Canonical asymmetric coupled-resonator filters, *IEEE Trans. Microwave Theory Tech*. **MTT-30**:1335–1340 (Sept. 1982).
14. R. Levy and S. B. Cohn, A history of microwave filter research, design, and development, *IEEE Trans. Microwave Theory Tech*. **MTT-32**: 1055–1067 (Sept. 1984).
15. M. Dishal, A simple design procedure for small percentage bandwidth round-rod interdigital filters (corresp.), *IEEE Trans. Microwave Theory Tech*. **MTT-13**:696–698 (Sept. 1965).
16. S. B. Cohn, Generalized design of bandpass and other filters by computer optimization, *IEEE MTT-S Int. Microwave Symp. Digest*, 1974, Vol. I, pp. 272–274.
17. E. G. Cristal, Tapped-line coupled transmission lines with applications to interdigital and combline filters, *IEEE Trans. Microwave Theory Tech*. **MTT-23**:1007–1012 (Dec. 1975).
18. S. Caspi and J. Adelman, Design of combline and interdigital filters with tapped-line input, *IEEE Trans. Microwave Theory Tech*. **MTT-36**:759–763 (April 1988).
19. W.-T. Lo and C.-K. C. Tzuang, K-band quasi-planar tapped combline filter and diplexer, *IEEE Trans. Microwave Theory Tech*. **MTT-41**:215–223 (Feb. 1993).
20. C. Ernst and V. Postoyalko, Tapped-line interdigital filter equivalent circuits, *IEEE MTT-S Int. Microwave Symp. Digest*, 1997, Vol. II, pp. 801–804.
21. R. Levy, H.-W. Yao, and K. A. Zaki, Transitional combline/evanescent-mode microwave filters, *IEEE Trans. Microwave Theory Tech*. **MTT-45**:2094–2099 (Dec. 1997).
22. R. Levy, Direct synthesis of cascaded quadruplet (CQ) filters, *IEEE Trans. Microwave Theory Tech*. **MTT-43**:2940–2945 (Dec. 1995).
23. R. Hershtig, R. Levy, and K. Zaki, Synthesis and design of cascaded trisection (CT) dielectric resonator filters, *Proc. 27th European Microwave Conf. and Exhibition*, Sept. 1997, Vol. 2, pp. 784–791.
24. W. A. Atia, K. A. Zaki, and A. E. Atia, Synthesis of general topology multiple coupled resonator filters by optimization, *IEEE MTT-S Int. Microwave Symp. Digest*, 1998, Vol. II, pp. 821–824.
25. J.-F. Liang and D. Zhang, General coupled resonator filters design based on canonical asymmetric building blocks, *IEEE MTT-S Int. Microwave Symp. Digest*, 1999, Vol. III, pp. 907–910.
26. R. J. Cameron, General coupling matrix synthesis methods for Chebyshev filtering functions, *IEEE Trans. Microwave Theory Tech*. **MTT-47**:433–442 (April 1999).
27. R. Levy and P. Petre, Design of CT and CQ filters using approximation and optimization, *IEEE Trans. Microwave Theory Tech*. **MTT-49**:2350–2356 (Dec. 2001).
28. E. G. Cristal and G. L. Matthaei, A technique for the design of multiplexers having contiguous channels, *IEEE Trans. Microwave Theory Tech*. **MTT-12**:88–93 (Jan. 1964).
29. R. J. Wenzel and W. G. Erlinger, Narrowband contiguous multiplexing filters with arbitrary amplitude and delay response, *IEEE MTT-S Int. Microwave Symp. Digest*, 1976, Vol. I, pp. 116–118.
30. A. E. Atia, Computer-aided design of waveguide multiplexer, *IEEE Trans. Microwave Theory Tech*. **MTT-22**:332–336 (March 1974).
31. J. D. Rhodes, Design formulas for bandpass channel diplexers, *IEEE MTT-S Int. Microwave Symp. Digest*, 1976, Vol. I, pp. 112–115.
32. J. L. Haine and J. D. Rhodes, Direct design formulas for asymmetric bandpass channel diplexers, *IEEE Trans. Microwave Theory Tech*. **MTT-25**:807–813 (Oct. 1977).
33. J. D. Rhodes and R. Levy, A generalized multiplexer theory, *IEEE Trans. Microwave Theory Tech*. **MTT-27**:99–111 (Feb. 1979).
34. J. D. Rhodes and S. A. Alseyab, A design procedure for bandpass channel multiplexers connected at a common junction, *IEEE Trans. Microwave Theory Tech*. **MTT-28**:246–253 (March 1980).
35. P. M. LaTourrette, Multi-octave combline-filter multiplexer, *IEEE MTT-S Int. Microwave Symp. Digest*, 1977, Vol. I, pp. 298–301.
36. P. M. LaTourrette and J. L. Roberds, Extended-junction combline multiplexers, *IEEE MTT-S Int. Microwave Symp. Digest*, 1978, Vol. I, pp. 214–216.
37. P. M. LaTourrette, Wide-bandwidth combline filters with high selectivity, *IEEE MTT-S Int. Microwave Symp. Digest*, 1979, Vol. I, pp. 275–277.
38. W.-T. Lo and C.-K. C. Tzuang, K-band quasi-planar tapped combline filter and diplexer, *IEEE Trans. Microwave Theory Tech*. **MTT-41**:215–223 (Feb. 1993).
39. G. Pfitzenmaier, Synthesis and realization of narrow-band canonical microwave bandpass filters exhibiting linear phase and transmission zeros, *IEEE Trans. Microwave Theory Tech*. **MTT-30**:1300–1311 (Sept. 1982).
40. A. Fukasawa, Analysiss and composition of a new microwave filter configuration with inhomogeneous dielectric medium, *IEEE Trans. Microwave Theory Tech*. **MTT-30**:1367–1375 (Sept. 1982).
41. M. Sagawa, M. Makimoto, and S. Yamashita, A design method of bandpass filters using dielectric-filled coaxial resonators, *IEEE Trans. Microwave Theory Tech*. **MTT-33**:152–157 (Feb. 1985).
42. K. Hano, H. Kohriyama, and K.-I. Sawamoto, A direct-coupled $\lambda/4$-coaxial resonator bandpass filter for land mobile communications, *IEEE Trans. Microwave Theory Tech*. **MTT-34**:972–976 (Sept. 1986).

43. Y. Isota, M. Miyazaki, O. Ishida, and F. Takeda, A grooved monoblock combline filter suppressing the third harmonics, *IEEE MTT-S Int. Microwave Symp. Digest*, 1987, Vol. I, pp. 383–386.
44. R. Levy, Simplified analysis of inhomogeneous dielectric block combline filters, *IEEE MTT-S Int. Microwave Symp. Digest*, 1990, Vol. I, pp. 135–138.
45. T. Ishizaki and T. Uwano, A stepped impedance combline filter fabricated by using ceramic lamination technique, *IEEE MTT-S Int. Microwave Symp. Digest*, 1994, Vol. II, pp. 617–620.
46. H. Matsumoto, H. Ogura, and T. Nishikawa, A miniaturized dielectric monoblock bandpass filter for 800 MHz band cordless telephone system, *IEEE MTT-S Int. Microwave Symp. Digest*, 1994, Vol. I, pp. 249–252.
47. H. Matsumoto, T. Tsujiguchi, and T. Nishikawa, A miniaturized dielectric monoblock duplexer matched by the buried impedance transforming circuit, *IEEE MTT-S Int. Microwave Symp. Digest*, 1995, Vol. III, pp. 1539–1542.
48. H. -W. Yao, K. A. Zaki, A. E. Atia, and R. Hershtig, Full wave modeling of conducting posts in rectangular waveguides and its applications to slot coupled combline filters, *IEEE Trans. Microwave Theory Tech*. **MTT-43** (Part II):2823–2829 (Dec. 1995).
49. J.-F. Liang and W. D. Blair, High-Q TE01 mode DR filters for PCS wireless base stations, *IEEE Trans. Microwave Theory Tech*. **MTT-46** (Part II):2493–2500 (Dec. 1998).
50. T. Olsson, P. Anderson, U. Jordan, M. Lisak, V. Semenov, and M. Ahlander, Microwave breakdown in air-filled resonators, *IEEE MTT-S Int. Microwave Symp. Digest*, June 1999, Vol. 3, pp. 915–918.
51. C. Wang and K. A. Zaki, Temperature compensation of combline resonators and filters, *1999 IEEE MTT-S Int. Microwave Symp. Digest*, June 1999, Vol. 3, pp. 1041–1044.
52. C. Wang and K. A. Zaki, Analysis of power handling capacity of bandpass filters, *2001 IEEE MTT-S Int. Microwave Symp. Digest*, May 2001, Vol. 3, pp. 1611–1614.

# COMPLEX MEDIA

LE-WEI LI
WEN-YAN YIN
National University of Singapore
Kent Ridge, Singapore

## 1. CONSTITUTIVE RELATIONS

For most media, the general form of constitutive relations that account for multiple effects resulting from interaction between electromagnetic waves and media can be expressed by [1]

$$D_i = \varepsilon_{ij}E_j + \gamma_{ij}^{E}\partial_t E_j + \xi_{ijk}^{E}\Delta_j E_k + \beta_{ij}^{E}B_j + \alpha_{ij}^{E}\partial_t B_j + \eta_{ijk}^{E}\Delta_j B_k + \cdots \tag{1a}$$

$$H_i = \mu_{ij}^{-1}B_j + \gamma_{ij}^{B}\partial_t B_j + \eta_{ijk}^{B}\Delta_j B_k + \beta_{ij}^{B}E_j + \alpha_{ij}^{B}\partial_t E_j + \eta_{ijk}^{B}\Delta_j E_k + \cdots \tag{1b}$$

where $E_k$ and $H_i$ are the electric and magnetic field components; $D_i$ and $B_k$ are electric and magnetic induction components; and $\varepsilon_{ij}$, $\gamma_{ij}^{B}$, $\eta_{ijk}^{E}$, and so on are constitutive tensors of different ranks. The space $\Delta_j$ and time $\partial_t$ derivatives take into account spatial and temporal variations of the field.

For linear, stationary, and dispersive bianisotropic media in the frequency domain, their constitutive relations can be described by a set of equations as follows [2–25] ($e^{j\omega t}$):

$$\vec{D} = \varepsilon_0[\varepsilon(\omega)]\vec{E} + \sqrt{\mu_0\varepsilon_0}[\xi(\omega)]\vec{H} \tag{2a}$$

$$\vec{B} = \mu_0[\mu(\omega)]\vec{H} + \sqrt{\mu_0\varepsilon_0}[\eta(\omega)]\vec{E} \tag{2b}$$

where $\omega$ is the operating angular frequency; the tensors $[\varepsilon(\omega)]$, $[\mu(\omega)]$, $[\xi(\omega)]$ and $[\eta(\omega)]$ are the relative permittivity, permeability and magnetoelectric tensors, respectively. Apparently, Eqs. (2a) and (2b) are applicable for the constitutive description of electromagnetically anisotropic, biisotropic chiral, uniaxially, or biaxially bianisotropic media [26–45]. Therefore, Eqs. (2a), and (2b) can incorporate most practical applications of complex linear media used in RF engineering.

## 2. CLASSIFICATION OF BIANISOTROPIC[1] MEDIA

### 2.1. Continuous Groups of Symmetry (CGS)

In Eqs. (2a) and (2b), four constitutive tensors are usually described by a $3 \times 3$ matrix, respectively. However, according to the theory of continuous groups of symmetry (CGS) developed by Dmitriev [1,46–49], the number of independent elements in $[\varepsilon(\omega)]$, $[\mu(\omega)]$, $[\xi(\omega)]$ and $[\eta(\omega)]$ for a given bianisotropic medium is completely governed by a certain magnetic group of symmetry. From CGS theory, we can understand the four constitutive tensors if the CGS of medium is known. Typically, these tensors correspond to the following CGSs:

$$\begin{gathered} D_{4h}(D_{2d}),\ D_{4h}(D_{2h}),\ C_{4h}(S_4),\ C_{4h}(C_{2h}),\\ D_4(D_2),\ D_{2d}(S_4),\ D_{2d}(D_2),\ D_{2d}(C_{2v}),\\ C_{4v}(C_{2v}),\ D_{2h}(D_2),\ D_{2h}(C_{2h}),\\ D_{2h}(C_{2v}),\ S_4(C_2),\ C_4(C_2),\ D_2(C_2),\ C_{2h}(C_i),\\ C_{2h}(C_2),\ C_{2h}(C_s),\ C_{2v}(C_2),\\ C_{2v}(C_s),\ C_i(C_1),\ C_2(C_1),\ C_s(C_1) \end{gathered} \tag{3}$$

[1]The term *bianisotropic* denotes the property of being biisotropic and/or anisotropic.

The constitutive tensors for these 23 linear complex media are given as follows [1]:

$$1^\circ(D_{4h}(D_{2d})\colon N_\mathrm{f}=5)\colon [\varepsilon]=\begin{bmatrix}\varepsilon_{xx}&0&0\\0&\varepsilon_{xx}&0\\0&0&\varepsilon_{zz}\end{bmatrix},$$

$$[\mu]=\begin{bmatrix}\mu_{xx}&0&0\\0&\mu_{xx}&0\\0&0&\mu_{zz}\end{bmatrix} \tag{4a}$$

$$[\xi]=\begin{bmatrix}0&\xi_{xy}&0\\\xi_{xy}&0&0\\0&0&0\end{bmatrix},\quad [\eta]=[\xi]$$

$$2^\circ(D_{4h}(D_{2h})\colon N_\mathrm{f}=\mathbf{4})\colon [\varepsilon]=\begin{bmatrix}\varepsilon_{xx}&0&0\\0&\varepsilon_{xx}&0\\0&0&\varepsilon_{zz}\end{bmatrix},$$

$$[\mu]=\begin{bmatrix}\mu_{xx}&0&0\\0&\mu_{xx}&0\\0&0&\mu_{zz}\end{bmatrix} \tag{4b}$$

$$[\xi]=[\eta]=[0]$$

$$3^\circ(C_{4h}(S_4)\colon N_\mathrm{f}=\mathbf{6})\colon [\varepsilon]=\begin{bmatrix}\varepsilon_{xx}&0&0\\0&\varepsilon_{xx}&0\\0&0&\varepsilon_{zz}\end{bmatrix},$$

$$[\mu]=\begin{bmatrix}\mu_{xx}&0&0\\0&\mu_{xx}&0\\0&0&\mu_{zz}\end{bmatrix} \tag{4c}$$

$$[\xi]=\begin{bmatrix}\xi_{xx}&\xi_{xy}&0\\\xi_{xy}&-\xi_{xx}&0\\0&0&0\end{bmatrix},$$

$$[\eta]=[\xi]$$

$$4^\circ(C_{4h}(C_{2h})\colon N_\mathrm{f}=\mathbf{4})\colon [\varepsilon]=\begin{bmatrix}\varepsilon_{xx}&0&0\\0&\varepsilon_{xx}&0\\0&0&\varepsilon_{zz}\end{bmatrix},$$

$$[\mu]=\begin{bmatrix}\mu_{xx}&0&0\\0&\mu_{xx}&0\\0&0&\mu_{zz}\end{bmatrix} \tag{4d}$$

$$[\xi]=[\eta]=[0]$$

$$5^\circ(D_4(D_2)\colon N_\mathrm{f}=\mathbf{7})\colon [\varepsilon]=\begin{bmatrix}\varepsilon_{xx}&0&0\\0&\varepsilon_{xx}&0\\0&0&\varepsilon_{zz}\end{bmatrix},$$

$$[\mu]=\begin{bmatrix}\mu_{xx}&0&0\\0&\mu_{xx}&0\\0&0&\mu_{zz}\end{bmatrix} \tag{4e}$$

$$[\xi]=\begin{bmatrix}\xi_{xx}&0&0\\0&\xi_{yy}&0\\0&0&\xi_{zz}\end{bmatrix},$$

$$[\eta]=-[\xi]$$

$$6^\circ(D_{2d}(S_4)\colon N_\mathrm{f}=\mathbf{8})\colon [\varepsilon]=\begin{bmatrix}\varepsilon_{xx}&\varepsilon_{xy}&0\\-\varepsilon_{xy}&\varepsilon_{xx}&0\\0&0&\varepsilon_{zz}\end{bmatrix},$$

$$[\mu]=\begin{bmatrix}\mu_{xx}&\mu_{xy}&0\\-\mu_{xy}&\mu_{xx}&0\\0&0&\mu_{zz}\end{bmatrix} \tag{4f}$$

$$[\xi]=\begin{bmatrix}\xi_{xx}&\xi_{xy}&0\\\xi_{xy}&-\xi_{xx}&0\\0&0&0\end{bmatrix},$$

$$[\eta]=\begin{bmatrix}\xi_{xx}&-\xi_{xy}&0\\-\xi_{xy}&-\xi_{xx}&0\\0&0&0\end{bmatrix}$$

$$7^\circ(D_{2d}(D_2)\colon N_\mathrm{f}=\mathbf{6})\colon [\varepsilon]=\begin{bmatrix}\varepsilon_{xx}&0&0\\0&\varepsilon_{xx}&0\\0&0&\varepsilon_{zz}\end{bmatrix},\quad [\mu]=\begin{bmatrix}\mu_{xx}&0&0\\0&\mu_{xx}&0\\0&0&\mu_{zz}\end{bmatrix},\quad [\xi]=\begin{bmatrix}\xi_{xx}&0&0\\0&\xi_{xx}&0\\0&0&\xi_{zz}\end{bmatrix},\quad [\eta]=\begin{bmatrix}\xi_{xx}&0&0\\0&\xi_{xx}&0\\0&0&\xi_{zz}\end{bmatrix} \tag{4g}$$

$$8^\circ(D_{2d}(C_{2v})\colon N_\mathrm{f}=\mathbf{6})\colon [\varepsilon]=\begin{bmatrix}\varepsilon_{xx}&0&0\\0&\varepsilon_{xx}&0\\0&0&\varepsilon_{zz}\end{bmatrix},\quad [\mu]=\begin{bmatrix}\mu_{xx}&0&0\\0&\mu_{xx}&0\\0&0&\mu_{zz}\end{bmatrix},\quad [\xi]=\begin{bmatrix}0&\xi_{xy}&0\\\xi_{yx}&0&0\\0&0&0\end{bmatrix},\quad [\eta]=-[\xi] \tag{4h}$$

$$9^\circ(C_{4v}(C_{2v})\colon N_\mathrm{f}=\mathbf{6})\colon [\varepsilon]=\begin{bmatrix}\varepsilon_{xx}&0&0\\0&\varepsilon_{xx}&0\\0&0&\varepsilon_{zz}\end{bmatrix},\quad [\mu]=\begin{bmatrix}\mu_{xx}&0&0\\0&\mu_{xx}&0\\0&0&\mu_{zz}\end{bmatrix},\quad [\xi]=\begin{bmatrix}0&\xi_{xy}&0\\\xi_{yx}&0&0\\0&0&0\end{bmatrix},\quad [\eta]=[\xi] \tag{4i}$$

$$10^\circ(D_{2h}(D_2)\colon N_\mathrm{f}=\mathbf{9})\colon [\varepsilon]=\begin{bmatrix}\varepsilon_{xx}&0&0\\0&\varepsilon_{yy}&0\\0&0&\varepsilon_{zz}\end{bmatrix},\quad [\mu]=\begin{bmatrix}\mu_{xx}&0&0\\0&\mu_{yy}&0\\0&0&\mu_{zz}\end{bmatrix},\quad [\xi]=\begin{bmatrix}\xi_{xx}&0&0\\0&\xi_{yy}&0\\0&0&\xi_{zz}\end{bmatrix},\quad [\eta]=[\xi] \tag{4j}$$

$$11^\circ(D_{2h}(C_{2h})\colon N_\mathrm{f}=\mathbf{8})\colon [\varepsilon]=\begin{bmatrix}\varepsilon_{xx}&\varepsilon_{xy}&0\\-\varepsilon_{xy}&\varepsilon_{yy}&0\\0&0&\varepsilon_{zz}\end{bmatrix},\quad [\mu]=\begin{bmatrix}\mu_{xx}&\mu_{xy}&0\\-\mu_{xy}&\mu_{yy}&0\\0&0&\mu_{zz}\end{bmatrix},\quad [\xi]=[\eta]=[0] \tag{4k}$$

$$12^\circ(D_{2h}(C_{2v})\colon N_\mathrm{f}=\mathbf{8})\colon [\varepsilon]=\begin{bmatrix}\varepsilon_{xx}&0&0\\0&\varepsilon_{yy}&0\\0&0&\varepsilon_{zz}\end{bmatrix},\quad [\mu]=\begin{bmatrix}\mu_{xx}&0&0\\0&\mu_{yy}&0\\0&0&\mu_{zz}\end{bmatrix},\quad [\xi]=\begin{bmatrix}0&\xi_{xy}&0\\\xi_{yx}&0&0\\0&0&0\end{bmatrix},\quad [\eta]=\begin{bmatrix}0&\xi_{yx}&0\\\xi_{xy}&0&0\\0&0&0\end{bmatrix} \tag{4l}$$

$$13^\circ(S_4(C_2)\text{: } N_\mathrm{f}=\mathbf{9})\text{: } [\varepsilon]=\begin{bmatrix}\varepsilon_{xx} & 0 & 0\\ 0 & \varepsilon_{xx} & 0\\ 0 & 0 & \varepsilon_{zz}\end{bmatrix},$$

$$[\mu]=\begin{bmatrix}\mu_{xx} & 0 & 0\\ 0 & \mu_{xx} & 0\\ 0 & 0 & \mu_{zz}\end{bmatrix}$$

$$[\xi]=\begin{bmatrix}\xi_{xx} & \xi_{xy} & 0\\ \xi_{yx} & \xi_{yy} & 0\\ 0 & 0 & \xi_{zz}\end{bmatrix}, \tag{4m}$$

$$[\eta]=\begin{bmatrix}\xi_{yy} & -\xi_{xy} & 0\\ -\xi_{yx} & \xi_{xx} & 0\\ 0 & 0 & \xi_{zz}\end{bmatrix}$$

$$14^\circ(C_4(C_2)\text{: } N_\mathrm{f}=\mathbf{9})\text{: } [\varepsilon]=\begin{bmatrix}\varepsilon_{xx} & 0 & 0\\ 0 & \varepsilon_{xx} & 0\\ 0 & 0 & \varepsilon_{zz}\end{bmatrix},$$

$$[\mu]=\begin{bmatrix}\mu_{xx} & 0 & 0\\ 0 & \mu_{xx} & 0\\ 0 & 0 & \mu_{zz}\end{bmatrix}$$

$$[\xi]=\begin{bmatrix}\xi_{xx} & \xi_{xy} & 0\\ \xi_{yx} & \xi_{yy} & 0\\ 0 & 0 & \xi_{zz}\end{bmatrix}, \tag{4n}$$

$$[\eta]=\begin{bmatrix}-\xi_{yy} & \xi_{xy} & 0\\ \xi_{yx} & -\xi_{xx} & 0\\ 0 & 0 & -\xi_{zz}\end{bmatrix}$$

$$15^\circ(D_2(C_2)\text{: } N_\mathrm{f}=\mathbf{13})\text{: } [\varepsilon]=\begin{bmatrix}\varepsilon_{xx} & \varepsilon_{xy} & 0\\ -\varepsilon_{xy} & \varepsilon_{yy} & 0\\ 0 & 0 & \varepsilon_{zz}\end{bmatrix},$$

$$[\mu]=\begin{bmatrix}\mu_{xx} & \mu_{xy} & 0\\ -\mu_{xy} & \mu_{yy} & 0\\ 0 & 0 & \mu_{zz}\end{bmatrix}$$

$$[\xi]=\begin{bmatrix}\xi_{xx} & \xi_{xy} & 0\\ \xi_{yx} & \xi_{yy} & 0\\ 0 & 0 & \xi_{zz}\end{bmatrix}, \tag{4o}$$

$$[\eta]=\begin{bmatrix}-\xi_{xx} & \xi_{yx} & 0\\ \xi_{xy} & -\xi_{yy} & 0\\ 0 & 0 & -\xi_{zz}\end{bmatrix}$$

$$16^\circ(C_{2h}(C_i)\text{: } N_\mathrm{f}=\mathbf{12})\text{: } [\varepsilon]=\begin{bmatrix}\varepsilon_{xx} & \varepsilon_{xy} & \varepsilon_{xz}\\ \varepsilon_{xy} & \varepsilon_{yy} & \varepsilon_{yz}\\ -\varepsilon_{xz} & -\varepsilon_{yz} & \varepsilon_{zz}\end{bmatrix},$$

$$[\mu]=\begin{bmatrix}\mu_{xx} & \mu_{xy} & \mu_{xz}\\ \mu_{xy} & \mu_{yy} & \mu_{yz}\\ -\mu_{xz} & -\mu_{yz} & \mu_{zz}\end{bmatrix} \tag{4p}$$

$$[\xi]=[\eta]=[0]$$

$$17^\circ(C_{2h}(C_2)\text{: } N_\mathrm{f}=\mathbf{13})\text{: } [\varepsilon]=\begin{bmatrix}\varepsilon_{xx} & \varepsilon_{xy} & 0\\ \varepsilon_{xy} & \varepsilon_{yy} & 0\\ 0 & 0 & \varepsilon_{zz}\end{bmatrix},$$

$$[\mu]=\begin{bmatrix}\mu_{xx} & \mu_{xy} & 0\\ \mu_{xy} & \mu_{yy} & 0\\ 0 & 0 & \mu_{zz}\end{bmatrix}$$

$$[\xi]=\begin{bmatrix}\xi_{xx} & \xi_{xy} & 0\\ \xi_{yx} & \xi_{yy} & 0\\ 0 & 0 & \xi_{zz}\end{bmatrix}, \tag{4q}$$

$$[\eta]=\begin{bmatrix}\xi_{xx} & \xi_{yx} & 0\\ \xi_{xy} & \xi_{yy} & 0\\ 0 & 0 & \xi_{zz}\end{bmatrix}$$

$18^\circ(C_{2h}(C_s)\text{: } N_\mathrm{f} = \mathbf{12})\text{: } [\varepsilon] = \begin{bmatrix} \varepsilon_{xx} & \varepsilon_{xy} & 0 \\ \varepsilon_{xy} & \varepsilon_{yy} & 0 \\ 0 & 0 & \varepsilon_{zz} \end{bmatrix},$

$$[\mu] = \begin{bmatrix} \mu_{xx} & \mu_{xy} & 0 \\ \mu_{xy} & \mu_{yy} & 0 \\ 0 & 0 & \mu_{zz} \end{bmatrix} \tag{4r}$$

$$[\xi] = \begin{bmatrix} 0 & 0 & \xi_{xz} \\ 0 & 0 & \xi_{yz} \\ \xi_{zx} & \xi_{zy} & 0 \end{bmatrix},$$

$$[\eta] = \begin{bmatrix} 0 & 0 & \xi_{zx} \\ 0 & 0 & \xi_{zy} \\ \xi_{xz} & \xi_{yz} & 0 \end{bmatrix}$$

$19^\circ(C_{2v}(C_2)\text{: } N_\mathrm{f} = \mathbf{13})\text{: } [\varepsilon] = \begin{bmatrix} \varepsilon_{xx} & \varepsilon_{xy} & 0 \\ -\varepsilon_{xy} & \varepsilon_{yy} & 0 \\ 0 & 0 & \varepsilon_{zz} \end{bmatrix},$

$$[\mu] = \begin{bmatrix} \mu_{xx} & \mu_{xy} & 0 \\ -\mu_{xy} & \mu_{yy} & 0 \\ 0 & 0 & \mu_{zz} \end{bmatrix} \tag{4s}$$

$$[\xi] = \begin{bmatrix} \xi_{xx} & \xi_{xy} & 0 \\ \xi_{yx} & \xi_{yy} & 0 \\ 0 & 0 & \xi_{zz} \end{bmatrix},$$

$$[\eta] = \begin{bmatrix} \xi_{xx} & -\xi_{yx} & 0 \\ -\xi_{xy} & \xi_{yy} & 0 \\ 0 & 0 & \xi_{zz} \end{bmatrix}$$

$20^\circ(C_{2v}(C_s)\text{: } N_\mathrm{f} = \mathbf{12})\text{: } [\varepsilon] = \begin{bmatrix} \varepsilon_{xx} & 0 & 0 \\ 0 & \varepsilon_{yy} & \varepsilon_{yz} \\ 0 & -\varepsilon_{yz} & \varepsilon_{zz} \end{bmatrix},$

$$[\mu] = \begin{bmatrix} \mu_{xx} & 0 & 0 \\ 0 & \mu_{yy} & \mu_{yz} \\ 0 & -\mu_{yz} & \mu_{zz} \end{bmatrix} \tag{4t}$$

$$[\xi] = \begin{bmatrix} 0 & \xi_{xy} & \xi_{xz} \\ \xi_{yx} & 0 & 0 \\ \xi_{zx} & 0 & 0 \end{bmatrix},$$

$$[\eta] = \begin{bmatrix} 0 & -\xi_{yx} & \xi_{zx} \\ -\xi_{xy} & 0 & 0 \\ \xi_{xz} & 0 & 0 \end{bmatrix}$$

$21^\circ(C_i(C_1)\text{: } N_\mathrm{f} = \mathbf{21})\text{: } [\varepsilon] = \begin{bmatrix} \varepsilon_{xx} & \varepsilon_{xy} & \varepsilon_{xz} \\ \varepsilon_{xy} & \varepsilon_{yy} & \varepsilon_{yz} \\ \varepsilon_{xz} & \varepsilon_{yz} & \varepsilon_{zz} \end{bmatrix},$

$$[\mu] = \begin{bmatrix} \mu_{xx} & \mu_{xy} & \mu_{xz} \\ \mu_{xy} & \mu_{yy} & \mu_{yz} \\ \mu_{xz} & \mu_{yz} & \mu_{zz} \end{bmatrix} \tag{4u}$$

$$[\xi] = \begin{bmatrix} \xi_{xx} & \xi_{xy} & \xi_{xz} \\ \xi_{yx} & \xi_{yy} & \xi_{yz} \\ \xi_{zx} & \xi_{zy} & \xi_{zz} \end{bmatrix},$$

$$[\eta] = \begin{bmatrix} \xi_{xx} & \xi_{yx} & \xi_{zx} \\ \xi_{xy} & \xi_{yy} & \xi_{zy} \\ \xi_{xz} & \xi_{yz} & \xi_{zz} \end{bmatrix}$$

$$22^{\circ}(C_2(C_1)\text{: } N_{\mathrm{f}}=\mathbf{21})\text{: } [\varepsilon]=\begin{bmatrix} \varepsilon_{xx} & \varepsilon_{xy} & \varepsilon_{xz} \\ \varepsilon_{xy} & \varepsilon_{yy} & \varepsilon_{yz} \\ -\varepsilon_{xz} & -\varepsilon_{yz} & \varepsilon_{zz} \end{bmatrix},$$

$$[\mu]=\begin{bmatrix} \mu_{xx} & \mu_{xy} & \mu_{xz} \\ \mu_{xy} & \mu_{yy} & \mu_{yz} \\ -\mu_{xz} & -\mu_{yz} & \mu_{zz} \end{bmatrix} \tag{4v}$$

$$[\xi]=\begin{bmatrix} \xi_{xx} & \xi_{xy} & \xi_{xz} \\ \xi_{yx} & \xi_{yy} & \xi_{yz} \\ \xi_{zx} & \xi_{zy} & \xi_{zz} \end{bmatrix},$$

$$[\eta]=\begin{bmatrix} -\xi_{xx} & -\xi_{yx} & \xi_{zx} \\ -\xi_{xy} & -\xi_{yy} & \xi_{zy} \\ \xi_{xz} & \xi_{yz} & -\xi_{zz} \end{bmatrix}$$

$$23^{\circ}(C_{\mathrm{s}}(C_1)\text{: } N_{\mathrm{f}}=\mathbf{21})\text{: } [\varepsilon]=\begin{bmatrix} \varepsilon_{xx} & \varepsilon_{xy} & \varepsilon_{xz} \\ \varepsilon_{xy} & \varepsilon_{yy} & \varepsilon_{yz} \\ -\varepsilon_{xz} & -\varepsilon_{yz} & \varepsilon_{zz} \end{bmatrix},$$

$$[\mu]=\begin{bmatrix} \mu_{xx} & \mu_{xy} & \mu_{xz} \\ \mu_{xy} & \mu_{yy} & \mu_{yz} \\ -\mu_{xz} & -\mu_{yz} & \mu_{zz} \end{bmatrix} \tag{4w}$$

$$[\xi]=\begin{bmatrix} \xi_{xx} & \xi_{xy} & \xi_{xz} \\ \xi_{yx} & \xi_{yy} & \xi_{yz} \\ \xi_{zx} & \xi_{zy} & \xi_{zz} \end{bmatrix},$$

$$[\eta]=\begin{bmatrix} \xi_{xx} & \xi_{yx} & -\xi_{zx} \\ \xi_{xy} & \xi_{yy} & -\xi_{zy} \\ -\xi_{xz} & -\xi_{yz} & \xi_{zz} \end{bmatrix}$$

It is obvious that the constitutive features of normal uniaxially anisotropic media such as microwave laminates can be represented by the CGSs of $C_{4h}(C_{2h})$ or $D_{4h}(D_{2h})$. Uniaxially bianisotroic media, such as chiroomega media, can be described by $D_{2d}(C_{2v})$ or $C_{4v}(C_{2v})$. For gyroelectric and gyromagnetic anisotropic media, their constitutive features can be represented by $D_{2h}(C_{2h})$. On the other hand, it should be pointed out that in these constitutive tenors, each element could be the function of operating frequency, or even a complex quantity. The interaction features of electromagnetic waves with various composite bianisotropic structures can be found in the literature [50–54]. The constitutive tensors of some CGSs of bianisotropic media are described in detail below.

### 2.2. Ferroelectric Materials [55–57]

Ferroelectric thin films can be used as the substrate or superstrate of various microstrip- or coplanar-waveguide-based microwave devices (Fig. 1) that possess certain tunabilities in their electromagnetic features. When the crystalline principal axes of the ferroelectric film are oriented in the coordinate directions, the film is reduced to the simplified case of the CGS described above, namely, $D_{2h}(C_{2v})$ and $[\mu]=\mu_0\,\bar{\bar{I}}$, $\xi_{xy}=\xi_{yx}=0$. The film's permittivity tensor $\lfloor \varepsilon_{\mathrm{f}} \rfloor$ in the unbiased condition, the biasing electric field $\vec{E}_{\mathrm{bias}}=0$, can be expressed by

$$[\varepsilon_{\mathrm{f}}(0)]=\begin{bmatrix} \varepsilon_{xx}(0) & 0 & 0 \\ 0 & \varepsilon_{yy}(0) & 0 \\ 0 & 0 & \varepsilon_{zz}(0) \end{bmatrix} \tag{5}$$

When the biasing DC electric field is applied, $\lfloor \varepsilon_{\mathrm{f}} \rfloor$ becomes

$$[\varepsilon_{\mathrm{f}}(\vec{E}_{\mathrm{bias}})]=\begin{bmatrix} \varepsilon_{xx}(\vec{E}_{\mathrm{bias}}) & 0 & 0 \\ 0 & \varepsilon_{yy}(\vec{E}_{\mathrm{bias}}) & 0 \\ 0 & 0 & \varepsilon_{zz}(\vec{E}_{\mathrm{bias}}) \end{bmatrix} \tag{6}$$

Here, each element $[\varepsilon_{\mathrm{f}}(\vec{E}_{\mathrm{bias}})]$ can be a function of each of the three bias field components $E_{x,y,z,\mathrm{bias}}$. If we assume, for simplicity, diagonal functional projection of the bias field components onto the permittivity tensor $\lfloor \varepsilon_{\mathrm{f}} \rfloor$ elements, then we have

$$[\varepsilon_{\mathrm{f}}(\vec{E}_{\mathrm{bias}})]=\begin{bmatrix} \varepsilon_{xx}(E_{x,\mathrm{bias}}) & 0 & 0 \\ 0 & \varepsilon_{yy}(E_{y,\mathrm{bias}}) & 0 \\ 0 & 0 & \varepsilon_{zz}(E_{z,\mathrm{bias}}) \end{bmatrix} \tag{7}$$

Using the hexagonal perovskite crystalline form for $Ba_xSr_{1-x}TiO_3$ (BSTO) thin film, with the $c$ axis parallel to the $y$ axis and having properties different from those in the $a$- and $b$-axis directions parallel to the $xz$ plane and having the same effects, $\lfloor \varepsilon_{\mathrm{f}} \rfloor$ takes an uniaxial form as

$$[\varepsilon_{\mathrm{f}}(0)]=\begin{bmatrix} \varepsilon_{xx}(0) & 0 & 0 \\ 0 & \varepsilon_{yy}(0) & 0 \\ 0 & 0 & \varepsilon_{xx}(0) \end{bmatrix} \tag{8}$$

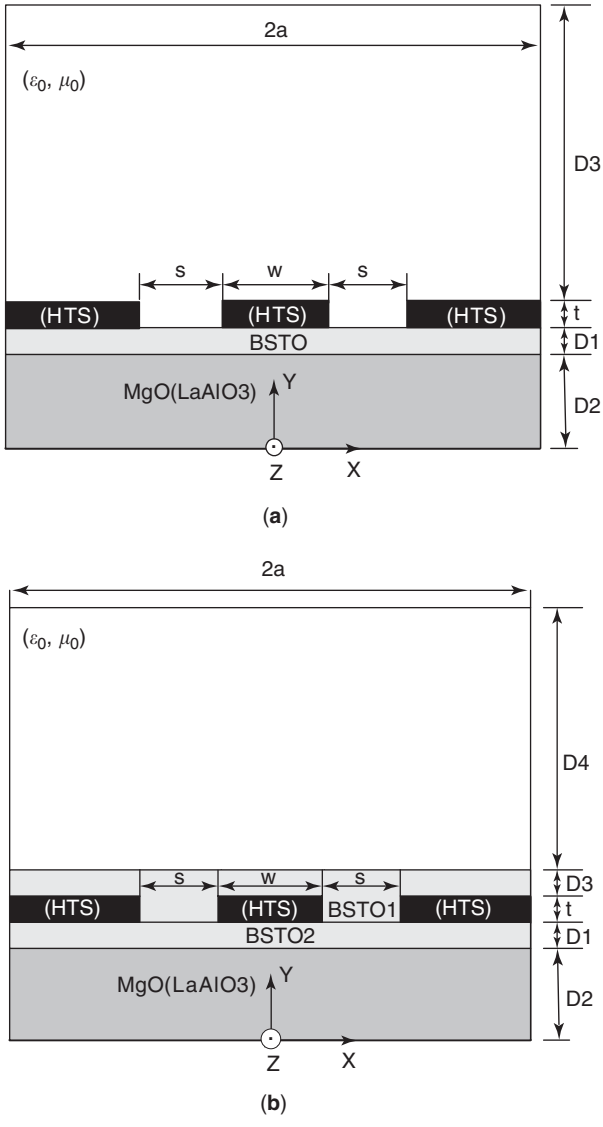


**Figure 1.** Cross-sectional views of two composite ferroelectric coplanar waveguides: (a) BSTO substrate; (b) BSTO superstrate-substrate.

In the case of $E_{\text{bias}} = E_x$, the ferroelectric effect renders $\lfloor \varepsilon_f \rfloor$ as

$$[\varepsilon_f(E_{\text{bias}})] = \begin{bmatrix} \varepsilon_{xx}(E_{x,\text{bias}}) & 0 & 0 \\ 0 & \varepsilon_{yy}(0) & 0 \\ 0 & 0 & \varepsilon_{xx}(0) \end{bmatrix} \tag{9}$$

and $\lfloor \varepsilon_f(E_{\text{bias}}) \rfloor$ is biaxial.

It is understood that, as a rule, the losses in ferroelectrics decreases with decreasing temperature. So, after the discovery of high-temperature superconductivity (HTS), much effort has been devoted to combining HTS with ferroelectrics to realize the tunability of microwave devices in a low-loss situations. The modified microstrip structure in Fig. 1 consists of a dielectric substrate (LAO or MgO, typically 254 μm thick), a ferroelectric thin-film layer with thickness ranging from 300 to 2000 nm for various applications, and a gold or YBCO thin film of 0.35 or 2 μm thick for the top strip, respectively.

On the other hand, in order to achieve the desired propagation characteristics of a ferroelectric microstrip line or coplanar waveguide, an additional ferrite layer can also be introduced in the substrate or superstrate–substrate structures presented above.

### 2.3. Sapphire

A nonmagnetic sapphire is also very important for high-frequency applications, and its relative permittivity tensor can be expressed by

$$[\varepsilon] = \begin{bmatrix} \varepsilon_{xx} & \varepsilon_{xy} & 0 \\ \varepsilon_{yx} & \varepsilon_{yy} & 0 \\ 0 & 0 & \varepsilon_{zz} \end{bmatrix} \tag{10a}$$

$$\varepsilon_{xx} = \varepsilon_x(T)\cos^2\theta_\varepsilon + \varepsilon_y(T)\sin^2\theta_\varepsilon$$

$$\varepsilon_{xy} = \varepsilon_{yx}(T) = [\varepsilon_y(T) - \varepsilon_x(T)]\sin\theta_\varepsilon\cos\theta_\varepsilon$$

$$\varepsilon_{yy} = \varepsilon_x(T)\sin^2\theta_\varepsilon + \varepsilon_y(T)\cos^2\theta_\varepsilon, \varepsilon_{zz} = \varepsilon_z(T) \tag{10b}$$

where $\theta_\varepsilon$ ($0^\circ \le \theta_\varepsilon \le 360^\circ$) is the misalignment angle between the coordinates of the line and principal axes of $\lfloor \varepsilon \rfloor$ with respect to the $x$ direction in $x$–$y$ plane, $\varepsilon_{x,y,z}(T)$ are the three principal-axis permittivities, and $T$ is the operating temperature of sapphire.

### 2.4. Gyroelectric Media [58–61]

A great deal of attention has been paid to the microwave propagation in gyroelectric or solid-state magnetoplasmas in the past a few decades, since this type of medium ($\lfloor \xi \rfloor = \lfloor \eta \rfloor = 0$) can be used to make various nonreciprocal devices for microwave and millimeter-wave applications, such as gyroelectric waveguides and planar microstrip transmission lines, as shown in Figs. 2a–2d. These models provide a basis for further developing planar integrated nonreciprocal devices, where the bulk gyroelectric media present the advantage of a very good coupling between the wave and the media. So, owing to the good mobility of the media, the losses are reduced.

In Fig. 2a, the longitudinal DC magnetic field is along the $z$-axis direction. On the other hand, if the DC magnetic field is wrapped around the $z$ axis into a cylindrical shape, it forms an azimuthally magnetized solid-state plasma-filled coaxial waveguide that can support the cylindrically symmetric $TM_{01}$ mode, and the corresponding permittivity tensor can be written as [61]

$$[\varepsilon] = \begin{bmatrix} \varepsilon_{xx} & 0 & \varepsilon_{xz} \\ 0 & \varepsilon_{yy} & 0 \\ -\varepsilon_{xz} & 0 & \varepsilon_{xx} \end{bmatrix} \tag{11}$$

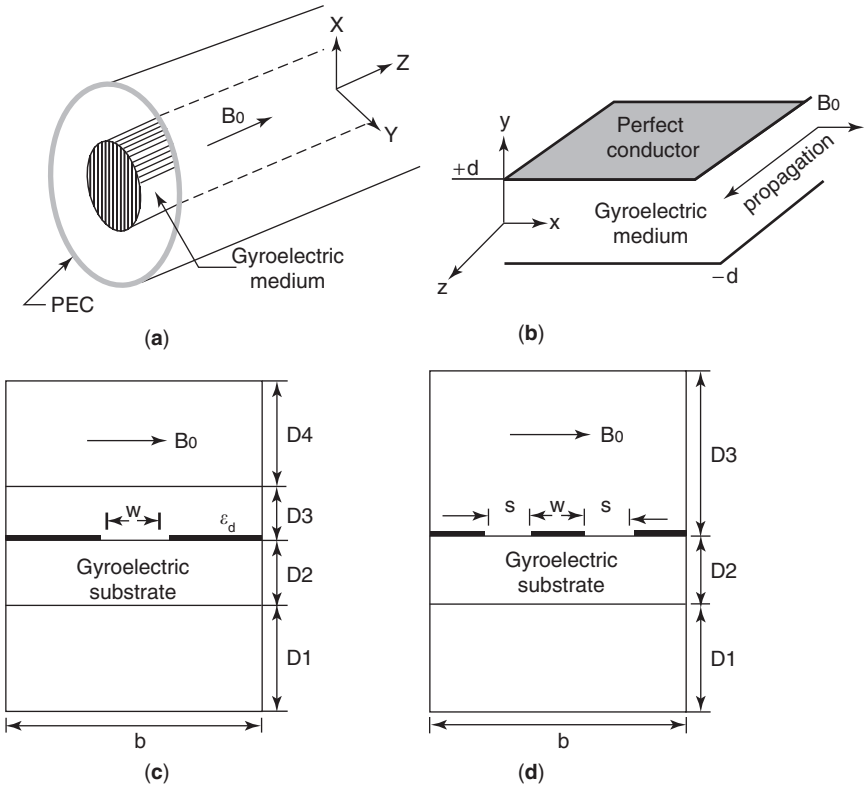


**Figure 2.** Schematic diagrams of gyroelectric waveguides and planar transmission lines: (a) circular; (b) planar; (c) slotline; (d) coplanar waveguide.

In Fig. 2b, there is a transversely magnetized plasma between two perfectly conducting parallel plates separated by a distance $2d$, where the static magnetic field is applied in the $x$ direction and wave propagation is in the $z$ direction. If the plasma is magnetized in the $y$ direction, normal to the conducting plates, the modes are not, in general, separable into TE and TM modes. Here the relative permittivity tensor can be written in the form

$$[\varepsilon] = \begin{bmatrix} \varepsilon_{xx} & 0 & 0 \\ 0 & \varepsilon_{yy} & \varepsilon_{yz} \\ 0 & -\varepsilon_{yz} & \varepsilon_{zz} \end{bmatrix} \tag{12}$$

where each element in (12) is given in Ref. 61. Figure 2c shows a suspended single-slotline structure and Fig. 2d, a suspended coplanar waveguide.

When the biasing DC magnetic field $\vec{B}_0$ of the solid-state plasma in Fig. 2 is in an arbitrary direction $(\varphi_0,\theta_0)$, its permittivity tensor can be described by $(e^{j\omega t})$

$$[\varepsilon(\omega)] = \begin{bmatrix} \varepsilon_{xx}(\omega) & \varepsilon_{xy}(\omega) & \varepsilon_{xz}(\omega) \\ \varepsilon_{yx}(\omega) & \varepsilon_{yy}(\omega) & \varepsilon_{yz}(\omega) \\ \varepsilon_{zx}(\omega) & \varepsilon_{zy}(\omega) & \varepsilon_{zz}(\omega) \end{bmatrix} \tag{13a}$$

$$\begin{aligned}
\varepsilon_{xx}(\omega) &= \varepsilon_1(\omega) + [\varepsilon_2(\omega) - \varepsilon_1(\omega)] \sin^2 \nu \cos^2 \psi \\
\varepsilon_{xy}(\omega) &= -jg(\omega) \cos \nu + [\varepsilon_2(\omega) - \varepsilon_1(\omega)] \sin \psi \cos \psi \sin^2 \nu \\
\varepsilon_{xz}(\omega) &= \{jg(\omega) \sin \psi + [\varepsilon_2(\omega) - \varepsilon_1(\omega)] \cos \psi \cos \nu\} \sin \nu \\
\varepsilon_{yx}(\omega) &= jg(\omega) \cos \nu + [\varepsilon_2(\omega) - \varepsilon_1(\omega)] \sin \psi \cos \psi \sin^2 \nu \\
\varepsilon_{yy}(\omega) &= \varepsilon_1(\omega) + [\varepsilon_2(\omega) - \varepsilon_1(\omega)] \sin^2 \nu \sin^2 \psi \\
\varepsilon_{yz}(\omega) &= \{-jg(\omega) \cos \psi + [\varepsilon_2(\omega) - \varepsilon_1(\omega)] \sin \psi \cos \nu\} \sin \nu \\
\varepsilon_{zx}(\omega) &= \{-jg(\omega) \sin \psi + [\varepsilon_2(\omega) - \varepsilon_1(\omega)] \cos \psi \cos \nu\} \sin \nu \\
\varepsilon_{zy}(\omega) &= \{jg \cos \psi + [\varepsilon_2(\omega) - \varepsilon_1(\omega)] \sin \psi \cos \nu\} \sin \nu \\
\varepsilon_{zz}(\omega) &= \varepsilon_1(\omega) \sin^2 \nu + \varepsilon_2(\omega) \cos^2 \nu
\end{aligned} \tag{13b}$$

In (13b), two consecutive rotations of angles $\psi$ and $\nu$ are determined by the spherical angles $\varphi_0$ and $\theta_0$ by

$$\cos \psi = \frac{\sin \theta_0 \cos \varphi_0}{\sqrt{(\sin^2 \theta_0 \cos^2 \varphi_0 + \cos^2 \theta_0)}} \tag{13c}$$

$$\cos \nu = \sin \theta_0 \sin \varphi_0 \tag{13d}$$

$$\varepsilon_1(\omega) = \varepsilon_s - \frac{\omega_p^2(\omega - j\tau^{-1})}{\omega\varepsilon_0[(\omega - j\tau^{-1})^2 - \omega_c^2]} \tag{13e}$$

$$\varepsilon_2(\omega) = \varepsilon_s - \frac{\omega_p^2}{\omega\varepsilon_0(\omega - j\tau^{-1})} \tag{13f}$$

$$g(\omega) = -\frac{\omega_p^2\omega_c}{\omega\varepsilon_0[(\omega - j\tau^{-1})^2 - \omega_c^2]} \tag{13g}$$

where $\omega_p = \sqrt{(ne^2/\varepsilon_0 m^*)}$ represents the plasma frequency; $\omega_c = eB_0/m^*$, the cyclotron frequency; $n$, the carrier concentration; $e$, the electron charge; $m^*$, the electron effective mass (kg) (i.e., $0.067\,m_e$ for GaAs); $m_e$, the electron rest mass; $B_0$, the DC magnetizing field; $\varphi$, the orientation angle of $B_0$ in the $x$–$y$ plane; $\tau$, the momentum relaxation time of the semiconductor material; and $\varepsilon_s$, the relative dielectric permittivity of the semiconductor.

### 2.5. Ferrites

Ferrites have been widely used as important elements in microwave and millimeter-wave devices, such as phase shifters, resonance isolators, circulators, and superstrates or substrates of microwave integrated circuits (MICs). One of the main advantages of using magnetized ferrites is that their characteristic parameters, as in Fig. 2, can be controlled by adjusting an applied DC magnetic bias field. Hence, various tunable microwave devices can also be designed when we combine ferrites with other materials, as shown in Fig. 3.

In Fig. 3b [62], a high-temperature superconductor (HTS) strip (2) of a width $W$ is located on top of the dielectric substrate (1) and separated by a dielectric layer (3) from an epitaxial ferrite film (4) deposited on a dielectric substrate (5). The structure may contain either an HTS or metal bottom electrode (0), the microstrip resonator, or two HTS electrodes (Fig. 2a), placed at a distance $W_1$ from each other, the CPW resonator. The thickness of the HTS electrodes (2), ferrite layer (4), bottom electrode (0), and dielectric layers (1), (3), and (5) are $t$, $t_f$, $t_0$ and $t_1$, $t_3$, $t_5$, respectively. An external DC biasing magnetic field $H_e$ is applied parallel to the plane of the structure and makes an angle $\phi$ with the central stripline direction.

When the biasing DC magnetic field $\bar{B}_0$ takes an arbitrary orientation ($\varphi_0$,$\theta_0$), the permeability tensor $[\mu(\omega)]$ of ferrites can be written as [34]

$$[\mu(\omega)] = \begin{bmatrix} \mu_{xx}(\omega) & \mu_{xy}(\omega) & \mu_{xz}(\omega) \\ \mu_{yx}(\omega) & \mu_{yy}(\omega) & \mu_{yz}(\omega) \\ \mu_{zx}(\omega) & \mu_{zy}(\omega) & \mu_{zz}(\omega) \end{bmatrix} \tag{14a}$$

$$\mu_{xx}(\omega) = \mu(\omega) + [1 - \mu(\omega)]\sin^2\theta_0\cos^2\varphi_0$$

$$\mu_{xy}(\omega) = [1 - \mu(\omega)]\sin\varphi_0\cos\varphi_0\sin^2\theta_0 - j\kappa\cos\theta_0$$

$$\mu_{xz}(\omega) = j\kappa\sin\varphi_0\sin\theta_0 + [1 - \mu(\omega)]\sin\theta_0\cos\theta_0\cos\varphi_0$$

$$\mu_{yx}(\omega) = [1 - \mu(\omega)]\sin\varphi_0\cos\varphi_0 \times \sin^2\theta_0 + j\kappa\cos\theta_0$$

$$\mu_{yy}(\omega) = \mu(\omega) + [1 - \mu(\omega)]\sin^2\theta_0\sin^2\varphi_0$$

$$\mu_{yz}(\omega) = -j\kappa\cos\varphi_0\sin\theta_0 + [1 - \mu(\omega)]\sin\theta_0\cos\theta_0\sin\varphi_0$$

$$\mu_{zx}(\omega) = -j\kappa\sin\varphi_0\sin\theta_0 + [1 - \mu(\omega)]\sin\theta_0\cos\theta_0\cos\varphi_0$$

$$\mu_{zy}(\omega) = j\kappa\cos\varphi_0\sin\theta_0 + [1 - \mu(\omega)]\sin\theta_0\cos\theta_0\sin\varphi_0$$

$$\mu_{zz}(\omega) = 1 - [1 - \mu(\omega)]\sin^2\theta_0$$

$$\mu(\omega) = \mu_1(\omega) - j\mu_2(\omega) \tag{14b}$$

$$\mu_1(\omega) = 1 + \frac{\omega_0\omega_m[\omega_0^2 - \omega^2(1 - \alpha_m^2)]}{F_m}$$

$$\mu_2(\omega) = \frac{\omega\omega_m\alpha_m[\omega_0^2 + \omega^2(1 + \alpha_m^2)]}{F_m}$$

$$\kappa(\omega) = \kappa_1(\omega) - j\kappa_2(\omega)$$

$$\kappa_1(\omega) = -\frac{\omega\omega_m[\omega_0^2 - \omega^2(1 + \alpha_m^2)]}{F_m}$$

$$\kappa_2 = -\frac{2\omega_m\omega_0\alpha_m\omega^2}{F_m}$$

$$F_m = [\omega_0^2 - \omega^2(1 + \alpha_m^2)]^2 + 4(\omega\omega_0\alpha_m)^2$$

where $\omega = |\gamma|H_0$, $\omega_m = |\gamma|M_s$, $M_s$ is the saturation magnetization of the ferrite, $\gamma$ denotes to the gyromagnetic ratio ($= -2.21 \times 10^5\,\text{rad}\cdot\text{m/C}$), $\alpha_m$ identifies the Landau damping coefficient, and the loss is taken into account.

### 2.6. Biisotropic Chiral Medium

Since the early 1990s many researchers have explored the diverse chirality effects in biisotropic chiral media on electromagnetic wave propagation, radiation, and scattering. Electromagnetic waves in chiral media show some very interesting features, such as optical rotatory dispersion (ORD), which causes the rotation of polarization; and circular dichroism, due to the different absorption coefficients of right- and left-handed circularly polarized waves. Some component models using chiral media have been proposed, such as chirowaveguides, chirolens, chirodomes, chirostrip antennas, chiral resonators, and chiral-mode transformers [63–83].

The constitutive equation for biisotropic chiral media can be easily obtained from Eqs. (2a) and (2b), as follows

$$\vec{D} = \varepsilon_0\varepsilon_r\vec{E} + \sqrt{\mu_0\varepsilon_0}\xi\vec{H} \tag{15a}$$

$$\vec{B} = \mu_0\mu_r H + \sqrt{\mu_0\varepsilon_0}\eta\vec{E} \tag{15b}$$

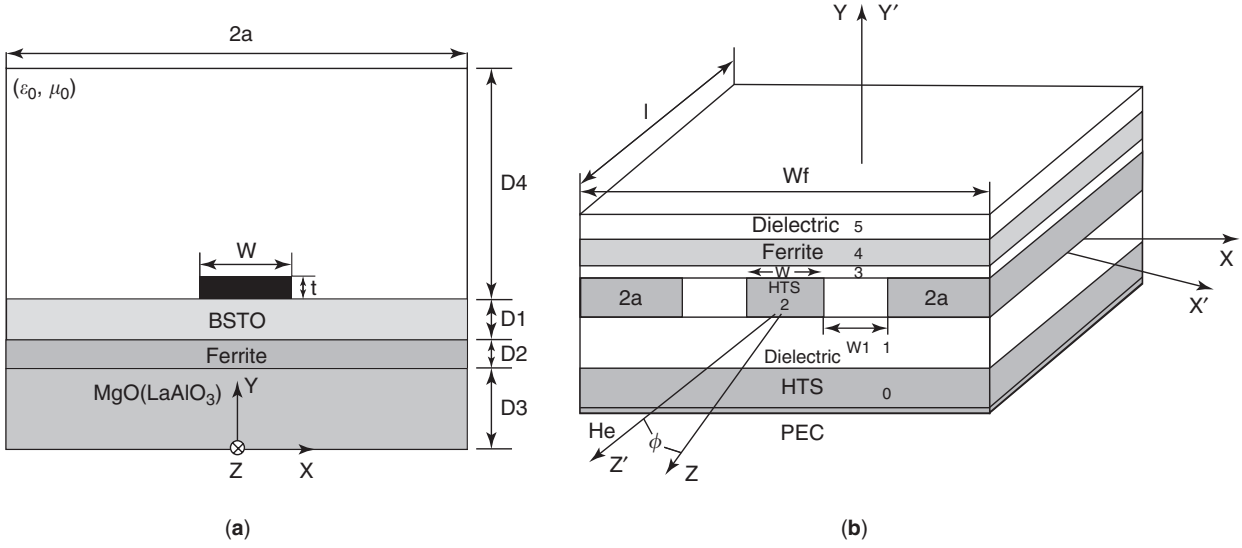


**Figure 3.** Geometries of ferrite-based tunable microstrip line and coplanar resonator: (a) BSTO–ferrite microstrip line; (b) multilayer composite HTS–ferrite coplanar resonator.

where we let $[\underline{\varepsilon}]=\varepsilon_r \overline{\overline{I}}$, $[\underline{\mu}]=\mu_r \overline{\overline{I}}$, $[\xi]=\xi \overline{\overline{I}}=j\kappa \overline{\overline{I}}$, and $[\eta]=\xi^* \overline{\overline{I}}=-j\kappa \overline{\overline{I}}$, where $\overline{\overline{I}}$ is the unit dyad, $\kappa$ is the chirality parameter, and the frequency-dependent property of constitutive quantities should be understood but here $\omega$ is suppressed. In a chiral medium, the eigenmodes are the left- and right-handed circular polarized waves, as observed in ferrites. However, there is no biasing DC magnetic field needed. Some models of chiral devices are outlined as follows.

**2.6.1. Chirowaveguides.** Figure 4 shows the geometries of circular (a) and a rectangular (b) chirowaveguides, which have been extensively studied by some researchers.

The guided-mode characteristics in chirowaveguides in Fig. 4 are completely controlled by chirality parameter. It can be predicated that the ordinary modes of transverse electric TE$_{nm}$, transverse magnetic TM$_{nm}$, or transverse electromagnetic (TEM) modes cannot be supported in circular bianisotropic waveguides. The propagating modes along $z$ axis are always hybrid, but they can be classified into hybrid modes $HE_{nm}$ and $EH_{nm}$. The descriptor $EH_{nm}$ is used here for hybrid modes originating in ordinary TM$_{nm}$ modes, and $HE_{nm}$ is used for hybrid modes stemming from ordinary TE$_{nm}$ modes. Here $n(=-\infty,\ldots, 0, \ldots,\infty)$ and $m(=1,\ldots,\infty)$ respectively denote the azimuthal and radial quantum numbers, of which $n$ implies an azimuthal variation $e^{-jn\varphi}$ and $m$ implies that the mode is number $m$ when ordered after increasing cutoff frequency for given $n$.

The longitudinal components $E_z$ and $H_z$ are coupled with each other; however, $E_z$ and $H_z$ can be decoupled as follows

$$E_z = S_+ U_+ + S_- U_- \tag{16a}$$

$$H_z = q_+ U_+ + q_- U_- \tag{16b}$$

where $U_\pm$ are determined by

$$\nabla_t^2 U_\pm + S_\pm U_\pm = 0 \tag{16c}$$

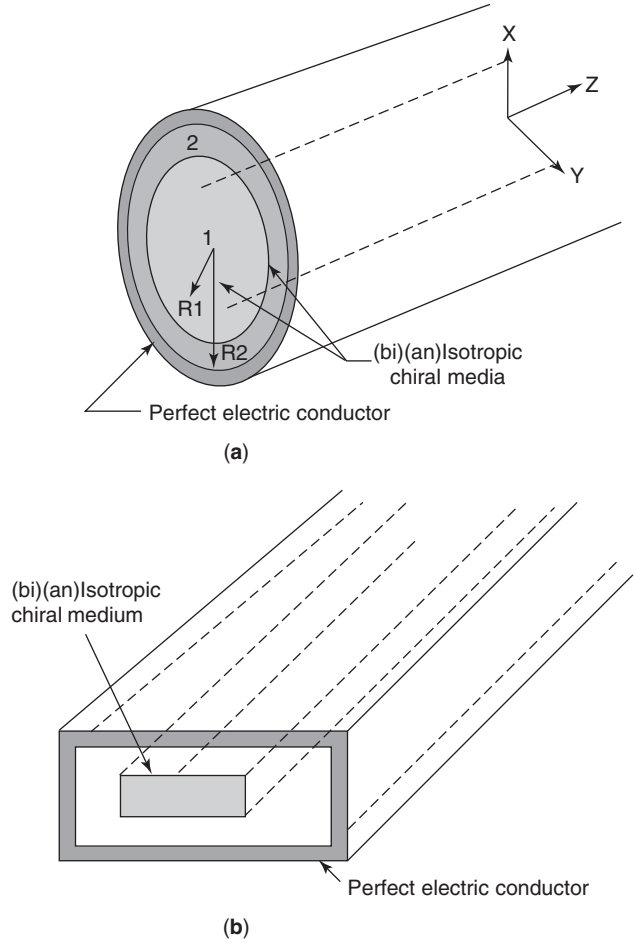


**Figure 4.** Geometries of chirowaveguides: (a) circular; (b) rectangular.

and more generally, by

$$S_{\pm} = \frac{-(C_1 + C_4) \pm \sqrt{(C_1 - C_4)^2 + 4C_2C_3}}{2} \tag{16d}$$

$$q_{\pm} = \frac{-S_{\pm}(S_{\pm} + C_1)}{C_2} \tag{16e}$$

$$C_1 = \frac{j\omega(A_{43}\eta_{zz} + A_{41}\varepsilon_{zz})}{\Delta_0}, \quad C_2 = \frac{j\omega(A_{43}\mu_{zz} + A_{41}\xi_{zz})}{\Delta_0}$$

$$C_3 = -\frac{j\omega(A_{21}\varepsilon_{zz} + A_{23}\eta_{zz})}{\Delta_0}, \quad C_4 = -\frac{j\omega(A_{21}\xi_{zz} + A_{23}\mu_{zz})}{\Delta_0}$$

$$\Delta_0 = A_{21}A_{43} - A_{23}A_{41} \tag{16f}$$

Further, the transverse components electric and magnetic fields inside the chirowaveguide can be expressed in terms of $E_z$ and $H_z$ as follows [31,32,35,69–71]

$$\begin{bmatrix} E_x \\ E_y \\ H_x \\ H_y \end{bmatrix} = \begin{bmatrix} A_{22} & A_{21} & A_{42} & A_{41} \\ -A_{21} & A_{22} & -A_{41} & A_{42} \\ A_{24} & A_{23} & A_{44} & A_{43} \\ -A_{23} & A_{24} & -A_{43} & A_{44} \end{bmatrix} \begin{bmatrix} \dfrac{\partial E_z}{\partial x} \\ \dfrac{\partial E_z}{\partial y} \\ \dfrac{\partial H_z}{\partial x} \\ \dfrac{\partial H_z}{\partial y} \end{bmatrix} \tag{17a}$$

where

$$A_{21} = \frac{a_3b_2 + a_4b_3 - a_2b_1}{\Delta}, \quad A_{22} = \frac{a_1b_1 + a_4b_2 - a_3b_3}{\Delta}$$

$$A_{23} = \frac{a_1b_2 + a_2b_3 - a_4b_4}{\Delta}, \quad A_{24} = \frac{a_3b_4 - a_1b_3 - a_2b_2}{\Delta}$$

$$A_{41} = \frac{a_1b_5 + a_2b_8 - a_6b_9}{\Delta}, \quad A_{42} = \frac{a_2b_5 - a_3b_6 + a_4b_7}{\Delta}$$

$$A_{43} = \frac{a_1b_7 + a_3b_9 + a_2b_{10}}{\Delta}, \quad A_{44} = \frac{a_1b_6 + a_2b_8 + a_4b_9}{\Delta}$$

$$b_1 = a_7^2 + a_8^2,\ b_2 = a_6a_7 - a_5a_8, b_3 = a_6a_8 + a_5a_7,$$

$$b_4 = a_5^2 + a_6^2, \quad b_5 = a_3a_8 - a_4a_7$$

$$b_6 = a_1a_7 - a_3a_5,\ b_7 = a_4a_5 - a_1a_8,$$

$$b_8 = a_2a_7 - a_3a_6,\ b_9 = a_1a_6 - a_2a_5$$

$$a_1 = -(\gamma + \omega\eta_{xy}),\ a_2 = j\omega\eta_{xx},\ a_3 = -\omega\mu_{xy},$$

$$a_4 = j\omega\mu_{xx},\ a_5 = \omega\varepsilon_{xy},\ a_6 = -j\omega\varepsilon_{xx}$$

$$a_7 = -(\gamma - \omega\xi_{xy}),\ a_8 = -j\omega\xi_{xx}$$

$$\begin{aligned}\Delta = {} & a_1(a_1b_1 + a_2b_4 - a_3b_3) + a_2(a_2b_1 - a_4b_3 - a_3b_2) \\ & + a_3(a_3b_4 - a_2b_2 - a_1b_3) \\ & + a_4(a_1b_2 - a_2b_3 + a_4b_4)\end{aligned} \tag{17b}$$

where $\gamma$ is the mode propagation constant. In Fig. 4a, six field components of the guided hybrid modes $HE(EH)_{nm}$ can be expressed in a set of closed-form equations. For example, in the inner chiral region ($\rho \le R_1$) in Fig. 4a, the tangential field components are given by [69]

$$E_z^{(1)} = [D_1^{(1)}S_+^{(1)}J_n(\sqrt{S_+^{(1)}}\rho) + D_2^{(1)}S_-^{(1)}J_n(\sqrt{S_-^{(1)}}\rho)]e^{-jn\varphi} \tag{18a}$$

$$\begin{aligned}E_\varphi^{(1)} = {} & \{D_1^{(1)}[-M_+^{(1)}J_n'(\sqrt{S_+^{(1)}}\rho) - \frac{jnN_+^{(1)}}{\rho}J_n(\sqrt{S_+^{(1)}}\rho)] \\ & + D_2^{(1)}[-M_-^{(1)}J_n'(\sqrt{S_-^{(1)}}\rho) - \frac{jnN_-^{(1)}}{\rho}J_n(\sqrt{S_-^{(1)}}\rho)]\}e^{-jn\varphi}\end{aligned} \tag{18b}$$

$$H_z^{(1)} = [D_1^{(1)}q_+^{(1)}J_n(\sqrt{S_+^{(1)}}\rho) + D_2^{(1)}q_-^{(1)}J_n(\sqrt{S_-^{(1)}}\rho)]e^{-jn\varphi} \tag{18c}$$

$$\begin{aligned}H_\varphi^{(1)} = {} & \{D_1^{(1)}[-X_+^{(1)}J_n'(\sqrt{S_+^{(1)}}\rho) - \frac{jnY_+^{(1)}}{\rho}J_n(\sqrt{S_+^{(1)}}\rho)] \\ & + D_2^{(1)}[-X_-^{(1)}J_n'(\sqrt{S_-^{(1)}}\rho) - \frac{jnY_-^{(1)}}{\rho} \\ & \times J_n(\sqrt{S_-^{(1)}}\rho)]\}e^{-jn\varphi}\end{aligned} \tag{18d}$$

where $D_1^{(1)}$ and $D_2^{(1)}$ are unknown mode-expanding constants to be determined. Here, $J_n$ and $J_n'$ are the Bessel function of the first kind and its derivative, respectively. After some mathematical treatments, the mode dispersion and attenuation characteristics in chirowaveguides can be understood.

As in normal waveguides, various discontinuities may also exist in chirowaveguides, as shown in Fig. 5. This structure is symmetric in the $z$-axis direction, and the scattering of the guided mode may be analyzed in terms of the symmetric and asymmetric excitations as indicated in Ref. 79.

Figure 6 shows two cases of a normal waveguide partially filled with bianisotropic chiral media, and these may be easily met in the measurement of chiral parameter using some standard waveguide methods.

In the case of coaxial line filled with a biisotropic chiral medium, the influence of permittivity and length of chiral sample $W$ on the amplitude of scattering parameters is depicted in Fig. 7, where $a = 3.04$ mm, $b = 7.0$ mm, $c = 6.0$ mm, $\xi_c = 10^{-4}$ mho, and $\mu = \mu_0$.

**2.6.2. Chiral Resonators.** Chiral media can be used to produce circular cylindrical and spherical dielectric resonators that are further used in filters and antennas. Figure 8 shows the configurations of two chiral spherical resonators [81].

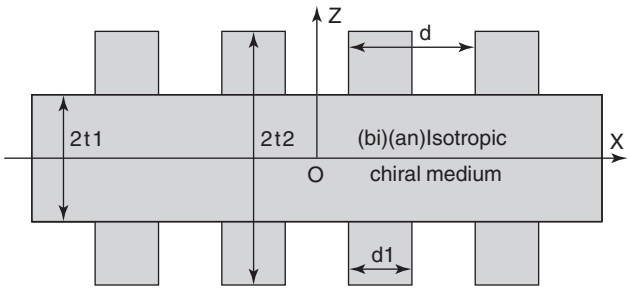


**Figure 5.** Cross-sectional view of a chirowaveguide grating [79].

The inner and outer electromagnetic fields of the chiral sphere shown in Fig. 8a can be expressed by

$$\begin{aligned}\vec{E}^{(1)}_{\text{chiral}} = &-\sum_{m,n}\{ja_{mn}[\vec{N}^{(1)}_{\text{e},mn}(k_+r)+\vec{M}^{(1)}_{\text{e},mn}(k_+r)\\ &+jb_{mn}[\vec{N}^{(1)}_{\text{o},mn}(k_+r)+\vec{M}^{(1)}_{\text{o},mn}(k_+r)]\\ &+c_{mn}[\vec{N}^{(1)}_{\text{e},mn}(k_-r)-\vec{M}^{(1)}_{\text{e},mn}(k_-r)]\\ &+d_{mn}[\vec{N}^{(1)}_{\text{o},mn}(k_-r)-\vec{M}^{(1)}_{\text{o},mn}(k_-r)]\}\end{aligned} \tag{19a}$$

$$\begin{aligned}\vec{H}^{(1)}_{\text{chiral}} = &\frac{1}{\eta_c}\sum_{m,n}\{a_{mn}[\vec{N}^{(1)}_{\text{e},mn}(k_+r)+\vec{M}^{(1)}_{\text{e},mn}(k_+r)\\ &+b_{mn}[\vec{N}^{(1)}_{\text{o},mn}(k_+r)+\vec{M}^{(1)}_{\text{o},mn}(k_+r)]\\ &+jc_{mn}[\vec{N}^{(1)}_{\text{e},mn}(k_-r)-\vec{M}^{(1)}_{\text{e},mn}(k_-r)]\\ &+jd_{mn}[\vec{N}^{(1)}_{\text{o},mn}(k_-r)-\vec{M}^{(1)}_{\text{o},mn}(k_-r)]\}\end{aligned} \tag{19b}$$

and

$$\begin{aligned}\vec{E}_{\text{free}} = &-\sum_{m,n}[je_{mn}\vec{N}^{(4)}_{\text{e},mn}(k_0r)+jf_{mn}\vec{N}^{(4)}_{\text{o},mn}(k_0r)\\ &+g_{mn}\vec{M}^{(4)}_{\text{e},mn}(k_0r)+h_{mn}\vec{M}^{(4)}_{\text{o},mn}(k_0r)]\\ \vec{H}_{\text{free}} = &\frac{1}{\eta_0}\sum_{m,n}[-jg_{mn}\vec{N}^{(4)}_{\text{e},mn}(k_0r)-jh_{mn}\vec{N}^{(4)}_{\text{o},mn}(k_0r)\\ &+e_{mn}\vec{M}^{(4)}_{\text{e},mn}(k_0r)+f_{mn}\vec{M}^{(4)}_{\text{o},mn}(k_0r)]\end{aligned} \tag{19c}$$

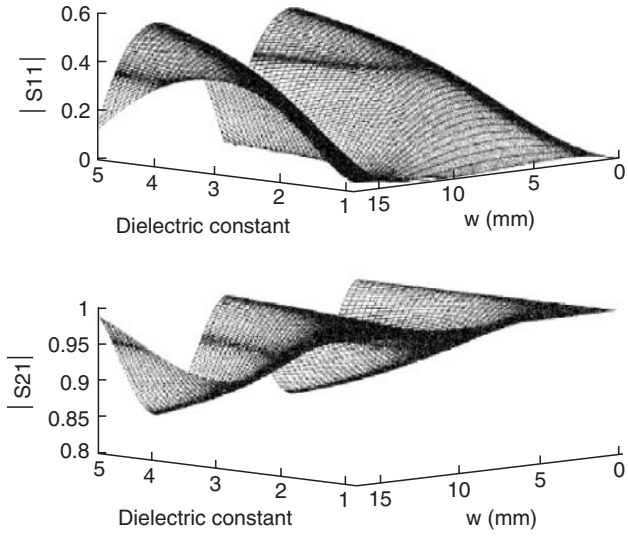


**Figure 7.** Influence of dielectric constant and length of chiral sample on the amplitude of scattering parameters for a coaxial line partially filled with case [80].

where $a_{mn}, b_{mn}, c_{mn}, d_{mn}, e_{mn}, f_{mn}, g_{mn}, h_{mn}$, are unknown coefficients that can be determined by boundary conditions at $r=R_1$; $\vec{M}^{(1,4)}_{\text{e(o)}mn}(k_{+(0)}r)$ and $\vec{N}^{(1,4)}_{\text{e(o)}mn}(k_{+(0)}r)$ are spherical vector wavefunctions. In the case of a multilayer chiral spherical resonator, as shown in Fig. 8b, the electromagnetic fields in each layer can be easily obtained as given in Refs. 72 and 73. Straightforwardly, a set of characteristic equations can be derived after some mathematical treatments, and the $Q$ factor as a function of chirality parameter is shown in Fig. 9 for hybrid modes of different orders [81]. As an example, the $Q$ factor of hybrid mode $HE_{m22}$ varies from 30 to 500 as $\xi_r$ increases from zero to one.

**2.6.3. Chiral Striplines and Chiral Slotlines.** A chiral medium can also be combined with other materials, such as ferrites, to form some novel nonreciprocal chirostrip transmission lines. Figure 10 shows the shielded chiralstripline and two chiral slotlines with chiral and ferrite substrates [42].

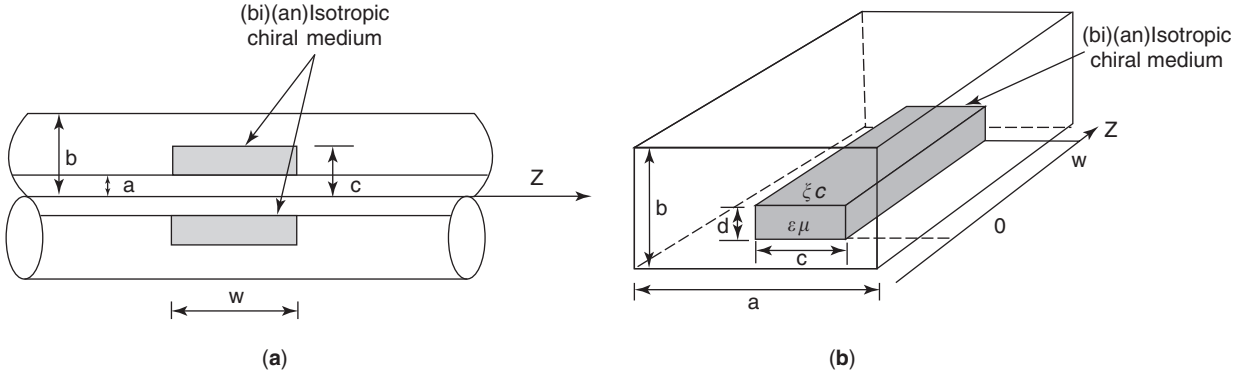


**Figure 6.** A waveguide partially filled with chiral media: (a) coaxial line; (b) rectangular waveguide.

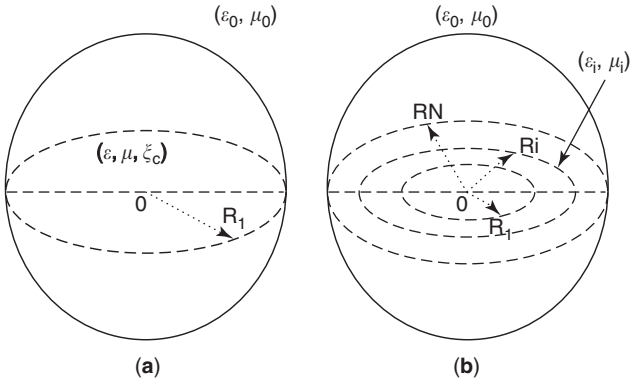


**Figure 8.** A single- (a) and a multilayer (b) chiral resonators.

Using the technique of exponential matrix in the spectral domain, together with the Galerkin MoM (method of moments) procedure, the mode dispersion characteristics in these structures can be understood. As an example, Fig. 11 shows the frequency dependence of effective permittivity $\varepsilon_{\text{eff}+}$ in the structure shown in Fig. 10b, and both chirality and gyrotropy are considered here. The parameters chosen for calculation are assumed to be $f = 40$ GHz, $a = 3.556$ mm, $D_1 = D_4 = 3.3935$ mm, $D_2 = D_3 = 0.1625$ mm, $[\varepsilon^{(2)}(\omega)] = 12.6\,\underline{\underline{I}}$, $M_s^{(2)} \quad \mu_0 = 0.275$, $\omega_0^{(2)}/\omega_m^{(2)} = 0.30$, $\underline{\alpha}_m^{(2)} = 0.0$, $\theta_0^{(2)} = 90^\circ$, $\varphi_0^{(2)} = 0^\circ$, $[\xi^{(2)}(\omega)] = [\eta^{(2)}(\omega)]^* = 10^{-6}\,\underline{\underline{I}}$, $\left[\varepsilon^{(3)}(\omega)\right] = 2.2\,\underline{\underline{I}}$, $\left[\mu^{(3)}(\omega)\right]\underline{\underline{I}}$, $\left[\xi^{(3)}(\omega)\right] = \left[\eta^{(3)}(\omega)\right]^* = j0.5\,\underline{\underline{I}}\,(a)$, and $j0.8\,\underline{\underline{I}}\,(b)$.

In Fig. 11, the ferrite substrate is magnetically biased by a magnetic field fixed to the $x$-axis direction with saturation magnetization $M_s^{(2)}\mu_0 = 0.275$, $\omega_0^{(2)}/\omega_m^{(2)} = 0.3$. Physically, such a unilateral chiral ferrite slotline is a nonreciprocal structure, but only the effective dielectric constant of forward wave is demonstrated here. It is obvious that, at high frequency $f = 40$ GHz and for strong chirality, $\varepsilon_{\text{eff}}$ decreases rapidly with increasing the slot width.

**2.6.4. Faraday Chiral Media.** Faraday chiral media are classified as chiroplasmas or chiroferrites in which the effects of both gyrotropy and chirality are combined [49,84]. Corresponding to the CGS of $C_\infty$, their four constitutive tensors can be described by

$$[C] = \begin{bmatrix} C_{xx} & -jC_{xy} & 0 \\ jC_{xy} & C_{xx} & 0 \\ 0 & 0 & C_{zz} \end{bmatrix}, \quad C = \varepsilon, \mu, \xi, \eta \tag{20}$$

where these tensors contain a total of 12 scalar quantities. When a circular waveguide is filled with Faraday chiral media, as shown in Fig. 4a, the longitudinal components $E_z$ and $H_z$ can be decoupled and expressed by Eqs. (16a) and (16b). Following a procedure similar to that described in Refs. 32 and 35, the field distribution in each layer can be derived, and also the mode dispersion characteristics can be understood. Some hybrid analytical and numerical techniques, as proposed in Refs. 85–89, can be employed to study the combined effects of gyrotropy and chirality on the guided hybrid mode characteristics. On the other hand, it should be mentioned that to design and fabricate Faraday chiral media, and further to extract their constitutive parameters at microwave frequencies, is very challenging work. Although some methods have been proposed [90], many difficult problems need to be explored by the researchers in both material and microwave fields.

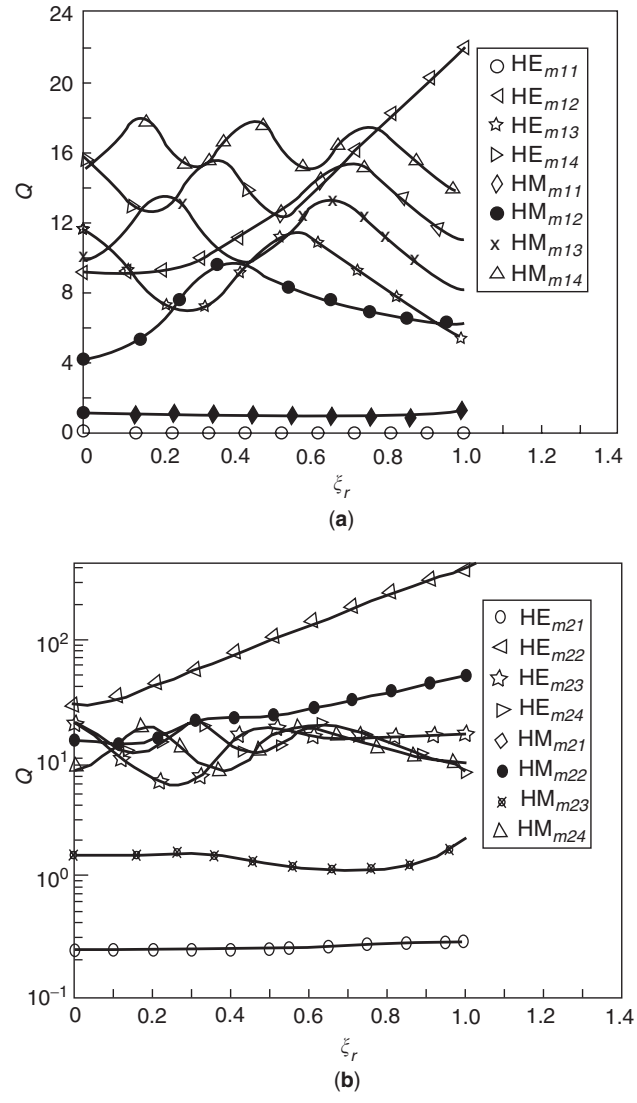


**Figure 9.** $Q$ factor versus chirality parameter for hybrid modes of different orders: (a) $\varepsilon_r = 10$, $\mu_r = 1$, $n = 1$; (b) $\varepsilon_r = 10$, $\mu_r = 1$, $n = 2$.

## 3. TYPICAL METHODOLOGIES

### 3.1. Exponential Matrix Technique in the Spectral Domain

Among the techniques used to deal with the interaction of an electromagnetic wave with multilayer bianisotropic media, we should mention the exponential matrix technique proposed by Tsalamengas [4], which has been successfully used to study source radiation and wave

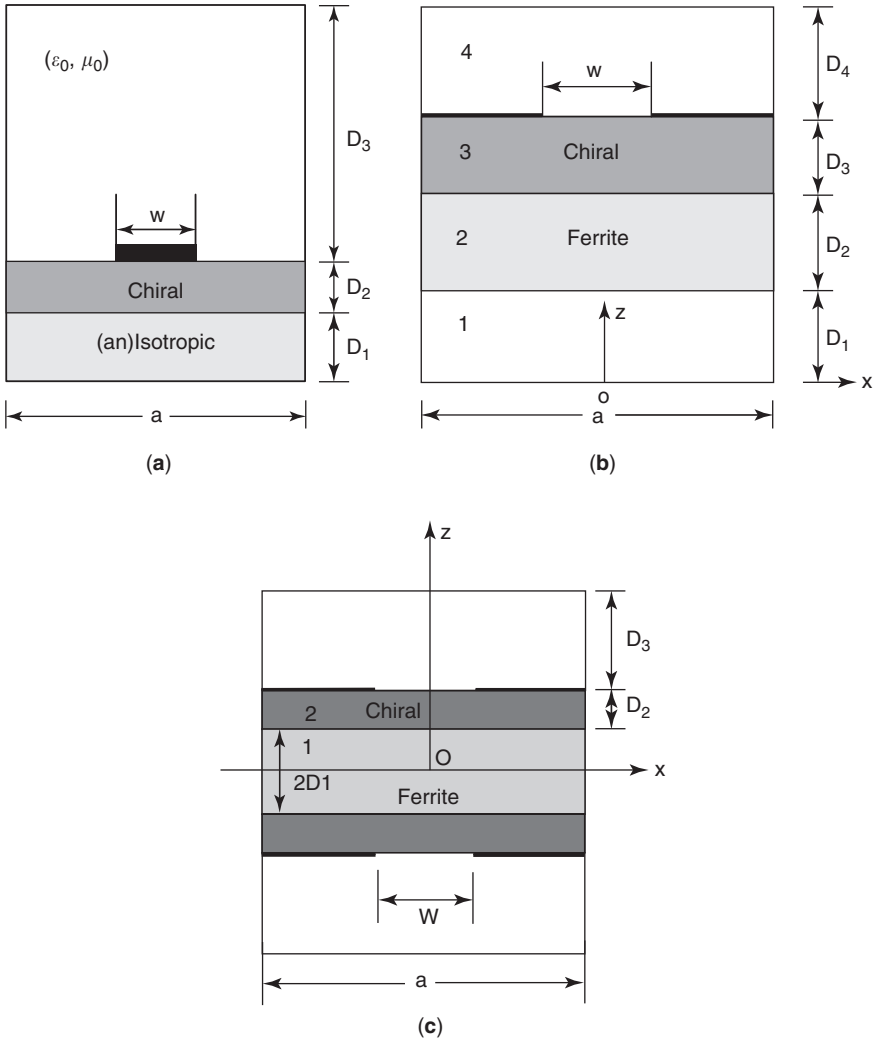


**Figure 10.** Cross-sectional views of three microstrip transmission lines with chiral and ferrite substrate: (a) chiral stripline; (b) unilateral chiral slotline; (c) bilateral chiral slotline.

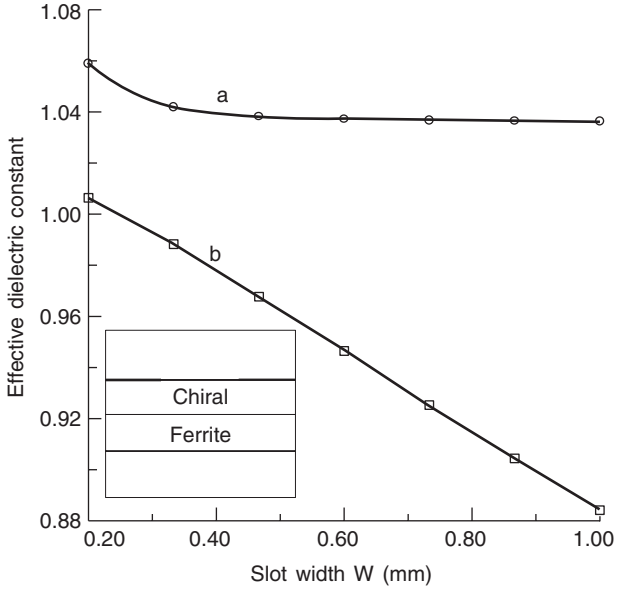


**Figure 11.** Slot width dependence of $\varepsilon_{\text{eff}+}(\beta_+/k_0)^2$ in a unilateral slotline on a double-layer chiral-ferrite substrate.

propagation problems related to single-, double-, and multilayer bianisotropic structures [34,38–40,42,50–54] as shown in Fig. 12. Here, we let the $z$ axis of a rectangular coordinate system be normal to all boundaries and the $x$ and $y$ axes lie in the plane of the top interface. In the $z$-axis direction, the geometry has discrete variation in material characteristics, and this structure may be with or without a backed plane at $z = -d^{(N)}$ ($d^{(N)} = \sum_{i=1}^{N} D^{(i)}$). For the nonbacked case the regions $z > 0$ and $z < -d^{(N)}$ are usually assumed to be free space $(\varepsilon_0, \mu_0)$. The thickness of each layer is denoted by $D^{(1)},\ldots,D^{(i)}$ ($|d^{(i)} - d^{(i-1)}|$), . . . , and $D^{(N)}$. Mathematically, the four constitutive tensors $[\varepsilon^{(i)}(\omega)]$, $[\mu^{(i)}(\omega)]$, $[\xi^{(i)}(\omega)]$, and $[\eta^{(i)}(\omega)]$ $(i = 1,\ldots,N)$ of each layer may take any type of the above mentioned 23 CGSs or even another form [1].

Assuming that a linearly polarized electromagnetic wave is obliquely incident on a multilayer bianisotropic medium, as shown in Fig. 12, four propagating modes with different phase velocities can be generated in each layer. After propagation through the medium, the polarization of the transmitted field is rotated with respect to the polarization of the incident wave. Now we introduce the

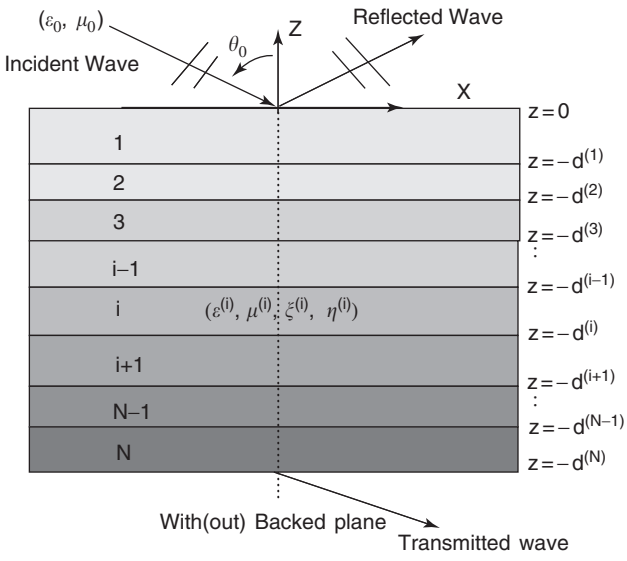


**Figure 12.** Cross section of multilayer bianiostropic medium with(out) backed plane.

one-dimensional Fourier transform domain defined by

$$\tilde{\psi}(k_x,z)=\frac{1}{2\pi}\int_{-\infty}^{+\infty}\psi(x;z)e^{jk_x x}dx \tag{21a}$$

$$\psi(x,z)=\int_{-\infty}^{+\infty}\tilde{\psi}(k_x;z)e^{-jk_x x}dk_x \tag{21b}$$

into the following Maxwell equations ($e^{j\omega t}$):

$$\begin{aligned}\nabla\times\tilde{\boldsymbol{H}}^{(i)}=&j\omega\{\varepsilon_0[\varepsilon^{(i)}(\omega)]\tilde{\boldsymbol{E}}^{(i)}\\&+\sqrt{\mu_0\varepsilon_0}[\xi^{(i)}(\omega)]\tilde{\boldsymbol{H}}^{(i)}\},\end{aligned} \tag{22a}$$

$$\begin{aligned}\nabla\times\tilde{\boldsymbol{E}}^{(i)}=&-j\omega\{\mu_0[\mu^{(i)}(\omega)]\tilde{\boldsymbol{H}}^{(i)}\\&+\sqrt{\mu_0\varepsilon_0}[\eta^{(i)}(\omega)]\tilde{\boldsymbol{E}}^{(i)}\}\end{aligned} \tag{22b}$$

Following a procedure similar to that proposed in Ref. 4, the transverse field components in each layer of multilayered bianisotropic slabs can be expressed as

$$\frac{d}{dz}\begin{bmatrix}\tilde{E}_x^{(i)}(k_x;z)\\ \tilde{E}_y^{(i)}(k_x;z)\\ \tilde{H}_x^{(i)}(k_x;z)\\ \tilde{H}_y^{(i)}(k_x;z)\end{bmatrix}=\begin{bmatrix}q_{11}^{(i)} & q_{12}^{(i)} & q_{13}^{(i)} & q_{14}^{(i)}\\ q_{21}^{(i)} & q_{22}^{(i)} & q_{23}^{(i)} & q_{24}^{(i)}\\ q_{31}^{(i)} & q_{32}^{(i)} & q_{33}^{(i)} & q_{34}^{(i)}\\ q_{41}^{(i)} & q_{42}^{(i)} & q_{43}^{(i)} & q_{44}^{(i)}\end{bmatrix}\times\begin{bmatrix}\tilde{E}_x^{(i)}(k_x;z)\\ \tilde{E}_y^{(i)}(k_x;z)\\ \tilde{H}_x^{(i)}(k_x;z)\\ \tilde{H}_y^{(i)}(k_x;z)\end{bmatrix} \tag{23}$$

where the matrix elements $q_{11}^{(i)}-q_{44}^{(i)}$ are functions of spectral variable $k_x$ and material parameters (all the elements of $[\varepsilon^{(i)}(\omega)]$, $[\mu^{(i)}(\omega)]$, $[\xi^{(i)}(\omega)]$ and $[\eta^{(i)}(\omega)]$). After some mathematical manipulations, their exact expressions can be derived and presented [38]. Furthermore, the general solution to the vector differential Eq. (23) can be written as follows:

$$\begin{bmatrix}\tilde{E}_x^{(i)}(k_x;z)\\ \tilde{E}_y^{(i)}(k_x;z)\\ \tilde{H}_x^{(i)}(k_x;z)\\ \tilde{H}_y^{(i)}(k_x;z)\end{bmatrix}=\begin{bmatrix}T_{11}^{(i)}(\overleftrightarrow{z}) & T_{12}^{(i)}(\overleftrightarrow{z}) & T_{13}^{(i)}(\overleftrightarrow{z}) & T_{14}^{(i)}\overleftrightarrow{z})\\ T_{21}^{(i)}(\overleftrightarrow{z}) & T_{22}^{(i)}(\overleftrightarrow{z}) & T_{23}^{(i)}(\overleftrightarrow{z}) & T_{24}^{(i)}(\overleftrightarrow{z})\\ T_{31}^{(i)}(\overleftrightarrow{z}) & T_{32}^{(i)}(\overleftrightarrow{z}) & T_{33}^{(i)}(\overleftrightarrow{z}) & T_{34}^{(i)}(\overleftrightarrow{z})\\ T_{41}^{(i)}(\overleftrightarrow{z}) & T_{42}^{(i)}(\overleftrightarrow{z}) & T_{43}^{(i)}(\overleftrightarrow{z}) & T_{44}^{(i)}(\overleftrightarrow{z})\end{bmatrix}_{\tilde{z}=-(z+d^{(i)})}\times\begin{bmatrix}\tilde{E}_x^{(i)}(k_x;-d^{(i)})\\ \tilde{E}_y^{(i)}(k_x;-d^{(i)})\\ \tilde{H}_x^{(i)}(k_x;-d^{(i)})\\ \tilde{H}_y^{(i)}(k_x;-d^{(i)})\end{bmatrix} \tag{24}$$

The matrix $[T^{(i)}(\overleftrightarrow{z})]_{4\times4}$ in (24) is a transmission matrix, which physically relates to the tangential electromagnetic fields on one surface $z=-d^{(i)}$ to the tangential fields on another surface in the $i$th layer. Further, $[T^{(i)}(\overleftrightarrow{z})]_{4\times4}$ can be expressed in the form of exponential matrix as follows:

$$[T^{(i)}(z)]_{4\times4}=e^{z[q^{(i)}]_{4\times4}} \tag{25}$$

The procedure for calculating the exponential matrix in (25) can be followed as described in Ref. 4, and is omitted here.

The incident plane wave in the spectral domain can be expressed as a superposition of TM and TE (with respect to the $y$ axis) as follows:

$$\begin{bmatrix}\tilde{\boldsymbol{E}}^{\text{inc}}(k_x;z)\\ \tilde{\boldsymbol{H}}^{\text{inc}}(k_x;z)\end{bmatrix}=\begin{bmatrix}-E_{\text{inc}}^{\text{TM}}\vec{e}_y-E_{\text{inc}}^{\text{TE}}\vec{e}_+\\ [-E_{\text{inc}}^{\text{TM}}\vec{e}_+ +E_{\text{inc}}^{\text{TE}}\vec{e}_y]/\eta_0\end{bmatrix}\times e^{-jk_0(x\sin\theta_0-z\cos\theta_0)} \tag{26}$$

where $\theta_0$ is the incident angle, $k_0=\omega\sqrt{\mu_0\varepsilon_0}$, $k_x=k_0\sin\theta_0$, $\eta_0=\sqrt{\mu_0/\varepsilon_0}$, $\vec{e}_\pm=\pm\vec{e}_x\cos\theta_0+\vec{e}_z\sin\theta_0$, and $\vec{e}_x$, $\vec{e}_y$, and $\vec{e}_z$ are the three unit vectors, respectively. The reflected wave fields in the spectral domain can be written as a superposition of TM and TE (to $y$)

$$\begin{bmatrix}\tilde{\boldsymbol{E}}^{(\text{r})}(k_x;z)\\ \tilde{\boldsymbol{H}}^{(\text{r})}(k_x;z)\end{bmatrix}=\begin{bmatrix}-E_0^{\text{TM}}\vec{e}_y-E_0^{\text{TE}}\vec{e}_-\\ [-E_0^{\text{TM}}\vec{e}_- +E_0^{\text{TE}}\vec{e}_y]/\eta_0\end{bmatrix}\times e^{-jk_0z\cos\theta_0} \tag{27}$$

where $E_0^{\mathrm{TM}}$ and $E_0^{\mathrm{TE}}$ refer to the TM and TE components in the reflected waves, respectively. In Fig. 12, if there is no backed plane at $z=-d^{(N)}$, the transmitted waves into region $z<-d^{(N)}$ are denoted by

$$\begin{bmatrix} \tilde{E}^{(\mathrm{t})}(k_x;z) \\ \tilde{H}^{(\mathrm{t})}(k_x;z) \end{bmatrix} = \begin{bmatrix} -E_2^{\mathrm{TM}}\vec{e}_y - E_2^{\mathrm{TE}}\vec{e}_+ \\ [-E_2^{\mathrm{TM}}\vec{e}_+ + E_2^{\mathrm{TE}}\vec{e}_y]/\eta_0 \end{bmatrix} \times e^{jk_0(z+d^{(N)})\cos\theta_0} \tag{28}$$

where $E_2^{\mathrm{TM}}$ and $E_2^{\mathrm{TE}}$ refer to the TM and TE components in transmitted waves, respectively. Furthermore, $E_{0,2}^{\mathrm{TM}}$ and $E_{0,2}^{\mathrm{TE}}$ above can be determined by enforcing the boundary conditions at each interface in Fig. 12. When the structure shown above is backed by a perfectly conducting backed plane, we have

$$\begin{bmatrix} E_0^{\mathrm{TE}} \\ E_0^{\mathrm{TM}} \end{bmatrix} = \begin{bmatrix} R_{11} & R_{21} \\ R_{12} & R_{22} \end{bmatrix} \begin{bmatrix} E_{\mathrm{inc}}^{\mathrm{TE}} \\ E_{\mathrm{inc}}^{\mathrm{TM}} \end{bmatrix} \tag{29}$$

where $R_{11,22}$ denotes for the copolarized reflection coefficients and $R_{12,21}$ represents the cross-polarized reflection coefficients [4]. In the no-backing case, the transmitted matrix is determined by

$$\begin{bmatrix} E_2^{\mathrm{TE}} \\ E_2^{\mathrm{TM}} \end{bmatrix} = \begin{bmatrix} T_{11} & T_{12} \\ T_{21} & T_{22} \end{bmatrix} \begin{bmatrix} E_{\mathrm{inc}}^{\mathrm{TE}} \\ E_{\mathrm{inc}}^{\mathrm{TM}} \end{bmatrix} \tag{30}$$

where $T_{11,12}$ and $T_{12,21}$ are the co- and cross-polarized transmission coefficients, respectively. A more detailed study on the co- and cross-polarized reflection and transmission characteristics of different layered omega(chiro)-ferrite geometries can be seen in Ref. 53. As an example, Fig. 13 shows the variations of the co(cross)-polarized reflection and transmission coefficients as a function of the incident angle for a chiroferrite slab in free space, and we let

$$\varepsilon_{xx}^{(1)} = \varepsilon_{yy}^{(1)} = 5.0,\ \varepsilon_{zz}^{(1)} = 6.0,\ \varepsilon_{xy}^{(1)} = -\varepsilon_{yx}^{(1)} = j0.3$$

$$\mu_{xx}^{(1)} = \mu_{yy}^{(1)} = 0.9,\ \mu_{zz}^{(1)} = 1.5,\ \mu_{xy}^{(1)} = -\mu_{yx}^{(1)} = j0.4$$

$$\xi_{xx}^{(1)} = \eta_{xx}^{(1)} = \xi_{yy}^{(1)} = \eta_{yy}^{(1)} = j0.5,\ \xi_{zz}^{(1)} = \eta_{zz}^{(1)} = j0.9$$

$$\xi_{xy}^{(1)} = \eta_{xy}^{(1)} = j0.1,\ \xi_{yx}^{(1)} = \eta_{yx}^{(1)} = -j0.1$$

The biasing DC magnetic fields $\bar{H}_0$ of all chiroparticles are all along the $z$ axis.

On the other hand, the technique described above, combined with the Galerkin MoM procedure, can also be extended to treat bianisotropic microstrip structures, as shown in the literature [39,40,42,54]. However, it should be mentioned that to deal with the mode dispersion characteristics in a microstrip transmission line with bianisotropic material, a general multilayer model is shown in Fig. 14. It is evident that this model can incorporate various applications [55–57]. However, we need to be careful about the destroy in image symmetry of the constitutive tensors [54,91].

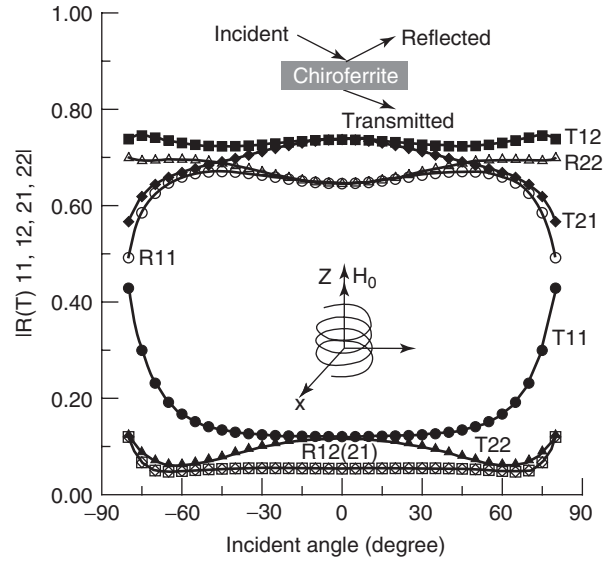


**Figure 13.** $R(T)_{pq}$ $(pq = 11,22,12,21)$ as a function of the incident angle $\theta_0$ for a single-layer chiroferrite slab in free space (solid dotted lines—$T_{11;12;21;22}$; empty dotted lines—$R_{11;12;21;22}$), $D^{(1)}/\lambda = 0.5$ (where $\lambda$ is the incident wavelength).

### 3.2. Extended Finite-Element Method (FEM)

The extended FEM as well as the FEM–boundary-element method (FEM-BEM) is able to treat wave propagation and

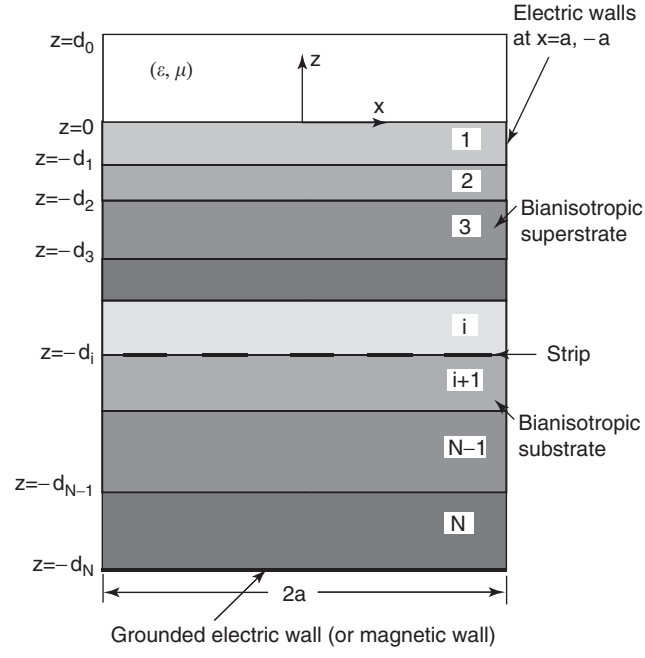


**Figure 14.** Cross-sectional view of a multiple microstrip transmission lines embedded in a multilayer bianisotropic superstrate–substrate.

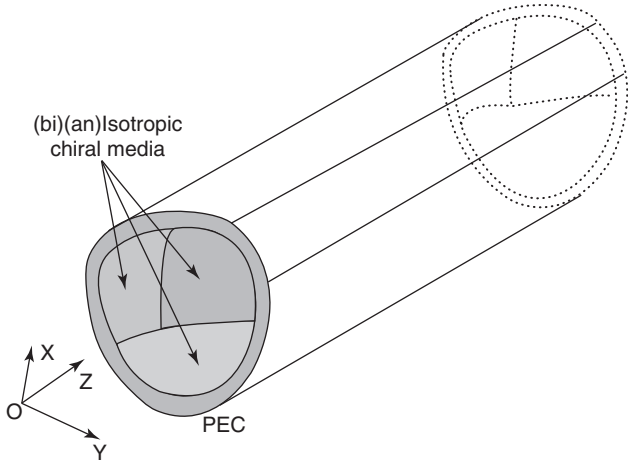


**Figure 15.** The bianisotropic waveguide with an arbitrary cross section.

radiation problems related to complex bianisotropic media [26,92,93]. Figure 15 shows the geometry of a bianisotropic waveguide with an arbitrary cross section, where the filled bianisotropic medium can be lossless or lossy. More generally, the bianisotropic region may consist of several types of bianisotropic media, but the structure must be homogeneous in the $z$-axis direction.

Following a procedure similar to that used in Refs. 92–94, for admissible test functions $\vec{E}_{\text{test}}$ and $\vec{H}_{\text{test}}$, we must have

$$\sum_e \int\int_e \{\vec{E}^*_{\text{test}} \cdot [j\nabla \times \vec{H} + \omega([\varepsilon]\vec{E} + [\xi]\vec{H})] + \vec{H}^*_{\text{test}} \cdot [-j\nabla \times \vec{E} + \omega([\mu]\vec{H} + [\eta]\vec{E})]dx\,dy = 0 \tag{31}$$

where the appropriate interelement and boundary conditions are handled during the assembly $\sum_e$ over all elements. Here, both the necessary continuity requirements on $\vec{n} \times \vec{E}$ and $\vec{n} \times \vec{H}$ and the additional requirements on $\vec{n} \cdot \vec{B}$ and $\vec{n} \cdot \vec{D}$ are, as described below, explicitly enforced on the test and expansion functions. The six components of the electric and magnetic test and expansion fields are approximated on each element in terms of the values at each nodal point according to

$$\begin{Bmatrix} \vec{E} \\ \vec{H} \end{Bmatrix} = [N]^{\text{T}} \begin{Bmatrix} \{E_x\} \\ \{E_y\} \\ \{E_z\} \\ \{H_x\} \\ \{H_y\} \\ \{H_z\} \end{Bmatrix} e^{-j\beta z} \tag{32a}$$

where

$$[N] = \begin{bmatrix} Z_0\{N\} & \{0\} & \{0\} & \{0\} & \{0\} & \{0\} \\ \{0\} & Z_0\{N\} & \{0\} & \{0\} & \{0\} & \{0\} \\ \{0\} & \{0\} & -jZ_0\{N\} & \{0\} & \{0\} & \{0\} \\ \{0\} & \{0\} & \{0\} & \{N\} & \{0\} & \{0\} \\ \{0\} & \{0\} & \{0\} & \{0\} & \{N\} & \{0\} \\ \{0\} & \{0\} & \{0\} & \{0\} & 0 & -j\{N\} \end{bmatrix} \tag{32b}$$

and $Z_0 = \sqrt{\mu_0/\varepsilon_0}$. The real $m \times 1$ column vector $\{N\}$ is the element shape function vector, $m$ is the number of nodal points on each element, $\{0\}$ is a $m \times 1$ null vector, and the superscript "T" denotes a matrix transposition. The column vectors $\{E_x\}$, $\{E_y\}$, $\{E_z\}$, $\{H_x\}$, $\{H_y\}$, and $\{H_z\}$ are $m \times 1$ complex field vectors representing the nodal point values of, respectively, $E_x/Z_0$, $E_y/Z_0$, $jE_z/Z_0$, $H_x$, $H_y$, and $jH_z$ on each element.

By employing the standard Galerkin procedure with the expansion in (32a) and (32b), we can obtain the following generalized eigenvalue equation

$$\{\omega[P] + \beta[Q] + [R]\} \begin{Bmatrix} \{E_x\} \\ \{E_y\} \\ \{E_z\} \\ \{H_x\} \\ \{H_y\} \\ \{H_z\} \end{Bmatrix} = \{0\} \tag{33}$$

where the column vector is composed of all the nodal point variables used to represent $\vec{E}$ and $\vec{H}$ throughout the waveguide cross section. Note that both the complex propagation constant $\beta$ and the real angular frequency $\omega$ may be treated as the eigenvalue, depending on which is numerically most advantageous or of primary interest.

By expanding (31) in component form, the quadratic sparse matrices $[P]$, $[Q]$, and $[R]$ take forms similar to those in Ref. 94, and

$$[Q] = -Z_0 \sum_e \iint_e \begin{bmatrix} \{0\} & \{0\} & \{0\} & \{0\} & -\{A\} & \{0\} \\ \{0\} & \{0\} & \{0\} & \{A\} & \{0\} & \{0\} \\ \{0\} & \{0\} & \{0\} & \{0\} & \{0\} & \{0\} \\ \{0\} & \{A\} & \{0\} & \{0\} & \{0\} & \{0\} \\ -\{A\} & \{0\} & \{0\} & \{0\} & \{0\} & \{0\} \\ \{0\} & \{0\} & \{0\} & \{0\} & \{0\} & \{0\} \end{bmatrix} dx\,dy \tag{34}$$

$$[R] = Z_0 \sum_e \iint_e \begin{bmatrix} \{0\} & \{0\} & \{0\} & \{0\} & \{0\} & -\{C\} \\ \{0\} & \{0\} & \{0\} & \{0\} & \{0\} & \{B\} \\ \{0\} & \{0\} & \{0\} & -\{C\} & \{B\} & \{0\} \\ \{0\} & \{0\} & \{C\} & \{0\} & \{0\} & \{0\} \\ \{0\} & \{0\} & -\{B\} & \{0\} & \{0\} & \{0\} \\ \{C\} & -\{B\} & \{0\} & \{0\} & \{0\} & \{0\} \end{bmatrix} dx\, dy \tag{35}$$

and

$$[A] = \{N\}\{N\}^{\mathrm{T}} \tag{36a}$$

$$[B] = \{N\}\frac{\partial \{N\}^{\mathrm{T}}}{\partial x} \tag{36b}$$

$$[C] = \{N\}\frac{\partial \{N\}^{\mathrm{T}}}{\partial y} \tag{36c}$$

The continuity of $\vec{n} \times \vec{E}$, $\vec{n} \times \vec{H}$, $\vec{n} \cdot \vec{D}$, and $\vec{n} \cdot \vec{B}$, where $\vec{n}$ is the unit normal vector perpendicular to an element side in the transversal $x$–$y$ plane, is enforced. Also, the sample third-order triangular mesh is shown in Fig. 16, and in order to satisfy the interelement conditions, it is sufficient to apply the following at each nodal point along each internal side

$$\vec{n} \times (E_p - \vec{E}_q) = 0 \tag{37}$$

$$\vec{n} \times (\vec{H}_p - \vec{H}_q) = 0 \tag{38}$$

$$\vec{n} \cdot ([\varepsilon_p]\vec{E}_p + [\xi_p]\vec{H}_p - [\varepsilon_q]\vec{E}_q - [\xi_q]\vec{H}_q) = 0 \tag{39}$$

$$\vec{n} \cdot ([\mu_p]\vec{H}_p + [\eta_p]\vec{E}_p - [\mu_q]\vec{H}_q - [\eta_q]\vec{E}_q) = 0 \tag{40}$$

where $\{\vec{E}_p, \vec{H}_p\}$ and $\{E_q, \vec{H}_q\}$ represent unconnected field components in adjacent elements, $p$ and $q$. To satisfy the external boundary conditions at each nodal point along each external side it is sufficient to enforce

$$\vec{n} \times \vec{E}_p = 0 \tag{41a}$$

$$\vec{n} \cdot ([\mu_p]\vec{H}_p + [\eta_p]\vec{E}_p) = 0 \tag{41b}$$

on electric walls and

$$\vec{n} \times \vec{H}_p = 0 \tag{42a}$$

$$\vec{n} \cdot ([\varepsilon_p]\vec{E}_p + [\xi_p]\vec{H}_p) = 0 \tag{42b}$$

on magnetic walls. From these equations, it can be found that the total number of unknown is $\leq 6N_{\mathrm{p}}$, where $N_{\mathrm{p}}$ is the number of nodal points.

As indicated in Ref. 94, the most important property of the eigenvalue problem (30) now is the $O(1/N)$ density of the matrices $[P]$, $[Q]$, and $[R]$. This property ensures that the maximum number of nontrivial matrix elements on each row is independent of the dimension of the matrices. Thus an upper bound of the densities becomes $\rho = NN_z/N^2 \sim O(1/N)$, where $N_z$ is the maximum number of nonzero elements on each row and $N$ is the matrix dimension. Therefore, for large problems, sparse eigenvalue codes can be used to save significant amounts of computer time an memory.

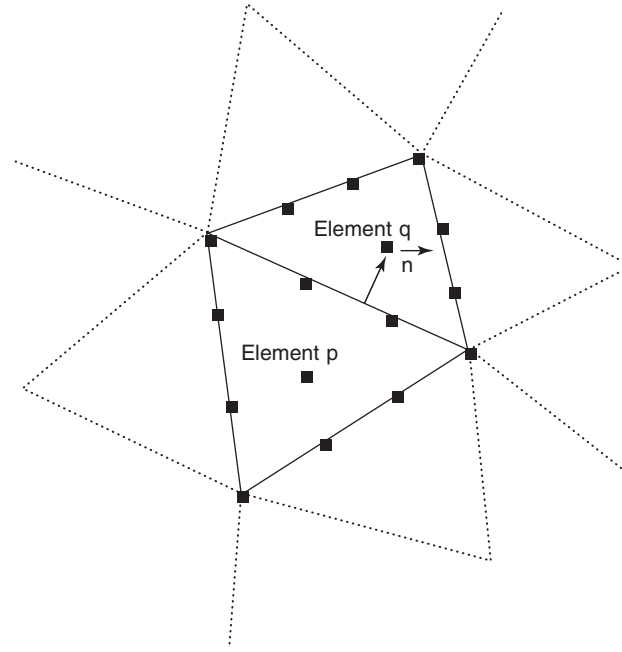


**Figure 16.** A portion of a sample of third-order mesh in the bianisotropic region.

### 3.3. Extended Method of Line (MoL)

The normal method of line (MoL) [28] is very useful in the analysis of planar radiative and transmissive microwave components. This method was developed by mathematicians and physicists in order to solve partial-differential equations in the electromagnetic analysis of optical and microwave devices, for the numerical solution of the partial-differential Helmholtz equation. Originally developed to study planar waveguides, MoL was also extended to study stratified microwave components with arbitrarily shaped cross sections and microstrip discontinuities, including one-dimensional and bidimensional resonators and antennas. The latest extensions of this method have been achieved to study gyrotropic media and microwave components mounted on cylindrical or spherical structures.

The standard version of MoL, does not allow for the study of elements with bianisotropic superstrate–substrates. More recently, an extended MoL numerical procedure, which allows for the analysis of components in the presence of any linear, inhomogeneous, or lossy bianisotropic medium, has been developed [28]. Such an extension is based on the generalization of the transmission-line equations for a general linear medium.

Applying the curl Maxwell equations in a sourceless bianisotropic region, and after some mathematical manipulations, a set of transmission-line equations for a bianisotropic medium in Cartesian coordinates can be derived as follows ($e^{j\omega t}$)

$$\frac{\partial[\mathbf{E}_t]}{\partial \bar{z}} = \begin{bmatrix} A_{xx} & A_{xy} \\ A_{yx} & A_{yy} \end{bmatrix} [\mathbf{E}_t] + \begin{bmatrix} Z_{xx} & Z_{xy} \\ Z_{yx} & Z_{yy} \end{bmatrix} [\tilde{\mathbf{H}}_t] \qquad (43a)$$

$$\frac{\partial[\mathbf{H}_t]}{\partial \bar{z}} = \begin{bmatrix} Y_{xx} & Y_{xy} \\ Y_{yx} & Y_{yy} \end{bmatrix} [\mathbf{E}_t] + \begin{bmatrix} B_{xx} & B_{xy} \\ B_{yx} & B_{yy} \end{bmatrix} [\tilde{\mathbf{H}}_t] \qquad (43b)$$

where $[\mathrm{E_t}] = \begin{bmatrix} E_x \\ E_y \end{bmatrix}$, $[\mathbf{H}_t] = \begin{bmatrix} H_x \\ H_y \end{bmatrix}$, $[\tilde{\mathbf{H}}_t] = \eta_0[\mathbf{H}_t]$, and $\eta_0 = \sqrt{\mu_0/\varepsilon_0}$. The 16 operatorial tensor elements $A_{ij}, B_{ij}, Y_{ij}, Z_{ij}$, where $i, j = x, y, z$, involve both the constitutive tensor entries and the transverse derivatives and are given in Ref. 28 and omitted here, and are very similar to the expressions shown in Ref. 34.

It should be noted that Eqs. (43a) and (43b) can be decoupled only for particular bianisotropic media whose constitutive parameters allow the coupling matrices $[A]$ and $[B]$ to vanish. The necessary and sufficient condition on the medium constitutive tensors to obtain decoupled equations, independently from the excitation, can be written in the following form [28]

$$[\varepsilon] = \begin{pmatrix} \varepsilon_{xx} & \varepsilon_{xy} & 0 \\ \varepsilon_{yx} & \varepsilon_{yy} & 0 \\ 0 & 0 & \varepsilon_{zz} \end{pmatrix}, \; [\mu] = \begin{pmatrix} \mu_{xx} & \mu_{xy} & 0 \\ \mu_{yx} & \mu_{yy} & 0 \\ 0 & 0 & \mu_{zz} \end{pmatrix},$$

$$[\xi] = \begin{pmatrix} 0 & 0 & \xi_{xz} \\ 0 & 0 & \xi_{yz} \\ \xi_{zx} & \xi_{zy} & 0 \end{pmatrix}, \; [\eta] = \begin{pmatrix} 0 & 0 & \eta_{xz} \\ 0 & 0 & \eta_{yz} \\ \eta_{zx} & \eta_{zy} & 0 \end{pmatrix} \qquad (44)$$

which represents the CGS of $C_{2h}(C_s)$ above. Under such circumstances, a standard MoL procedure similar to that expressed in (43) can be used, and we have

$$\frac{\partial^2[\mathbf{E}_t]}{\partial \bar{z}^2} = -[P_E][\mathbf{E}_t], \quad \frac{\partial^2[H_t]}{\partial \bar{z}^2} = -[Q_E][H_t]. \qquad (45a,b)$$

This set of equations can be easily discretized in two dimensions and then diagonalized, and the electromagnetic characteristics of the structure, as shown in Figs. 17a and 17b, can be further understood.

In the general case, an extended version of MoL needs to be developed, as discussed in Ref. 28. Starting from (43a) and (43b) and discretizing in the transverse plane as in the standard MoL, a set of equations involving transverse field components can be derived as follows

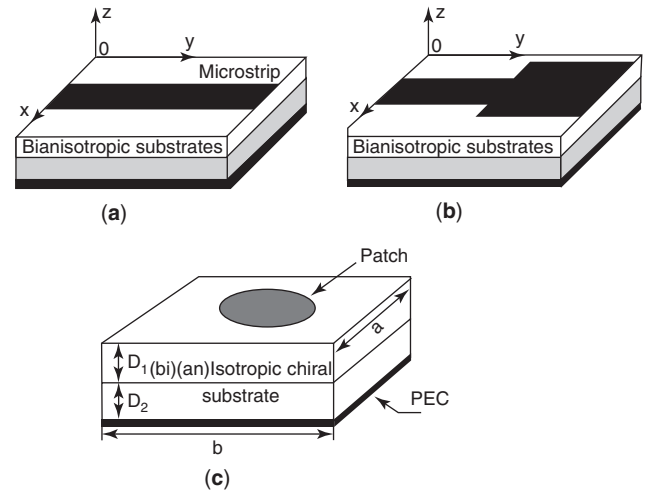


**Figure 17.** Microstrip transmission lines and antenna on bianisotropic substrates.

$$\frac{d[\hat{\mathbf{E}}_t]}{d\bar{z}} = [\hat{\mathbf{A}}][\hat{\mathbf{E}}_t] + [\hat{\mathbf{Z}}][\hat{\mathbf{H}}_t] \qquad (46a)$$

$$\frac{d[\hat{\mathbf{H}}_t]}{d\bar{z}} = [\hat{\mathbf{Y}}][\hat{\mathbf{E}}_t] + [\hat{\mathbf{B}}][\hat{\mathbf{H}}_t] \qquad (46b)$$

where the symbol $\wedge$ stands for bidimensional discretization. Here $[\hat{\mathbf{E}}_t]$ and $[\hat{\mathbf{H}}_t]$ depend only on $z$, respectively, as shown in Fig. 18, where $\hat{\mathbf{E}}_x$ and $\hat{\mathbf{H}}_y$ are calculated on lines denoted by "o", while $\hat{\mathbf{E}}_y$ and $\hat{\mathbf{H}}_x$ are sampled on lines denoted by ●. The other two sets, denoted by empty and solid square dots, respectively, contain the lines in which the central-difference derivatives are computed.

In Fig. 18, $d_x$ and $d_y$ are the discretization steps for the central-difference operators along $x$ and $y$, respectively. The matrices $[\hat{\mathbf{A}}]$, $[\hat{\mathbf{Z}}]$, $[\hat{\mathbf{Y}}]$, and $[\hat{\mathbf{B}}]$ are obtained from Eqs. (4), given in Ref. 28, substituting their elements with discretized quantities. First of all, partial derivatives are substituted with central-difference matrices $[\hat{\mathbf{D}}]$, also including the boundary conditions.

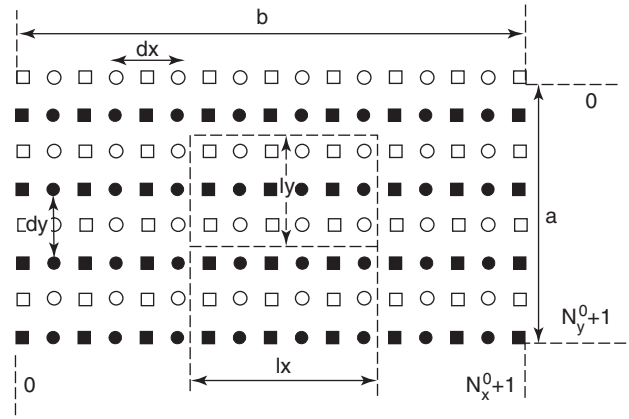


**Figure 18.** Rectangular patch with discretization lines.

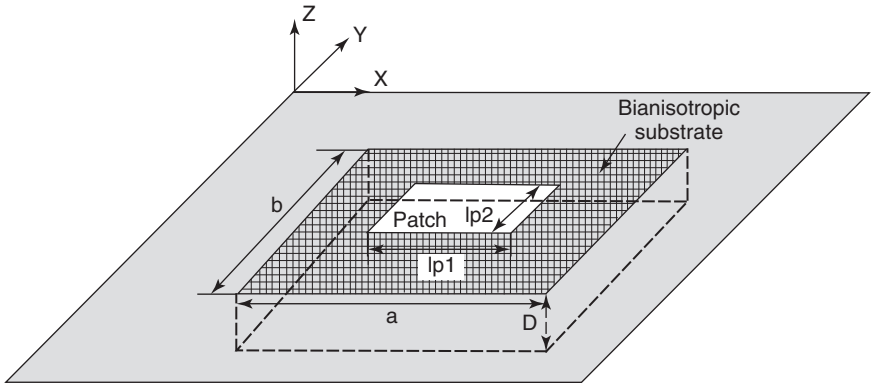


**Figure 19.** A patch cavity resonator loaded with a bianisotropic substrate.

Equations (46a) and (46b) are the algebraic discretized versions of the generalized transmission line equations, and they can be changed into

$$\frac{d[\hat{\psi}]}{d\bar{z}} = \begin{bmatrix} \hat{\mathbf{A}} & \hat{\mathbf{Z}} \\ \hat{\mathbf{Y}} & \hat{\mathbf{B}} \end{bmatrix} [\hat{\psi}] \tag{47}$$

where $[\hat{\psi}] = \begin{bmatrix} \hat{\mathbf{E}}_t & \hat{\mathbf{H}}_t \end{bmatrix}^T$ and the superscript "T" represents the transpose of matrix. It is evident that the solution to (47) is in the form of an exponential matrix, which is well documented in Ref. 4 and used elsewhere in the literature [34,38–40,50–54] by enforcing certain boundary conditions.

As a numerical example, Fig. 19 shows the geometry of a patch cavity resonator loaded with a bianisotropic substrate, and the resonant frequency versus patch side length is depicted in Fig. 20 for $\varepsilon_r = 2.0$, $D = 0.8$ mm, and $a = b = 10$ cm.

In Fig. 18, the bianisotropic substrate is characterized by the CGS of $D_{2d}(C_{2v})$, and

$$[\varepsilon] = \varepsilon_0 \varepsilon_r \begin{bmatrix} 1 & 0 & 0 \\ 0 & 1 & 0 \\ 0 & 0 & 1 \end{bmatrix}, \quad [\mu] = \mu_0 \begin{bmatrix} 1 & 0 & 0 \\ 0 & 1 & 0 \\ 0 & 0 & 1 \end{bmatrix},$$
$$[\xi] = c_0^{-1} \begin{bmatrix} 0 & j\xi & 0 \\ j\xi & 0 & 0 \\ 0 & 0 & 0 \end{bmatrix}, \quad [\eta] = -[\xi] \tag{48}$$

where $c_0 = 3 \times 10^8$ m/s. It is seen that, compared to the isotropic case, the resonant frequency changes very little for a given patch width, and this is because the bianisotropic substrate is supposed to be very thin and the magnetoelectric coupling effect is very weak [28].

### 3.4. Finite-Difference Time-Domain Method (FDTD)

The finite-difference time-domain (FDTD) method [95] is the most popular three-dimensional full-wave numerical algorithm that has been used to model electromagnetic phenomena and interactions in various fields. The simplicity and effectiveness of FDTD method stem from the utilization of a Cartesian grid from the discretization of the structure, with appropriate staggering of the unknown discrete values of the components of the electric and magnetic field vectors in such a manner that the curl operations in Maxwell's equations can be approximated in terms of second-order accurate finite differences. The staggering of the fields is known as the *Yee lattice*. This discretization results in a state space representation of the discrete values of all six components of the electric and magnetic fields on the grid. The simplicity and versatility of the FDTD algorithm, combined with its suitability for parallel implementation, has prompted aggressive research and development toward its further enhancement.

In the time domain, the constitutive equations of biisotropic chiral media can be expressed by

$$\vec{D}(t) = \varepsilon \vec{E}(t) + \frac{\chi}{c_0} \vec{H}(t) - \frac{1}{c_0} \int_0^t \kappa'(\tau) \vec{H}(t-\tau) d\tau \tag{49a}$$

$$\vec{B}(t) = \mu \vec{H}(t) + \frac{\chi}{c_0} \vec{E}(t) - \frac{1}{c_0} \int_0^t \kappa'(\tau) \vec{E}(t-\tau) d\tau \tag{49b}$$

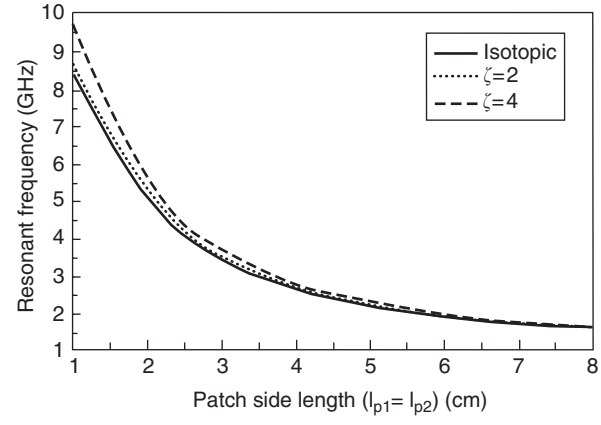


**Figure 20.** Resonant frequency versus patch side length [28].

and (49a) and (49b) respectively can be further discretized as

$$\vec{D}(n)=\varepsilon\vec{E}(n)+\frac{\chi}{c_0}\vec{H}(n) -\frac{1}{c_0}\sum_{m=0}^{n-1}\vec{H}(n-m)\int_{m\Delta t}^{(m+1)\Delta t}\kappa'(\tau)d\tau \tag{50a}$$

$$\vec{B}(n)=\mu\vec{H}(n)+\frac{\chi}{c_0}\vec{E}(n) -\frac{1}{c_0}\sum_{m=0}^{n-1}\vec{E}(n-m)\int_{m\Delta t}^{(m+1)\Delta t}\kappa'(\tau)d\tau \tag{50b}$$

The complex time-domain chirality parameter $\hat{\kappa}'(t)$ is defined as [95]

$$\hat{\kappa}'(t)=-j\frac{\tau\omega_0^2}{\sqrt{1-\xi^2}}e^{[-\xi\omega_0 t+j(\phi-\omega_0\sqrt{1-\xi^2}t]} \tag{51}$$

while the time-domain chirality parameter should be the real part of $\hat{\kappa}'(t)$, and

$$\kappa'(m\Delta t)=\int_{m\Delta t}^{(m+1)\Delta t}\kappa'(\tau)d\tau \tag{52a}$$

$$\hat{\kappa}'(m\Delta t)=\int_{m\Delta t}^{(m+1)\Delta t}\hat{\kappa}'(\tau)d\tau \tag{52b}$$

In the time domain, the time dependences of both permittivity and permeability are described by the following equations:

$$\varepsilon(t)=\varepsilon_0\left[\varepsilon_\infty\delta(t)+\frac{(\varepsilon_s-\varepsilon_\infty)\omega_{0e}e^{-\omega_{0e}\xi_e t}}{\sqrt{1-\xi_e^2}}\sin(\omega_{0e}\sqrt{1-\xi_e^2}t)\right] \tag{53a}$$

$$\mu(t)=\mu_0\left[\mu_\infty\delta(t)+\frac{(\mu_s-\mu_\infty)\omega_{0m}e^{-\omega_{0m}\xi_m t}}{\sqrt{1-\xi_m^2}}\sin(\omega_{0m}\sqrt{1-\xi_m^2}t)\right] \tag{53b}$$

Further, (50a) and (50b) respectively become [95]

$$\vec{D}(n)=\varepsilon_0\varepsilon_\infty\vec{E}(n)+\frac{\chi}{c_0}\vec{H}(n)+\varepsilon_0\mathrm{Re}[\hat{\chi}_e(0)]\vec{E}(n) +\varepsilon_0\mathrm{Re}\left[\hat{\vec{\psi}}_{\chi_e}^{E}(n-1)e^{(-\xi_e+j\sqrt{1-\xi_e^2})\omega_{0e}\Delta t} -\frac{\mathrm{Re}[\hat{\kappa}'(0)]}{c_0}\vec{H}(n)-\frac{1}{c_0}\mathrm{Re}[\hat{\vec{\psi}}_{\kappa}^{H}(n-1) \times e^{(-\xi-j\sqrt{1-\xi^2})\omega_0\Delta t}]\right] \tag{54a}$$

$$\vec{B}(n)=\mu_0\mu_\infty\vec{H}(n)+\frac{\chi}{c_0}\vec{E}(n)+\mu_0\mathrm{Re}[\hat{\chi}_m(0)]\vec{H}(n) +\mu_0\mathrm{Re}\left[\hat{\vec{\psi}}_{\chi_m}^{H}(n-1)e^{(-\xi_m+j\sqrt{1-\xi_m^2})\omega_{0m}\Delta t} +\frac{\mathrm{Re}[\hat{\kappa}'(0)]}{c_0}\vec{E}(n)+\frac{1}{c_0}\mathrm{Re}[\hat{\vec{\psi}}_{\kappa}^{E}(n-1) \times e^{(-\xi-j\sqrt{1-\xi^2})\omega_0\Delta t}]\right] \tag{54b}$$

where

$$\hat{\vec{\psi}}_{\varphi}^{F}(n)=\sum_{m=0}^{n-1}\vec{F}(n-m)\hat{\varphi}(m) \tag{54c}$$

Finally, the general algorithm for dispersive biisotropic chiral media can be found, and in this algorithm [95], we must

1. Update the $y$ component of the electric displacement $D_{i+(1/2)}^{y}(n+\frac{1}{2})$ and the magnetic flux density $B_{i+(1/2)}^{y}(n+(\frac{1}{2}))$ by

$$D_{i+1/2}^{y}\left(n+\frac{1}{2}\right)=\varepsilon_0\varepsilon_\infty E_{i+1/2}^{y}\left(n+\frac{1}{2}\right) +\varepsilon_0\mathrm{Re}[\hat{\chi}_e(0)]E_{i+1/2}^{y}\left(n+\frac{1}{2}\right) +\varepsilon_0\mathrm{Re}[\hat{\psi}_{\chi_{e_{i+(1/2)}}}^{E^y}\left(n-\frac{1}{2}\right)e^{(-\xi_e+j\sqrt{1-\xi_e^2})\omega_{0e}\Delta t} +\frac{\chi}{c_0}H_{i+(1/2)}^{y}\left(n+\frac{1}{2}\right) -\frac{\mathrm{Re}[\hat{\kappa}'(0)]}{c_0}H_{i+(1/2)}^{y}\left(n+\frac{1}{2}\right) -\frac{1}{c_0}\mathrm{Re}[\hat{\psi}_{\kappa_{i+(1/2)}}^{H^y}\left(n-\frac{1}{2}\right)e^{(-\xi-j\sqrt{1-\xi^2})\omega_0\Delta t}]] \tag{55a}$$

$$B_{i+1/2}^{y}\left(n+\frac{1}{2}\right)=\mu_0\mu_\infty H_{i+1/2}^{y}\left(n+\frac{1}{2}\right) +\mu_0\mathrm{Re}[\hat{\chi}_e(0)]H_{i+1/2}^{y}\left(n+\frac{1}{2}\right) +\mu_0\mathrm{Re}[\hat{\psi}_{\chi_m i+(1/2)}^{E^y}\left(n-\frac{1}{2}\right)e^{(-\xi_m+j\sqrt{1-\xi_m^2})\omega_{0m}\Delta t} +\frac{\chi}{c_0}E_{i+1/2}^{y}\left(n+\frac{1}{2}\right) +\frac{\mathrm{Re}[\hat{\kappa}'(0)]}{c_0}E_{i+(1/2)}^{y}\left(n+\frac{1}{2}\right) +\frac{1}{c_0}\mathrm{Re}[\hat{\psi}_{\kappa_{i+(1/2)}}^{E^y}\left(n-\frac{1}{2}\right)e^{(-\xi-j\sqrt{1-\xi^2})\omega_0\Delta t}]] \tag{55b}$$

2. Update the $x$ component of the electric displacement $D_i^x(n+1)$ and the magnetic flux density $B_{i+1}^x(n+1)$ by

$$\begin{aligned} D_i^x(n+1) &= \varepsilon_0\varepsilon_\infty E_{i+1}^x(n+1) + \varepsilon_0 \mathrm{Re}[\hat{\chi}_e(0)]E_{i+1}^x(n+1) \\ &\quad + \varepsilon_0 \mathrm{Re}[\hat{\psi}^{E^x}_{\chi_{e_{i+(1)}}}(n) e^{(-\xi_e + j\sqrt{1-\xi_e^2})\omega_{0e}\Delta t} + \frac{\chi}{c_0} H_i^x(n+1) \\ &\quad - \frac{\mathrm{Re}[\hat{\kappa}(0)]}{c_0} H_i^x(n+1) \\ &\quad - \frac{1}{c_0}\mathrm{Re}[\hat{\psi}^{H^x}_{\kappa_i}(n) e^{(-\xi - j\sqrt{1-\xi^2})\omega_0\Delta t}]] \end{aligned} \tag{56a}$$

$$\begin{aligned} B_i^x(n+1) &= \mu_0\mu_\infty H_i^x(n+1) \\ &\quad + \mu_0 \mathrm{Re}[\hat{\chi}_m(0)]H_i^x(n+1) \\ &\quad + \mu_0 \mathrm{Re}[\hat{\psi}^{Ex}_{\chi_{mi}}(n) e^{(-\xi_m + j\sqrt{1-\xi_m^2})\omega_{0m}\Delta t} \\ &\quad + \frac{\chi}{c_0} E_i^x(n+1) + \frac{\mathrm{Re}[\hat{\kappa}'(0)]}{c_0} E_i^x(n+1) \\ &\quad + \frac{1}{c_0}\mathrm{Re}[\hat{\psi}^{Ex}_{\kappa i}(n) e^{(-\xi - j\sqrt{1-\xi^2})\omega_0\Delta t}]] \end{aligned} \tag{56b}$$

On the basis of (56a) and (56b), the interaction of a transient microwave signal with biisotropic media can be fully understood, in particular the material dispersion and loss effects.

To use biisotropic and bianisotropic chiral media to fabricate certain microwave devices, there are still many challenging problems that need to be explored further, such as the control or optimization of material parameters and their measurements.

## BIBLIOGRAPHY


1. V. Dmitriev, Table of the second rank constitutive tensors for linear homogeneous media described by the point magnetic groups of symmetry, *Prog. Electromagn. Res.* **PIER-28**:43–95 (2000).
2. D. Graglia, P. L. E. Uslenghi, and R. E. Zich, Reflection and transmission for planar structures of bianisotropic media, *Electromagnetics* **11**:193–208 (1991).
3. F. L. Mesa, R. Marques, and M. Horno, A general algorithm for computing the bidimensional spectral Green's dyad in multilayered complex bianisotropic media: The equivalent boundary method, *IEEE Trans. Microwave Theory Tech.* **MTT-39**:1640–1649 (1991).
4. J. L. Tsalamengas, Interaction of electromagnetic waves with general bianisotropic slabs, *IEEE Trans. Microwave Theory Tech.* **MTT-40**:1870–1878 (1992).
5. I. V. Lindell, S. A. Tretyakov, and A. J. Viitanen, Plane-wave propagation in a uniaxial chiro-omega medium, *Microwave Opt. Technol. Lett.* **6**:517–520 (1993).
6. I. V. Lindell and A. J. Viitanen, Plane wave propagation in uniaxial bianisotropic medium, *Electron. Lett.* **29**:150–152 (1993).
7. A. Lakhtakia and W. S. Weiglhofer, Axial propagation in general helicoidal bianisotropic media, *Microwave Opt. Technol. Lett.* **6**:804–806 (1993).
8. S. A. Tretyakov and A. A. Sochava, Proposed composite materials for nonreflected shields and antenna radomes, *Electron. Lett.* **29**:1048–1049 (1993).
9. A. J. Viitanen and I. V. Lindell, Plane wave propagation in a uniaxial bianisotropic medium with an application to a polarization transformer, *Int. J. Infrared Millimeter Waves* **14**:1993–2010 (1993).
10. S. He and I. V. Lindell, Propagation eigenmodes for plane waves in a uniaxial bianisotropic medium and reflection from a planar interface, *IEEE Trans. Anten. Propag.* **AP-41**: 1659–1664 (1993).
11. S. He, Wave propagation through dielectric-uniaxial bianisotropic interface and the computation of Brewster angles, *J. Opt. Soc. Am. A* **11**:2403–2409 (1993).
12. S. He, Y. Hu, and S. Strom, Electromagnetic scattering from a stratified bianisotropic slab, *IEEE Trans. Anten. Propag.* **AP-42**:856–858 (1994).
13. M. Norgren and S. He, General scheme for electromagentic reflection and transmission for composite structures of complex materials, *IEE Proc. Microwave Anten. Propag.* **142**:52–56 (1995).
14. A. Lakhtakia and W. S. Weiglhofer, Influence of pitch on attenuation and handedness of axial propagation modes in helicoidal bianisotropic media, *Opt. Commun.* **111**:199 (1994).
15. A. Lakhtakia and W. S. Weiglhofer, On light propagation in helicoidal bianisotropic medium, *Proc. Roy. Soc. Lond. A* **438**:419–437 (1995).
16. A. Lakhtakia and W. S. Weiglhofer, Further results on light propagation in helicoidal bianisotropic mediums: oblique propagation, *Proc. Roy. Soc. Lond. A* **453**:93–105 (1997).
17. M. Norgren, Optimal design using stratified bianisotropic media: Application to anti-reflection coatings, *J. Electromagn. Waves Appl.* **12**:939–959 (1998).
18. D. Y. Khaliullin and S. A. Tretyakov, Reflection and transmission coefficients for thin bianisotropic layers, *IEE Proc. Microwave Anten. Propag.* **145**:163–168 (1998).
19. C. R. Simovski, M. S. Kondratjev, P. A. Belov, and S. A. Tretyakov, Interaction effects in two-dimensional bianisotropic arrays, *IEEE Trans. Anten. Propag.* **AP-47**:1429–1439 (1999).
20. V. Losada, R. R. Boix, and M. H. Horno, Full-wave analysis of circular microstrip resonators in multilayered media containing uniaxial anisotropic dielectric, magnetized ferrites, and chiral materials, *IEEE Trans. Anten. Propag.* **AP-48**: 1057–1064 (2000).
21. A. Toscano and L. Vegni, Analysis of printed-circuit antennas with chiral substrates with the method of lines, *IEEE Trans. Anten. Propag.* **AP-49**:48–54 (2001).
22. E. O. Kamenetskii, Nonreciprocal microwave bianisotropic materials: Reciprocity theorem and network reciprocity, *IEEE Trans. Anten. Propag.* **AP-49**:361–366 (2001).
23. L. Vegni, F. Bilotti, and A. Toscano, Analysis of cavity backed rectangular patch antennas with inhomogeneous chiral substrates via a FEM-BEM formulation, *IEEE Trans. Magn.* **37**:3260–3263 (2001).
24. E. L. Tan, Vector wave function expansions of dyadic Green's functions for bianisotropic media, *IEE Proc. H, Microwaves Anten. Propag.* **149**:57–63 (2002).

25. W. S. Weiglhofer and A. Lakhtakia, Analytical investigation of electromagnetic waves in bianisotropic media, *IEE Proc. H, Microwaves Anten. Propag.* **149**:138–139 (2002).
26. F. Bilotti, A. Toscano, and L. Vegni, FEM-BEM formulation for the analysis of cavity-backed patch antennas on chiral substrates, *IEEE Trans. Anten. Propag.* **AP-51**:306–311 (2003).
27. F. Bilotti, L. Vegni, and A. Toscano, Radiation and scattering features of patch antennas with bianisotropic substrates, *IEEE Trans. Anten. Propag.* **AP-51**:449–456 (2003).
28. A. Alu, F. Bilotti, and L. Vegni, Extended method of line procedure for the analysis of microwave components with bianisotropic inhomogeneous media, *IEEE Trans. Anten. Propag.* **AP-51**:1582–1589 (2003).
29. W. Y. Yin, W. Wan, and W. B. Wang, Guided electromagnetic waves in parallel-plate gyroelectromagnetic biaxial chirowaveguides, *J. Modern Opt.* **41**:59–65 (1994).
30. W. Y. Yin and W. Wan, Spectral-domain decoupling method of electromagnetic waves propagation and radiating in bianisotropic gyroelectromagnetic chiral media, *Microwave Opt. Technol. Lett.* **7**:187–193 (1994).
31. W. Y. Yin, W. Wan, and W. B. Wang, Mode characteristics in a circular uniaxial chiro-omega waveguide, *Electron. Lett.* **30**:1072–1073 (1994).
32. W. Y. Yin, W. Wan, and W. B. Wang, Guided electromagnetic waves in gyrotropic chirowave-guides, *IEEE Trans. Microwave Theory Tech.* **42**:2156–2163 (1994).
33. W. Y. Yin and W. Wan, The combined effect of dispersion and damping on the scattering characteristics of Faraday chiral cylindrical scatterers, *Microwave Opt. Technol. Lett.* **10**: 189–194 (1995).
34. W. Y. Yin, W. Wan, and W. B. Wang, Radiation from a dipole antenna on two-layer grounded Faraday chiral substrates, *J. Electromagn. Waves Appl.* **7**:1027–1044 (1995).
35. W. Y. Yin, W. Wan, and W. B. Wang, Mode bifurcation and attenuation in circular Faraday chirowaveguide-summary, *J. Electromagn. Waves Appl.* **10**:1389–1394 (1996).
36. W. Y. Yin, Scattering by a linear array of uniaxial bianisotropic chiral cylinders, *Microwave Opt. Technol. Lett.* **12**: 287–295 (1996).
37. W. Y. Yin, Scattering by two parallel cladded bianisotropic uniaxial chiral fibers, *J. Opt. Soc. Am. B* **13**:2833–2840 (1996).
38. W. Y. Yin, G. H. Nan, and I. Wolff, The combined effects of chiral operation in multilayered bianisotropic substrates, *Prog. Electromagn. Res.* **PIER-20**:153–178 (1998).
39. W. Y. Yin and I. Wolff, Bilateral coplanar waveguide and periodic microstrip line in bianisotropic superstrate-substrate structures, *J. Electromagn. Waves Appl.* **13**:259–275 (1999).
40. W. Y. Yin, L. W. Li, and I. Wolff, The compatible effects of gyrotropy and chirality in biaxially bianisotropic chiral- and chiro-ferrite microstrip line structures, *Int. J. Num. Model. Electron. Networks Devices Fields* **10**:209–227 (1999).
41. W. Y. Yin and L.W. Li, Multiple scattering from gyrotropic bianisotropic cylinders of arbitrary cross-sections using the modeling technique, *Phys. Rev. E* **60**:918–925 (1999).
42. W. Y. Yin, L.W. Li, and M. S. Leong, Hybrid effects of gyrotropic and chirality in ferrite fin-lines, *Microwave Opt. Technol. Lett.* **25**:40–44 (2000).
43. W. Y. Yin, L.W. Li, T. S. Yeo, and M. S. Leong, Effects of double helical conductances of surfaces on multiple scattering of eccentrically two-layered bianisotropic cylinder array: The case of $TE_z$-wave incidence, *Electromagnetics* **20**:369–382 (2000).
44. W. Y. Yin and L.W. Li, Effects of helical conductance of surfaces on multiple interaction of composite eccentrically bianisotropic cylinders: The case of $TM_z$-wave incidence, *Prog. Electromagn. Res.* **PIER-23**:221–236 (2001).
45. W. Y. Yin, L.W. Li, M. S. Leong, and T. S. Yeo, Indirect modeling of the scattering from two-dimensional composite uniaxial bianisotropic cylinders of arbitrary cross sections, *Int. J. Num. Model. Electron. Networks Devices Fields* **14**:237–256 (2001).
46. V. Dmitriev, Constitutive tensors and general properties of complex and bianisotropic media described by continuous groups of symmetry, *Electron. Lett.* **34**:532–534 (1998).
47. V. Dmitriev, Group theoretical approach to determine structure of complex and composite media constitutive tensors, *Electron. Lett.* **34**:743–745 (1998).
48. V. Dmitriev, Symmetry description of continuous homogeneous isotropic media under external perturbation, *Electron. Lett.* **34**:745–747 (1998).
49. V. Dmitriev, Constitutive tensor nomenclature of Kamenetskii's media, *Microwave Opt. Technol. Lett.* **18**:280–284 (1998).
50. W. Y. Yin and L.W. Li, Reflection and transmission characteristics of bianisotropic slabs with(out) a soft- and hard-surface: The clarification of the continuous magnetic group of symmetry, *Microwave Opt. Technol. Lett.* **21**:351–356 (1999).
51. W. Y. Yin and L. W. Li, Radiation patterns of a dipole antenna array on bianisotropic substrates with a soft- and hard-surface: The clarification of the continuous magnetic group of symmetry, *J. Electromagn. Waves Appl.* **13**:1173–1189 (1999).
52. W. Y. Yin, L.W. Li, T. S. Yeo, and M. S. Leong, The Muller matrix and scattering cross section of a linear array of eccentrically two-layered bianisotropic cylinders with double surface helical conductances: Clarifications of the magnetic symmetry groups—abstract, *J. Electromagn. Waves Appl.* **14**:1135–1137 (2000).
53. W. Y. Yin, B. Guo, and X. T. Dong, Comparative study on the interaction of electromagnetic waves with multi-layer omega(chiro)ferrite slabs, *J. Electromagn. Waves Appl.* **17**:15–29 (2003).
54. W. Y. Yin, B. Guo, L. W. Li, Y. B. Gan, and I. Wolff, Constitutive parameter effects in some multilayered bianisotropic microstrip lines: Clarification of magnetic groups of symmetry, *IEE Proc. Microwave Anten. Propag.* **150**:18–22 (2003).
55. C. M. Krowne, Full-wave spectral Green's function integral equation calculation of coplanar ferroelectric thin film transmission structures, *Microwave Opt. Technol. Lett.* **26**:187–192 (2000).
56. C. M. Krowne, Theoretical considerations for finding anisotropic permittivity in layered ferroelectric/ferromagnetic structures from full-wave electromagnetic simulations, *Microwave Opt. Technol. Lett.* **28**:63–69 (2001).
57. C. M. Krowne, M. Daniel, S. W. Kirchoefer, and J. M. Pond, Anisotropic permittivity and attenuation extraction from propagation constant measurements using an anisotropic full-wave Green's function solver for coplanar ferroelectric thin-film devices, *IEEE Trans. Microwave Theory Tech.* **MTT-50**:537–548 (2002).
58. C. M. Krowne, Waveguiding structures employing the solid-state magnetoplasma effect for microwave and millimeter-wave propagation, *IEE Proc. Microwave Anten. Propag.* **140**:147–164 (1993).
59. R. Pregla, Method of lines for the analysis of multilayered gyrotropic waveguide structures, *IEE Proc. Microwave Anten. Propag.* **140**:183–192 (1993).

60. F. Mesa and M. Horno, Application of the spectral domain method for the study of surface slow waves in nonreciprocal planar structures with a multilayered gyrotropic substrate, *IEE Proc. Microwave Anten. Propag.* **140**:193–200 (1993).
61. L. E. Davis, R. Sloan, and D. K. Paul, $TM_{0m}$ modes in transversely magnetized semiconductor-filled coaxial waveguide and parallel plates, *IEE Proc. Microwave Anten. Propag.* **140**:211–218 (1993).
62. T. Nurgaliev, S. Miteva, A. P. Jenkins, and D. D. Hughes, Investigation of MW characteristics of HTS microstrip and coplanar resonators with ferrite thin-film components, *IEEE Trans. Microwave Theory Tech.* **51**:33–40 (2003).
63. I. V. Lindell, Variational method for the analysis of lossless biisotropic (nonreciprocal chiral) waveguides, *IEEE Trans. Microwave Theory Tech.* **MTT-40**:402–405 (1992).
64. P. Pelet and N. Engheta, Modal analysis for rectangular chirowaveguides with metallic walls using the finite-difference method, *J. Electromagn. Waves Appl.* **6**:1277–1285 (1992).
65. P. K. Koivisto, S. A. Tretyakov, and M. I. Oksanen, Waveguides filled with biisotropic media, *Radio Sci.* **28**:675–686 (1993).
66. H. Cory and S. Waxman, Coupling between chiral slabs, *J. Electromagn. Waves Appl.* **7**:1609–1622 (1993).
67. A. L. Topa and C. R. Pavia, New biorthogonality relations for inhomogeneous biisotropic planar waveguides, *IEEE Trans. Microwave Theory Tech.* **MTT-42**:629–634 (1994).
68. W. Y. Yin and W. B. Wang, Transverse coupling between two general biisotropic slabs, *Int. J. Infrared Millimeter Waves* **15**:1065–1072 (1994).
69. W. Y. Yin, W. Wan, and W. B. Wang, Hybrid mode characteristics in multilayered Faraday chirowaveguides, *Prog. Electromagn. Res.* **PIER-13**:149–168 (1996).
70. L. W. Li, M. S. Leong, P. S. Kooi, T. S. Yeo, and K.-H. Tan, Rectangular modes and dyadic Green's functions in rectangular chirowaveguides, I. Theory, *IEEE Trans. Microwave Theory Tech.* **MTT-47**:67–73 (1999).
71. L. W. Li, M. S. Leong, P. S. Kooi, T. S. Yeo, and K.-H. Tan, Rectangular modes and dyadic Green's functions in rectangular chirowaveguides, II. Numerical results, *IEEE Trans. Microwave Theory Tech.* **MTT-47**:74–81 (1999).
72. W. Y. Yin and P. Li, The focal points of radially spherical chirolenses, *Microwave Opt. Technol. Lett.* **6**:561–564 (1993).
73. W. Y. Yin and P. Li, The theory of multilayered spherical chirodome, *Microwave Opt. Technol. Lett.* **7**:179–182 (1993).
74. P. Pelet and N. Engheta, Chirostrip antenna: Line source problem, *J. Electromagn. Waves Appl.* **6**:771–794 (1992).
75. W. Y. Yin and W. B. Wang, The analysis of the radiation characteristics of a two-layered chirostrip dipole antenna using dyadic Green's function, *Microwave Opt. Technol. Lett.* **6**:221–223 (1993).
76. A. Toscano and L. Vegni, A new efficient moment of method formulation for the design of microstrip antennas over a chiral grounded slab, *J. Electromagn. Waves Appl.* **11**: 567–592 (1997).
77. A. J. Viitanen, Chiral soft-surface waveguide mode transformer, *Microwave Opt. Technol. Lett.* **27**:168–171 (2000).
78. A. J. Viitanen, Chiral hard surface waveguide mode transformer, *IEEE Trans. Microwave Theory Tech.* **MTT-48**:1077–1079 (2000).
79. X. Wu and D. L. Jaggard, Discontinuities in planar chirowaveguides, *IEEE Trans. Microwave Theory Tech.* **MTT-45**: 640–647 (2000).
80. X. Wu and D. L. Jaggard, A comprehensive study of discontinuities in chirowaveguides, *IEEE Trans. Microwave Theory Tech.* **MTT-50**:2320–2330 (2002).
81. D. Worasawate, J. R. Mautz, and E. Arvas, Electromagnetic resonances and Q factors of a chiral sphere, *IEEE Trans. Anten. Propag.* **AP-52**:213–219 (2004).
82. M. Zhang, T. S. Yeo, L. W. Li, and M. S. Leong, Electromagnetic scattering by a multilayer gyrotropic bianisotropic circular cylinder, *Prog. Electromagn. Res.* **PIER-40**:91–111 (2003).
83. M. Zhang, L. W. Li, T. S. Yeo, and M. S. Leong, Scattering by a gyrotropic bianisotropic cylinder of arbitrary cross section: An analysis using generalized multipole technique, *Prog. Electromagn. Res.* **PIER-40**:315–333 (2003).
84. W. S. Weiglhofer and S. O. Hansen, Faraday chiral media revisited-I fields and sources, *IEEE Trans. Anten. Propag.* **AP-47**:807–814 (1999).
85. R. D. Graglia, M. S. Sarto, and P. L. E. Uslenghi, TE and TM modes in cylindrical metallic structures filled with bianisotropic materials, *IEEE Trans. Microwave Theory Tech.* **MTT-44**:1470–1477 (1996).
86. F. Olyslager, Properties of and generalized full-wave transmission line models for hybrid bianisotropic waveguides, *IEEE Trans. Microwave Theory Tech.* **MTT-44**:2064–2075 (1996).
87. V. Dmitriev, Comments on "Properties of and generalized full-wave transmission line models for hybrid bianisotropic waveguides". *IEEE Trans. Microwave Theory Tech.* **MTT-47**:655–659 (1999).
88. Xu Yansheng and R. G. Bosisio, A study on the solutions of chirowaveguides and bianisotropic waveguides with the used of coupled-mode analysis, *Microwave Opt. Technol. Lett.* **14**:308–311 (1997).
89. P. L. E. Uslenghi, TE-TM decoupling for guided propagation in bianisotropic media. *IEEE Trans. Anten. Propag.* **AP-45**:284–286 (1997).
90. E. O. Kamenetskii, On the technology of making chiral and bianisotropic waveguides or microwave propagation, *Microwave Opt. Technol. Lett.* **14**:103–107 (1996).
91. G. Plaza, F. Mesa, and F. Medina, On the use of SDA for the analysis of boxed planar lines with complex media, *IEEE Trans. Microwave Theory Tech.* **49**:1365–1368 (2001).
92. L. Valor and J. Zapata, An efficient finite element formulation to analyze waveguides with lossy inhomogeneous bi-anisotropic materials, *IEEE Trans. Microwave Theory Tech.* **MTT-44**:291–296 (1996).
93. L. Valor and J. Zapata, A simplified formulation to analyze inhomogeneous waveguide with lossy chiral media using the finite-element method, *IEEE Trans. Microwave Theory Tech.* **MTT-46**:185–187 (1998).
94. J. A. M. Svedin, Propagation analysis of chirowaveguides using finite-element method, *IEEE Trans. Microwave Theory Tech.* **MTT-38**:1488–1496 (1990).
95. A. Grande, A. C. L. Cabeceira, J. Represa, P. P. M. So, and W. J. R. Hoefer, FDTD modeling of transient microwave signals in dispersive and lossy bi-isotropic media, *IEEE Trans. Microwave Theory Tech.* **MTT-52**:773–784 (2004).